

# Investigations of lithium insertion into transition metal oxide cathodes

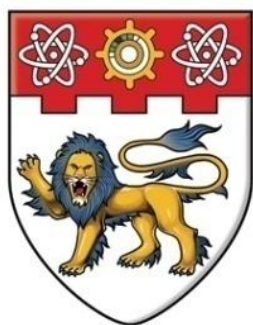
Ko, Yah Wen

2014

Ko, Y. W. (2014). Investigations of lithium insertion into transition metal oxide cathodes.  
Doctoral thesis, Nanyang Technological University, Singapore.

<https://hdl.handle.net/10356/62374>

<https://doi.org/10.32657/10356/62374>



**NANYANG**  
**TECHNOLOGICAL**  
**UNIVERSITY**

**INVESTIGATIONS OF LITHIUM INSERTION  
INTO TRANSITION METAL OXIDE  
CATHODES**

**KO YAH WEN**

**SCHOOL OF MATERIALS SCIENCE AND ENGINEERING  
2014**



**INVESTIGATIONS OF LITHIUM INSERTION  
INTO TRANSITION METAL OXIDE  
CATHODES**

**KO YAH WEN**

**SCHOOL OF MATERIALS SCIENCE AND ENGINEERING**

A thesis submitted to the Nanyang Technological University in partial  
fulfillment of the requirement for the degree of

Doctor of Philosophy

2014





---

# Abstract

To the pursuit of powerful lithium ion battery for integration into future automobiles and various advanced applications, new generation cathode with good storage ability and sustainability is intensively studied and explored. Transition metal oxides with ordered rocksalt structure are one the mostly investigated candidates, which are able to insert/extract lithium ions with good structural tolerance for low power applications. However, the practicality of ordered rocksalt-based materials for high power applications are still restrained several intrinsic issues. Therefore, advancement in current lithium ion batteries technology are demanded to fulfill the application requirements.

In this thesis, preparation of several lithium transition metal oxides with rocksalt structure by different synthesis methods is presented. Their electrochemical properties as lithium ion battery cathode are discussed. This thesis aims to address the core issues related to ordered rocksalt-based materials from two perspectives, *i.e.* applicability of nanomaterials in improving the battery performance and comprehensive studies on the effect of cation substitution on the electrochemical characteristics. Another aim is to extend the investigation into feasibility of disordered-rocksalt based material to be applied as lithium ion battery cathode, which includes detailed studies on the effect of cation ordering on the electrochemical properties.

Based on the results of systematic experiments in ordered-rocksalt based material (lithium trivanadate,  $\text{Li}_{1.2}\text{V}_3\text{O}_8$ ) with different morphology, the electrochemical performance of rocksalt-based cathodes is highly dependent on the particle size and morphology of intercalation host. Optimum cation substitution on ordered rocksalt-based  $\text{Li}_{1.2}\text{V}_3\text{O}_8$  demonstrates the possibility to circumvent the structural instability issues and further enhance lithium storage capabilities, indicating their promising potential to replace conventional  $\text{LiCoO}_2$  cathode. The study is then extended to exploration of lithium intercalation into partially disordered rocksalt-based  $\text{Li}_2\text{NiTiO}_4$ . To deepen the understanding of lithium insertion mechanism in correlation with structural properties, detailed characterizations on cycled electrodes are conducted.

# Acknowledgements

The author would like to express her deepest gratitude to:

Assoc. Prof. Madhavi Srinivasan

Dr. Stevin Snellius Pramana

Dr. Grace Wee Tsyh Ying

Dr. Tay Yee Yan

Dr. Cheah Yan Ling

Dr. Teh Pei Fen

Dr. Wong Chui Ling

Dr. Mak Wai Fatt

Mr. Sutanto

Ms. Tan Hui Teng

Mr. Arun Nagasubramanian

Ms. Li Linlin

Ms. Chen Hanyi

Mr. Lee Chee Siang

Mr. Rohit Satish

Ms. Shubha Nageswaran

Mr. Vivek Nair

Mr. Paul Wang Lu Yuan

Mr. Shen Nan

Ms. Zheng Xi

Laboratory technicians in FACTS Lab, Inorganic Lab and Consumable Stores  
(NTU, MSE)

My families and my dearest friends

I am really appreciative and fortunate to know each of you. Thanks for your valuable companionship and understanding whenever I am facing difficulties or being demotivated. I am truly appreciative of your constant support, encouragement, guidance, inspiration and insightful suggestions during the course of this dissertation. It would not have been possible to finish this thesis without you.

# Table of Contents

Abstract .....	i
Acknowledgements .....	ii
Table of Contents .....	iii
List of Figures .....	viii
List of Tables .....	xii
List of Schemes .....	xiii
List of Abbreviations .....	xiv
Chapter 1    Introduction .....	1
1.1    Problem Statement .....	1
1.2    Motivation .....	2
1.3    Research Scope and Objectives .....	4
1.3.1    Investigate the effect of nanostructuring and surface modification of transition metal oxides in battery performance .....	4
1.3.2    Investigate the influence of cation substitution in ordered rocksalt structure on structural and electrochemical properties .....	4
1.3.3    Investigate the structural evolution of cathodes during lithium intercalation and deintercalation .....	5
1.4    Dissertation overview .....	5
1.5    Findings and Outcomes .....	6
Chapter 2    Literature Review .....	7
2.1    Basic Principles of Lithium Ion Batteries .....	7
2.2    Lithium Intercalation Mechanism of Cathodes in LIBs .....	8
2.2.1    Lithium Intercalation into Ordered Rock Salt Type Structure .....	9
2.2.1.1    Three-dimensional (3D) Framework - Spinel $\text{LiMn}_2\text{O}_4$ .....	9
2.2.1.2    Two-dimensional (2D) Framework – $\text{LiMO}_2$ .....	10

2.2.1.3	Two-dimensional (2D) Framework – Vanadium-based Oxide .....	11
2.3	Current Issues in Vanadium-based Oxides .....	12
2.3.1	Vanadium Oxide .....	12
2.3.2	Alkaline Metal Trivanadate $AV_3O_8$ (A = Li, Na, K) .....	14
2.4	Exploration on Potential of Lithium Intercalation into Disordered Rocksalt .....	21
2.4.1	Current Issues in Disordered Rock salt Materials.....	25
2.4.2	Titanium-based Oxides .....	26
Chapter 3	Materials and Methods.....	28
3.1	Materials Synthesis.....	28
3.1.1	High energy ball milling .....	28
3.1.2	Electrospinning .....	29
3.1.2.1	Preparation of $Li_{1.2}V_3O_8$ single nanobelt and hierarchical nanobelt.....	29
3.1.2.2	Preparation of $Li_{1.2}V_{3-x}Al_xO_8$ (x = 0.03, 0.05) hierarchical nanobelt.....	30
3.1.2.3	Preparation of $Na_{1.2}V_3O_8$ single nanobelt and hierarchical nanobelt.....	31
3.1.3	Sol Gel.....	31
3.1.3.1	Carbon coating on $Li_2NiTiO_4$ .....	32
3.2	Characterization procedures .....	32
3.2.1	Microscopy methods .....	32
3.2.1.1	Field emission scanning electron microscope (FESEM).....	32
3.2.1.2	Transmission electron microscope (TEM) .....	32
3.2.2	Diffraction methods .....	33
3.2.2.1	Powder x-ray diffraction (XRD).....	33
3.2.2.2	Thin film x-ray diffraction (XRD).....	33
3.2.2.3	Selected area electron diffraction (SAED) .....	33
3.2.3	Spectroscopy methods.....	34
3.2.3.1	Fourier transform infrared spectroscopy (FTIR) .....	34
3.2.3.2	Energy dispersive x-ray spectroscopy (EDS).....	34
3.2.4	Thermal analysis .....	34
3.2.4.1	Thermogravimetric analysis (TGA) .....	34
3.3	Electrochemical Studies .....	35

3.3.1	2016 Cell fabrication.....	35
3.3.2	Cyclic voltammetry.....	35
3.3.3	Galvanostatic cycling.....	35
3.3.4	Electrochemical impedance spectroscopy .....	36
3.3.5	Ex situ electrode preparation .....	36
Chapter 4	Results.....	37
4.1	$\text{Li}_{1.2}\text{V}_3\text{O}_8$ .....	37
4.1.1	Ball milled $\text{Li}_{1.2}\text{V}_3\text{O}_8$ .....	38
4.1.2	Ball milled $\text{Li}_{1.2}\text{V}_3\text{O}_8$ nanoparticles: Comparison of electrochemical performance .....	41
4.1.3	Electrospun $\text{Li}_{1.2}\text{V}_3\text{O}_8$ nanobelts: Effect of sintering temperature on morphology growth.....	45
4.1.4	Electrospun $\text{Li}_{1.2}\text{V}_3\text{O}_8$ nanobelts: Materials characterization .....	47
4.1.5	Electrospun $\text{Li}_{1.2}\text{V}_3\text{O}_8$ nanobelts: Comparison of electrochemical performance .....	50
4.1.6	Electrospun $\text{Li}_{1.2}\text{V}_{3-x}\text{Al}_x\text{O}_8$ nanobelts: Materials characterization .....	53
4.1.7	Electrospun $\text{Li}_{1.2}\text{V}_{3-x}\text{Al}_x\text{O}_8$ nanobelts: Comparison of electrochemical performance .....	56
4.1.8	Ball milled $\text{Na}_{1.2}\text{V}_3\text{O}_8$ nanoparticles: Materials characterization .....	59
4.1.9	Ball milled $\text{Na}_{1.2}\text{V}_3\text{O}_8$ nanoparticles: Comparison of electrochemical performance .....	61
4.1.10	Electrospun $\text{Na}_{1.2}\text{V}_3\text{O}_8$ nanobelts: Effect of sintering profile on morphology growth .....	64
4.1.11	Electrospun $\text{Na}_{1.2}\text{V}_3\text{O}_8$ nanobelt: Materials characterization .....	66
4.1.12	Electrospun $\text{Na}_{1.2}\text{V}_3\text{O}_8$ nanobelts: Comparison of electrochemical performance .....	71
4.2	$\text{Li}_2\text{NiTiO}_4$ .....	75

4.2.1	Sol gel synthesized $\text{Li}_2\text{NiTiO}_4$ nanoparticles: Materials characterization ...	75
4.2.2	Sol gel synthesized $\text{Li}_2\text{NiTiO}_4$ nanoparticles: Electrochemical performance . .....	76
4.2.3	Sol gel synthesized lithium excess LNT nanoparticles: Materials characterization .....	81
4.2.4	Sol gel synthesized lithium excess LNT nanoparticles: Comparison of electrochemical performance .....	82
4.2.5	Effect of carbon coating on sol gel synthesized $\text{Li}_2\text{NiTiO}_4$ nanoparticles: Materials characterization .....	84
4.2.6	Effect of carbon coating on sol gel synthesized $\text{Li}_2\text{NiTiO}_4$ nanoparticles: Electrochemical performance .....	88
Chapter 5	Discussion .....	92
5.1	Effect of nanostructuring .....	92
5.1.1	Effect of particle size .....	92
5.1.2	Effect of morphology .....	95
5.2	Effect of cation substitution .....	98
5.2.1	Substitution at vanadium sites of $\text{Li}_{1.2}\text{V}_3\text{O}_8$ .....	98
5.2.2	Substitution at lithium sites of $\text{Li}_{1.2}\text{V}_3\text{O}_8$ .....	104
5.2.2.1	General comparison between $\text{Li}_{1.2}\text{V}_3\text{O}_8$ and $\text{Na}_{1.2}\text{V}_3\text{O}_8$ .....	105
5.2.2.2	Effect of crystallinity on electrochemical behavior of $\text{Li}_{1.2}\text{V}_3\text{O}_8$ and $\text{Na}_{1.2}\text{V}_3\text{O}_8$ .....	107
5.3	Lithium intercalation/deintercalation mechanism into rocksalt structure .....	109
5.3.1	Structural evolution study of $\text{Na}_{1.2}\text{V}_3\text{O}_8$ nanobelts .....	109
5.3.2	Structural evolution study of $\text{Li}_2\text{NiTiO}_4$ .....	112
Chapter 6	Conclusion .....	115
6.1	Novel Contributions .....	117
6.1.1	Scientific contributions .....	117
6.1.2	Technological significances .....	118
Chapter 7	Recommendations for Future Works .....	119

---

7.1	Fundamental studies on structural evolution by <i>in situ</i> characterizations.....	119
7.2	Exploration on mixed-metal solid solution derivative of $\text{Li}_2\text{Ni}_{1-x}\text{MTiO}_4$ (M = Fe, Co) .....	120
7.3	Application in Full LIB .....	120
References.....		121
Publications.....		134



# List of Figures

<b>Figure 2-1</b>	Schematic diagram of a lithium ion cell. The cell is composed of a cathode, anode, separator and electrolyte.[26] .....7
<b>Figure 2-2</b>	Crystal structure of $\text{LiMn}_2\text{O}_4$ and $\text{Li}_2\text{Mn}_2\text{O}_4$ (Yellow: $\text{LiO}_6$ octahedral; Light Blue: $\text{MnO}_6$ octahedral) .....10
<b>Figure 2-3</b>	Crystal structure of $\text{LiCoO}_2$ (Green: Lithium ions, Blue: $\text{CoO}_6$ octahedral) .....10
<b>Figure 2-4</b>	Crystal structure of $\text{LiV}_3\text{O}_8$ and $\text{Li}_{4.77}\text{V}_3\text{O}_8$ (Green: Lithium ions, Brown: $\text{VO}_n$ polyhedral).....12
<b>Figure 2-5</b>	Illustrations of four common types of cubic rocksalt structures. (a) $\alpha$ - $\text{LiFeO}_2$ , (b) layered $\alpha$ - $\text{NaFeO}_2$ , (c) spinel $\text{LiCoO}_2$ and (d) $\gamma$ - $\text{LiFeO}_2$ [15] .....22
<b>Figure 2-6</b>	Illustration of local environment for o-t-o lithium diffusion in rocksalt type lithium transition metal oxide. (a) o-t-o diffusion: two tetrahedral path connect a pair of neighbouring octahedral sites, (b) 0-TM channel: the activation state is not face-shared with any octahedral transition metal, (c) 1-TM: the activation state shares faces with one transition metal, (d) 2-TM: the activation state shares faces with two transition metal. [14].....23
<b>Figure 2-7</b>	Crystal structure of $\text{Li}_2\text{NiTiO}_4$ with (a) disordered rocksalt (Green: $\text{LiO}_6$ , $\text{MO}_6$ and $\text{TiO}_6$ octahedral randomly distributed within the structure) and (b) ordered $\text{Li}_2\text{TiO}_3$ structure (Blue: $\text{TiO}_6$ octahedral; Green: Lithium ions); the full lithium ions layer of $\text{Li}_2\text{TiO}_3$ represents the lithium-rich $[\text{Li}_{2/3}(\text{Ni,Ti})_{1/3}]$ cation layer; the partial lithium layer with $\text{TiO}_6$ octahedral represents the lithium-poor $[\text{Li}_{1/3}(\text{Ni,Ti})_{2/3}]$ cation layer [120]. .....27
<b>Figure 4-1</b>	FESEM images of annealed $\text{Li}_{1.2}\text{V}_3\text{O}_8$ at different temperature. (a) LVO-NP300, (b) LVO-NP400 and (c) LVO-NP500 .....38
<b>Figure 4-2</b>	XRD patterns and Rietveld refinements of LVO-NP300, LVO-NP400 and LVO-NP500.....39
<b>Figure 4-3</b>	FTIR analysis of LVO-NP300, LVO-NP400 and LVO-NP500.....40
<b>Figure 4-4</b>	CV of (a)LVO-NP300, (b) LVO-NP400 and (c) LVO-NP500 at $0.01 \text{ mV s}^{-1}$ for first three cycles .....42
<b>Figure 4-5</b>	Comparison of cycling performance between LVO-NP300, LVO-NP400 and LVO-NP500.....44
<b>Figure 4-6</b>	Galvanostatic cycling results of annealed $\text{Li}_{1.2}\text{V}_3\text{O}_8$ at current density of $200 \text{ mA g}^{-1}$ : (a) 1 <sup>st</sup> cycle and (b) 100 <sup>th</sup> cycle at scan rate of $0.1 \text{ mV s}^{-1}$ .44
<b>Figure 4-7</b>	TGA of as-spun $\text{Li}_{1.2}\text{V}_3\text{O}_8$ nanofibers. ....45
<b>Figure 4-8</b>	FESEM images of (a) as-spun nanofibers, (b) LVO-HNB400 and (c) LVO-SNB500 .....47
<b>Figure 4-9</b>	Rietveld refinement of XRD pattern for $\text{Li}_{1.2}\text{V}_3\text{O}_8$ nanobelts .....48
<b>Figure 4-10</b>	FTIR analysis of $\text{Li}_{1.2}\text{V}_3\text{O}_8$ formation. (a) PVP, (b) As-spun nanofibers, (c) LVO-HNB400 and (d) LVO-SNB500 (left). Enlarged version of

	FTIR with specific bands for (c) LVO-HNB400 and (d) LVO-SNB500. ....49
<b>Figure 4-11</b>	CV of (a) LVO-HNB400, (b) LVO-SNB500 at $0.1 \text{ mV s}^{-1}$ for first three cycles and (c) comparison of first cycle CV scan between LVO-HNB400 and LVO-SNB500.....50
<b>Figure 4-12</b>	Cycling performance of LVO-HNB400 and LVO-SNB500 at different current densities.....51
<b>Figure 4-13</b>	Galvanostatic profiles of electrospun $\text{Li}_{1.2}\text{V}_3\text{O}_8$ nanobelts: (a) LVO-HNB400 and (b) LVO-SNB500 for first three cycles at current density of $200 \text{ mA g}^{-1}$ . Comparison of galvanostatic charge/discharge curves between LVO-HNB400 and LVO-SNB500 for (c) first cycle and (d) second cycle.....52
<b>Figure 4-14</b>	FESEM images of (a) $\text{Li}_{1.2}\text{V}_{2.97}\text{Al}_{0.03}\text{O}_8$ (LVA3O-HNB) and (b) $\text{Li}_{1.2}\text{V}_{2.95}\text{Al}_{0.05}\text{O}_8$ (LVA5O-HNB). ....54
<b>Figure 4-15</b>	XRD Rietveld refined patterns of pristine LVO-HNB, LVA3O-HNB and LVA5O-HNB.....54
<b>Figure 4-16</b>	FTIR analysis of LVO-HNB400, LVA3O-HNB400 and LVA5O-HNB400.....55
<b>Figure 4-17</b>	CV of (a) LVO-HNB400, (b) LVA3O-HNB400 and (c) LVA5O-HNB400 for first three cycles at scan rate of $0.1 \text{ mV s}^{-1}$ .....57
<b>Figure 4-18</b>	Cycling performance of LVO, LVA3O and LVA5O at current density of (a) $200 \text{ mA g}^{-1}$ and (b) $600 \text{ mA g}^{-1}$ .....58
<b>Figure 4-19</b>	Galvanostatic cycling of $\text{Li}_{1.2}\text{V}_{3-x}\text{Al}_x\text{O}_8$ ( $x = 0, 0.03$ and $0.05$ ). (a) 1 <sup>st</sup> cycle and (b) 2 <sup>nd</sup> cycle at current density of $200 \text{ mA g}^{-1}$ ; (c) 1 <sup>st</sup> cycle and (d) 2 <sup>nd</sup> cycle at current density of $600 \text{ mA g}^{-1}$ . ....58
<b>Figure 4-20</b>	FESEM images of sintered $\text{Na}_{1.2}\text{V}_3\text{O}_8$ nanoparticles at (a) $400^\circ\text{C}$ (NVO-NP400) and (b) $500^\circ\text{C}$ (NVO-NP500). ....59
<b>Figure 4-21</b>	XRD patterns and Rietveld refinements of sintered $\text{Na}_{1.2}\text{V}_3\text{O}_8$ at temperature of $400^\circ\text{C}$ (NVO-NP400) and $500^\circ\text{C}$ (NVO-NP500).....60
<b>Figure 4-22</b>	FTIR analysis of $\text{Na}_{1.2}\text{V}_3\text{O}_8$ by HEBM and sintering at $400^\circ\text{C}$ (NVO-NP400) and $500^\circ\text{C}$ (NVO-NP500) .....60
<b>Figure 4-23</b>	CV of (a) NVO-NP400 and (b) NVO-NP500 at $0.01 \text{ mV s}^{-1}$ for first three cycles. ....62
<b>Figure 4-24</b>	Galvanostatic cycling of (a) NVO-NP400 and (b) NVO-NP500 for first, tenth and fortieth cycles at current density of $200 \text{ mA g}^{-1}$ , cycled between 1.5 to 4.0 V .....62
<b>Figure 4-25</b>	Cycling performance of NVO-NP400 and NVO-NP500.....64
<b>Figure 4-26</b>	Thermogravimetric analysis (TGA) of as-spun $\text{Na}_{1.2}\text{V}_3\text{O}_8$ nanofibers was conducted between $30^\circ\text{C}$ to $700^\circ\text{C}$ in air. ....64
<b>Figure 4-27</b>	FESEM images of (a) as-spun nanofibers, (b) hierarchical nanobelt (NVO-HNB) and (c) single nanobelt (NVO-SNB) .....66
<b>Figure 4-28</b>	Rietveld refinements of NVO-SNB and NVO-HNB .....67
<b>Figure 4-29</b>	FTIR of (a) PVP, (b) as-spun nanofibers, (c) NVO-SNB and (d) NVO-HNB (left). Enlarged version of FTIR with specified bands for (c) NVO-SNB and (d) NVO-HNB (right) .....68
<b>Figure 4-30</b>	(a) TEM micrograph of NVO-SNB, (b) HRTEM showing the lattice fringe of (001) and (010) plane of NVO-SNB which is 1.18 nm and 0.37

	nm and (c) its corresponding FFT, (d) TEM micrograph of NVO-HNB with the inset showing its hierarchical assembly in higher magnification, (e) HRTEM showing the lattice fringe of (101) plane of NVO-HNB which is 0.52 nm and (f) its corresponding FFT. ....69
<b>Figure 4-31</b>	Surface atom configurations of (a) NVO-SNB and (b) NVO-HNB with schematic top and side views of lithium diffusion path into active sites. (From the top view, lithium diffusion is directed into the plane).....70
<b>Figure 4-32</b>	Cyclic voltammetry of (a) NVO-SNB and (b) NVO-HNB at $0.1 \text{ mV s}^{-1}$ for 1st cycle, 2nd cycle and 3rd cycle.....72
<b>Figure 4-33</b>	Galvanostatic cycling of NVO-SNB and NVO-HNB for (a) 1st cycle, (b) 10th cycle and (c) 40th cycle. ....73
<b>Figure 4-34</b>	(a) Cycling performance of NVO-SNB and NVO-HNB at current density of $200 \text{ mAh g}^{-1}$ (b) Rate capability at various current densities. ....74
<b>Figure 4-35</b>	Powder XRD results of (a) LNT-PO and (b) LNT-DO.....76
<b>Figure 4-36</b>	(a) Galvanostatic profiles of partially ordered structured (LNT-PO) disordered structured (LNT-DO) $\text{Li}_2\text{NiTiO}_4$ for first cycle at current density of $10 \text{ mA g}^{-1}$ . (b) Magnified first charge profile between 3.0 – 4.0 V. ....77
<b>Figure 4-37</b>	Cycling performance of (a) LNT-PO, (b) LNT-DO at current density of $29 \text{ mA g}^{-1}$ , (c) comparison of discharge capacities between LNT-PO and LNT-DO. ....78
<b>Figure 4-38</b>	CV profiles of (a) LNT-PO and (b) LNT-DO for first four cycles at scan rate of $0.1 \text{ mV s}^{-1}$ .....79
<b>Figure 4-39</b>	XRD patterns of LNT2.4 and LNT3.6, the structural information was derived by Rietveld refinement method. ....82
<b>Figure 4-40</b>	CV scans of (a) LNT2.4 and (b) LNT3.6 for first three cycles at scan rate of $0.1 \text{ mV s}^{-1}$ . ....82
<b>Figure 4-41</b>	First galvanostatic cycling of LNT, LNT2.4 and LNT3.6.....83
<b>Figure 4-42</b>	Cycling performance of (a) LNT-PO, (b) LNT2.4 and (c) LNT3.6 at current density of $29 \text{ mA g}^{-1}$ .....84
<b>Figure 4-43</b>	TGA of LNT/C-3 and LNT/C-8. ....86
<b>Figure 4-44</b>	Observed and calculated XRD patterns of pristine LNT-PO, LNT/C-3 and LNT/C-8.....86
<b>Figure 4-45</b>	FESEM (left) and HRTEM (right) images of (a) LNT-PO; (b) LNT/C-3; and (c) LNT/C-8 .....87
<b>Figure 4-46</b>	CV scans of (a) LNT/C-3 and (b) LNT/C-8 at scan rate of $0.1 \text{ mV s}^{-1}$ between the potential range of 1.0 to 5.0 V .....88
<b>Figure 4-47</b>	First and second galvanostatic cycling of (a) LNT-PO, (b) LNT/C-3 and (c) LNT/C-8 at current density of $29 \text{ mA g}^{-1}$ .....88
<b>Figure 4-48</b>	Cycling performance of LNT-PO, LNT/C-3 and LNT/C-8 at current density of $29 \text{ mA g}^{-1}$ ; (b) Cycling test at current density of $10 \text{ mA g}^{-1}$ and $290 \text{ mA g}^{-1}$ for LNT-PO and LNT/C-8.....90
<b>Figure 4-49</b>	Nyquist plot of pristine LNT-PO, LNT/C-3 and LNT/C-8. ....91
<b>Figure 5-1</b>	Nyquist plots for (a) LVO-NP300, (b) LVO-NP400 and (c) LVO-NP500 .....94

<b>Figure 5-2</b>	Equivalent circuit used to fit the NYquist plot (Figure 5-1). The circuit elements are denoted as electrolyte resistance ( $R_e$ ), impedance of surface passivating film ( $R_{sf}$ ), associated constant phase element ( $CPE_{sf}$ ), charge transfer resistance ( $R_{ct}$ ) and the Warburg impedance ( $W$ ). .....94
<b>Figure 5-3</b>	Average diffusion time for nanoparticle and nanobelt with the same volume. ....97
<b>Figure 5-4</b>	(a) First galvanostatic profiles of pristine LVO, LVA3O and LVA5O at current density of $200 \text{ mA g}^{-1}$ , (b) Magnified view within potential range of 1.5-1.6 V .....99
<b>Figure 5-5</b>	(a) First galvanostatic curve of LVA3O and LVO-SNB500 at current density of $200 \text{ mA g}^{-1}$ , (b) magnified view within potential range of 1.5-2.75 V. ....103
<b>Figure 5-6</b>	(a) First galvanostatic profiles of LVO-HNB400, LVA3O and LVA5O at current density of $500 \text{ mA g}^{-1}$ , (b) Magnified view within potential range of 1.5-3.0 V.....104
<b>Figure 5-7</b>	Comparison between electrochemical behaviour of LVO-HNB400 and NVO-SNB by (a) CV scans at $0.1 \text{ mV s}^{-1}$ and (b) galvanostatic cycling at current density of $200 \text{ mA g}^{-1}$ .....105
<b>Figure 5-8</b>	Crystal structure of (a) $\text{Li}_{1.2}\text{V}_3\text{O}_8$ and (b) $\text{Na}_{1.2}\text{V}_3\text{O}_8$ .....108
<b>Figure 5-9</b>	The XRD pattern of NVO-SNB at different states of discharge and charge, (b) and (c) showing enlarged portion of partial XRD patterns. ....112
<b>Figure 5-10</b>	Selected regions of ex situ XRD patterns for pristine $\text{Li}_2\text{NiTiO}_4$ electrode materials during charging and discharging – (a) <b>133</b> peak; (b) <b>312</b> peak; (c) <b>002</b> peak. The 002 peak disappeared after charging and does not appear after discharge. This indicates that certain degree of cationic disorder had been introduced into the structure after lithium ion extraction. ....114

# List of Tables

<b>Table 2-1</b>	Electrochemical performance of $V_2O_5$ with different morphologies.....	13
<b>Table 2-2</b>	Electrochemical performance of $Li_{1+x}V_3O_8$ with different morphologies ....	15
<b>Table 2-3</b>	Electrochemical performance of cation substituted $Li_{1+x}V_3O_8$ .....	18
<b>Table 2-4</b>	Electrochemical performance of $Na_{1+x}V_3O_8$ with different morphologies ...	21
<b>Table 2-5</b>	Theoretical average voltage versus $Li/Li^+$ , specific capacity, and specific energy during reactions with lithium for transition metal oxides.....	25
<b>Table 3-1</b>	Synthesis methods used to prepare transition metal oxides presented in this thesis .....	28
<b>Table 4-1</b>	Lattice parameter of ball milled $Li_{1.2}V_3O_8$ computed by Rietveld refinement .....	39
<b>Table 4-2</b>	Lattice parameters and crystallite sizes of $Li_{1.2}V_3O_8$ computed by Rietveld refinement .....	48
<b>Table 4-3</b>	Lattice parameters and crystallite sizes of LVA3O and LVA5O computed by Rietveld refinement. ....	54
<b>Table 4-4</b>	Lattice parameters of sintered $Na_{1.2}V_3O_8$ computed by Rietveld refinement .....	59
<b>Table 4-5</b>	The refined lattice parameters of the as-prepared $Na_{1.2}V_3O_8$ by altering the sintering profile.....	67
<b>Table 4-6</b>	Table of first discharge capacities for LNT-PO and LNT/C-8 at different current densities. ....	90
<b>Table 5-1</b>	Impedance values of ball milled $Li_{1.2}V_3O_8$ based on Nyquist plot in Figure 5-1 using the circuit in Figure 5-2.....	94
<b>Table 5-2</b>	Comparison of electrochemical performance between $Li_{1.2}V_3O_8$ and $Na_{1.2}V_3O_8$ with different morphologies synthesized by electrospinning and HEBM.....	96
<b>Table 5-3</b>	Comparison of battery performance between pristine LVO-HNB400, LVA3O and LVA5O. ....	98
<b>Table 5-4</b>	The V=O stretching frequencies for all LVO samples and their relative intensities .....	101
<b>Table 5-5</b>	Comparison between battery performance of LVO-HNB and NVO-SNB	106
<b>Table 5-6</b>	The V-O-V asymmetric and symmetric stretching frequencies for all LVO and NVO samples and their electrochemical performance. ....	107
<b>Table 5-7</b>	Results of Rietveld refinement of the fresh and cycled electrodes.....	113

# List of Schemes

<b>Scheme 3-1</b>	Schematic illustration of electrospinning set up, inset shows magnified details of the as-spun fibers which composed of PVP as the polymer agent and dispersed metallic precursors. ....	30
<b>Scheme 4-1</b>	Schematic illustration of $\text{Li}_{1.2}\text{V}_3\text{O}_8$ formation mechanism. If the as-spun nanofibers is heated at lower temperature of 400 °C, the fibrous network can be retained, forming hierarchical configuration of nanobelt (LVO-HNB). By further increasing the temperature to 500 °C, destroy of fibrous framework and further grain growth lead to formation of single nanobelt (LVO-SNB).....	47
<b>Scheme 4-2</b>	Schematic representation of formation mechanism of single nanobelt (NVO-SNB) by one-step sintering and hierarchical nanobelt (NVO-HNB) by two-step sintering. ....	66
<b>Scheme 4-3</b>	Schematic illustration of formation process for carbon-coated $\text{Li}_2\text{NiTiO}_4$ with partially ordered structure (LNT-PO). Thin layer of carbon coating is formed on the surface of agglomerated particles and brings the particles into close proximity.....	85

# List of Abbreviations

CV	Cyclic Voltammetry
EDS	Energy Dispersive X-ray Spectroscopy
EIS	Electrochemical Impedance Spectroscopy
EVs	Electric Vehicles
FESEM	Field Emission Scanning Electron Microscope
FTIR	Fourier Transformed Infra Red
HEBM	High Energy Ball Milling
HEVs	Hybrid Electric Vehicles
HRTEM	High Resolution Transmission Electron Microscope
IC	Internal Combustion
LIB	Lithium Ion Battery
NMP	N-Methyl-2-pyrrolidone
PVP	Poly(vinylpyrrolidone)
SAED	Selected Area Electron Diffraction
TEM	Transmission Electron Microscope
TGA	Thermogravimetric Analysis
XRD	X-Ray Diffraction
0D	0-Dimension
1D	1-Dimension

# Chapter 1 Introduction

## 1.1 Problem Statement

Depletion of fossil fuels and emerging environmental concerns such as extensive pollution due to CO<sub>2</sub> emission has accelerated the needs in developing alternative clean energy technologies. The development of these alternative energy sources, including geothermal,[1] solar[2] and wind energy[3] have made impressive progress over the years but they are intermittent. These renewable sources require robust energy storage systems to sustain continuous power supply. However, the energy storage technology is still lagging behind to store these energy sources with long-term stability for high power demand. Hence, numerous efforts should be invested to accelerate the advancement of energy storage system.

Electrochemical energy system is the most efficient form of energy storage. Lithium ion batteries (LIBs) have been predicted to be the most potential candidate of energy storage device in the future. LIBs are a type of rechargeable batteries with the highest energy density developed up-to-date, which can be as high as 150 Wh kg<sup>-1</sup>. Its life cycle can last for more than 10000 cycles depending on the working conditions and applications.[4] Hence, LIBs have been widely implemented for small electronic devices such as consumer portable electronics (e.g. mobile phones and tablets), medical implants, power tools, *etc.* Current ongoing research has been intensively focused on the improvement of electrochemical performance of LIBs associated with operations in automobile applications, such as electric vehicles, hybrid electric vehicle and plug-in electric vehicle.

Hybrid Electric Vehicles (HEVs) are powered up by an electric motor which consists of conventional Internal Combustion Engine (ICE) vehicle and rechargeable battery. The combustion by HEV provides better gas mileage compared to an ICE vehicle. Besides, the gasoline consumption of HEV can be reduced about 30 % compared to common vehicle.[5] Plug-In Hybrid Vehicles (PHEV) employ this concept and take one step further by adding additional batteries to the design. This enables the vehicle to be charged at night and be powered entirely from stored electrical energy during the day. By using PHEV, there are various energy sources to be used. LIBs exhibit best performance than other established commercial rechargeable battery, such as nickel metal hydride system,



lead acid battery, *etc.* However, for LIBs to be implemented in large scale and high power PHEV, current LIBs technology is facing great challenge for its limitation in the aspect of energy density, cycle life and safety issues. In order to fulfil the requirements for powering EVs with a 300-400 mile range, current LIBs technology is still lacking of two to three times of energy density. [6]

Commercial LIBs use the  $\text{LiCoO}_2$  as cathode material since the introduction of LIBs into commercial market in 1991.[7] It can deliver capacity of about  $140 \text{ mAh g}^{-1}$ , which is only half of its theoretical capacity. The relatively lower practical capacity of this material is due to its intrinsic structural instability when more than half of the lithium ions are extracted. Severe capacity fading will occur due to oxygen loss at a highly delithated state, when charged to more than 4.3 V. Besides, there are a few shortcomings for this material such as environmental problem due to toxicity of Co, high cost and safety issues.

Besides, major researches for current LIB technologies have been focused on anode materials with high capacity but high working voltage ( $> 1 \text{ V}$ ). [8] However, the comparatively low capacity of most cathode materials has been recognized as a major limiting factor for LIBs. In order to increase the energy density of LIBs, it is essential to explore new cathode material with higher capacity and working voltage ( $\geq 3 \text{ V}$ ).

## 1.2 Motivation

In order to develop alternative cathode materials for LIBs, it is important to understand the correlation between materials' structural properties and lithium intercalation mechanism. Conventional LIBs employ  $\text{LiCoO}_2$  as the cathode which constitutes two dimensional (2D), ordered rocksalt type structure of alternating layers of  $\text{LiO}_6$  and  $\text{CoO}_6$  octahedra.[9] Transition metal oxide with ordered rocksalt type is an important class of lithium intercalation materials due to existence of facile lithium diffusion channel within the lattice.

However,  $\text{LiCoO}_2$  used in conventional LIBs is still unsatisfactory to be used for high power applications due to its low practical capacity originated from the structural instability during deep delithiation process. During charging, only  $\sim 0.5$  lithium ions can be extracted from  $\text{LiCoO}_2$  as further removal of all lithium ions will lead to collapse of the ordered arrangement of  $\text{LiO}_6$  and  $\text{CoO}_6$  slabs within the lattice. Many studies had been conducted to explore alternative transition metal oxides with ordered rocksalt type

structure with similar lithium intercalation mechanism as  $\text{LiCoO}_6$  but with the capability to provide higher specific capacity.[10] Most of the attention has been focused on exploring the possibility to extract/insert more than one lithium ions during discharging/charging. Among them, lithium vanadium-based oxides are one of the most potential cathodes. They have gained much attention due to the multi-valence characteristics of vanadium (i.e. +3, +4 and +5) which enable three lithium intercalation leads to high capacity of  $\sim 300 \text{ mAh g}^{-1}$ . [11] However, lithium vanadium-based oxides exhibit similar shortcoming as  $\text{LiCoO}_2$  with deteriorated capacity upon prolonged cycling due to structural instability. Hence, a continuation of efforts is necessary to tackle this core issue of ordered rocksalt structure in order to improve their applicability as high performance cathodes.

Cation disorder has always been recognized to be detrimental to LIB performance as irregular occupation of lithium and transition metal ions within the lattice will cause obstruction to lithium diffusion route in the lattice during charging and discharging.[12, 13] However, recent discoveries have found out that suitable degree of cation disorder is beneficial in providing good electrochemical performance in terms of capacity and cyclability.[14, 15] Optimum extent of cation disorder is beneficial in retaining the parent structure compared to ordered structure without causing large strain upon lithium insertion and extraction. There are also a few reported works on feasible lithium intercalation into disordered structure without regular arrangement of lithium and transition metal ions. For instance,  $\text{Li}_2\text{MTiO}_4$  ( $\text{M} = \text{Fe, Mn, Co, and Ni}$ ) [16-19] with disordered rocksalt structure without facile lithium diffusion channel is able electrochemically deintercalate lithium ions. These findings though counter-intuitive, but are rather inspiring as it opens up opportunities in exploration of more potential cathodes in which previously are deemed to be restricted to materials with ordered structure.

Therefore, the aims of this thesis are not limited to research on possible solution for core problem encountered by ordered rocksalt structure but also pave a path towards investigation on the viability of disordered rocksalt structure in lithium intercalation.

## **1.3 Research Scope and Objectives**

The main research scope of this thesis is to investigate lithium transition metal oxide with ordered and disordered rocksalt structures as alternative high energy density cathodes for lithium ion batteries. The sub-objectives are proposed below:

### **1.3.1 Investigate the effect of nanostructuring and surface modification of transition metal oxides in battery performance**

Numerous efforts have been invested to develop alternative cathodes to enhance battery performance. Materials nanostructuring has been one of the main focus as particle size and morphology of electrode materials impose huge impact on electrochemical performance of LIBs. By downsizing the particle size into nano-level provides more surface area for electrolyte contact and improves electronic conductivities.[20, 21] The reaction kinetics will be further enhanced due to shorter diffusion length between reacting particles, leading to high energy density provided by nano-architected electrodes. However, there is a limit on going into excessive nano-level as to circumvent the occurrence of undesired electrolyte reactions, which will be elaborated with experimental observations in this thesis.

Besides, the study also extended to effect of morphology on diffusion kinetics of electrode materials for LIBs. Cathodes with zero-dimensional (0D) and one-dimensional (1D) nanostructures were synthesized by simple and versatile synthesis methods to study the effect of particle shape on the battery performance.

The effectiveness of surface modification in improving the capacity retention and rate capability has been demonstrated in literature.[22, 23] In this thesis, carbon coating approach is employed to enhance the battery performance. The formation of thin layer of conductive carbon on the surface of particles facilitates electron transfer between particles.

### **1.3.2 Investigate the influence of cation substitution in ordered rocksalt structure on structural and electrochemical properties**

As mentioned earlier, the structural characteristics of ordered rocksalt materials provide both advantages and challenges to battery performance. Eventhough the ordered

arrangement of cations provides facile diffusion channels for lithium insertion and extraction, the capacity or cyclability may be hampered due to structural instability upon prolonged cycling. Foreign atom substitution is a common approach employed to “pin” the crystal structure in order to reduce structural destruction induced during lithium extraction process.[24, 25] However, the amount of cation substitution requires stringent optimization as not to reduce much of the electrochemical reactivity of pristine sample especially due to substitution of redox species with electrochemically inactive atoms which will reduce the capacity, but sufficient to provide structural support to enhance the cyclability for long term battery performance. In this thesis, the effect of cation substitution of larger ionic radius and similar ionic radius in lithium transition metal oxide on the battery performance will be discussed.

### **1.3.3 Investigate the structural evolution of cathodes during lithium intercalation and deintercalation**

In order to understand the lithium intercalation mechanism, the study on structural evolution during charging and discharging needs to be conducted. In this thesis, ex situ x-ray characterization method will be used to investigate the correlation between structural changes and electrochemical characteristics of cathode materials. This will also provide better understanding on the effect of lithium insertion on changes in structural properties, including expansion or contraction of cell volume, lattice strain and distortion, *etc.* The observations will serve as essential guidelines in engineering the cathode materials to enhance the battery performance.

## **1.4 Dissertation overview**

This thesis's organization is as follows:

The introduction (Chapter 1) provides the research justification and constructs the working scope and objectives. The thesis aims to investigate and optimize the battery performance of lithium transition metal oxides with ordered and disordered rocksalt structures as LIB cathodes to promote them as a viable replacement for conventional  $\text{LiCoO}_2$ .

Chapter 2 briefly reviews the current development progress of lithium ion batteries, the construction and working principles. Cathodes currently under research are classified into

different classes based on their structural viability to intercalate lithium, the advantages and disadvantages will be evaluated. A detailed review regarding lithium transition metal oxides with rocksalt structures as LIB cathodes is provided. The benefits of nanomaterials application in LIBs are also discussed.

Chapter 3 introduces the various synthesis methods to produce cathodes with different particle size and morphology. Detailed procedures of materials characterization are provided. Device fabrication and electrochemical testing methods are also discussed.

Chapter 4 presents experimental observations and results followed by further interpretation and discussion in chapter 5. The applicability of nanomaterials in LIBs is experimental investigated. The lithium intercalation mechanism correlating with structural properties of a few lithium transition metal oxides of rocksalt structure are proposed. Tailoring of cation substitution and its influences on electrochemical properties are also discussed.

Chapter 6 concludes the whole project and Chapter 7 propose future works which facilitates deeper understanding towards lithium intercalation principles for rocksalt-based cathodes. Recommendations are provided to pave a way for promoting the applicability of these materials in real life applications.

## **1.5 Findings and Outcomes**

The studies presented in this thesis contribute to several outcomes:

- Demonstrating easy and cost effective methods to prepare nanomaterials.
- Formulating cation substitution approach to enhance battery performance
- Proposing lithium intercalation mechanism for a few rocksalt-based cathodes.

# Chapter 2 Literature Review

## 2.1 Basic Principles of Lithium Ion Batteries

A lithium ion battery comprises of a few cells connected in series to provide a substantial amount of energy density for commercial applications. The basic working principle of a lithium ion cell is illustrated in Figure 2-1. There are three key components in a LIB system: cathode (positive electrode), anode (negative electrode) and electrolyte.

In commercialized LIB system, the transition metal oxide as cathode and graphite as anode are host materials with specific sites for lithium ions to be inserted in. The electrodes composed of a metal current collector, the active materials ( $\text{LiCoO}_2$  or carbon in common commercialized LIBs) and additives including various types of carbon to increase the electronic conductivity and polymeric binder such as polyvinylidene fluoride to improve adhesion and mechanical strength. The system is assembled in discharged state with all lithium ions in the cathode sites. During charging, lithium ions are extracted from the cathode host, solvate into and move through the non-aqueous electrolyte, and inserted into the anode host. Simultaneously, electrons move from cathode to anode through the current collector forming an electric circuit to maintain charge balance. A LIB system works as an energy storage device by converting chemical energy to electrical energy and vice versa. The electrical energy is generated by converting the chemical energy of the electrodes via redox reactions.

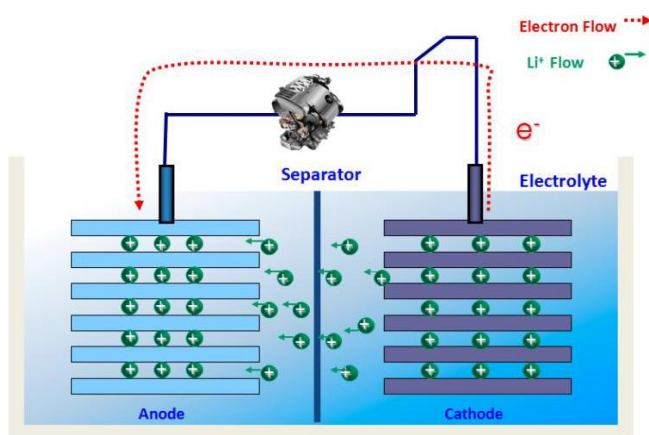
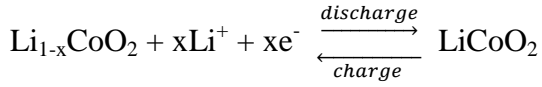


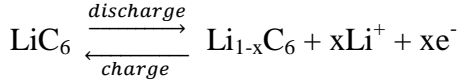
**Figure 2-1** Schematic diagram of a lithium ion cell. The cell is composed of a cathode, anode, separator and electrolyte.[26]

The half cell reactions at the two electrodes during the charge-discharge process of a lithium ion cell are shown below:

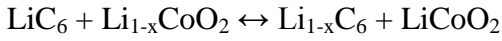
At the cathode:



At the anode:



Net cell reactions:



The cathode and anode are separated by a porous membrane which is ionically conducting but electronically non-conducting to allow penetration of electrolyte for lithium ions transportation.

## 2.2 Lithium Intercalation Mechanism of Cathodes in LIBs

In 1991, SONY combined the  $\text{LiCoO}_2$  cathode with a graphite anode to produce the first commercialized LIBs.[7, 27] Both electrodes act as lithium intercalation hosts for transporting lithium ion and to electrochemically insert into and extract from the layered structure. This mechanism was first proposed and termed as “rocking chair” behavior by Armand[28].

Intercalation reaction constitutes the insertion of a guest species, i.e. atoms, ions or molecules into a solid host without causing structural alteration of the host. Practically, the chemical bonding within the host may be slightly distorted upon ion insertion, or in some cases, may cause structural modification, which will affect the reaction reversibility.

Ideally, it is a topotactic reaction which is reversible and facilitates repeated lithium ion insertion and extraction without causing drastic changes in crystal structure of intercalation host[29]. Various materials have been studied as intercalation host for lithium ions, including graphite, chalcogenides and transition metal oxides.[30] For a

material to be employed as intercalation host, the structural framework is an important criterion to be put into consideration. The host structure shall allow no hindrance to incoming lithium intercalation and deintercalation.

Transition metal oxide with ordered rocksalt type structure is an important class of cathode materials which is the most extensively studied in current LIB technology. The conventional  $\text{LiCoO}_2$  also falls under this category.

## 2.2.1 Lithium Intercalation into Ordered Rock Salt Type Structure

The host structure with ordered rocksalt structure consists of periodic arrangement of lithium and transition metal ions within the lattice, which allows facile lithium diffusion pathway. Generally, the rocksalt type structural frameworks for lithium intercalation are usually built up of three-dimensional (3D) constitution with interconnected channels or tunnels, and two-dimensional (2D) layered configuration.

This section will include a few examples of ordered rocksalt structure with 3D and 2D configurations to provide clearer overview of lithium intercalation into rocksalt type structure.

### 2.2.1.1 Three-dimensional (3D) Framework - Spinel $\text{LiMn}_2\text{O}_4$

Spinel  $\text{LiMn}_2\text{O}_4$  was first proposed by Thackeray *et al.* [31] as cathode for LIBs in 1983. The structure of  $\text{LiMn}_2\text{O}_4$  is shown in Figure 2-2. The oxygen framework of  $\text{LiMn}_2\text{O}_4$  is the same as that of layered compound  $\text{LiMO}_2$ . Transition metal cations (Mn) occupy the octahedral site but  $\frac{1}{4}$  of them are located in the lithium layer, leaving  $\frac{1}{4}$  of the sites in transition metal layer vacant. Lithium ions occupy the tetrahedral sites in lithium layer which shares faces with the empty octahedral sites in the transition metal layer. This structure enables three-dimensional lithium diffusion pathways based on the three-dimensional  $\text{MO}_2$  host and the vacancies in the transition metal layer. Topotactic lithium intercalation into this spinel structure generates  $\text{Li}_2\text{Mn}_2\text{O}_4$  with an ordering between Mn and Li cations within the rocksalt type structure. The lithium intercalation and deintercalation process involves transformation from spinel to rocksalt and vice versa.

This material exhibits severe capacity fading problem. The main reasons suggested for capacity fading include Mn dissolution into the electrolyte[32] and generation of new phases accompanied with micro-strain during cycling.[32, 33]



In order to improve the poor cycling performance, several works by partial substituting of Mn with other metal ions such as Ni, Mg, Al, Zn, Ti, Cr, Cu, Fe *etc.* [34-37] had been reported. Higher voltage plateau can be obtained by some transition metal doping. However, this will cause electrolyte decomposition as voltage window of current electrolyte is not able to sustain this material under long-term cycling. An electrolyte which is stable at high voltage range will be required to promote this material for practical utilization.

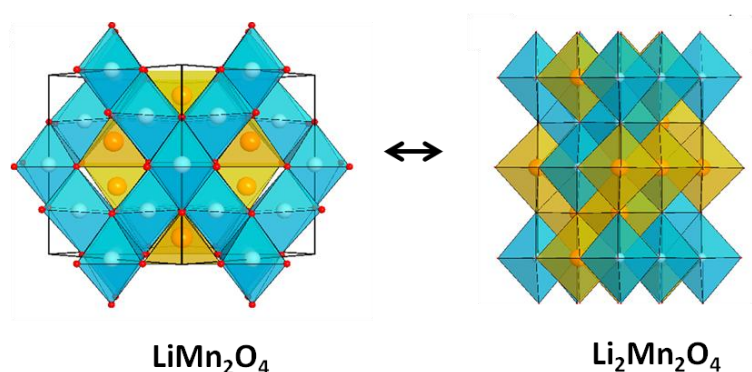


**Figure 2-2** Crystal structure of  $\text{LiMn}_2\text{O}_4$  and  $\text{Li}_2\text{Mn}_2\text{O}_4$  (Yellow:  $\text{LiO}_6$  octahedral; Light Blue:  $\text{MnO}_6$  octahedral)

### 2.2.1.2 Two-dimensional (2D) Framework – $\text{LiMO}_2$

Layered lithium transition metal oxides  $\text{LiMO}_2$  ( $\text{M} = \text{Co}, \text{Ni}$  or  $\text{Mn}$ ) have been intensively studied as cathodes for lithium ion batteries.  $\text{LiCoO}_2$  consists of  $\text{NaFeO}_2$  structure with the oxygen atoms arranged in cubic rocksalt arrangement as shown in Figure 2-3. The lithium and cobalt ions occupy the octahedral sites in alternating layer. The oxygen layers rearrange themselves to give hexagonal close packing of the oxygen in  $\text{CoO}_2$  upon the removal of lithium.[38]

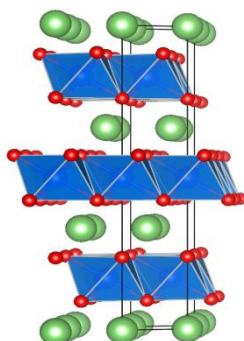


**Figure 2-3** Crystal structure of  $\text{LiCoO}_2$  (Green: Lithium ions, Blue:  $\text{CoO}_6$  octahedral)

The theoretical capacity of  $\text{LiCoO}_2$  is  $272 \text{ mAh g}^{-1}$ . However, when the cell is charged above 4.2 V, there will be significant phase transition and structural change due to oxygen loss, severe capacity fading will occur[38, 39]. The cell is only charged to 4.2 V for commercial application which is equivalent to  $140 \text{ mAh g}^{-1}$ , only extracts about 0.5 mole of lithium.

Although  $\text{LiCoO}_2$  dominates as cathode for commercial LIBs, there are a few drawbacks to this which are limited supply, high price and toxicity of cobalt as well as some safety issues. This limits the potential of LIBs for small scale applications only. To be employed for large scale applications such as PHEV, an alternative cathode material is required.

### 2.2.1.3 Two-dimensional (2D) Framework – Vanadium-based Oxide

Pure vanadium oxide,  $\text{V}_2\text{O}_5$  and lithium vanadium oxide,  $\text{LiV}_3\text{O}_8$  are the most widely studied electrode materials for LIBs among all vanadium-based oxides.

Lithium intercalation into layered  $\text{V}_2\text{O}_5$  was first demonstrated by Whittingham *et al.*[40] in 1976 and has gained much attentions due to its unique structural characteristics. Single crystalline  $\text{V}_2\text{O}_5$  is composed of layers of  $\text{VO}_5$  square pyramids with shared edges and corners in periodic arrangement.[41, 42] The adjacent layers are connected by non-covalent forces which are primarily Van der Waals interactions. The interlayer spacing in between allows guest ion intercalation. Lithium intercalation into  $\text{V}_2\text{O}_5$  generates end member of fully lithiated  $\omega\text{-Li}_3\text{V}_2\text{O}_5$  with a rocksalt type structure.[43]

The phase transformations from  $\text{V}_2\text{O}_5$  to  $\omega\text{-Li}_3\text{V}_2\text{O}_5$  are fairly complex process with a few intermediate phase,  $\alpha$ ,  $\epsilon$ ,  $\delta$ ,  $\gamma\text{-Li}_x\text{V}_2\text{O}_5$ . The formation of  $\omega\text{-Li}_3\text{V}_2\text{O}_5$  involves large distortion of parent structure  $\text{V}_2\text{O}_5$  induced by inserted lithium ions to create interstitial positions of favorable coordination geometry. However, the complete delithiation of  $\omega\text{-Li}_3\text{V}_2\text{O}_5$  is rarely reported in literature due to irreversible strain relaxation during complicated phase transformation.[44]

$\text{LiV}_3\text{O}_8$  is another interesting candidate which has been studied extensively. The structure consists of  $\text{VO}_6$  octahedra and  $\text{VO}_5$  distorted trigonal bipyramids forming sheets by sharing edges and corners as shown in Figure 2-4. The sheets are held together by lithium ions in octahedral interlayer sites forming rocksalt type structure. Initial stage of lithium intercalation constitutes filling of tetrahedral sites available in the lattice until formation of  $\text{Li}_3\text{V}_3\text{O}_8$ . Then, this is followed by transformation to end member, fully lithiated  $\text{Li}_{4.77}\text{-}$

$\text{V}_3\text{O}_8$  consists of  $\text{LiO}_6$  edge sharing with  $\text{VO}_6$  octahedra.[45] The phase transformation from  $\text{LiV}_3\text{O}_8$  to  $\text{Li}_{4.77}\text{V}_3\text{O}_8$  involves shortening of original V-O distances to enable transition in coordination from trigonal bipyramidal to octahedral for the vanadium and lithium ion is displaced to octahedral sites.

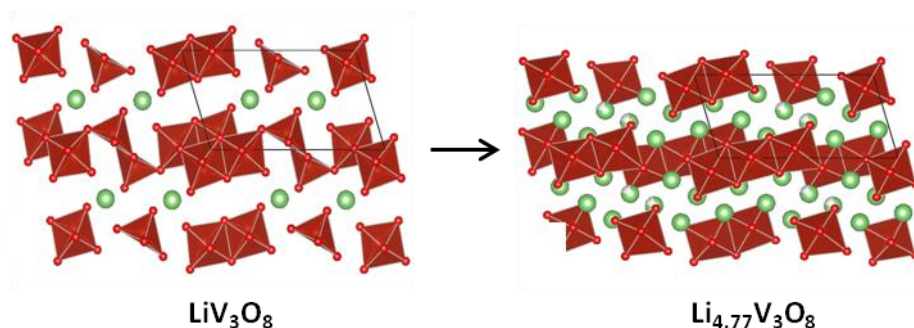


**Figure 2-4** Crystal structure of  $\text{LiV}_3\text{O}_8$  and  $\text{Li}_{4.77}\text{V}_3\text{O}_8$  (Green: Lithium ions, Brown:  $\text{VO}_n$  polyhedral)

## 2.3 Current Issues in Vanadium-based Oxides

Vanadium-based oxides have always been an attractive subject to be studied for vast applications including electrochromic, electrochemical as related to supercapacitors and batteries due to its rich chemistry to adopt various oxidation states (i.e. +3, +4 and +5). As mentioned earlier, the layered structures of vanadium-based oxides, making it capable to accommodate and release small guest species without causing large extend of structural modifications. This main structural characteristic has fulfilled the vital criteria to be employed as intercalation electrodes in LIB applications.

Eventhough vanadium-based oxide is gaining much attention as viable candidate to be used as cathodes for LIBs; there are still some underlying drawbacks owing to its inherent issues rendering it to be utilized for large scale consumer battery applications. Therefore, there are still lots of room to be researched on vanadium-based oxide to optimize its applicability for commercial practice.

### 2.3.1 Vanadium Oxide

$\text{V}_2\text{O}_5$  has been recognized as a potential candidate to be used as cathode materials in LIBs due to its high theoretical capacity of  $294 \text{ mAh g}^{-1}$  with two lithium ions intercalation/extraction. Nevertheless, its practical applications in high power LIBs has been rendered by its intrinsic bulk properties including sluggish electrochemical reaction

kinetics due to low electronic conductivity[46] and poor cycling stability due to amorphization upon prolonged cycling[47]. Over the years, various approaches have been employed to fine tune the size and morphology for  $V_2O_5$ . [48, 49]

Table 2-1 summarizes the dependence of electrochemical performance on morphologies for  $V_2O_5$ . Better electrochemical performance can be obtained by materials nanoscaling due to shortened lithium diffusion pathway and increased surface area for electrolyte penetration into active materials. For example, Pan *et al.*[50] has demonstrated that  $V_2O_5$  with nanosized rod-like particles ( $\sim 260 \text{ mAh g}^{-1}$ ) is capable to provide more than twice of the discharge capacity contributed by commercial  $V_2O_5$  powder in micron-sized ( $\sim 100 \text{ mAh g}^{-1}$ ). Overall, the capacity retention achieved for nanostructured  $V_2O_5$  is still not satisfactory. The core problem leading to capacity fading lies in the difficulty of control in structural transformation upon repeated lithium intercalation and extraction. Irreversible electrochemical reaction upon prolonged cycling causes amorphization and collapse of layered framework, hamper its possibility to be used directly in commercial battery applications.

**Table 2-1** Electrochemical performance of  $V_2O_5$  with different morphologies

<b>Morphology</b>	<b>1<sup>st</sup> Discharge Capacity (mAh g<sup>-1</sup>)</b>	<b>Reversible Capacity/N<sup>th</sup> Cycle (mAh g<sup>-1</sup>)</b>	<b>Current Density</b>	<b>Capacity Retention/ N<sup>th</sup> cycle (%)</b>	<b>References</b>
<b>Commercial powder</b>	~98	~100/30 <sup>th</sup>	14.7 mA g <sup>-1</sup>	~100%/30th	[50]
<b>Thin film</b>	327	205/20 <sup>th</sup>	294 mA g <sup>-1</sup>	~63%/20th	[51]
<b>Nanoparticles</b>	266	240/30 <sup>th</sup>	147 mA g <sup>-1</sup>	~90%/30th	[50]
<b>Nanorods</b>	385	230/50 <sup>th</sup>	0.4 mA cm <sup>-2</sup>	~60%/50th	[52]
<b>Nanosheet</b>	~260	206/100 <sup>th</sup>	500 mA g <sup>-1</sup>	~79%/100th	[53]
<b>Nanowires</b>	390	201/50 <sup>th</sup>	30 mA g <sup>-1</sup>	~51%/50th	[54]
<b>Nanobelt</b>	290	230/50 <sup>th</sup>	500 mA g <sup>-1</sup>	~79%/50th	[55]
<b>Nanofibers</b>	230	170/50 <sup>th</sup>	35 mA g <sup>-1</sup>	74%/50th	[56]
<b>Porous microsphere</b>	276	245/20 <sup>th</sup>	58.8 mA g <sup>-1</sup>	~89%/20th	[57]
<b>Hierarchical nanoflower</b>	275	239/50 <sup>th</sup>	50 mA g <sup>-1</sup>	87%/50th	[58]

<b>Nanosheet- assembled microflower</b>	277	211/100 <sup>th</sup>	300 mA g <sup>-1</sup>	~76%/100th	[59]
---	-----	-----------------------	------------------------	------------	------

### 2.3.2 Alkaline Metal Trivanadate $AV_3O_8$ (A = Li, Na, K)

Due to the intrinsic structural limitation of  $V_2O_5$ , which renders its capability to be employed directly as cathode materials, much of the attention has been focused on other vanadium-based oxides. Lithium trivanadate,  $Li_{1+x}V_3O_8$  ( $x < 1.0$ ) are another promising candidate to be applied as cathode materials for high power LIBs.  $Li_{1+x}V_3O_8$  are formed when the lightest alkaline metal, lithium ions are introduced into the layered  $V_2O_5$  framework.

Eventhough the theoretical energy density of  $Li_{1+x}V_3O_8$  is slightly lower than that of  $V_2O_5$ , this material has better advantage of totally reversible electrochemical process owing to better structural stability during lithium insertion and extraction. Hence, it is worth to devote more effort in exploring its possibility to surpass the electrochemical performance of  $V_2O_5$  in practical applications.

$Li_{1+x}V_3O_8$  exhibit the common shortcoming as  $V_2O_5$  due to the intrinsic bulk properties of vanadium-based oxide which leads to slow lithium diffusion kinetics. Similar approaches of materials nanoscaling can be utilized to improve the electronic and ionic conductivities resulting in enhanced electrochemical performance. Table 2-2 summarizes the effect of nanostructuring on electrochemical characteristics of  $Li_{1+x}V_3O_8$ . A few reports have shown that higher capacities are achievable by downsizing the particles from micron to nano-range.[60-62]

In addition, synthesis of  $Li_{1+x}V_3O_8$  is generally accompanied with formation of impurities such as  $Li_{0.3}V_2O_5$  or  $LiV_2O_5$ . This is usually due to employment of low temperature synthesis method or with the usage of precursors or surfactants with reducing properties causing partial reduction of vanadium (V) ions to lower oxidation states. According to several studies reported up-to-date, the influence of the electrochemically active Li-V-O phase on the overall electrochemical characteristics of  $Li_{1+x}V_3O_8$  is rather contradictory. Tran and co-workers[62] had demonstrated in their work that the presence of these Li-V-O phases is beneficial in providing higher practical capacity compared to pure  $Li_{1.1}V_3O_8$ . The electrochemical characteristics of the Li-V-O composite containing  $xLiV_3O_8-yLi_{0.3}$ -

$V_2O_5$  ( $x > y$ ) had been systematically investigated and reported by Dubarry *et al.*[63] and Qiao *et al.*[64]. By taking into consideration of the beneficial electrochemical properties contributed by  $Li_xV_2O_5$  phases, Sun *et al.*[65] had incorporated  $LiV_3O_8$  with  $Li_xV_2O_5$  as a coating layer with appropriated thickness to ameliorate the cycling stability of  $LiV_3O_8$ . On the contrary, Zhou *et al.*[66] and Wu *et al.*[67] had reported in their work that the electrochemical performance of  $LiV_3O_8$  was hampered due to the presence of the second Li-V-O phase. Besides, Kim *et al.*[68] had demonstrated the occurrence of severely deteriorated cycling performance because less lithium ions being able to be intercalated due to lithium ion trapping in the defective  $Li_{0.3}V_2O_5$  phase upon galvanostatic cycling. By comparing a few works in literature, single crystalline  $LiV_3O_8$  seems to be capable to exhibit better capacity retention compared to that of  $LiV_3O_8/Li_{0.3}V_2O_5$  compounds. For example, single crystalline  $LiV_3O_8$  nanorods fabricated by Liu *et al.*[69] had reported to contribute cycling stability of 96% with specific capacity of  $\sim 263 \text{ mAh g}^{-1}$  after 100 cycles, which has surpassed the capacity retention of only  $\sim 78\%$  for  $LiV_3O_8/Li_{0.3}V_2O_5$  nanorods ( $\sim 250 \text{ mAh g}^{-1}$ ) prepared by Pan *et al.*[60]; though with higher initial specific capacity ( $\sim 320 \text{ mAh g}^{-1}$ ). The advantageous criteria owing to the existence of second Li-V-O phase is still questionable and yet to be justified. Furthermore, the fabrication of composite material is generally underlying the concern in controlling the optimized amount of the second phase which constitutes tedious procedures that will impose difficulty of scaling up to industrial production level in real life applications.

Hence, our studies presented in this thesis will focus on the synthesis and electrochemical characterization of single phase  $Li_{1+x}V_3O_8$ , with extension into effect of morphology and cation substitution on its electrochemical properties.

**Table 2-2** Electrochemical performance of  $Li_{1+x}V_3O_8$  with different morphologies

Chemical Formula	Morphology	1 <sup>st</sup> Discharge Capacity ( $\text{mAh g}^{-1}$ )	Reversible Capacity/ N <sup>th</sup> Cycle ( $\text{mAh g}^{-1}$ )	Current Density	Capacity Retention/N <sup>th</sup> cycle (%)	References
$LiV_3O_8$	Microparticles	180	180/50 <sup>th</sup>	100 $\text{mA g}^{-1}$	$\sim 100\%/50^{\text{th}}$	[60]
$LiV_3O_8$	Submicron particles	270	217/40 <sup>th</sup>	150 $\text{mA g}^{-1}$	80%/40 <sup>th</sup>	[70]
$LiV_3O_8$	Nanorods	246	236/100 <sup>th</sup>	100 $\text{mA g}^{-1}$	$\sim 96\%/100^{\text{th}}$	[69]

<b>LiV<sub>3</sub>O<sub>8</sub>/Li<sub>0.3</sub>V<sub>2</sub>O<sub>5</sub></b>	Nanorods	320	250/100 <sup>th</sup>	100 mA g <sup>-1</sup>	~78%/100 <sup>th</sup>	[60]
<b>LiV<sub>3</sub>O<sub>8</sub>/Li<sub>0.3</sub>V<sub>2</sub>O<sub>5</sub></b>	Nanowires	176	140/100 <sup>th</sup>	1500 mA g <sup>-1</sup>	~79%/100 <sup>th</sup>	[71]
<b>LiV<sub>3</sub>O<sub>8</sub></b>	Glassy-like agglomeration	347	351/100 <sup>th</sup>	50 mA g <sup>-1</sup>	~100%/100 <sup>th</sup>	[72]
<b>LiV<sub>3</sub>O<sub>8</sub></b>	Nanobelt	234	196/30 <sup>th</sup>	100 mA g <sup>-1</sup>	84%/30 <sup>th</sup>	[73]
<b>Li<sub>1+x</sub>V<sub>3</sub>O<sub>8</sub></b>	Nanobelt	278	232/40 <sup>th</sup>	40 mA g <sup>-1</sup>	83%/40 <sup>th</sup>	[74]
<b>LiV<sub>3</sub>O<sub>8</sub></b>	Mesoporous nanoparticles	301	290/50 <sup>th</sup>	40 mA g <sup>-1</sup>	96%/50 <sup>th</sup>	[75]
<b>Li<sub>1+x</sub>V<sub>3</sub>O<sub>8</sub></b>	1D array of nanosheet	~352	255/40 <sup>th</sup>	40 mA g <sup>-1</sup>	72%/40 <sup>th</sup>	[76]
<b>LiV<sub>3</sub>O<sub>8</sub>/Li<sub>0.3</sub>V<sub>2</sub>O<sub>5</sub></b>	Hierarchical plate-array	~255	~226/60 <sup>th</sup>	50 mA g <sup>-1</sup>	~89%/60 <sup>th</sup>	[77]
<b>LiV<sub>3</sub>O<sub>8</sub></b>	Nanosheet	260	262/100 <sup>th</sup>	100 mA g <sup>-1</sup>	100%/100 <sup>th</sup>	[78]

According to literature, capacity degradation of single crystalline Li<sub>1+x</sub>V<sub>3</sub>O<sub>8</sub> is primarily due to non-uniform vanadium dissolution[79], crack formation[80], irreversible phase transformation[81] and undesired reaction with electrolyte[82, 83]. Numerous effort have been devoted to alleviate these problems to improve the cycling stability, including doping the compounds with suitable metal ions to preserve the structural framework or tailoring feasible coating to restrain the electrodes from electrolyte invasion. Table 2-3 summarizes the most of reported works on metal ions substitution into Li<sub>1+x</sub>V<sub>3</sub>O<sub>8</sub> compounds on the electrochemical performance of Li<sub>1+x</sub>V<sub>3</sub>O<sub>8</sub> compounds. Most of the studies reported are centered on metal ions substitution on the vanadium sites, only a few on lithium sites. Generally, larger metal ions, i.e. Ga<sup>3+</sup> (0.62 Å)[84], Zr<sup>4+</sup> (0.615 Å)[85], Ti<sup>4+</sup> (0.68 Å)[86], *etc.* are substituted on the vanadium sites (0.59 Å) to facilitate expansion of the interlayer spacing, enabling faster lithium diffusion into/out of the structure upon charging and discharging. With the bridging effect contributed by the additional metal ion with the vanadium via oxygen bridge forming M-O-V bonds, this is beneficial in suppression of phase transition and formation of stable lithium intercalation route during lithium insertion and extraction which in turns stabilize the structure.[87]

On the contrary, partial ions substitution at the lithium sites reported to date are only limited to  $\text{Ag}^+$  and  $\text{Cu}^+$ . As reported by Rozier *et al.*[88],  $\text{Cu}^+$  substitution can function as an extra conductive additive by Li-driven Cu-extrusion mechanism process, which can also be applicable for Ag substitution. However, the electrochemical performance in terms of specific capacity and cycling retention decreased with increasing amount of  $\text{Cu}^+$  substitution into lithium sites. Partial substitution of lithium sites with optimized amount of  $\text{Ag}^+$  had been shown to increase the interlayer distance which constituted the similar effect as ion substitution at the vanadium sites, improved the lithium diffusion kinetics.[89]

There have been reported attempts to replace the lithium ions, or full substitution with larger foreign cations, e.g.  $\text{Na}^+$ [90-94],  $\text{K}^+$ [95-97],  $\text{Ag}^+$ [98] *etc.* to investigate their effect on electrochemical activity. These larger metal ions serve as supporting pillars which stabilize the structural framework and thus enable repeated lithium insertion and extraction upon prolonged cycling.



**Table 2-3** Electrochemical performance of cation substituted  $\text{Li}_{1+x}\text{V}_3\text{O}_8$ 

Chemical Formula	Dopant Content	Morphology	Discharge Capacity of undoped sample/ $\text{N}^{\text{th}}$ cycle ( $\text{mAh g}^{-1}$ )	Discharge capacity of doped sample/ $\text{N}^{\text{th}}$ cycle ( $\text{mAh g}^{-1}$ )	Current Density	Capacity Retention/ $\text{N}^{\text{th}}$ cycle of undoped sample (%)	Capacity Retention/ $\text{N}^{\text{th}}$ cycle of doped sample (%)	References
$\text{Cu}^+-\text{Li}_{1.3}\text{V}_3\text{O}_8$	Li: Cu: V	Microparticles	$\sim 350/1^{\text{st}}$	$\sim 275/1^{\text{st}}$	38/32 mA	$\sim 86/100^{\text{th}}$	$\sim 80/100^{\text{th}}$	[88]
	0.4: 0.9: 3		$\sim 300/100^{\text{th}}$	$\sim 220/100^{\text{th}}$	$\text{g}^{-1}$ (undoped /doped)			
$\text{Ag}^+-\text{LiV}_3\text{O}_8$	Li: Ag: V		$\sim 210/1^{\text{st}}$	$\sim 240/1^{\text{st}}$	300 mA $\text{g}^{-1}$	$\sim 71/10^{\text{th}}$	$\sim 85/10^{\text{th}}$	[89]
	0.96: 0.04: 3		$\sim 150/10^{\text{th}}$	$\sim 205/10^{\text{th}}$				
$\text{Ni}^{2+}-\text{LiV}_3\text{O}_8$	Li: V: Ni	Porous grains	$\sim 330/1^{\text{st}}$	$\sim 285/1^{\text{st}}$	150 mA $\text{g}^{-1}$	$\sim 64/30^{\text{th}}$	$\sim 88/30^{\text{th}}$	[99]
	1: 2.95: 0.05		$\sim 210/20^{\text{th}}$	$\sim 251/30^{\text{th}}$				
$\text{Cu}^{2+}-\text{LiV}_3\text{O}_8$	Li: V: Cu		$\sim 220/1^{\text{st}}$	$265/1^{\text{st}}$	150 mA $\text{g}^{-1}$	$\sim 68/100^{\text{th}}$	$86/100^{\text{th}}$	[100]
	1: 3: 0.05		$\sim 150/100^{\text{th}}$	$228/100^{\text{th}}$				
$\text{Cr}^{3+}-\text{LiV}_3\text{O}_8$	Li: V: Cr	Microparticles	$188/1^{\text{st}}$	$265/1^{\text{st}}$	150 mA $\text{g}^{-1}$	N.A. (due to activation)	$94/100^{\text{th}}$	[101]
	1: 3: 0.1		$215/100^{\text{th}}$	$250/100^{\text{th}}$				
$\text{Y}^{3+}-\text{LiV}_3\text{O}_8$	Li: V: Y	Sheet-like microparticles	$\sim 250/1^{\text{st}}$	$\sim 250/1^{\text{st}}$	40 mA $\text{g}^{-1}$	$56/30^{\text{th}}$	$86/30^{\text{th}}$	[102]
	1: 3: 0.1		$\sim 140/30^{\text{th}}$	$\sim 214/30^{\text{th}}$				

<b>Ga<sup>3+</sup>-LiV<sub>3</sub>O<sub>8</sub></b>	Li: V: Ga		237/2 <sup>nd</sup>	277/2 <sup>nd</sup>	30 mA g <sup>-1</sup>	78/50 <sup>th</sup>	82/50 <sup>th</sup>	[84]
	1: 2.94: 0.06		~185/50 <sup>th</sup>	226/50 <sup>th</sup>				
<b>Ce<sup>3+</sup>-LiV<sub>3</sub>O<sub>8</sub></b>	Li: V: Ga	Plate-like	262/1 <sup>st</sup>	262/1 <sup>st</sup>	75 mA g <sup>-1</sup>	88/50 <sup>th</sup>	99/50 <sup>th</sup>	[103]
	1: 2.99: 0.01	micrograins	~230/50 <sup>th</sup>	~259/50 <sup>th</sup>				
<b>Nd<sup>3+</sup>-Li<sub>1.05</sub>V<sub>3</sub>-O<sub>8</sub></b>	Li: V: Nd	Irregular	276/1 <sup>st</sup>	300/1 <sup>st</sup>	30 mA g <sup>-1</sup>	94/15 <sup>th</sup>	95/15 <sup>th</sup>	[104]
	1: 2.96: 0.04	microparticles	~259/15 <sup>th</sup>	~286/15 <sup>th</sup>				
<b>Ti<sup>4+</sup>-LiV<sub>3</sub>O<sub>8</sub></b>	Li: V: Ti	Agglomerated	230/1 <sup>st</sup>	349/1 <sup>st</sup>	60 mA g <sup>-1</sup>	~44/50 <sup>th</sup>	65/50 <sup>th</sup>	[86]
	1: 2.968: 0.04	microparticles	~100/50 <sup>th</sup>	226/50 <sup>th</sup>				
<b>Si<sup>4+</sup>-LiV<sub>3</sub>O<sub>8</sub></b>	Li: V: Si		~250/1 <sup>st</sup>	~275/1 <sup>st</sup>	150 mA g <sup>-1</sup>	~40/300 <sup>th</sup>	~52/300 <sup>th</sup>	[105]
	1: 3: 0.05		~100/300 <sup>th</sup>	143/300 <sup>th</sup>				
<b>Zr<sup>4+</sup>-LiV<sub>3</sub>O<sub>8</sub></b>	Li: V: Zr	Microparticles	212/1 <sup>st</sup>	270/1 <sup>st</sup>	30 mA g <sup>-1</sup>	73/50 <sup>th</sup>	91/50 <sup>th</sup>	[85]
	1: 2.94: 0.06		~155/50 <sup>th</sup>	247/50 <sup>th</sup>				

Table 2-4 summarizes the a few reported works on the electrochemical characteristics of  $\text{Na}_{1+x}\text{V}_3\text{O}_8$ . It is worth to note that the product  $\text{Na}_{1+x}\text{V}_3\text{O}_8$  obtained was usually accompanied with  $\text{NaV}_6\text{O}_{15}$  or  $\text{Na}_{0.33}\text{V}_2\text{O}_5$  as impurities which are electrochemically active,[90-92] as similar to  $\text{Li}_{1+x}\text{V}_3\text{O}_8$ . By comparing the reported works, single phase  $\text{Na}_{1+x}\text{V}_3\text{O}_8$  had shown to exhibit higher capacities, which indicate that the presence of impurities may be undesired for this material to be used as lithium intercalation host in battery applications. For example, pure  $\text{Na}_2\text{V}_6\text{O}_{16}\cdot x\text{H}_2\text{O}$  ( $\text{NaV}_3\text{O}_8\cdot x\text{H}_2\text{O}$ ) nanowires fabricated by Wang *et al.*[93] was able to deliver highest capacity of  $\sim 235 \text{ mAh g}^{-1}$ , which is slightly higher than that of  $\text{NaV}_3\text{O}_8$  (with the presence of  $\text{Na}_{0.33}\text{V}_2\text{O}_5$ ) nanoflakes synthesized by Tang *et al.*[91] ( $\sim 220 \text{ mAh g}^{-1}$ ) when cycled at the same current density of  $30 \text{ mA g}^{-1}$ . Therefore, it is highly desirable to synthesize single phase  $\text{Na}_{1+x}\text{V}_3\text{O}_8$  to investigate its electrochemical characteristics and its capability to be applied in high power density LIB applications.

Potassium ion,  $\text{K}^+$  which has an even larger ionic radius than that of Li and Na, is expected to be able to further increase the interlayer spacing of the layered structure. However, the crystal structure formed is slightly different from Li and Na trivanadates. It is built up of corrugated layers of distorted, edge sharing  $\text{VO}_6$  octahedra, with the  $\text{K}^+$  ions residing between the layers. Besides, it has more open structure relatively to its Li or Na counterparts.[97] From initial instinct, this compound should demonstrate more superior electrochemical activity than the Li and Na counterparts. However, Baddour-Hadjean *et al.*[95] and Manev *et al.*[96] had demonstrated that  $\text{KV}_3\text{O}_8$  is not suitable to be applied in LIBs due to their low capacities and inherent structural issues which resulted in slow lithium diffusivity and loss of crystallinity upon lithium intercalation/extraction.

Liang *et al.*[98] had synthesized  $\text{Ag}_{1.2}\text{V}_3\text{O}_8$ , which is a rarely reported compound and investigated their electrochemical activity as cathode materials LIBs. The main role of silver is to increase the electronic conductivity via Ag extrusion mechanism driven by lithium ion insertion upon discharging process, similarly reported by Rozier *et al.*[88] for partially Cu substituted  $\text{Li}_{1+x}\text{V}_3\text{O}_8$  compounds. Eventhough it is beneficial in improving the electrochemical performance of trivanadate-based compounds, silver is considered to be an expensive source which may not be viable for large scale industrial production.

According to literature,  $\text{Na}_{1+x}\text{V}_3\text{O}_8$  compound is capable to intercalate lithium ions without causing much structural destruction, making it as a promising candidate to be used as cathode materials in LIBs. Structural stability is an essential criterion for reversible intercalation mechanism of cathodes in LIBs during guest-host interaction.

Taking into consideration the great potential of  $\text{Na}_{1+x}\text{V}_3\text{O}_8$  to be applied in commercial LIB applications, this material will be studied comprehensively in this thesis.

**Table 2-4** Electrochemical performance of  $\text{Na}_{1+x}\text{V}_3\text{O}_8$  with different morphologies

Chemical Formula	Morphology	1 <sup>st</sup> Discharge Capacity ( $\text{mAh g}^{-1}$ )	Reversible Capacity/ N <sup>th</sup> Cycle ( $\text{mAh g}^{-1}$ )	Current Density ( $\text{mA g}^{-1}$ )	Capacity Retention/ N <sup>th</sup> cycle (%)	Reference
$\text{Na}_2\text{V}_6\text{O}_{16}$	Nanowires	~235	~215/30 <sup>th</sup>	30	91/30 <sup>th</sup>	[93]
$\text{NaV}_3\text{O}_8/\text{Na}_{0.33}\text{V}_2\text{O}_5$	Nanoflakes	~127	~167/100 <sup>th</sup>	150	n.a.	[91]
$\text{Na}_{1.25}\text{V}_3\text{O}_8$	Nanobelt	172	164/450 <sup>th</sup>	200	95/450	[94]
$\text{Na}_{1.08}\text{V}_3\text{O}_8/\text{NaV}_6\text{O}_{15}$	Nanobelt	184	174/30 <sup>th</sup>	300	95/30	[90]
$\text{Na}_{1.08}\text{V}_3\text{O}_8/\text{NaV}_6\text{O}_{15}$	Nanosheet	~174	~207/100 <sup>th</sup>	300	n.a	[92]

## 2.4 Exploration on Potential of Lithium Intercalation into Disordered Rocksalt

Since lithium intercalation mechanism into transition metal oxide and metal chalcogenides had been discovered in 1970s, various studies have been conducted to further investigate and understand the concept and its application in LIBs. Until 1990s, SONY had paced a great step in transiting the concept into large scale LIBs commercialization.

The transition metal employed in commercialized LIBs is lithium metal oxide with general formula  $\text{LiMO}_2$  ( $\text{M} = \text{Co}, \text{Fe}, \text{Mn}$ ). This class of material possesses the cubic NaCl rocksalt structure in which the oxygen atoms fill up at the sides of face-centered cubic (FCC) lattice and the cations (lithium and metal ions) reside the sublattice of octahedral interstices. The cation ordering is highly dependent on the size difference between the cations and synthesis condition, i.e temperature, pressure, *etc.* Hewston *et al.*[106] and Wu *et al.*[107] had provided detailed insights in their work regarding the

cations arrangement occurred in  $\text{LiMO}_2$ . The four common structures (Figure 2-5) being observed are: (i) the disordered rocksalt  $\alpha\text{-LiFeO}_2$  with random arrangement of the lithium and metal ions within the sublattice of the octahedral interstice, (ii) the layered  $\alpha\text{-NaFeO}_2$  structure with the cation preferentially arranged into layers in (111) direction, (iii) the  $\gamma\text{-LiFeO}_2$  with electrostatically favored ordering of cations which is obtained at temperature lower than 600 °C,[108, 109] and (iv) the spinel-based low temperature  $\text{LiCoO}_2$  form. Conventionally, the  $\alpha\text{-NaFeO}_2$  structure with alternating layers of lithium slab and transition metal slab is the most preferred type for lithium intercalation mechanism, due to its flexibility to relax the octahedral upon lithium insertion and extraction. The  $\text{LiCoO}_2$  used in commercialized LIBs adopts this structure, hence enabling reversible electrochemical reaction. However if this material is being charged until all the lithium ions being extracted, the structure will collapse due to destruction of the lithium slab. This is the main reason that the LIBs in current market can never charge above 4.2V.

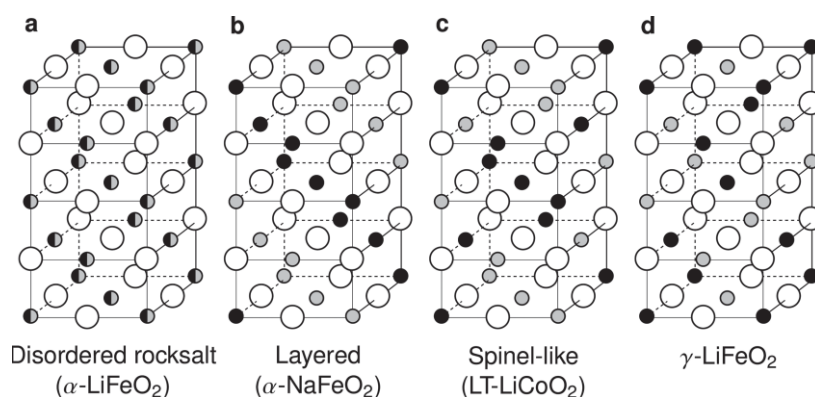


**Figure 2-5** Illustrations of four common types of cubic rocksalt structures. (a)  $\alpha\text{-LiFeO}_2$ , (b) layered  $\alpha\text{-NaFeO}_2$ , (c) spinel  $\text{LiCoO}_2$  and (d)  $\gamma\text{-LiFeO}_2$  [15]

Various studies over the years have been focused on materials with periodical cation arrangement because cation mixing has always been detrimental to reversible lithium insertion and extraction which often associated with capacity fading.[110] The materials with negligible or without any intermixing between lithium and transition metal sublattice are generally preferred but the choices of materials are also limited to be used as cathode for LIBs.

Despite vast quantity of reported works on well-ordered structured materials with superior performance, there are a few reports on the capability of disordered materials to be applied as cathode materials for LIBs.[16-19, 111] The ability of these materials to

reversibly intercalate and de-intercalate lithium ions without facile diffusion channels is against prevailing instinct. Until recently, Ceder and co-workers[14, 15] had provided a unifying theory to explain the counter-intuitive phenomenon of lithium intercalation into rocksalt structure without periodical cation arrangement by atomistic modeling. They utilized it as a design guideline and demonstrated experimentally the potential of Li-Cr-Mo-O with disordered cation arrangement to be used as high performance cathode materials due to its ability to provide facile lithium diffusion route.

In rocksalt-type structure, lithium diffuses from one octahedral site to another via a tetrahedral activated state (o-t-o diffusion) (Figure 2-6(a)).[112-115] The intermediate tetrahedral state with lithium ion shares faces with four octahedral sites, which is (i) a vacant site previously resided by itself, (ii, iii) another two sites either occupied by lithium, transition metal ion or a vacancy, and (iv) another vacancy it will proceed to. The formation of this intermediate state is subjected to an activation energy barrier which is highly dependent on electrostatic repulsion between the migrating lithium ion and the face-sharing neighbors.

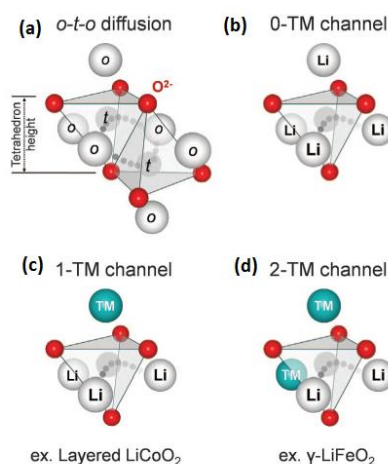


**Figure 2-6** Illustration of local environment for o-t-o lithium diffusion in rocksalt type lithium transition metal oxide. (a) o-t-o diffusion: two tetrahedral path connect a pair of neighbouring octahedral sites, (b) 0-TM channel: the activation state is not face-shared with any octahedral transition metal, (c) 1-TM: the activation state shares faces with one transition metal, (d) 2-TM: the activation state shares faces with two transition metal. [14]

To support this mechanism, there are two types of diffusion channels, which is 0-TM with no face-sharing transition metal ion (Figure 2-6(b)) and 1-TM with one face-sharing transition metal ion (Figure 2-6(c)). Lithium diffusion in LiCoO<sub>2</sub> is attributed to 1-TM channels. The activation energy barrier for intermediate tetrahedral state is correlated with the restrained relaxation distance of transition metal when lithium ion migrates into the

tetrahedral state. This distance corresponds to the slab separation in well-ordered layered structure.

On the contrary, for cation-disordered structure without the slab distance due to cation mixing, the maximum relaxation distance is indicated by the tetrahedron height, which is associated with the lattice parameter as  $h_{tetrahedron} = a/\sqrt{3}$  [14]. The allowed relaxation distance for disordered structure (2.35-2.45 Å) is smaller than that of ordered structure (2.60-2.70 Å), which means the lithium migration barrier into intermediate state is higher for disordered structure due to stronger electrostatic repulsion between cations. Therefore, 1-TM channels are deemed to be nearly inactive in disordered structure. The existence of 0-TM channels is the one which sustains lithium migration within disordered structure. Hence, this optimistic finding provides a prospective outlook for disordered materials to be included as the alternative cathodes worth to be researched on.

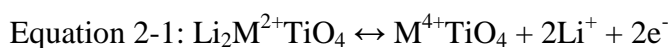
In order to sustain the lithium ion migration across the entire structure, this 0-TM diffusion channels have to be able to extend throughout the disordered structure forming feasible percolation network for lithium transport. In other words, it is possible to engineer materials in such a way that the local lithium-rich domains are connected within the structure to produce facile diffusion path. There are two ways in creating feasible 0-TM diffusion channels: (i) by increasing lithium amount to form more lithium-rich clusters and (ii) by altering the synthesis conditions, i.e. temperature, pressure to produce the viable lithium-rich domains. The former option had been demonstrated by several studies [116, 117] in which  $\text{Li}_{1+x}\text{M}_{1-x}\text{O}_2$  related compounds with excess lithium content are capable to provide higher energy density and better cyclability than the stoichiometric analogues. Systematic studies on the suitable amount of lithium have to be performed so that the amount of lithium is sufficient to form the viable percolation network but not too excessive to collapse the structure when nearly all the lithium ions being removed during charging process. Conversely, the second option is deemed to be thermodynamically favored arrangement due to synthesis condition which may apply to only some materials.

Thus, the recent findings on the lithium intercalation into disordered rocksalt-type materials have widen the boundary of intercalation concept which is only limited to well-ordered materials for over a few decades. This concept is not only limited to  $\text{LiMO}_2$  related compounds, but applies the same for other disordered rocksalt based materials, e.g.  $\text{Li}_2\text{MO}_3$  etc. Hence, this offers a vast space for research investigations on variable lithium amount and combination with one or more transition metals for non-stoichiometric rocksalt based oxides as well as optimization of their preparation conditions.

### 2.4.1 Current Issues in Disordered Rock salt Materials

To-date, reported works on applications of disordered materials as cathodes in LIBs are deemed to be limited.[118] Among them, titanium-based oxide with chemical formula of  $\text{Li}_2\text{MTiO}_4$  ( $\text{M} = \text{Fe, Mn, Co, Ni}$ ) is a relatively new candidate as lithium intercalation materials. The key feature of this material system lies in the possibility to exchange of two mole of lithium per transition metal, delivering higher capacity than  $\text{LiCoO}_2$  in which at most one lithium ion can be extracted.

$\text{Li}_2\text{MTiO}_4$  ( $\text{M} = \text{Fe, Mn, Co, Ni}$ ) has relatively high theoretical capacity due to two lithium atoms in the structure. In principle, two electron reaction per transition metal operating on both redox couples  $\text{M}^{2+}/\text{M}^{3+}$  and  $\text{M}^{3+}/\text{M}^{4+}$  is possible as shown in the half cell reaction as shown below:



Theoretical capacities according to above reaction are  $\sim 300$  mAh/g or higher when two lithium ions are extracted. The existence of titanium atom in the structure facilitates stabilization of oxygen in the structure to create  $\text{TiO}_4$  octahedral, which possibly contributes to thermal stability of these materials.

**Table 2-5** Theoretical average voltage versus  $\text{Li}/\text{Li}^+$ , specific capacity, and specific energy during reactions with lithium for transition metal oxides

	Cathode	Working potential (V)	Specific Capacity ( $\text{mAh g}^{-1}$ )	Specific Energy ( $\text{Wh kg}^{-1}$ )	References
<b>Ordered rocksalt</b>	$\text{LiMn}_2\text{O}_4$	3.95	148	585	[31]
	$\text{LiCoO}_2$	3.90	130	507	[38]
	$\text{V}_2\text{O}_5$	3.00	294	870	[41]
	$\text{Li}_{1+x}\text{V}_3\text{O}_8$	3.00	280	840	[119]
<b>Disordered rocksalt</b>	$\text{Li}_2\text{FeTiO}_4$	2.80	295	826	[16]
	$\text{Li}_2\text{MnTiO}_4$	3.60	296	1067	[16]
	$\text{Li}_2\text{CoTiO}_4$	4.00	289	1156	[111]
	$\text{Li}_2\text{NiTiO}_4$	4.30	290	1247	[16]



## 2.4.2 Titanium-based Oxides

Sebastian *et al.*[120] first reported  $\text{Li}_2\text{MTiO}_4$  ( $\text{M} = \text{Fe}, \text{Mn}, \text{Co}, \text{Ni}$ ) that exhibits chemical deintercalation of lithium, suggested that these materials are likely to deinsert lithium under electrochemical conditions. It has a cubic cation disordered rocksalt structure with the space group  $Fm\bar{3}m$ . The metal atoms (M and Ti) are disordered and randomly distributed at the octahedral sites of the cubic close packed array of oxygen atoms (Figure 2-7(a)).

The electrochemical performance for  $\text{Li}_2\text{NiTiO}_4$  was first published in 2004.[17] More work was done by Kuzma *et al.*[16, 18] in investigating  $\text{Li}_2\text{FeTiO}_4$  and  $\text{Li}_2\text{MnTiO}_4$  as cathodes for LIBs. Carbon-coated  $\text{Li}_2\text{FeTiO}_4$  was capable to achieve  $123 \text{ mAh g}^{-1}$  at  $60^\circ\text{C}$  while  $\text{Li}_2\text{MnTiO}_4$  exhibited  $132 \text{ mAh g}^{-1}$  with poor cycling performance. For  $\text{Li}_2\text{NiTiO}_4$ , it exhibits inferior cycling performance both at  $60^\circ\text{C}$  and room temperature. Recently, electrochemical performance of carbon-coated  $\text{Li}_2\text{CoTiO}_4$  was reported by Yang *et al.* [111] with high reversible capacity of  $144.3 \text{ mAh g}^{-1}$  when cycled at low current density of  $10 \text{ mA g}^{-1}$ .

The main issues associated with poor cycling stability of these titanates are: (i) lack of distinct tunnels as lithium ion transport pathway within disordered rocksalt structure; (ii) poor electronic and ionic conductivity. The latter issue can be alleviated by carbon coating and nanoscaling in particle size, as in reported works[16, 17, 111]. However, there is no reported work on efforts made by tackling the structural limitation issue.

Sebastian *et al.*[120] had successfully obtained a low temperature ordered derivative for  $\text{Li}_2\text{NiTiO}_4$ , which adopts a similar structure as  $\text{Li}_2\text{TiO}_3$ . Until now, there is no reported data on electrochemical performance for this ordered structure of  $\text{Li}_2\text{NiTiO}_4$  in LIBs application. They suggested the ordered structure consists of lithium-rich  $[\text{Li}_{2/3}(\text{Ni},\text{Ti})_{1/3}]$  and lithium-poor  $[\text{Li}_{1/3}(\text{Ni},\text{Ti})_{2/3}]$  cation layers alternate in the  $(111)_{\text{cubic}}$  planes of rocksalt anion array. Figure 2-7(b) presents the disordered cubic rocksalt and  $\text{Li}_2\text{TiO}_3$  related ordered structure. It can be observed that this structure is actually partially ordered with lithium-rich and lithium-poor alternating layers, which is slightly different from the ordered structure of  $\alpha\text{-NaFeO}_2$  structure with distinct separated lithium slab and transition metal slab as discussed in Section 2.2.1.2. However, this partially ordered structure seems to fulfill the requirement for providing 0-TM diffusion channels with the lithium-rich and lithium-poor layers connecting each other forming a percolation network spanning the

whole structure. Detailed studies are worth to be performed to investigate the electrochemical characteristics of this material.

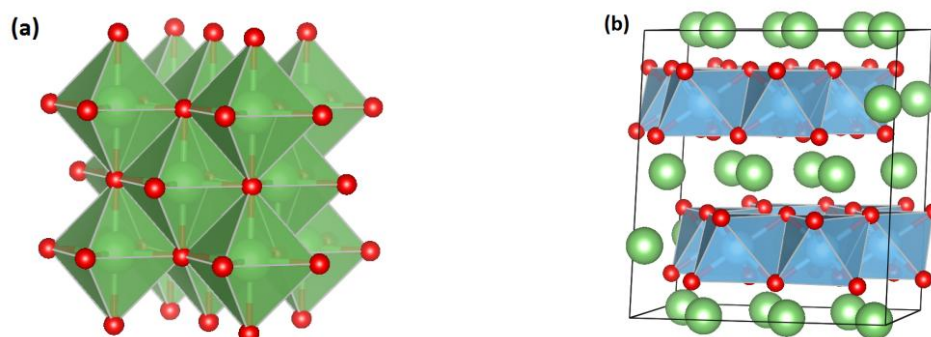


**Figure 2-7** Crystal structure of  $\text{Li}_2\text{NiTiO}_4$  with (a) disordered rocksalt (Green:  $\text{LiO}_6$ ,  $\text{MO}_6$  and  $\text{TiO}_6$  octahedral randomly distributed within the structure) and (b) ordered  $\text{Li}_2\text{TiO}_3$  structure (Blue:  $\text{TiO}_6$  octahedral; Green: Lithium ions); the full lithium ions layer of  $\text{Li}_2\text{TiO}_3$  represents the lithium-rich  $[\text{Li}_{2/3}(\text{Ni,Ti})_{1/3}]$  cation layer; the partial lithium layer with  $\text{TiO}_6$  octahedral represents the lithium-poor  $[\text{Li}_{1/3}(\text{Ni,Ti})_{2/3}]$  cation layer [120].

# Chapter 3 Materials and Methods

This chapter elaborates the experimental procedures conducted in the materials synthesis, characterization, and electrochemical studies of transition metal oxide for cathode materials in LIB applications.

## 3.1 Materials Synthesis

A few methods were used to synthesis transition metal oxides, generally categorized into two groups: (i) solid state reaction and (ii) wet chemical reaction. Solid state reaction usually involves ball milling or mixing of the solid precursors followed by sintering. Wet chemical synthesis constitutes initial reaction stage of precursors in liquid phase, in the presence of solvent, followed by sintering. The latter includes electrospinning and sol gel reaction which will be described in details in following section. Table 3-1 summarizes the synthesis method used to prepare different transition metal oxide in this thesis.

**Table 3-1** Synthesis methods used to prepare transition metal oxides presented in this thesis

Materials	Synthesis Method		
	High energy ball milling	Electrospinning	Sol Gel
$\text{Li}_{1.2}\text{V}_3\text{O}_8$	•	•	
$\text{Li}_{1.2}\text{V}_{3-x}\text{Al}_x\text{O}_8$		•	
$\text{Na}_{1.2}\text{V}_3\text{O}_8$	•	•	
$\text{Li}_2\text{NiTiO}_4$	•		•

### 3.1.1 High energy ball milling

High energy ball milling is a solid state approach to produce zero-dimensional (0D) fine particles. It is a low cost and versatile method to mechanically break down the solid precursors, followed by sintering to allow diffusion at atomic level to generate the end-

product. However, uncontrollable agglomeration and large distribution of particle size are the common disadvantages of this technique.

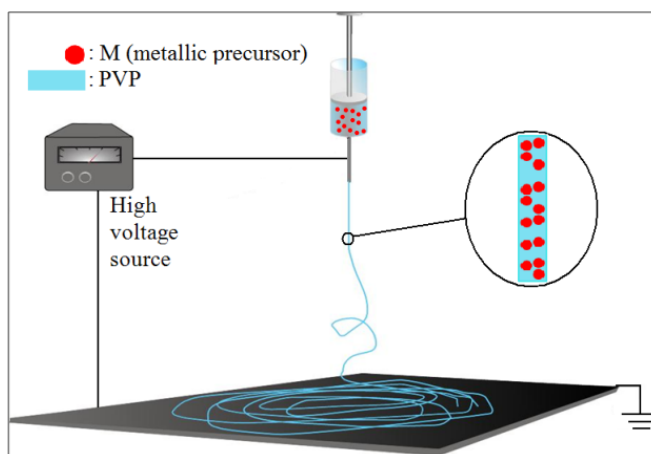
$A_{1.2}V_3O_8$  ( $A = \text{Li, Na}$ ) were prepared by mixing analytical pure lithium carbonate [ $\text{Li}_2\text{CO}_3$  (Merck)] or sodium hydrogen carbonate [ $\text{NaHCO}_3$  (Barker)] with vanadium pentoxide [ $\text{V}_2\text{O}_5$  (Sigma)] in 1.2: 3 stoichiometric molar ratio. High energy ball milling (Spex Sample preparation Mixer) was carried out in stainless steel vials with tungsten carbide balls (~5 mm in diameter) for 8 h, ball to powder weight ratio was 4: 1. Then, the as-milled powder was sintered at different temperature of 300, 400 or 500 °C for 5 h at ambient condition to form desired phase.

### 3.1.2 Electrospinning

Electrospinning is a facile and cost-effective technique to produce high aspect ratio one dimensional (1D) nanostructures. Electrospinning can be used to produce diverse fibrous arrays with tunable fiber diameters and lengths by varying a few experimental parameters such as applied voltage, solution concentration or viscosity, flow rate of solution, *etc.*[121] Electrospun 1D nanostructures such as nanobelt, nanowires, nanofibers, *etc.* are advantageous as electrode materials for LIBs. By tailoring the morphology into nano-dimension, faster diffusion kinetics will be provided due to shorter diffusion length.[122] Better electronic conductivities can be achieved by fast electron transfer via longitudinal direction which is beneficial over 0D nanoparticles in which the charge transfer relies on interparticle connectivity.

#### 3.1.2.1 Preparation of $\text{Li}_{1.2}\text{V}_3\text{O}_8$ single nanobelt and hierarchical nanobelt

The  $\text{Li}_{1.2}\text{V}_3\text{O}_8$  single nanobelt (LVO-SNB) and hierarchical nanobelt (LVO-HNB) were prepared by electrospinning. Stoichiometric amount of vanadium(V)oxytripropoxide [ $\text{OV}(\text{OC}_3\text{H}_7)_3$  (Sigma Aldrich)] and Lithium acetylacetonate [ $\text{C}_5\text{H}_7\text{LiO}_2$  (Aldrich)] were added to mixed glacial acetic acid (Tedia) and absolute ethanol (Sigma Aldrich) in weight ratio of 1:1 with vigorous stirring. Poly(vinylpyrrolidone) (PVP; Fluka) (molecular weight of 1,300,000) was dissolved in absolute ethanol to form a 6 wt% solution. Subsequently, PVP/ethanol solution was added to the metallic precursor/acetic acid solution followed by vigorous stirring to obtain a homogenous solution.



**Scheme 3-1** Schematic illustration of electrospinning set up, inset shows magnified details of the as-spun fibers which composed of PVP as the polymer agent and dispersed metallic precursors.

The precursor solution was connected to a high voltage power supply (Gamma High Voltage Research DC Power Supply). A positive voltage of 11 kV was applied between the needle tip and the grounded aluminium foil collector, with a distance of 21 cm. The solution was ejected at a constant flow rate of  $1 \text{ ml h}^{-1}$  by computer-controlled syringe pump (Kd Scientific). The as-spun fibers were heated in ambient atmosphere at different sintering temperature profiles involving optimization of ramp rate, duration and maximum temperature to obtain  $\text{Na}_{1.2}\text{V}_3\text{O}_8$  with different morphologies.  $\text{Li}_{1.2}\text{V}_3\text{O}_8$  hierarchical nanobelt (LVO-HNB) were prepared by heating the as-spun fibers directly to  $400^\circ\text{C}$  for 2 h at a ramp rate of  $2^\circ\text{C min}^{-1}$ .  $\text{Li}_{1.2}\text{V}_3\text{O}_8$  single nanobelt (LVO-SNB) were obtained when the as-spun fibers were heated to  $500^\circ\text{C}$  at  $2^\circ\text{C min}^{-1}$  and dwelled for 2 h, before cooling down to room temperature at  $2^\circ\text{C min}^{-1}$ .

### 3.1.2.2 Preparation of $\text{Li}_{1.2}\text{V}_{3-x}\text{Al}_x\text{O}_8$ ( $x = 0.03, 0.05$ ) hierarchical nanobelt

Similar experimental procedures in Section 3.1.2.1 were used to prepare  $\text{Li}_{1.2}\text{V}_{3-x}\text{Al}_x\text{O}_8$  ( $x = 0.03, 0.05$ ) hierarchical nanobelt (HNB), by adding aluminium acetylacetonate [ $\text{Al}(\text{C}_5\text{H}_7\text{O}_2)_3$  (Aldrich)] in stoichiometric amount.

The electrospinning setup used to prepare  $\text{Li}_{1.2}\text{V}_{3-x}\text{Al}_x\text{O}_8$  hierarchical nanobelt were similar as in the previous section (Section 3.1.2.1).  $\text{Li}_{1.2}\text{V}_{2.97}\text{Al}_{0.03}\text{O}_8$  (denoted by LVA3O) and  $\text{Li}_{1.2}\text{V}_{2.95}\text{Al}_{0.05}\text{O}_8$  (denoted by LVA5O) were prepared by heating the as-

spun fibers directly to 400 °C for 2 h at a ramp rate of 2 °C min<sup>-1</sup>, before cooling down to room temperature at 2 °C min<sup>-1</sup> respectively.

### 3.1.2.3 Preparation of Na<sub>1.2</sub>V<sub>3</sub>O<sub>8</sub> single nanobelt and hierarchical nanobelt

Similar experimental procedures 3.1.2.1 were used to prepare Na<sub>1.2</sub>V<sub>3</sub>O<sub>8</sub> single nanobelt (SNB) and hierarchical nanobelt (HNB), by replacing the lithium acetylacetonate by sodium acetate anhydrous [C<sub>2</sub>H<sub>3</sub>NaO<sub>2</sub> (Merck)].

The electrospinning setup used to prepare Na<sub>1.2</sub>V<sub>3</sub>O<sub>8</sub> is similar as in the previous section (Section 3.1.2.1). The as-spun fibers were heated in ambient atmosphere at different sintering temperature profiles involving optimization of ramp rate, duration and maximum temperature to obtain Na<sub>1.2</sub>V<sub>3</sub>O<sub>8</sub> with different morphologies. Na<sub>1.2</sub>V<sub>3</sub>O<sub>8</sub> single nanobelt (NVO-SNB) was prepared by heating the as-spun fibers directly to 400 °C for 2 h at a ramp rate of 2 °C min<sup>-1</sup>. Na<sub>1.2</sub>V<sub>3</sub>O<sub>8</sub> hierarchical nanobelt (NVO-HNB) was obtained when the as-spun fibers were heated to 350 °C at 2 °C min<sup>-1</sup> and dwelled for 3 h, followed by 400 °C at 2 °C min<sup>-1</sup>, dwelled for 2 h, before cooling down to room temperature at 2 °C min<sup>-1</sup>.

### 3.1.3 Sol Gel

Sol gel is a common method to synthesize materials in mass production as similar to high energy ball milling. The particle size of as-synthesized materials can be controlled by types of precursors used, gelation agent and aging temperature.[79] Basically, sol gel process involves hydrolysis and polycondensation of alkoxide or nitrate precursors to form a colloid, followed by aging and drying under ambient condition.

The titanates Li<sub>2</sub>NiTiO<sub>4</sub> were prepared via low temperature citric-acid assisted gel combustion method. The starting materials were titanyl nitrate prepared as reported elsewhere [123], nickel nitrate and lithium nitrate. Stoichiometric amounts of precursors were dissolved in deionized (DI) water with minimum amount of nitric acid under magnetic stirring, followed by addition of citric acid with weight ratio of 1:1 to total weight of metal precursors. The mixed solution was thoroughly stirred at 80 °C for 30 minutes, then the temperature was increased to 120 °C with continuous stirring to evaporate excess water. The continuous evaporation leads to gel formation. The

temperature was increased to 300 °C to obtain green-coloured product and it was then heat treated at 500 – 600 °C in air.

Two different samples of ordered and disordered structure were obtained separately by controlling the sintering temperature.

### **3.1.3.1 Carbon coating on $\text{Li}_2\text{NiTiO}_4$**

Carbon coating was done by mixing glucose with as-prepared  $\text{Li}_2\text{NiTiO}_4$  powders.. Different amount of glucose was added, weight ratio between glucose and as-prepared  $\text{Li}_2\text{NiTiO}_4$  was selected to as 3:100 (denoted as LNT/C-3) and 8:100 (denoted as LNT/C-8). The products were then calcined at 500 °C for 30 min in air to obtain carbon-coated  $\text{Li}_2\text{NiTiO}_4$ .

## **3.2 Characterization procedures**

### **3.2.1 Microscopy methods**

#### **3.2.1.1 Field emission scanning electron microscope (FESEM)**

The surface morphology of the sample was examined by FESEM (JEOL 7600F), with working distance of 6 cm and accelerating voltage of 5 kV. The samples were positioned on the aluminum sample holder with the adhesion by carbon tape and coated with ~10-15 nm of platinum by using a sputtering coater (JEOL JFC-1600) before imaging the samples under the instrument.

#### **3.2.1.2 Transmission electron microscope (TEM)**

To investigate the nanostructured characteristics of synthesized samples, JEOL 2100F TEM microscope were used to examine the morphological and crystallographic features. Since TEM was operated at 200 kV, extremely short wavelength of electron beam enables high resolution TEM (HRTEM) image to be captured by interfering the thin crystal within the samples. Electron interference patterns can be interpreted as projected potential of the crystal structure. Hence, this technique is useful for structure determination and investigations of materials at atomic scale.

### 3.2.2 Diffraction methods

#### 3.2.2.1 Powder x-ray diffraction (XRD)

The structural information was evaluated by powder XRD (Bruker D8 Advance, Cu K $\alpha$  radiation,  $\lambda = 1.54 \text{ \AA}$ ) with a step size of  $0.05^\circ$ . XRD instrument was collimated with a  $2.5^\circ$  soller,  $1^\circ$  divergence and 0.3 mm receiving slits with a scintillation counter and a secondary graphite monochromator. Rietveld refinement was performed by employing fundamental parameters peak shape profile [124] implemented in TOPAS.[125] A five-coefficient Chebychev polynomial background, a zero error, sample displacement, unit cell parameters, scale factor and crystallite sized were sequentially refined.

#### 3.2.2.2 Thin film x-ray diffraction (XRD)

The structural information of electrode materials was characterized by thin film XRD (Bruker D8 Discover, Cu K $\alpha$  radiation,  $\lambda = 1.54 \text{ \AA}$ ) with a step size of  $0.05^\circ$ . The XRD instrument is collimated 1 mm divergence slit and no receiving slit was used, with secondary graphite monochromator and a scintillation counter.

#### 3.2.2.3 Selected area electron diffraction (SAED)

Selected area electron diffraction (SAED) was conducted inside TEM column (Section 3.2.1.2). The principle of electron diffraction by TEM is similar with XRD on the basis of Bragg's law. Due to short wavelength of highly coherent electron beam in TEM column ( $0.0251 \text{ \AA}$ ), the wave-like electron passes through the lattice plane within the crystal which serve as diffraction grating, leads to electron diffraction. Information of crystal orientation, grains configurations can be extracted.

Samples for SAED were prepared by grinding under ethanol and drops of the resulting suspension deposited on holey-carbon coated copper grids, and fitted with a low background Gatan double tilt holder. Simulated images were calculated by the multislice method implemented in JEMS and the structure model obtained by Rietveld refinement was used as the input file.



### 3.2.3 Spectroscopy methods

#### 3.2.3.1 Fourier transform infrared spectroscopy (FTIR)

FTIR spectroscopy detects the molecular absorption and transmission characteristics of a material when exposed to infrared (IR) radiation. This technique was utilized on the electrospun products to understand the transformation of functional groups before and after sintering at different conditions. [126] For end product, FTIR was used to investigate the vibration bands of metallic ions in the crystal lattice.

General procedures of FTIR constitutes preparation of samples in KBR translucent pellets and the IR spectra was obtained via Perkin Elmer Spectrum GX in the range of 4000 – 400  $\text{cm}^{-1}$  at a resolution of 2  $\text{cm}^{-1}$  and scan number of 16.

#### 3.2.3.2 Energy dispersive x-ray spectroscopy (EDS)

Elemental composition of the samples were analyzed by energy dispersive x-ray spectroscopy (EDS) equipped to FESEM (Section 3.2.1.1). For EDS-FESEM, working distance of 15 cm and accelerating voltage of 20 kV were selected and scanned on an area of  $\sim 50 \mu\text{m} \times 50 \mu\text{m}$  for 10 min to obtain the spectrum. After irradiated by a focused electron beam, ground state electrons in energy level bounded to nucleus absorbs the incident energy and escape away from the orbital, leaving behind empty holes. An electron from higher energy shell subsequently fills up the hole and releases the energy difference between these two discrete shells in the form of a characteristic x-ray. Hence, energy dispersive spectrometer analyzes the quantity and energy values of characteristics and provides the elemental composition of the sample.[127]

### 3.2.4 Thermal analysis

#### 3.2.4.1 Thermogravimetric analysis (TGA)

Thermogravimetric analysis (TGA) was carried out by using TA instrument Q500 by heating the samples ( $\sim 30\text{-}50 \text{ mg}$ ) from room temperature to target temperature under air at a ramp rate of  $10 \text{ }^\circ\text{C min}^{-1}$ , with 40% air as sample gas and 60% nitrogen as balance gas.

### 3.3 Electrochemical Studies

#### 3.3.1 2016 Cell fabrication

The electrochemical performances of cathode materials were evaluated in a 2016-coin cell. The electrodes were prepared by mixing 60 wt% of active materials, 20 wt% of binder (Kynar) and 20 wt% of Super P (Timcal) in solvent, N-methyl-pyrrolidinone (NMP, Sigma Aldrich) to form a homogenous slurry. The slurry was coated on etched aluminum foil by doctor blade technique with thickness of  $\sim 20\text{-}40\ \mu\text{m}$  and dried at  $80\ ^\circ\text{C}$  in vacuum oven for 12 h. Subsequently, the coating was pressed between twin rollers to enhance the adhesion between aluminum foil and active materials. The electrodes were cut into circular disks with diameter of 16 mm, each disk contains  $\sim 2\text{-}5\ \text{mg}$  of active materials. The electrodes were assembled in an argon filled glovebox (MBraun, Germany) with oxygen and water content less than 1 ppm. Lithium metal served as a counter electrode, Celgard 2400 as the separator and 1 M solution of  $\text{LiPF}_6$  dissolved in ethylene carbonate/diethylene carbonate ( $\text{EC}:\text{DEC} = 1:1$  by volume, Charslton Technologies Pte Ltd.) was used as electrolyte. For  $\text{Li}_2\text{NiTiO}_4$  which was tested under higher voltage range ( $>4.8\text{V}$ ), LF 40 Selectilyte<sup>TM</sup> (1 M solution of Lithium tris(pentafluoroethyl)trifluorophosphate (in 1:1 by volume mixture of diethylene carbonate (DEC) /ethylene carbonate electrolyte (EC)), Merck) was used as electrolyte.

#### 3.3.2 Cyclic voltammetry

The cyclic voltammetry (CV) measurements were conducted using CHI model 1000A or Solartron 1470E in the voltage window of  $0.005 - 3.0\ \text{V}$  at room temperature with a constant scanning rate of  $0.1\ \text{mV s}^{-1}$ . To analyze the CV curve, cathodic peaks represent execution of reduction reaction which involves lithium insertion process, whereas anodic peaks indicate oxidation reaction which constitutes lithium extraction process.

#### 3.3.3 Galvanostatic cycling

Based on conventional LIB concept, all the active materials in this thesis were tested in half cell by using lithium metal as counter and reference electrode ( $\text{Li}^+/\text{Li}_0$ ,  $E^0$  with respect to  $\text{H}^+/\text{H}_0$  (SHE) =  $-3.04\ \text{V}$ ). The lithium intercalation and deintercalation behavior of samples were examined by galvanostatic cycling (Multichannel Battery Tester, Neware Technology Limited) in the voltage window of  $1.5 - 4.0\ \text{V}$  for vanadates and  $1.5 - 5.0\ \text{V}$

for titanates at room temperature, under constant current mode. To interpret the galvanostatic curve, lithium insertion process is represented by discharge curve whereas charge curve indicates lithium extraction reaction.

### 3.3.4 Electrochemical impedance spectroscopy

Electrochemical impedance spectroscopy (EIS) is a convenient electrochemical technique to understand the phase transformation, charge transfer and mass transfer kinetics during intercalation process upon charging and discharging.[128]

In this report, EIS was performed on bare and cycled electrodes. Firstly, the cells were galvanostatically discharged and charged or in reverse sequence, depending on conditions, at specific current density to a cutoff voltage and potentiostat being executed for at least 1 h. Subsequently, EIS was measured in the range of 100 MHz-0.1Hz by applying the bias voltage of 10 mV. The data was shown in the form of Nyquist plots ( $Z'$  vs.  $-Z''$ , where  $Z'$  and  $Z''$  are the real and imaginary parts of complex impedance) and an equivalent circuit to describe the electrochemical characteristic was included in the discussion.

### 3.3.5 Ex situ electrode preparation

For *ex situ* XRD characterization, electrodes were retrieved by disassembling the coin cells at different state of charge and rinsed them with adequate amount of DEC to remove the organic electrolyte. The electrodes were stored dry in glovebox for a few days and sealed in an air tight container during transportation before proceeding to characterization step.

## Chapter 4 Results

This chapter presents all the experimental results conducted in this thesis. Detailed observations in materials characterization and electrochemical testing were presented. Firstly,  $\text{Li}_{1.2}\text{V}_3\text{O}_8$  with different morphology was explored to investigate the viability of nanomaterials application in LIBs. This was then followed by cation substitution on  $\text{Li}_{1.2}\text{V}_3\text{O}_8$  to demonstrate the applicability of this approach to resolve the core issue of rocksalt-based cathodes.

To venture out of the field restricted by ordered rocksalt structure, investigation into possibility of disordered rocksalt-based materials as LIB cathodes was conducted.  $\text{Li}_2\text{-NiTiO}_4$  with different degree of cation ordering were synthesized by sol gel method with alteration in synthesis condition and lithium content.

### 4.1 $\text{Li}_{1.2}\text{V}_3\text{O}_8$

$\text{Li}_{1.2}\text{V}_3\text{O}_8$  nanoparticles of different particle size distribution were prepared by high energy ball milling (HEBM) to investigate the effect of particle size on electrochemical performance.

The studies were then extended to explore the effect of 1D nanostructuring on electrochemical characteristics. Therefore,  $\text{Li}_{1.2}\text{V}_3\text{O}_8$  nanobelts (hierarchical and standalone configuration) were synthesized by electrospinning.  $\text{Li}_{1.2}\text{V}_3\text{O}_8$  hierarchical nanobelts deliver promising electrochemical performance but cyclability was still unsatisfactory.

Subsequently, cation substitution was conducted on  $\text{Li}_{1.2}\text{V}_3\text{O}_8$  to investigate its impact on electrochemical performance in terms of cyclability and achievable capacity. Firstly, minor substitution of vanadium with aluminium of similar sized. This was then followed by full substitution of lithium with larger sodium ions. Detailed observations including structural and electrochemical aspects were presented.

### 4.1.1 Ball milled $\text{Li}_{1.2}\text{V}_3\text{O}_8$

$\text{Li}_{1.2}\text{V}_3\text{O}_8$  nanoparticles (LVO-NP) were synthesized by HEBM method. By sintering the ball milled precursors at different temperature resulted in nanoparticles with distinguishable size distribution. As-obtained products were employed for electrochemical testing to understand the correlation between particle size and electrochemical transformations.

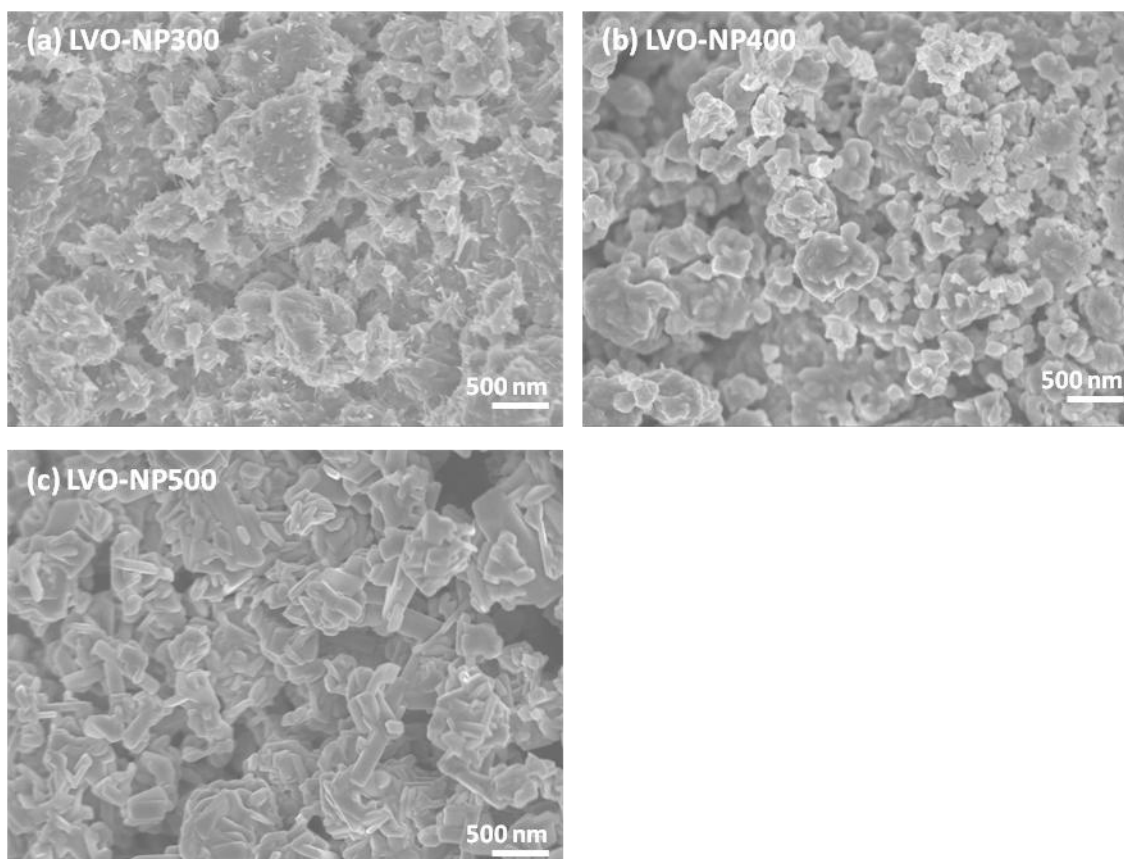


**Figure 4-1** FESEM images of annealed  $\text{Li}_{1.2}\text{V}_3\text{O}_8$  at different temperature. (a) LVO-NP300, (b) LVO-NP400 and (c) LVO-NP500

FESEM images of annealed  $\text{Li}_{1.2}\text{V}_3\text{O}_8$  at different sintering temperature of 300 °C, 400 °C and 500 °C (named as LVO-NP300, LVO-NP400 and LVO-NP500) reveal increment of particle size with increasing annealing temperature (Figure 4-1). The particle size is within the range of 40-80 nm for LVO-NP300, 90-140 nm for LVO-NP400 and 150-300 nm for LVO-NP500.

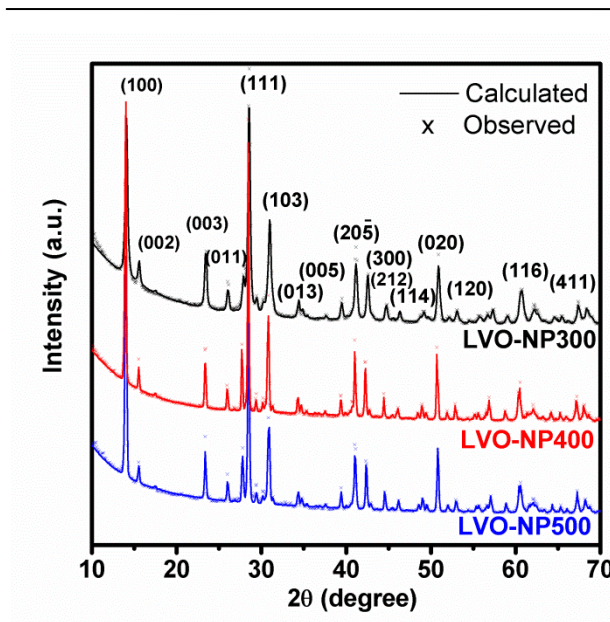


**Figure 4-2** XRD patterns and Rietveld refinements of LVO-NP300, LVO-NP400 and LVO-NP500

Crystal information was obtained from XRD data and Rietveld refinement (Figure 4-2). XRD patterns ensure the formation of monoclinic phase with space group of  $P2_1/m$ . The structural information of  $\text{Li}_{1.2}\text{V}_3\text{O}_8$  were refined by Rietveld method and tabulated in Table 4-1. The slight variation of lattice parameters may vary due to different sintering temperature.

**Table 4-1** Lattice parameter of ball milled  $\text{Li}_{1.2}\text{V}_3\text{O}_8$  computed by Rietveld refinement

Sample	Lattice parameter				
	a (Å)	b (Å)	c (Å)	$\beta$ (°)	V (Å <sup>3</sup> )
<b>LVO-NP300</b>	6.6183(1)	3.5901(4)	11.985(2)	107.87(9)	271.01(8)
<b>LVO-NP400</b>	6.6461(8)	3.5943(3)	12.004(1)	107.80(7)	273.02(5)
<b>LVO-NP500</b>	6.6659(5)	3.6005(2)	12.011(8)	107.72(5)	274.60(3)

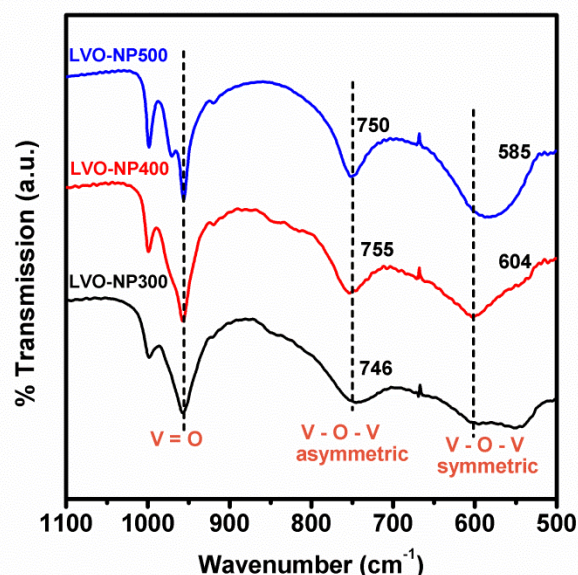


**Figure 4-3** FTIR analysis of LVO-NP300, LVO-NP400 and LVO-NP500.

FTIR characterization was applied to determine the vibration bands of vanadium ions in crystal lattice of sintered  $\text{Li}_{1.2}\text{V}_3\text{O}_8$  powders. Figure 4-3 shows the FTIR spectra of  $\text{Li}_{1.2}\text{V}_3\text{O}_8$  nanoparticles (LVO-NP) which were collected within frequency range of 500-1100  $\text{cm}^{-1}$  in transmission mode. The peaks in the range of  $\sim 950$ -1000  $\text{cm}^{-1}$  were attributed to the stretching vibration of three  $\text{V}=\text{O}$  bonds in  $\text{Li}_{1.2}\text{V}_3\text{O}_8$ , [129-131] corresponding to bond length  $< 1.65$  Å, [132, 133] at  $\sim 957$   $\text{cm}^{-1}$ ,  $\sim 971$   $\text{cm}^{-1}$  and  $\sim 999$   $\text{cm}^{-1}$ , as observed in spectra for all LVO-NP. It could be observed that the degree of distinct separation of these three peaks, especially the middle one decreased with decreasing sintering temperature. This was due to decreasing crystallinity with less ordered atomic configuration. [134] Another two distinguishable peaks which were observed at  $\sim 550$ -750  $\text{cm}^{-1}$ , can be assigned to stretching vibrations of  $\text{V}-\text{O}-\text{V}$  bonds. [133, 135] By comparing LVO-NP sintered at different temperature, the peaks at  $\sim 604$   $\text{cm}^{-1}$  for LVO-NP400 and  $\sim 585$   $\text{cm}^{-1}$  for LVO-NP500 were attributed for  $\text{V}-\text{O}-\text{V}$  symmetric stretching [136-138]. This peak was appeared as a broad band extending from  $\sim 542$  to 605  $\text{cm}^{-1}$ ; less structured for LVO-NP300. Another broad peak at  $\sim 746$   $\text{cm}^{-1}$  for LVO-NP300 was corresponding to asymmetric stretching mode of  $\text{V}-\text{O}-\text{V}$  bonds. [138] Similar phenomenon had been observed in literature due to less uniform  $\text{V}-\text{O}-\text{V}$  bond angle. [129] This stretching mode appeared as sharp peaks at  $\sim 750$   $\text{cm}^{-1}$  for LVO-NP300 and at  $\sim 755$   $\text{cm}^{-1}$  for LVO-NP400 respectively. By comparing the  $\text{V}-\text{O}-\text{V}$  bands for LVO-NP400 and LVO-NP500, both peaks were slightly red shifted for LVO-NP500. The  $\text{V}-\text{O}-\text{V}$  stretching are related to motion of oxygen atom shared by the  $\text{VO}_n$  polyhedral [131], the band shift to lower

wavenumber indicating existence of long-range ordering within the lattice. In other words, LVO-NP500 has higher degree of long-range ordering than LVO-NP400.

The separation between these two peaks, which is the wavenumber difference

$\Delta\nu = \nu_{as}(\text{VOV}) - \nu_s(\text{VOV})$  increases with increasing V-O-V angle.[139] Studies had shown that decreasing V-O-V angle was associated with increasing bond length which is related to larger lattice volume. The  $\Delta\nu$  for LVO-NP500 was the biggest which is  $165 \text{ cm}^{-1}$ , followed by that of LVO-NP400 with  $151 \text{ cm}^{-1}$  then LVO-NP300 with the smallest  $\Delta\nu$  of  $143 \text{ cm}^{-1}$ . Thus, LVO-NP500 with the highest V-O-V angle will have largest lattice volume. This was well aligned with the refinement of XRD pattern as shown earlier (Table 4-1).

#### 4.1.2 Ball milled $\text{Li}_{1.2}\text{V}_3\text{O}_8$ nanoparticles: Comparison of electrochemical performance

To study the redox behavior of  $\text{Li}_{1.2}\text{V}_3\text{O}_8$  in LIB applications, CV experiment was performed at very slow scan rate. Figure 4-4 shows CV profile of LVO-NP300, LVO-NP400 and LVO-NP500 at a scan rate of  $0.1 \text{ mV s}^{-1}$  which was cycled between 1.5 – 4.0 V *versus*  $\text{Li/Li}^+$ . During the first cycle, the CV curve of LVO-NP300 exhibited four main cathodic peaks at ~2.24, 2.52, 2.78 and 3.64 V and four main anodic peak at ~2.52, 2.70, 2.88 and 3.53 V, indicating occurrence of multistep phase transformation within the electrode material. The cathodic peaks at ~2.78 V represented lithium insertion into the tetrahedral sites[79, 140], with the redox peak pair during anodic scan at ~2.88 V attributed to lithium extraction. The second peak at ~2.52 V (cathodic) constituted co-existence of two-phases which involved phase transformation from  $\text{Li}_{1.2}\text{V}_3\text{O}_8$  to  $\text{Li}_4\text{V}_3\text{O}_8$  and during lithium extraction.[141] This was then followed by the shallow peak at ~2.24 V (cathodic) indicating formation of single phase  $\text{Li}_4\text{V}_3\text{O}_8$ . The multi-step electrochemical reaction involved change in oxidation states of vanadium ions from +5 to +4 upon formation of  $\text{Li}_4\text{V}_3\text{O}_8$ . [142] Another low intense coupled peak pair at ~3.64 V (cathodic) and 3.53 V (anodic) corresponded to lithium insertion/extraction into/from octahedral sites within the lattice.

By comparing the CV curve for LVO-NP300 with LVO-NP400 and LVO-NP500, the four main redox peaks appeared at almost same potentials for anodic and cathodic scan respectively, indicating the overall reactions were similar during first cycle. For LVO-



NP400, those cathodic peaks were at  $\sim 2.27$ ,  $2.43$ ,  $2.67$  and  $3.60$  V with the coupled anodic pairs at  $\sim 2.48$ ,  $2.80$ ,  $2.87$  and  $3.68$  V. It could be observed that the two anodic peaks which was appeared distinctly at  $\sim 2.70$  and  $\sim 2.88$  V for LVO-NP300 but was transformed into a split-single peaks for LVO-NP400 at  $\sim 2.79 - 2.87$  V and merged into a sharp intense peak at  $\sim 2.81$  V for LVO-NP500. This may be attributed to different diffusion kinetics[143] for lithium extraction because of different degrees of long-range ordering[144] as previously mentioned in FTIR characterization (Section 4.1.1).

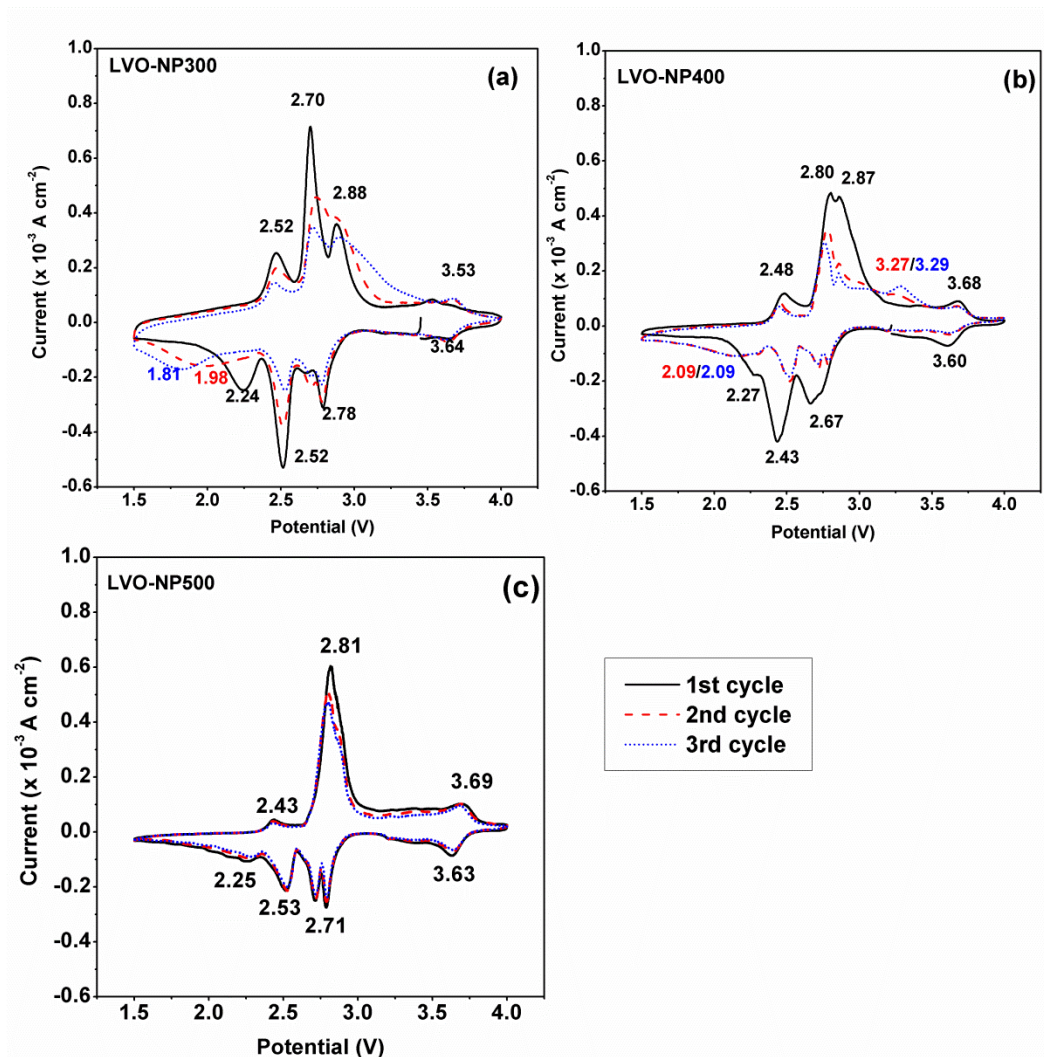


**Figure 4-4** CV of (a)LVO-NP300, (b) LVO-NP400 and (c) LVO-NP500 at  $0.01 \text{ mV s}^{-1}$  for first three cycles

After the first cycle of discharging and charging, the four redox peak pairs reappeared in second cycle indicating reversibility of corresponding electrochemical reactions for LVO-NP300, LVO-NP400 and LVO-NP500. However, additional cathodic peaks were observed at  $\sim 1.98$  V during second cycle and at  $\sim 1.81$  V during third cycle for LVO-NP300. Besides, broadening of the anodic peak at  $\sim 2.88$  V to  $\sim 3.30$  V could be observed.

For LVO-NP400, similar additional peaks could be noticed at  $\sim 2.09$  V (cathodic) and  $\sim 3.27/3.29$  V ( $2^{\text{nd}}/3^{\text{rd}}$  cycle; anodic) in subsequent cycles. Interestingly, it could be noticed that there was no additional peaks appeared at  $1.8 - 2.1$  V and  $2.88 - 3.30$  V in subsequent cycles for LVO-NP500 as observed in LVO-NP300 and LVO-NP400.

These additional peaks for LVO-NP300 and LVO-NP400 were associated with the emergence of new electrochemical processes. Previous studies had shown that these additional cathodic peaks at  $1.8 - 2.1$  V in subsequent cycles were associated with the spanning of anodic peak at  $\sim 2.88$  V in first cycle over larger potential range until  $\sim 3.30$  V in subsequent cycles.[82, 83] Tanguy *et al.*[82] had demonstrated in their work that the initiation of these new electrochemical reactions originated from electrolyte decomposition within  $2.0 - 2.6$  V due to intrinsic characteristics of the grain surface for  $\text{Li}_{1+x}\text{V}_3\text{O}_8$ . Electrolyte decomposition had caused formation of passive film that progressively propagated through the electrode upon cycling. This shut off the electronic conductivities within the nano-grains leading to reduced electrochemical activities of electrodes through the initial potential window. Besides, the electrolyte composition was expected to be altered that also resulted in decreased electrochemical reactivity. Previous studies had found out that the emergence of new electrochemical reactions at  $1.8 - 2.1$  V and  $2.88 - 3.30$  V were similar to structural phase transformation during first cycle, but less reactive.[82, 145] This was due to kinetics limitation caused by embedment of some nano-sized grains within the passive layer. This phenomenon was accounted for the capacity fading commonly observed in literature for nano sized  $\text{Li}_{1+x}\text{V}_3\text{O}_8$  until overall capacities reached stabilization upon prolonged cycling.[68, 146]

Similar reactions had been observed and shown in our work for long term cycling test (Figure 4-5). LVO-NP300 achieved highest capacity for first cycle, which was  $\sim 320$  mAh  $\text{g}^{-1}$  (equivalent to  $\sim 3.44$  moles of lithium ions), followed by LVO-NP400 ( $\sim 256$  mAh  $\text{g}^{-1}$ ,  $\sim 2.75$  moles of lithium ions) and LVO-NP500 ( $\sim 216$  mAh  $\text{g}^{-1}$ ,  $\sim 2.32$  moles of lithium ions) when they were cycled at a current density of  $200$  mA  $\text{g}^{-1}$  (Figure 4-5). After 100 cycles, the capacities was decreased and stabilized at  $\sim 50$  mAh  $\text{g}^{-1}$  ( $\sim 0.54$  mole of lithium ions) for LVO-NP300, at  $\sim 125$  mAh  $\text{g}^{-1}$  ( $\sim 1.34$  moles of lithium ions) for LVO-NP400 and at  $\sim 171$  mAh  $\text{g}^{-1}$  ( $\sim 1.84$  moles of lithium ions) for LVO-NP500.

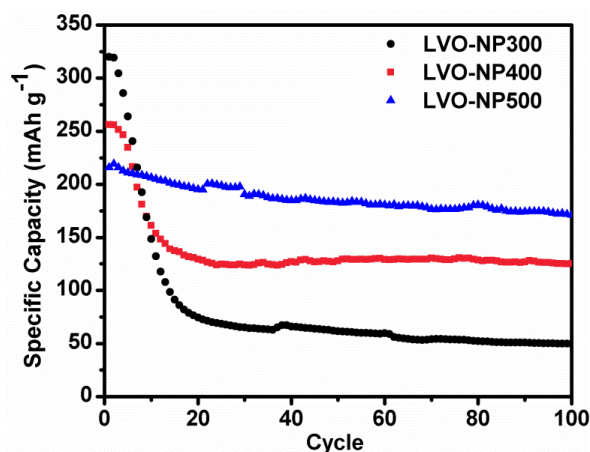


**Figure 4-5** Comparison of cycling performance between LVO-NP300, LVO-NP400 and LVO-NP500.

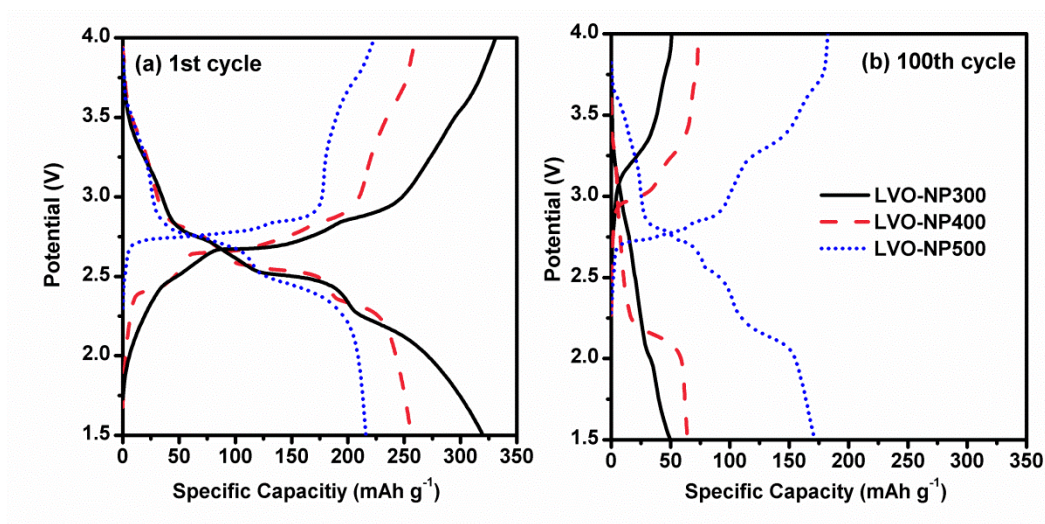


**Figure 4-6** Galvanostatic cycling results of annealed  $\text{Li}_{1.2}\text{V}_3\text{O}_8$  at current density of  $200 \text{ mA g}^{-1}$ : (a) 1<sup>st</sup> cycle and (b) 100<sup>th</sup> cycle at scan rate of  $0.1 \text{ mV s}^{-1}$ .

The galvanostatic curves for all LVO-NPs constituted multiple plateaus were well-aligned with CV scan which showed splitting of several redox peaks during first cycle. First charge/discharge behavior for LVO-NP300, LVO-NP400 and LVO-NP500 were almost similar. Multiple plateaus stretching from  $\sim 2.80 \text{ V}$  towards  $\sim 2.20 \text{ V}$  indicated lithium insertion process followed by charging process constituting plateaus extending from  $\sim 2.70 \text{ V}$  to  $\sim 3.00 \text{ V}$ . The plateaus were observed to be shorter and steeper with larger polarization for LVO-NP500 compared to that of LVO-NP400 and LVO-NP300, possibly due to slower kinetics in lithium diffusion process.[147] After 100 cycles, similar plateaus were preserved for LVO-NP500 though with more distinguishable separation between plateaus instead of smearing into nearly single plateau as observed in first cycle. Capacity

fading was inevitable but minimized for LVO-NP500, due to structural damage upon repeated lithium intercalation/deintercalation owing to intrinsic structural properties of  $\text{Li}_{1.2}\text{V}_3\text{O}_8$ . [68, 148, 149]

As the sintering temperature increases, the particle size of the as-synthesized LVO-NP increases as shown in Figure 4-1. LVO-NP500 with particle size of ~150 nm and above was able to provide satisfactory electrochemical performance as shown in Figure 4-5 though with lower initial capacities as compared to that of LVO-NP300 and LVO-NP400. Same redox peaks reappeared in subsequent cycles indicating good reversibility of electrochemical reaction for LVO-NP500. Hence, our observations showed that the particle size of electrode materials has large impact on the battery performance in terms of electrochemical reversibility, capacity and cyclability. The correlation between particles size and electrochemical characteristics of electrodes will be further discussed in Section 5.1.1.

#### 4.1.3 Electrospun $\text{Li}_{1.2}\text{V}_3\text{O}_8$ nanobelts: Effect of sintering temperature on morphology growth

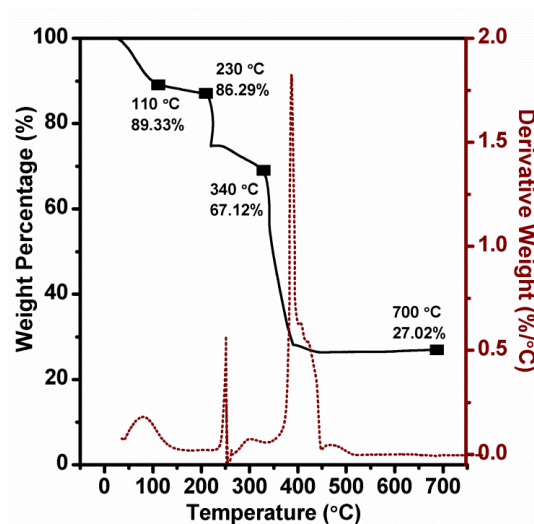
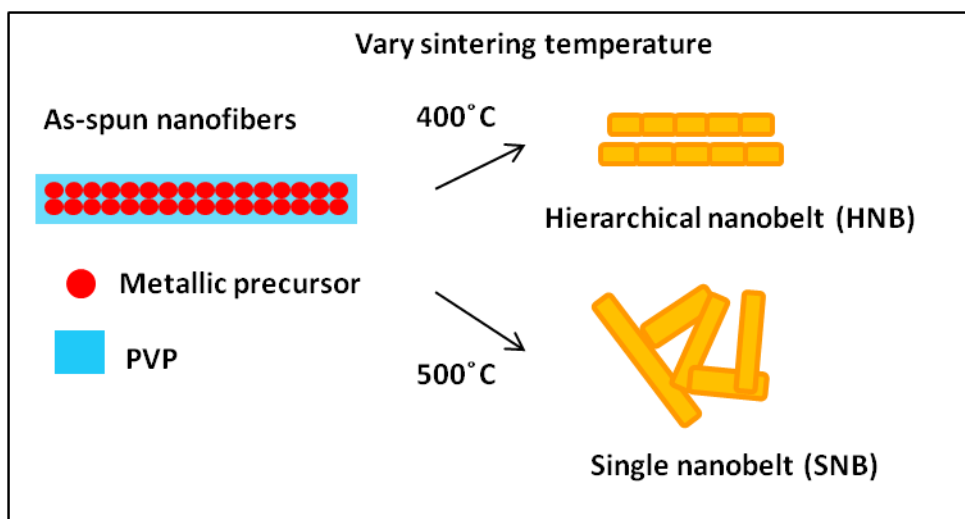


**Figure 4-7** TGA of as-spun  $\text{Li}_{1.2}\text{V}_3\text{O}_8$  nanofibers.

TGA was performed on as-spun nanofibers between 35 °C to 700 °C, to determine the sintering temperature. The weight loss of about 11 wt% within the range of 35 °C to 110 °C was due to the vaporization of volatile components, such as adsorbed moisture, residual ethanol and acetic acid. The vivid peak at 230 °C was related to the

decomposition of the metallic precursor, which was vanadium(V)oxytripropoxide and lithium acetylacetonate. Another peak at 340 °C was attributed to the removal of the PVP. There was no significant weight loss (stabilizes at about 27%) recorded at temperature above 400 °C, indicating the completion of chemical reaction. Therefore, the final sintering temperature was chosen to be above 400 °C.

Electrospinning is a facile approach to yield nanostructures with tunable morphology. Various parameters such as precursor concentration, type of polymers and experimental condition including applied voltage, working distance, solution feed rate, sintering temperature, *etc.* greatly affects the morphologies and size distribution of as-obtained 1D nanostructures. Previously, Li *et al.*[150] and Wang *et al.*[151] had reported that sintering temperature employed on as-spun nanofibers can be optimized to create spacing between nanograins to produce desired hierarchical or porous nanostructures. In present work, the as-spun nanofibers were sintered at 400 and 500 °C to investigate the morphology evolution under the influence of sintering temperature. Upon sintering the as-spun nanofibers to 400 °C, the PVP polymer template encapsulating the metallic precursor within the fibrous structure slowly decomposed and the reaction between the precursors occurred simultaneously to produce LVO nanoparticles. Decomposition of PVP involved oxidation into CO<sub>2</sub> and subsequent volatilization. The outward diffusion of CO<sub>2</sub> due to decomposition of PVP polymer backbone from the inner part accelerated the movement of LVO nanoparticles toward the surface. The LVO nanoparticles were still connected together but gradually grown into plate-like configuration due to self-limiting intrinsic characteristic of monoclinic structure. The growth of individual plate-like configuration involved consumption of neighboring nanograins, which promoted the formation of spacing between the plate-like structures, eventually assembled into hierarchical nanobelt (LVO-HNB400) (Figure 4-8(b)). By further increasing the sintering temperature to 500 °C, the fibrous framework was destroyed, facilitating the continuous growth of LVO plates into larger plates, forming single nanobelt (LVO-SNB500). The amount of nanobelt per unit area was reduced as shown in Figure 4-8(c), indicating that the small nanobelts were grown into larger ones. The diameter of as-spun nanofibers was 180-200 nm. After sintering, the diameter of LVO-HNB400 had shrunk to 120-150 nm due to decomposition of PVP. Upon increasing the sintering temperature to 500 °C, larger and standalone nanobelts (LVO-SNB500) with diameter of 175-200 nm were formed.



**Scheme 4-1** Schematic illustration of  $\text{Li}_{1.2}\text{V}_3\text{O}_8$  formation mechanism. If the as-spun nanofibers is heated at lower temperature of 400 °C, the fibrous network can be retained, forming hierarchical configuration of nanobelt (LVO-HNB400). By further increasing the temperature to 500 °C, destroy of fibrous framework and further grain growth lead to formation of single nanobelt (LVO-SNB500).

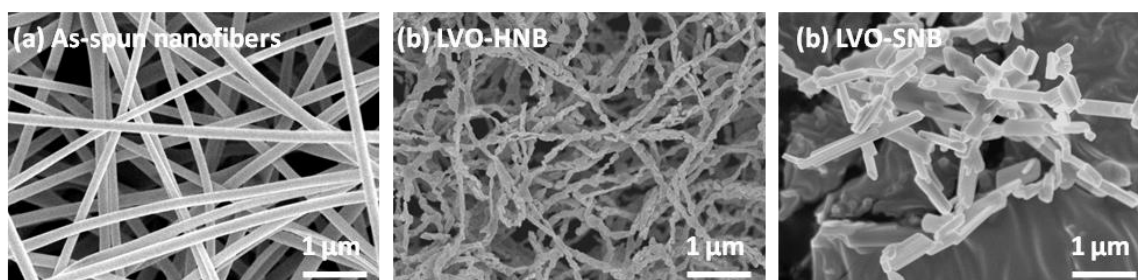


**Figure 4-8** FESEM images of (a) as-spun nanofibers, (b) LVO-HNB400 and (c) LVO-SNB500

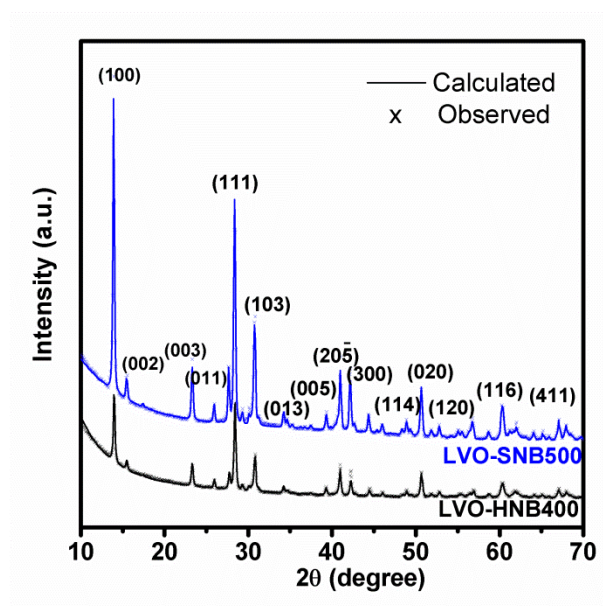
#### 4.1.4 Electrospun $\text{Li}_{1.2}\text{V}_3\text{O}_8$ nanobelts: Materials characterization

XRD pattern confirms the formation of single phase monoclinic structure (space group:  $P2_1/m$ ) for LVO-HNB400 and LVO-SNB500 respectively. Lattice parameters along with lattice volume of LVO-HNB400 and LVO-SNB500 obtained by Rietveld method are tabulated in Table 4-2.



**Table 4-2** Lattice parameters and crystallite sizes of  $\text{Li}_{1.2}\text{V}_3\text{O}_8$  computed by Rietveld refinement

Sample	Lattice parameter				$V (\text{\AA}^3)$	Crystallite size (nm)
	a ( $\text{\AA}$ )	b ( $\text{\AA}$ )	c ( $\text{\AA}$ )	$\beta$ ( $^\circ$ )		
<b>LVO-HNB400</b>	6.6547(1)	3.5983(3)	12.005(1)	107.74(6)	273.78(6)	40.1(1)
<b>LVO-SNB500</b>	6.6717(8)	3.6041(2)	12.015(1)	107.68(6)	275.25(5)	74.5(3)

**Figure 4-9** Rietveld refinement of XRD pattern for  $\text{Li}_{1.2}\text{V}_3\text{O}_8$  nanobelts

FTIR spectroscopy was employed to obtain the vibration modes for as-spun nanofibers and end-product in order to study the effect of sintering conditions on the transformations of functional groups (Figure 4-10). The FTIR spectra of as-spun nanofibers were observed to be almost identical to that of PVP. The broad band at  $\sim 3440 \text{ cm}^{-1}$  was attributed by the stretching vibration of the O-H bond due to the presence of adsorbed moisture, residual ethanol and acetic acid. Another two adjacent peaks were observed at  $\sim 2956 \text{ cm}^{-1}$  and  $\sim 2880 \text{ cm}^{-1}$ , correlated to the stretching of  $\text{CH}_2$  and C-H groups of PVP[126]. The vibration band at  $1662 \text{ cm}^{-1}$  was related to either C-N or C=O functional groups, accompanied with  $\text{CH}_2$  scissoring and wagging at  $1452 \text{ cm}^{-1}$  and  $1267 \text{ cm}^{-1}$  respectively. These bands were observed due to the presence of PVP, which did not appear in the FTIR spectra of end products due to the complete elimination after sintering.

The adjacent peaks at  $\sim 950 - 1000 \text{ cm}^{-1}$  observed in the spectra of as-spun nanofibers were attributed to stretching of V=O bonds due to addition of the vanadium precursor with the same peaks reappeared in end product. These peaks could be identified as three distinguishable peaks in LVO-SNB500 at  $\sim 957 \text{ cm}^{-1}$ ,  $971 \text{ cm}^{-1}$  and  $999 \text{ cm}^{-1}$  which can be assigned to three short V=O bonds,[130, 133] as similar to that LVO-NP in Section 4.1.1. Coherent peaks position could be observed for LVO-HNB400 except that the middle peak was almost indistinguishable due to lower crystallinity and less ordered atomic configuration,[134] as similarly demonstrated in LVO-NP of different sintering temperature in Section 4.1.1. Another two distinct peaks can be observed within  $550 - 760 \text{ cm}^{-1}$  in LVO-HNB400 and LVO-SNB500 indicating asymmetric and symmetric stretching of V-O-V bonds.[72, 129] Both the peaks were slightly red-shifted for LVO-SNB with higher degree of long-range ordering. Higher formation temperature for LVO-SNB had enabled the creation of more rigid configuration.

The  $\Delta\nu$  was estimated to be  $\sim 178 \text{ cm}^{-1}$ , which is bigger for LVO-SNB500 compared to  $\sim 150 \text{ cm}^{-1}$  for LVO-HNB400. In other words, LVO-SNB500 constitutes larger V-O-V angle with smaller bond length and larger lattice volume. This aligned with the XRD refinement which had been shown in Table 4-2.

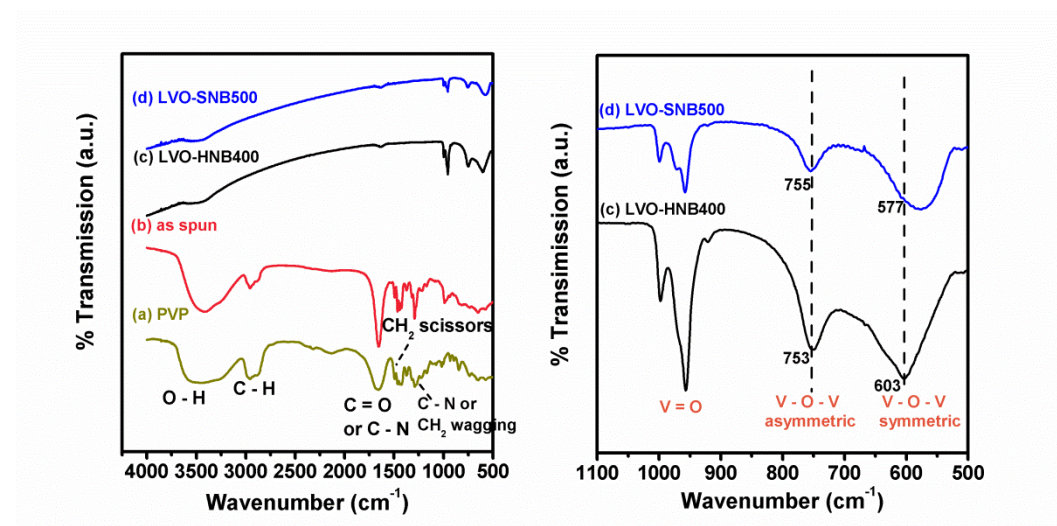


**Figure 4-10** FTIR analysis of  $\text{Li}_{1.2}\text{V}_3\text{O}_8$  formation. (a) PVP, (b) As-spun nanofibers, (c) LVO-HNB400 and (d) LVO-SNB500 (left). Enlarged version of FTIR with specific bands for (c) LVO-HNB400 and (d) LVO-SNB500.



### 4.1.5 Electrospun $\text{Li}_{1.2}\text{V}_3\text{O}_8$ nanobelts: Comparison of electrochemical performance

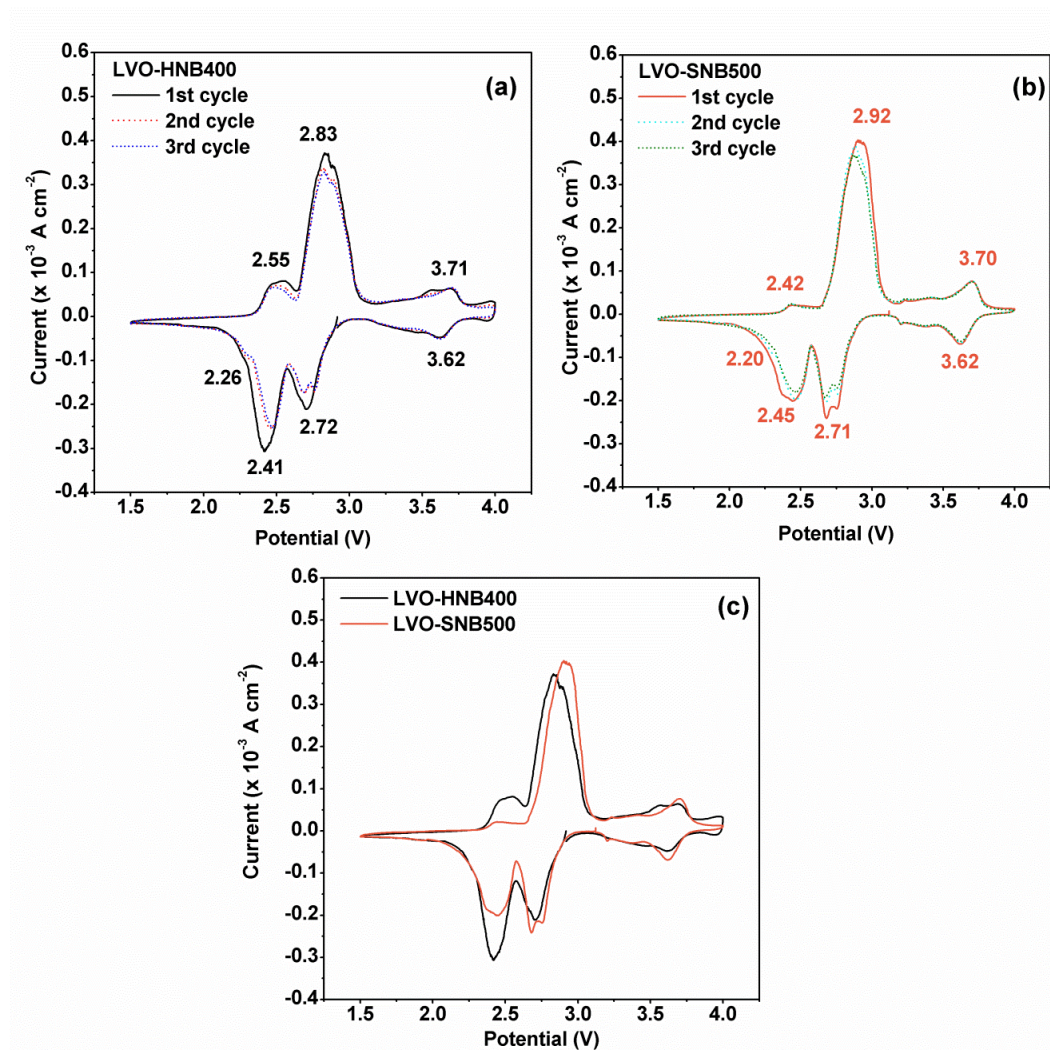


**Figure 4-11** CV of (a) LVO-HNB400, (b) LVO-SNB500 at  $0.1 \text{ mV s}^{-1}$  for first three cycles and (c) comparison of first cycle CV scan between LVO-HNB400 and LVO-SNB500.

The electrochemical behavior of electrospun  $\text{Li}_{1.2}\text{V}_3\text{O}_8$  was similar to LVO-NP as discussed in Section 4.1.2. As observed from the CV curve for LVO-HNB400, there were two well defined peaks between 3.0 to 2.0 V during the first cathodic scan. The first redox peaks at  $\sim 2.72$  V corresponded to insertion of lithium ions into the empty tetrahedral site. Initiation of redox reaction involved reduction of partial  $\text{V}^{5+}$  ions to  $\text{V}^{4+}$  ions. The second reduction peak at  $\sim 2.41$  V was attributed to filling of the octahedral sites.[140] It was a two-phase reaction constituting the transformations of  $\text{Li}_{1+x}\text{V}_3\text{O}_8$  to  $\text{Li}_4\text{V}_3\text{O}_8$  with the two

phases coexist in the material. This was then followed by a low intense peak at  $\sim 2.26$  V indicating formation of  $\text{Li}_4\text{V}_3\text{O}_8$  with all the octahedral sites being completely filled.[140, 152] The multi-step electrochemical reaction involved change in oxidation states of all vanadium ions from +5 to +4 upon formation of  $\text{Li}_4\text{V}_3\text{O}_8$ . [142] The coupled anodic peaks appeared as a pair-up redox peak at  $\sim 2.55$  and  $\sim 2.83$  V. The differences in intensities of anodic peaks with the corresponding cathodic pairs were due to different energy barrier for the lithium insertion and extraction processes.[149, 152] Another low intense coupled peak pair could be observed at  $\sim 3.62$  V (cathodic) and  $\sim 3.71$  V (anodic) representing lithium insertion and extraction into octahedral sites respectively.[143, 148] Overall, lithium insertion and extraction into  $\text{Li}_{1.2}\text{V}_3\text{O}_8$  framework occurred through multi-step redox reaction with different sites of different energy barrier within the lattice as indicated by splitting of several redox peaks.

From Figure 4-11(c), it could be observed that the LVO-SNB500 exhibited almost similar electrochemical reactions with LVO-HNB400. However, it was worth noting that the hysteresis for LVO-SNB500 was slightly more severe than that of LVO-HNB400, which may account for lower specific capacity as shown in Figure 4-12. As shown in Figure 4-11(c), it could be observed that the anodic peaks were slightly shifted for LVO-SNB500 at  $\sim 2.42$  V and  $\sim 2.90$  V in comparison with that of LVO-HNB400 at  $\sim 2.55$  and  $\sim 2.83$  V though the cathodic peaks were in similar potential values. The potential separation between redox peak pair for LVO-SNB500 was larger with  $\sim 0.21$  V (redox couple at  $\sim 2.71/2.92$  V) whereas for LVO-HNB400 was  $\sim 0.11$  V (redox couple at  $\sim 2.72/2.83$  V) indicating poorer diffusion kinetics[143] for LVO-SNB500.

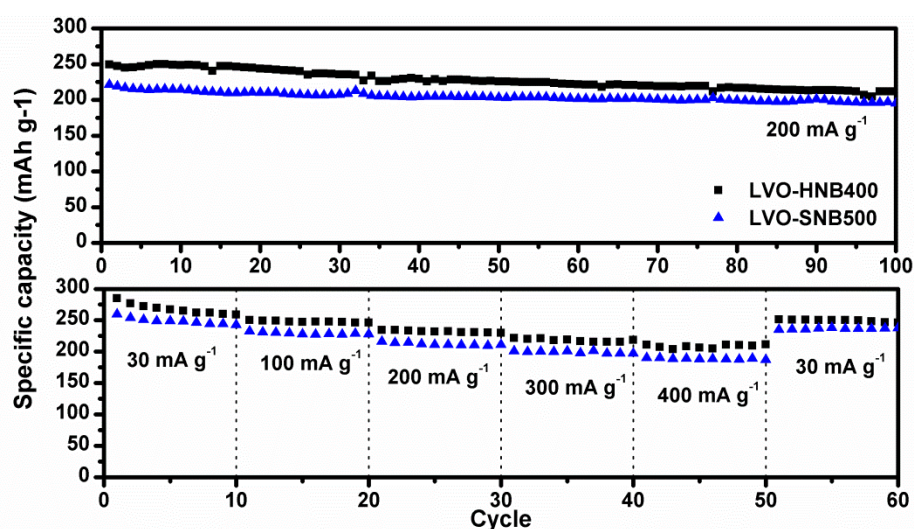


**Figure 4-12** Cycling performance of LVO-HNB400 and LVO-SNB500 at different current densities.



Galvanostatic profiles of LVO-HNB400 and LVO-SNB500 were consistent with electrochemical reactions as discussed earlier in CV scan. The charging and discharging curves for subsequent cycles were in analogue with that of first cycle for both LVO-HNB400 and LVO-SNB500 as shown in Figure 4-13(a) and (b), indicating good reversibility for electrochemical reactions. Better indication of higher polarization for LVO-SNB500 compared to LVO-HNB400 could be observed in Figure 4-13(c) and (d) with larger separation between the charging and discharging curve for first and second cycles respectively.

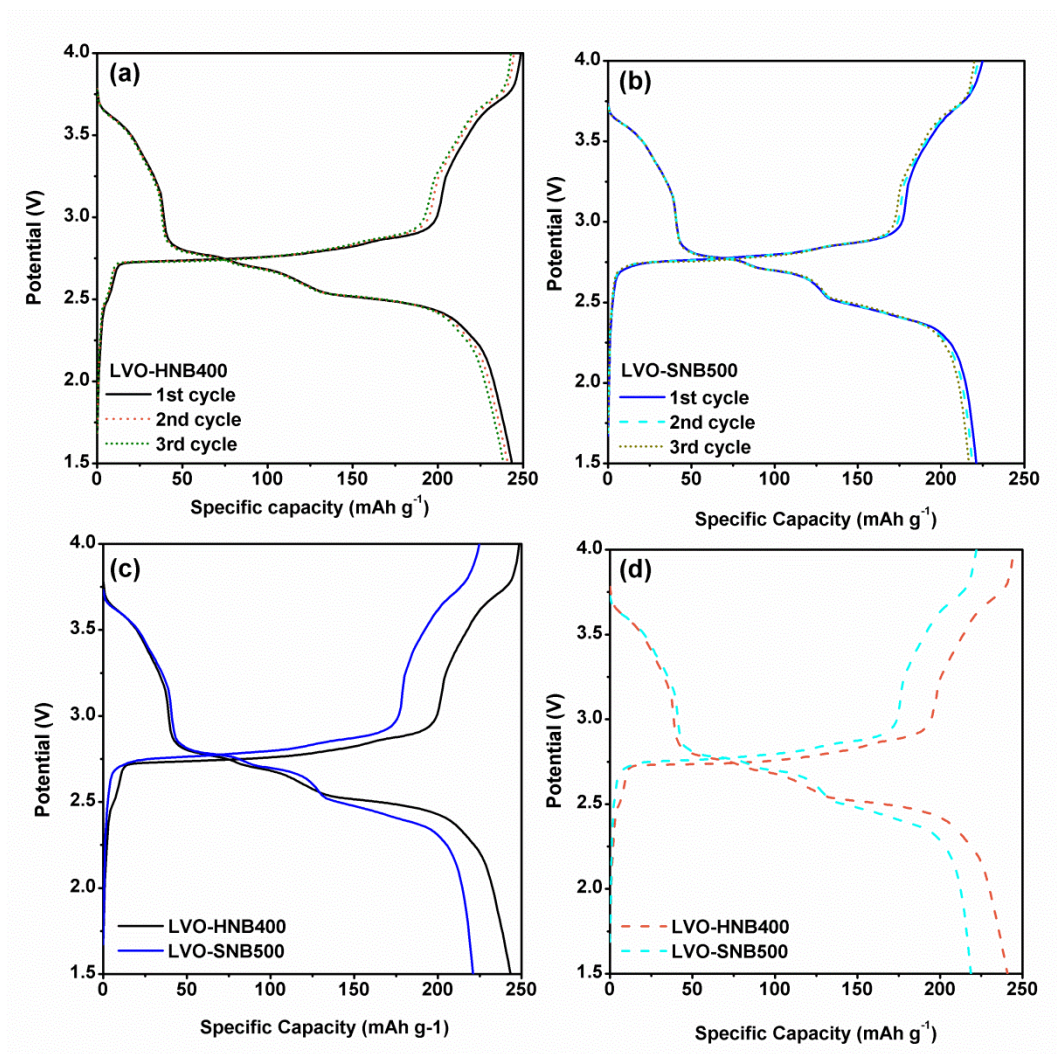


**Figure 4-13** Galvanostatic profiles of electrospun  $\text{Li}_{1.2}\text{V}_3\text{O}_8$  nanobelts: (a) LVO-HNB400 and (b) LVO-SNB500 for first three cycles at current density of  $200 \text{ mA g}^{-1}$ . Comparison of galvanostatic charge/discharge curves between LVO-HNB400 and LVO-SNB500 for (c) first cycle and (d) second cycle.

When both LVO-HNB400 and LVO-SNB500 were cycled at different current densities (Figure 4-12), LVO-HNB400 had exhibited higher overall capacities than that of LVO-SNB500. Initial discharge capacities for LVO-HNB400 and LVO-SNB500 were  $\sim 249 \text{ mAh g}^{-1}$  ( $\sim 2.7$  moles of lithium ions) and  $\sim 221 \text{ mAh g}^{-1}$  ( $\sim 2.4$  moles of lithium ions) respectively when they were cycled at  $200 \text{ mA g}^{-1}$ . Upon cycling until 100<sup>th</sup> cycle, the capacity was retained as  $\sim 211 \text{ mAh g}^{-1}$  ( $\sim 2.3$  moles of lithium ions) for LVO-HNB400 whereas for LVO-SNB500 was  $\sim 197 \text{ mAh g}^{-1}$  ( $\sim 2.1$  moles of lithium ions). Eventhough LVO-HNB400 had exhibited higher overall capacities, but the capacity retention was  $\sim 84\%$  of initial capacity, which was slightly lower than that of LVO-SNB500 ( $\sim 89\%$ ). Previous studies had shown that electrochemical performance of LVO is highly dependent on crystallinity and grain morphology (size and crystal shape).[72, 146, 147, 153] Lower degree of crystallinity and short range ordering for LVO are usually favorable to achieve high capacity due to faster kinetics and shorter penetration distance for lithium ions.[141, 154, 155] However, there is a limit on going into “very low” crystallinity or amorphous state so that the cycling stability is not undermined.[134, 153, 156] Capacity fading in LVO with low crystallinity was attributed to poor reversibility upon repeated lithium insertion and extraction. As the lithium ions reside irregularly within the layered structure, it may cause hindrance to incoming lithium ions during discharging.[119] Besides, some of the incoming lithium ions may occupy positions with higher energy barrier which deemed to be more difficult to be extracted in subsequent cycles.[149] Eventually, lithium ion trapping or local damage of lattice structure possibly occur which in turns causes irreversible reactions.[79]

In order to improve the cyclability of LVO-HNB400 and preserve its high capacity at the same time, we had attempted substitution of vanadium ( $0.540 \text{ \AA}$ )[157] sites in LVO-HNB400 by optimum amount of aluminum ( $0.535 \text{ \AA}$ ) with similar ionic radius to improve the structural stability upon prolonged cycling in which the results will be presented in Section 4.1.6.

#### 4.1.6 Electrospun $\text{Li}_{1.2}\text{V}_{3-x}\text{Al}_x\text{O}_8$ nanobelts: Materials characterization

FESEM images of  $\text{Li}_{1.2}\text{V}_{2.97}\text{Al}_{0.03}\text{O}_8$  (LVA3O) and  $\text{Li}_{1.2}\text{V}_{2.95}\text{Al}_{0.05}\text{O}_8$  (LVA5O) possessed the similar morphology as the pristine sample with hierarchically arrangement of nanobelts. This indicates the subsitution did not incur any changes in the nanostructures of LVO-HNB400 (Figure 4-14). The XRD refinement of LVA3O and LVA5O confirms the formation of monoclinic structure of  $\text{Li}_{1.2}\text{V}_3\text{O}_8$  (space group  $P2_1/m$ ) without additional

peaks being observed, indicating no impurities formation. The refined lattice parameters and crystallite sizes were tabulated in Table 4-3.

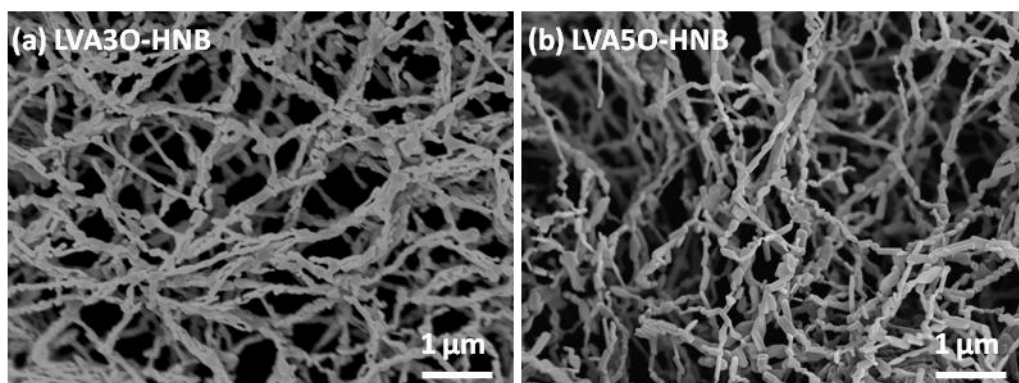


**Figure 4-14** FESEM images of (a)  $\text{Li}_{1.2}\text{V}_{2.97}\text{Al}_{0.03}\text{O}_8$  (LVA3O-HNB) and (b)  $\text{Li}_{1.2}\text{V}_{2.95}\text{Al}_{0.05}\text{O}_8$  (LVA5O-HNB).

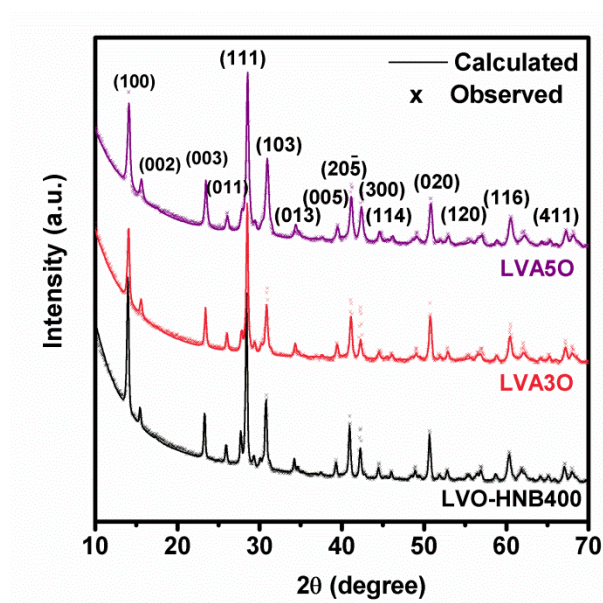


**Figure 4-15** XRD Rietveld refined patterns of pristine LVO-HNB, LVA3O-HNB and LVA5O-HNB.

**Table 4-3** Lattice parameters and crystallite sizes of LVA3O and LVA5O computed by Rietveld refinement.

Sample	Lattice parameters					Crystallite size (nm)
	a (Å)	b (Å)	c (Å)	$\beta$ (°)	V (Å <sup>3</sup> )	
LVA3O	6.6696(3)	3.6068(7)	12.023(3)	107.65(2)	275.61(2)	32.8(2)
LVA5O	6.6645(3)	3.6052(7)	12.015(3)	107.72(1)	274.99(1)	21.4(6)

The study presented in this section only limited to substitution up  $x = 0.05$  for  $\text{Li}_{1.2}\text{V}_{3-x}\text{Al}_x\text{O}_8$ . Further addition of  $x$  resulted in formation of impurities such as  $\text{LiVO}_3$  or  $\text{AlVO}_3$ , which deviates from the main intention of this study to investigate the effects of aluminum substitution on battery performance, as those impurities may be electrochemically active. The presence of aluminum in  $\text{Li}_{1.2}\text{V}_{3-x}\text{Al}_x\text{O}_8$  was further analyzed by inductively coupled plasma atomic emission spectroscopy (ICP-AES), slight deviation from the target composition was found in the final product,  $\text{Li}_{1.210}\text{V}_{2.948}\text{Al}_{0.026}\text{O}_8$  and  $\text{Li}_{1.212}\text{V}_{2.950}\text{Al}_{0.048}\text{O}_8$ , possibly due to volatility of precursors employed in synthesis.

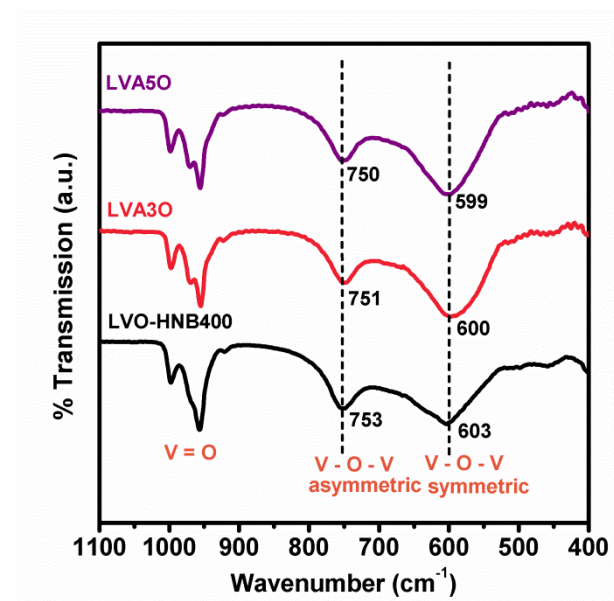


**Figure 4-16** FTIR analysis of LVO-HNB400, LVA3O-HNB400 and LVA5O-HNB400.

The FTIR spectra for  $\text{Li}_{1.2}\text{V}_{3-x}\text{Al}_x\text{O}_8$  ( $x = 0.03$  and  $0.05$ ) were almost in coherent with that of pristine sample, LVO-HNB400 (Figure 4-16). The two peaks representing the stretching of V-O-V bonds appeared consistently within the range of  $550\text{--}760\text{ cm}^{-1}$  for all the samples but were slightly red shifted for the substituted samples. This can be related to bonding of aluminum with vanadium via oxygen bridge, in which similar behavior had been shown in previous studies[84, 105] of doping  $\text{Li}_{1+x}\text{V}_3\text{O}_8$  with other elements on vanadium sites. Another difference was the distinctness of the adjacent peaks within the range of  $\sim 950\text{--}1000\text{ cm}^{-1}$  which were attributed to stretching vibration of three V=O bonds.[152] The three peaks could be observed to be more distinguishable with minor aluminum substitution compared to pristine LVO-HNB400. The intensity ratio of these V=O bonds gives indication of occupation sites for lithium ions within the lattice which

will affect the lithium insertion and extraction mechanism, which will be elaborated further in Section 5.2.1. The effect of aluminum substitution on the electrochemical performance of LVO-HNB400 will be presented in the following section.

#### 4.1.7 Electrospun $\text{Li}_{1.2}\text{V}_{3-x}\text{Al}_x\text{O}_8$ nanobelts: Comparison of electrochemical performance

After substitution of vanadium sites with a small amount of aluminum, the CV profiles were still in coherent with that of pristine LVO-HNB400. Identical redox peaks could be observed for pristine and substituted samples (Figure 4-17). This means that the electrochemical mechanism of substituted LVO-HNB were consistent with the pristine one without introducing additional electrochemical reactions. The galvanostatic charge/discharge profiles (Figure 4-19) exhibited by all samples were in agreement with the CV scans. All the redox peaks appeared consistently in galvanostatic curve as extending or short plateaus.

Nevertheless, it is worth noting that both the substituted samples, LVA3O and LVA5O had exhibited slightly higher intensity for reduction peak at  $\sim 2.26$  V and its coupled peak pair at  $\sim 2.55$  V. The reduction peak was appeared as a shallow peak in CV scan of LVO-HNB400. Similarly, a shoulder-like, short plateau between  $\sim 2.3$  to  $2.1$  V could be observed to be more obvious for LVA3O and LVA5O, but appeared as a smearing-down curve for pristine LVO-HNB400 in the first and second cycles of the galvanostatic profiles at current density of  $200 \text{ mA g}^{-1}$ . Besides, the polarization between charging and discharging curves in galvanostatic profiles were reduced with aluminum substitution. The decrement in polarization for substituted samples could be observed clearer for the galvanostatic profiles with higher current density of  $600 \text{ mA g}^{-1}$ .

The comparison of specific capacities achieved by all samples at current density of  $200 \text{ mA g}^{-1}$  and  $600 \text{ mA g}^{-1}$  are shown in Figure 4-18 (a) and (b) respectively. The first specific capacity exhibited by LVA3O was  $\sim 215 \text{ mAh g}^{-1}$  ( $\sim 2.3$  moles of lithium ions) whereas by LVA5O was  $\sim 256 \text{ mAh g}^{-1}$  respectively. The initial specific capacity for LVA3O was lower than that of pristine LVO-HNB400 whereas the one exhibited by LVA5O was slightly higher than that of pristine LVO-HNB400 ( $\sim 249 \text{ mAh g}^{-1}$ ). After cycling for 100 cycles at current density of  $200 \text{ mA g}^{-1}$ , LVA3O had retained  $\sim 88\%$  of the initial capacity whereas the capacity retention by LVA5O was  $\sim 86\%$ . In overall, the



specific capacities exhibited by LVA5O were slightly higher than that of pristine LVO-HNB400 whereas the overall capacities contributed by LVA3O were lower than that of pristine sample. The cycling stability of LVA5O was similar to that of pristine LVO-HNB400 when they were cycled at  $200 \text{ mA g}^{-1}$ . The differences in overall capacities between pristine LVO-HNB400 and LVA5O were more distinct when both of them are cycled at higher current density of  $600 \text{ mA g}^{-1}$ . The capacity retention achieved by pristine LVO-HNB400 was  $\sim 81\%$ , whereas for LVA3O and LVA5O were  $\sim 94\%$  and  $\sim 88\%$  respectively. Eventhough the overall capacities exhibited by LVA3O were lower than pristine LVO-HNB400, it had exhibited superior capacity retention over pristine LVO-HNB400. In summary, this section reveals that minor substitution of vanadium in LVO with aluminum is beneficial for improvement of battery performance in terms of capacity and cyclability. More details will be discussed in Section 5.2.1 to elucidate the effect of aluminum substitution on electrochemical performance of LVO-HNB400.

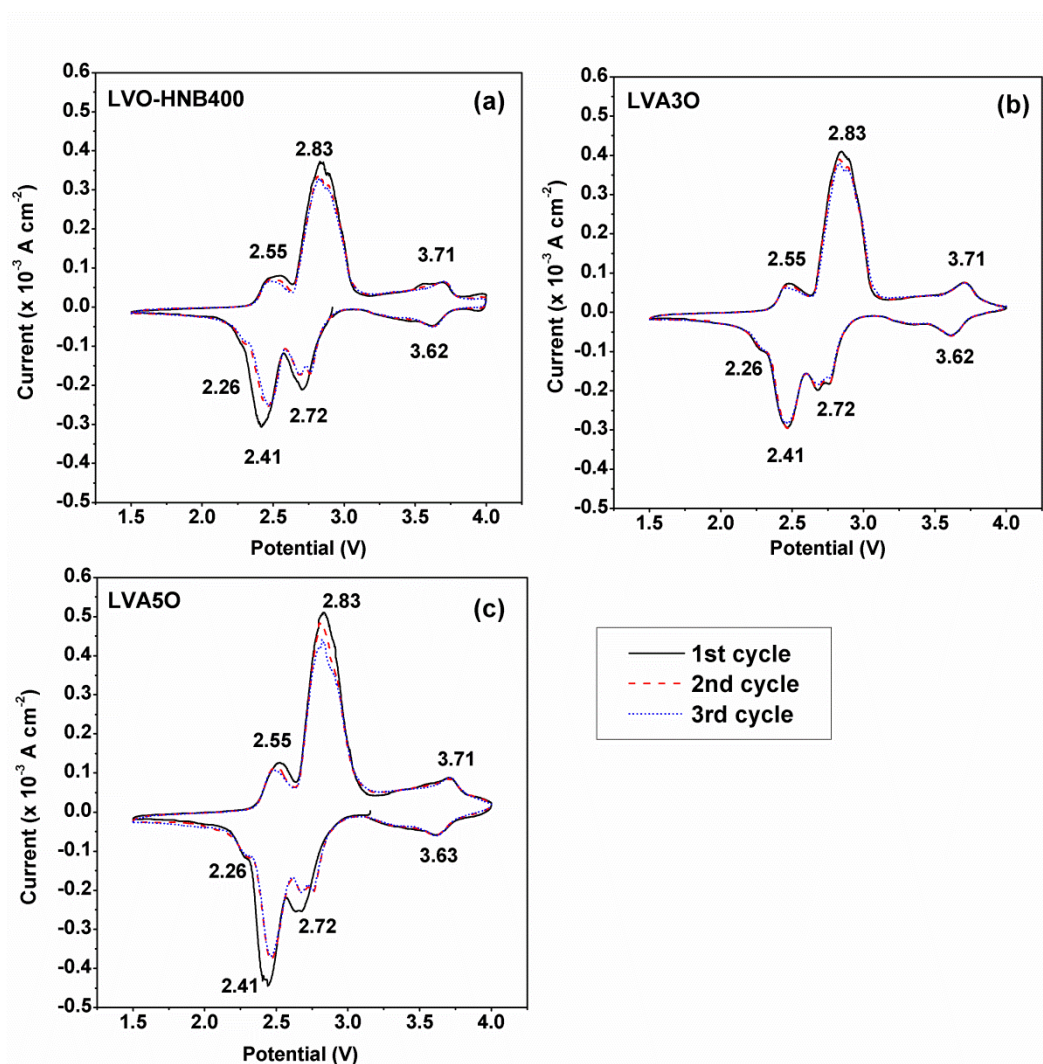


**Figure 4-17** CV of (a) LVO-HNB400, (b) LVA3O-HNB400 and (c) LVA5O-HNB400 for first three cycles at scan rate of  $0.1 \text{ mV s}^{-1}$ .



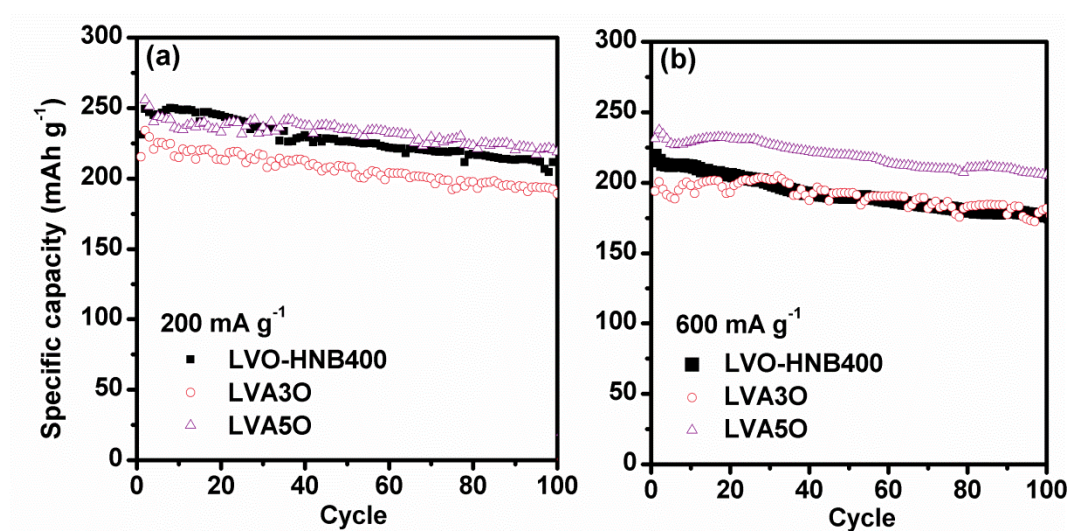


**Figure 4-18** Cycling performance of LVO, LVA3O and LVA5O at current density of (a) 200 mA g<sup>-1</sup> and (b) 600 mA g<sup>-1</sup>.

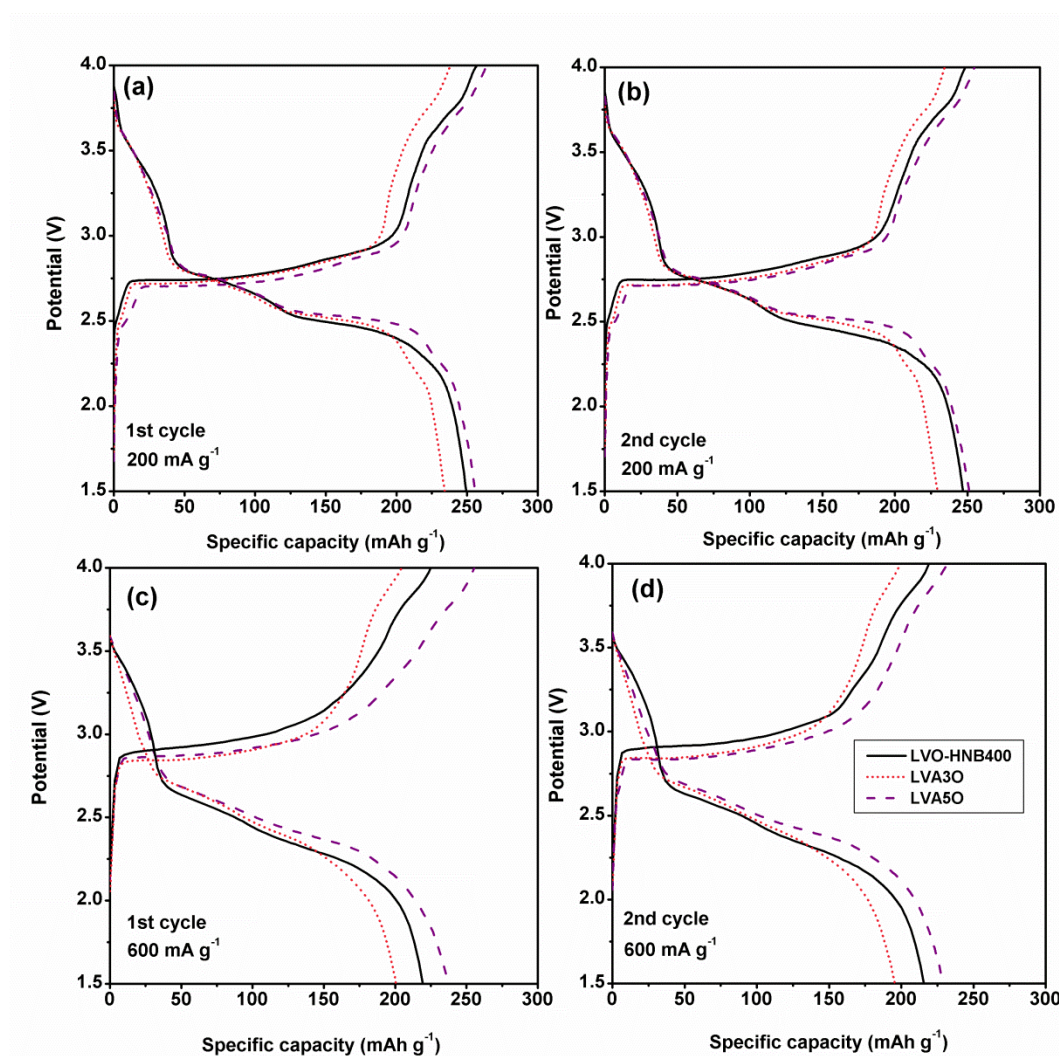


**Figure 4-19** Galvanostatic cycling of Li<sub>1.2</sub>V<sub>3-x</sub>Al<sub>x</sub>O<sub>8</sub> (x = 0, 0.03 and 0.05). (a) 1<sup>st</sup> cycle and (b) 2<sup>nd</sup> cycle at current density of 200 mA g<sup>-1</sup>; (c) 1<sup>st</sup> cycle and (d) 2<sup>nd</sup> cycle at current density of 600 mA g<sup>-1</sup>.

#### 4.1.8 Ball milled $\text{Na}_{1.2}\text{V}_3\text{O}_8$ nanoparticles: Materials characterization

FESEM images of sintered  $\text{Na}_{1.2}\text{V}_3\text{O}_8$  at temperature of 400 °C and 500 °C (named as NVO-NP400 and NVO-NP500) reveal the formation of different morphologies. NVO-NP400 constituted agglomerates of particles with size distribution between 100-150 nm whereas NVO-NP500 consisted of larger plate-like configurations with length of 1-3  $\mu\text{m}$  and width of 300-500 nm. Crystal information was retrieved from XRD data and Rietveld refinement (Figure 4-20). NVO-NP400 and NVO-NP500 were confirmed to crystalline in phase pure monoclinic (space group  $P2_1/m$ ) with the corresponding lattice parameters tabulated in Table 4-4. Similar to LVO-NP, slightly larger cell volume was obtained by NVO-NP500 with higher sintering temperature.

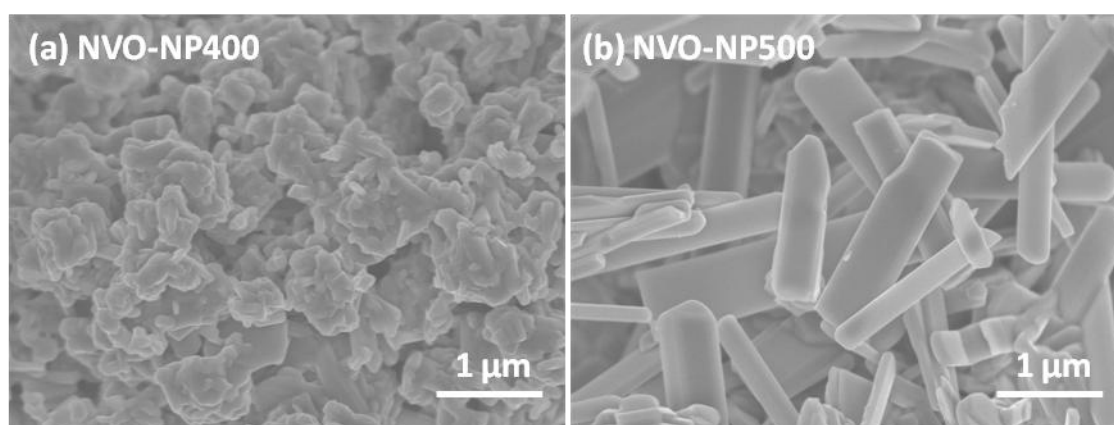


**Figure 4-20** FESEM images of sintered  $\text{Na}_{1.2}\text{V}_3\text{O}_8$  nanoparticles at (a) 400 °C (NVO-NP400) and (b) 500 °C (NVO-NP500).

**Table 4-4** Lattice parameters of sintered  $\text{Na}_{1.2}\text{V}_3\text{O}_8$  computed by Rietveld refinement

Sample	Lattice parameters				$V (\text{\AA}^3)$
	$a (\text{\AA})$	$b (\text{\AA})$	$c (\text{\AA})$	$\beta (^{\circ})$	
<b>NVO-NP400</b>	7.3336(7)	3.6107(2)	12.145(8)	107.313(6)	307.03(4)
<b>NVO-NP500</b>	7.3424(1)	3.6120(3)	12.157(1)	107.336(0)	307.76(8)

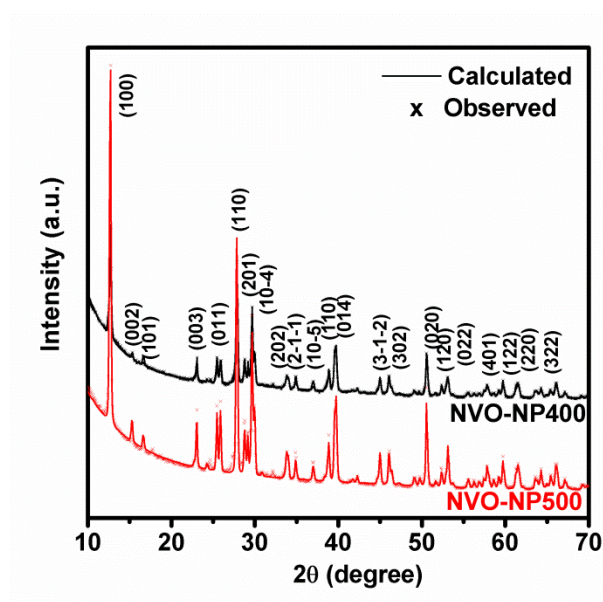


**Figure 4-21** XRD patterns and Rietveld refinements of sintered  $\text{Na}_{1.2}\text{V}_3\text{O}_8$  at temperature of 400 °C (NVO-NP400) and 500 °C (NVO-NP500).

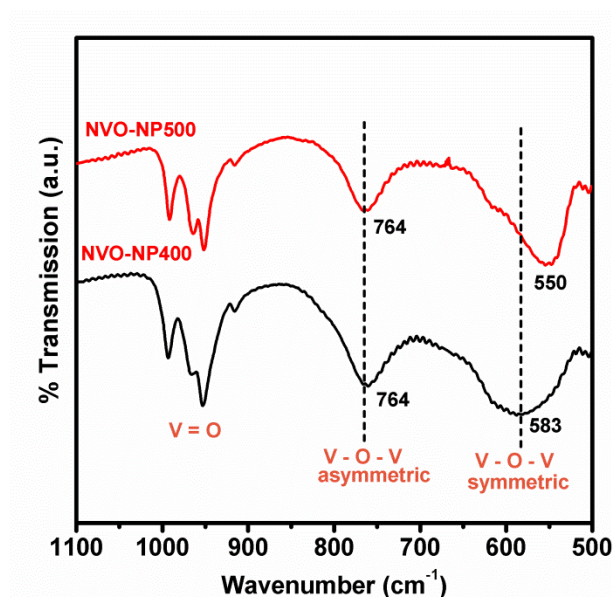


**Figure 4-22** FTIR analysis of  $\text{Na}_{1.2}\text{V}_3\text{O}_8$  by HEBM and sintering at 400 °C (NVO-NP400) and 500 °C (NVO-NP500)

FTIR characterization was collected between wavenumber range of 500-1100  $\text{cm}^{-1}$  to determine the vibration bands of vanadium ions in crystal lattice of  $\text{Na}_{1.2}\text{V}_3\text{O}_8$  sintered at 400 °C (NVO-NP400) and 500 °C (NVO-NP500) respectively (Figure 4-22). The spectra for NVO-NP400 and NVO-NP500 were almost identical except that there was slight band shift with respect to each other. The adjacent peaks within the range of 950 – 1000  $\text{cm}^{-1}$

were attributed to the three V=O bonds. The positions of the peaks were similar to those observed in LVO-NP, which were at  $\sim 995\text{ cm}^{-1}$ ,  $\sim 966\text{ cm}^{-1}$  and  $953\text{ cm}^{-1}$  respectively. Another two peaks which could be observed at  $\sim 583\text{ cm}^{-1}$  and  $\sim 764\text{ cm}^{-1}$  for NVO-NP400, were attributed to symmetric and asymmetric stretching of V-O-V bonds. The asymmetric stretching band for V-O-V was slightly red shifted to  $\sim 550\text{ cm}^{-1}$  for NVO-NP500. The  $\Delta\nu$  was estimated to be  $\sim 214\text{ cm}^{-1}$  for NVO-NP500 and  $\sim 181\text{ cm}^{-1}$  for NVO-NP400. This was well aligned with the XRD refinement (Table 4-4) of larger lattice volume for NVO-NP500 due to larger V-O-V angle and shorter bond length as deduced from the FTIR spectra.

#### 4.1.9 Ball milled $\text{Na}_{1.2}\text{V}_3\text{O}_8$ nanoparticles: Comparison of electrochemical performance

Figure 4-23 shows CV profile of NVO-NP400 and NVO-NP500 at a scan rate of  $0.1\text{ mV s}^{-1}$  which was cycled between  $1.5 - 4.0\text{ V}$  *versus*  $\text{Li/Li}^+$ . Overall, both NVO-NP400 and NVO-NP500 had shown similar redox behavior, indicating similar lithium insertion and extraction mechanism during discharging and charging.

In both CV profile, four well defined cathodic peaks could be observed for first and subsequent cycles, which were  $\sim 3.63, 3.14, 2.65$  and  $2.38\text{ V}$  for NVO-NP400;  $\sim 3.63, 3.14, 2.66$  and  $2.40\text{ V}$  for NVO-NP500. The coupled redox peak for  $\sim 2.65$  and  $2.38\text{ V}$  for NVO-NP400;  $\sim 2.66$  and  $2.40\text{ V}$  for NVO-NP had smeared into a single peak at  $\sim 2.59$  and  $2.60\text{ V}$  respectively. The lithium insertion process occurred via multi-steps reaction due to existence of sites with different energy barrier when lithium ions were intercalated into the tetrahedral sites (interstitial sites) of NVO.[158-160] Similar electrochemical mechanism had been observed in LVO as discussed in Section 4.1.1. The number of corresponding anodic peaks is less than that of during cathodic sweep indicating there may be differences in diffusion kinetics during lithium insertion and extraction respectively.[161]



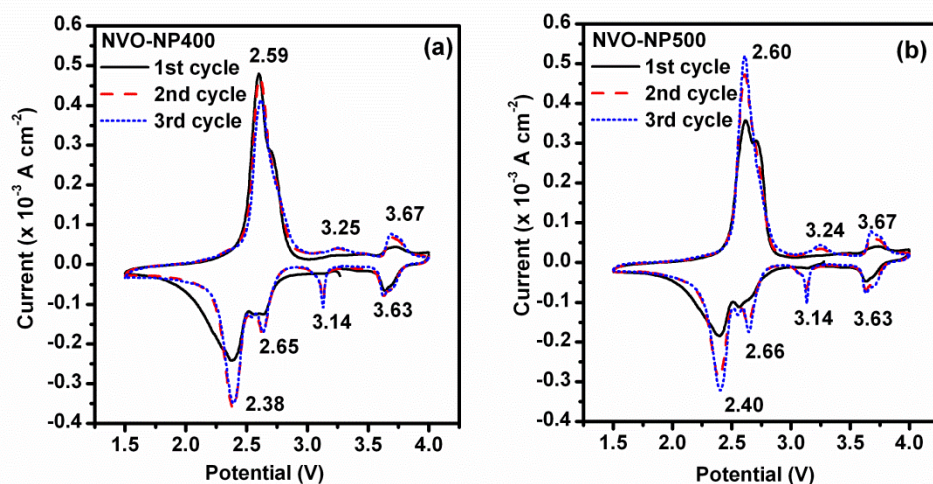


**Figure 4-23** CV of (a) NVO-NP400 and (b) NVO-NP500 at  $0.01 \text{ mV s}^{-1}$  for first three cycles.

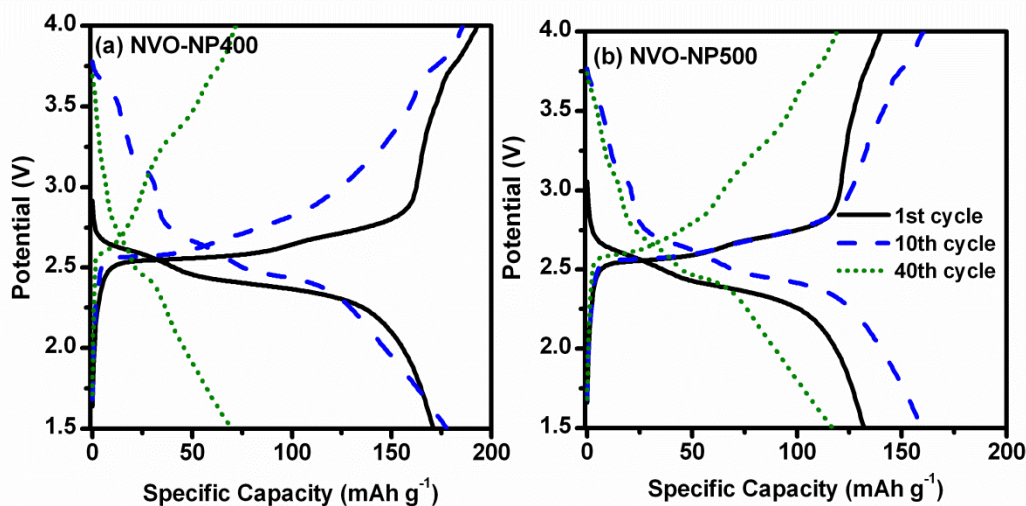


**Figure 4-24** Galvanostatic cycling of (a) NVO-NP400 and (b) NVO-NP500 for first, tenth and fortieth cycles at current density of  $200 \text{ mA g}^{-1}$ , cycled between 1.5 to 4.0 V

The galvanostatic profile (Figure 4-24) of first cycle for both NVO-NP400 and NVO-NP500 were well aligned with the CV scans as shown in Figure 4-23. For both NVO-NP400 and NVO-NP500, the first discharge plateau extended from  $\sim 2.70$  to  $2.30 \text{ V}$  and the charge plateau initiated from  $\sim 2.50$  to  $2.70 \text{ V}$ , which supports the observation in CV scans.

An increasing trend for the specific capacity during initial stage up to  $\sim 14^{\text{th}}$  cycle could be observed for both NVO-NP400 and NVO-NP500 (Figure 4-25). This was due to relaxation of the lattice to create a more facile lithium diffusion pathway for lithium intercalation and deintercalation.[91, 160, 162] The first specific capacity of  $\sim 171 \text{ mAh g}^{-1}$

<sup>1</sup> (~2.0 moles of lithium ions) achieved by NVO-NP400 was higher compared to ~132 mAh g<sup>-1</sup> (~1.5 moles of lithium ions) by NVO-NP500. In overall, NVO-NP400 exhibited higher capacities during initial stage until ~14<sup>th</sup> cycle with maximum specific capacity of ~201 mAh g<sup>-1</sup> (~2.3 moles of lithium ions) while the maximum specific capacity exhibited by NVO-NP500 was ~160 mAh g<sup>-1</sup> (~1.8 moles of lithium ions).

After ~20 cycles, the specific capacities for both NVO-NP400 and NVO-NP500 started to decline. During 100<sup>th</sup> cycle, their capacity stabilized at ~26 mAh g<sup>-1</sup> for NVO-NP400 and at ~63 mAh g<sup>-1</sup> for NVO-NP500 respectively. The capacity fading was possibly caused by incomplete lithium extraction upon prolonged cycling due strong interactions of lithium ions and surrounding oxygen ions within the lattice.[158, 161, 163] The remaining lithium ions within the structure had lead to irreversible electrochemical reactions as shown by shortening of plateau during 40<sup>th</sup> cycle for both NVO-NP400 and NVO-NP500 (Figure 4-24). The capacity deterioration occurred more rapidly for NVO-NP400 though higher initial capacities were achieved. Initial stage of lithium insertion and extraction were deemed to be easier for NVO-NP400 which was less crystalline with limited long-range ordering. However, the atomic arrangement was more prone to be disordered upon long term cycling due to relaxation of lattice.[161, 163] On the contrary, the crystal growth for NVO-NP500 was sufficiently large to have preferred orientation with plate-like morphology as shown in Figure 4-20(b). The structure was less flexible compared to NVO-NP400, which resulted in lower capacities exhibited during initial stage. Due to the rigid atomic arrangement, less disorder could be induced upon repeated lithium insertion and extraction, leads to better capacity retention during later stage. Therefore, it is essential for NVO to possess structure of sufficient long range ordering but flexible enough to compensate lattice reorganization to achieve high capacity and stable cyclability.

In the following sections, nanostructuring strategy had been employed to obtain NVO with aforementioned criteria and capability to achieve good battery performance. NVO nanobelts had been fabricated and electrochemical testing had been performed to investigate the possibility for nanostructuring of NVO in enhancing battery performance. Detailed results will be presented in following sections.

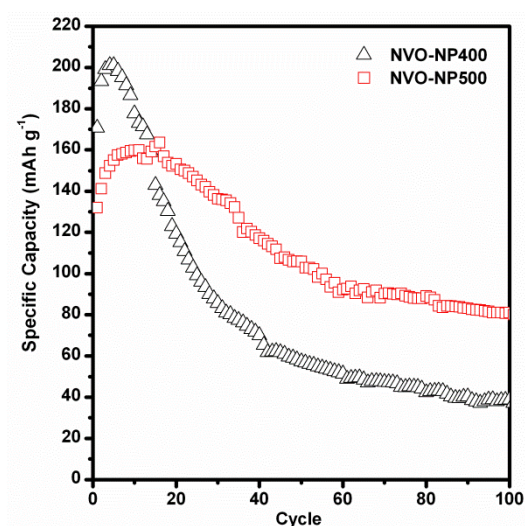


**Figure 4-25** Cycling performance of NVO-NP400 and NVO-NP500.

#### 4.1.10 Electrospun $\text{Na}_{1.2}\text{V}_3\text{O}_8$ nanobelts: Effect of sintering profile on morphology growth

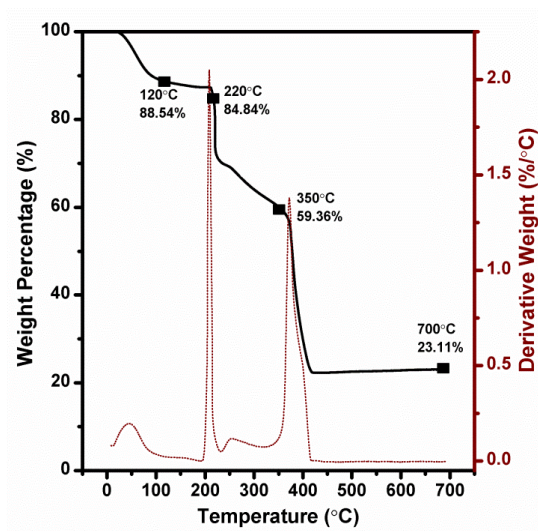


**Figure 4-26** Thermogravimetric analysis (TGA) of as-spun  $\text{Na}_{1.2}\text{V}_3\text{O}_8$  nanofibers was conducted between 30 °C to 700 °C in air.

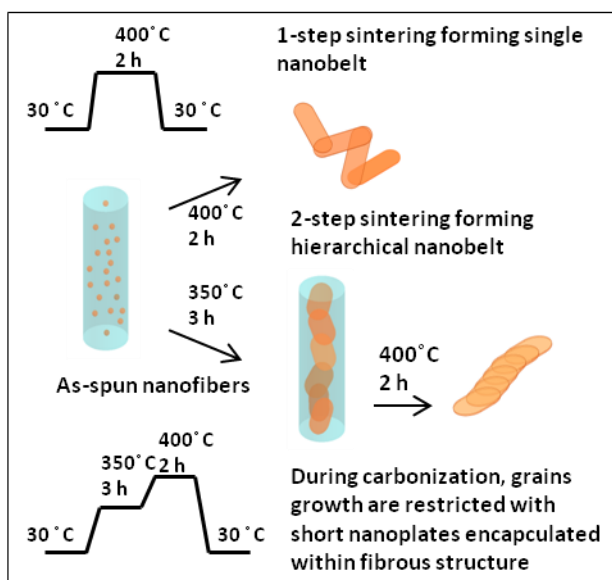
Thermogravimetric analysis was performed on as-spun nanofibers between 35 °C to 700 °C to determine the sintering temperature (Figure 4-26). The weight loss of about 11 wt% within the range of 35 °C to 120 °C was due to the vaporization of volatile components, such as adsorbed moisture, residual ethanol and acetic acid. The prominent peak at 200 °C was attributed to the decomposition of the metallic precursor, which is

vanadium(V)oxytripropoxide and sodium acetate anhydrous. Another peak at 350 °C could be related to the removal of the PVP. There is no significant weight loss (stabilizes at about 23%) recorded at temperature above 400 °C, indicating the completion of chemical reaction. Hence, 400 °C was chosen as the maximum sintering temperature.

Sintering profiles involving alteration of ramp rate, duration and temperatures applied on as-spun nanofibers affect the formation of crystal phase and morphology of end products.[164, 165] During the electrospinning process, polymers such as PVP[166], PAN[167], PVA[164] *etc.* act as a template for the formation of fibers. Typically, sintering[167-169] was employed to remove polymer backbone leading to the formation of product with desired morphology such as nanofibers,[168, 169] nanowires,[170] *etc.* In this work, both one-step and two-step sintering processes were conducted to understand the effect of carbonization step on the evolution of morphology (Scheme 4-2). For two-step sintering, the as-spun nanofibers were sintered at 350 °C for 3 h followed by 400 °C for 2 h to obtain the final product.

By sintering the as-spun nanofibers at 350 °C for 3 h, just prior the decomposition of PVP starts to occur, the carbonization step enables the conversion of PVP to carbonaceous products.[169] NVO nanoparticles gradually grow into small, flat plates due to self-limiting property of monoclinic structure. With the assistance of carbonaceous product enclosing the metallic precursor within fibrous structure, the growth of small plates into longer size is restricted, hence assembling into hierarchical nanobelt (NVO-HNB) (Figure 4-27(b)), with the short nanoplates aligned in array form. For one-step sintering without the carbonization step, the as-spun nanofibers were heat-treated at 400 °C. Due to sudden removal of PVP, NVO particles are grown into single nanobelt (NVO-SNB) separately (Figure 4-27(c)). Furthermore, NVO nanobelts grew into larger dimension than NVO-HNB when heating at 400 °C at the absence of PVP. Therefore, sintering profiles play a crucial role in controlling the morphology of end product, and carbonization step is beneficial in obtaining high aspect ratio NVO-HNB with smaller diameter.





**Scheme 4-2** Schematic representation of formation mechanism of single nanobelt (NVO-SNB) by one-step sintering and hierarchical nanobelt (NVO-HNB) by two-step sintering.

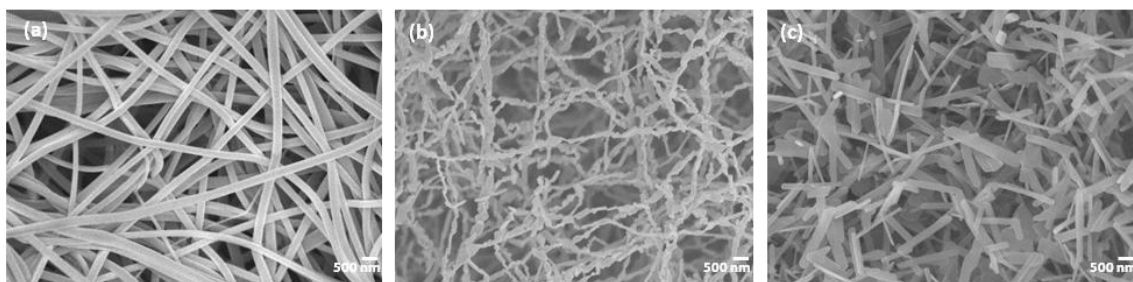


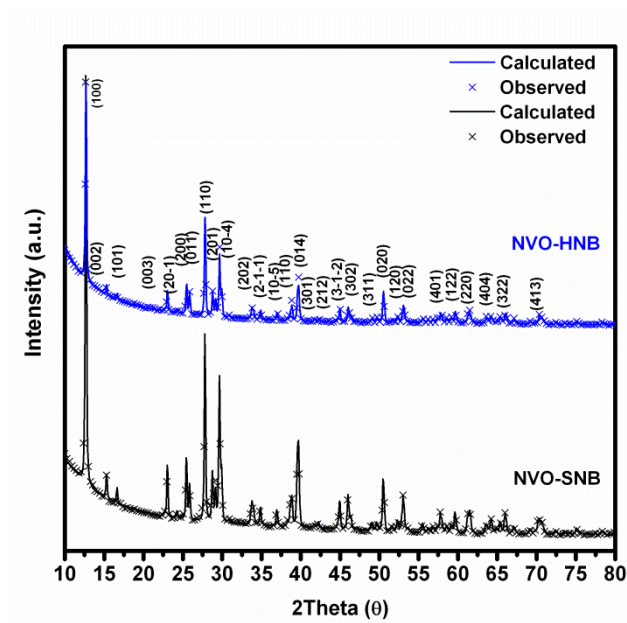
**Figure 4-27** FESEM images of (a) as-spun nanofibers, (b) hierarchical nanobelt (NVO-HNB) and (c) single nanobelt (NVO-SNB)

#### 4.1.11 Electrospun $\text{Na}_{1.2}\text{V}_3\text{O}_8$ nanobelt: Materials characterization

The XRD pattern shown in Figure 4-28 confirms the formation of the single-phase monoclinic crystalline  $\text{Na}_{1.2}\text{V}_3\text{O}_8$  phase (space group  $P2_1/m$ ). The refined lattice parameters for NVO-SNB and NVO-HNB are shown respectively in Table 4-5. NVO-SNB has slightly larger cell volume and smaller crystallite size compared to NVO-HNB. With the additional carbonization step, the crystallites tend to grow larger due to prolonged sintering duration.

**Table 4-5** The refined lattice parameters of the as-prepared  $\text{Na}_{1.2}\text{V}_3\text{O}_8$  by altering the sintering profile

Samples	$a/\text{\AA}$	$b/\text{\AA}$	$c/\text{\AA}$	$\beta(^{\circ})$	$V(\text{\AA}^3)$	Crystallite size (nm)
NVO-SNB	7.3454(6)	3.6155(2)	12.1565(6)	107.344(4)	308.16(3)	68.4(2)
NVO-HNB	7.3373(9)	3.6130(2)	12.1490(1)	107.344(7)	307.42(5)	85.6(4)

**Figure 4-28** Rietveld refinements of NVO-SNB and NVO-HNB

FTIR spectroscopy was employed to obtain the vibration modes for as-spun nanofibers and products obtained in order to study the effect of sintering conditions on the transformation of functional groups (Figure 4-29). Vibration modes observed for PVP were almost identical to those in as-spun nanofibers. These bands were observed due to the presence of PVP, which does not appear in the FTIR spectra of end products, indicating the complete elimination of PVP after sintering. The adjacent peaks at  $\sim 960 - 990 \text{ cm}^{-1}$  observed in the spectra of as-spun nanofibers are attributed to stretching of  $\text{V}=\text{O}$  bonds due to addition of the vanadium precursor, as similarly observed in the case of electrospun LVO. These peaks subsequently appeared in the end products as three distinct peaks at  $\sim 952 \text{ cm}^{-1}$ ,  $\sim 965 \text{ cm}^{-1}$  and  $\sim 993 \text{ cm}^{-1}$  which can be assigned to three short  $\text{V}=\text{O}$  bonds [72, 135] in the  $\text{Na}_{1.2}\text{V}_3\text{O}_8$ . In addition, another two distinct peaks appeared consistently between  $550\text{--}750 \text{ cm}^{-1}$  in NVO-SNB and NVO-HNB representing stretching

of V-O-V bonds[135, 171]. In comparison, the peaks at  $\sim 553\text{ cm}^{-1}$  and  $\sim 762\text{ cm}^{-1}$  for NVO-SNB, which are attributed to symmetric and asymmetric stretching mode for V-O-V, are both slightly blue-shifted to  $\sim 571\text{ cm}^{-1}$  and  $\sim 769\text{ cm}^{-1}$  for NVO-HNB. This is due to slightly different crystal growth process experienced by both samples. The shift is only observed for V-O-V groups but not for V=O groups. The V-O-V chains lengthen along the  $c$  axis within the lattice;[163, 172, 173] hence the band shift is attributed to small difference in lattice parameter  $c$ . This observation can be supported by longer lattice parameter  $c$  for NVO-SNB as shown in Table 4-5.

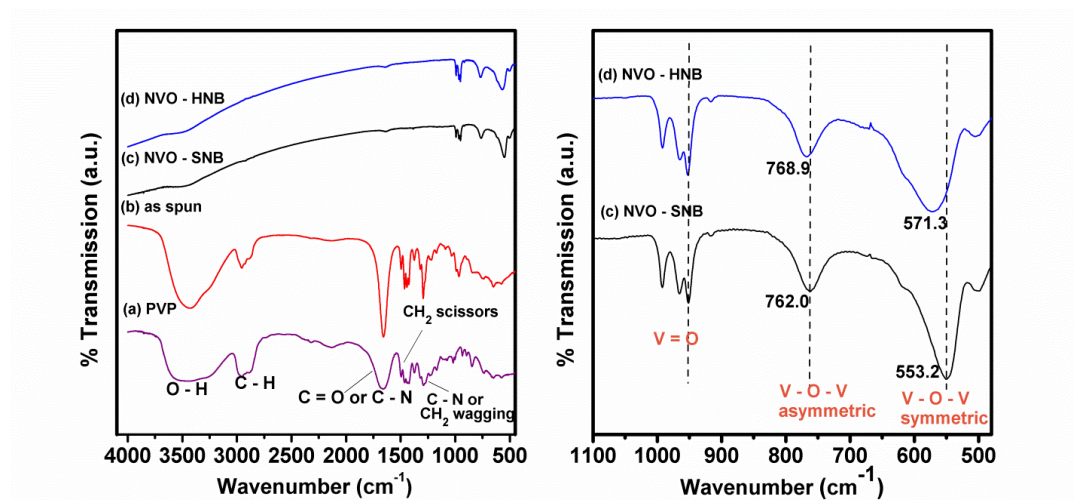


**Figure 4-29** FTIR of (a) PVP, (b) as-spun nanofibers, (c) NVO-SNB and (d) NVO-HNB (left). Enlarged version of FTIR with specified bands for (c) NVO-SNB and (d) NVO-HNB (right)

HRTEM micrographs and selected area electron diffraction (SAED) were taken to evaluate the detailed morphology and growth orientation of the NVO-SNB and NVO-HNB respectively (Figure 4-30). The NVO-SNB as shown in Figure 4-30(a) is composed of individual nanobelt, 135-170 nm in width, with non-agglomerated belt-like structure which provides more contact areas for electrolyte, allowing faster diffusion of lithium ions. The bright field TEM image in Figure 4-30(d) shows the hierarchical nature of the NVO-HNB, which is primarily composed of platelets subunits, 125-157 nm in width, aligned in array form forming hierarchical nanobelt. The HRTEM image of the NVO-SNB (Figure 4-30(b)) showed lattice fringes with a spacing of 1.18 nm and 0.37 nm respectively, which was in good agreement with the spacing of (001) and (010) planes of NVO as refined by XRD. The diffraction spots of the corresponding FFT (indexed as [100] zone axis) also can be indexed as (001) and (010) planes. For NVO-HNB (Figure 4-

30(e)), the HRTEM image showed lattice fringe with a spacing of 0.52 nm with the corresponding FFT (indexed as  $[\bar{1}01]$  zone axis) of (101) and (010) planes.

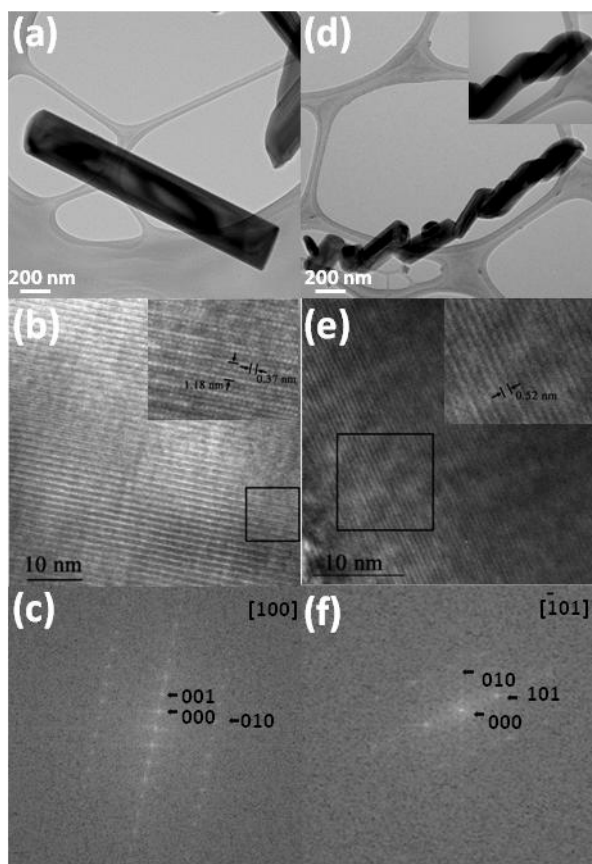


**Figure 4-30** (a) TEM micrograph of NVO-SNB, (b) HRTEM showing the lattice fringe of (001) and (010) plane of NVO-SNB which is 1.18 nm and 0.37 nm and (c) its corresponding FFT, (d) TEM micrograph of NVO-HNB with the inset showing its hierarchical assembly in higher magnification, (e) HRTEM showing the lattice fringe of (101) plane of NVO-HNB which is 0.52 nm and (f) its corresponding FFT.

Many reported studies[164, 174, 175] have proved that the surface facet orientation of nanocrystalline materials has significant effect on the electrochemical performance of LIB electrodes. Facet exposure with easily accessible diffusion channels for mass transport of lithium ions is highly desirable for high performance LIBs. The monoclinic structure of NVO is composed of layers of octahedral  $\text{VO}_6$  and  $\text{VO}_5$  trigonal pyramidal, linked by corner sharing oxygen atoms with the sodium ions as the pillars between the layers.[176] The additional lithium ions during discharging are inserted into the interstitial sites between the layers.[158, 177] Crystal plane effect plays an important role

in facilitating lithium insertion and extraction. The kinetics of lithium insertion and extraction into/from the lattice is highly dependent on the diffusion length. Figure 4-31 depicts the surface atomic configuration of (100) facet for NVO-SNB and ( $\bar{1}01$ ) facet for NVO-HNB respectively. NVO-HNB with exposed ( $\bar{1}01$ ) facet has longer diffusion length than NVO-SNB with exposed (100) facet. With the exposed (100) facet, the surface atoms configuration on the belt-like structure facilitates faster lithium diffusion with more directly accessible lithium diffusion channels. Lithium movement into NVO-SNB can be achieved by perpendicular diffusion across the belt-like structure whereas lithium ions have to travel in a slightly tilted direction across NVO-HNB to reach the hindered lithium insertion sites accurately. Nevertheless, electrospinning method had successfully fabricated single phase NVO with belt-like nanostructures. The morphology and crystal plane orientation of end product can be tuned by altering the sintering profiles of as-spun nanofibers. NVO-SNB and NVO-HNB were prepared by one-step and two-step sintering respectively.

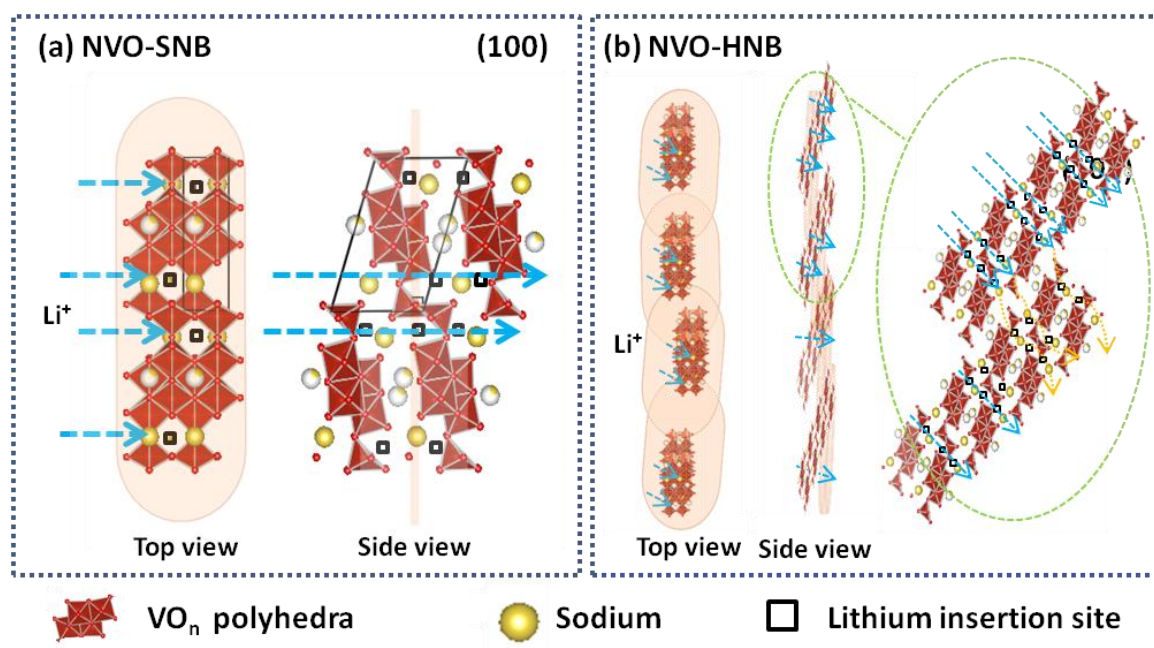


**Figure 4-31** Surface atom configurations of (a) NVO-SNB and (b) NVO-HNB with schematic top and side views of lithium diffusion path into active sites. (From the top view, lithium diffusion is directed into the plane)



#### 4.1.12 Electrospun $\text{Na}_{1.2}\text{V}_3\text{O}_8$ nanobelts: Comparison of electrochemical performance

The CV scans for electrospun NVO (Figure 4-31) were similar to NVO-NPs (Figure 4-23). Overall, both NVO-SNB and NVO-HNB have shown similar electrochemical behaviors, indicating similar lithium insertion and extraction mechanism during charging and discharging.

During the first cathodic sweep of both NVO-SNB and NVO-HNB, four well-defined peaks can be observed, which are  $\sim 3.14$ ,  $2.65$ ,  $2.54$  and  $2.39$  V, indicating occurrence of multi-step lithium insertion. The weak cathodic peak at  $\sim 3.14$  V can be attributed to the insertion of lithium ions into the tetrahedral sites (interstitial sites) of NVO. The corresponding weak anodic peak can be observed at around  $\sim 3.66$  V. Additional lithium ions then starts to occupy the remaining interstitial sites as the cathodic sweep is further proceeded to lower voltage region at  $\sim 2.64$ ,  $2.54$  and  $2.39$  V. Their coupled anodic peaks appear as a pair-up redox peak at  $\sim 2.64$  V. The splitting of redox peaks are attributed to lithium insertion sites with different energy barriers.[160] The first galvanostatic discharge/charge profile (Figure 4-33(a)) exhibits short plateau at  $\sim 3.20$  V followed by extending plateau from  $\sim 2.70$  to  $\sim 2.30$  V, which supports our observation in CV scan. However, the number of corresponding anodic redox peaks is less than that during cathodic sweep indicating that there may be differences in diffusion kinetics for lithium insertion and extraction respectively, as similar observed in NVO-NPs. The cathodic and anodic peaks during the first cycles are slightly distinguishable from the subsequent cycles. This is due to structural rearrangement upon lithium insertion and extraction into NVO lattice structure, which will be further discussed in Section 5.3.1..

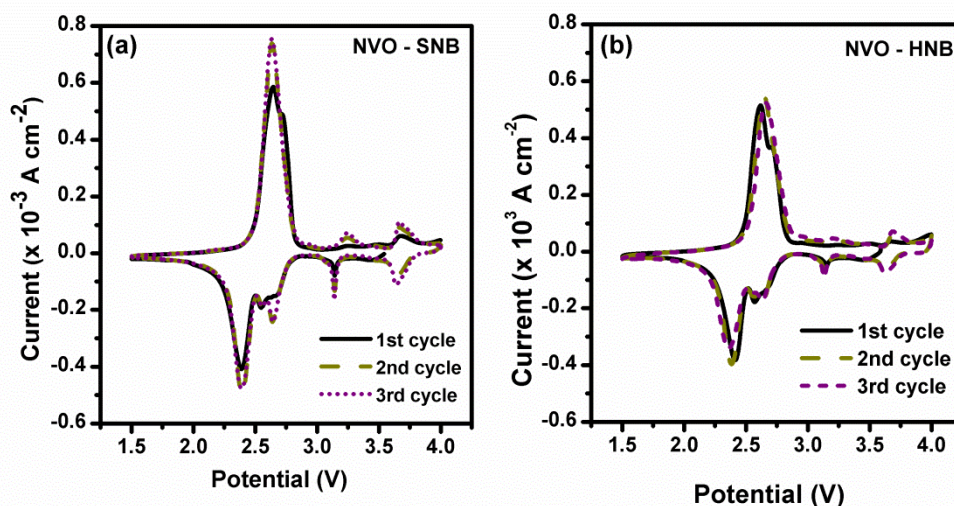


**Figure 4-32** Cyclic voltammetry of (a) NVO-SNB and (b) NVO-HNB at  $0.1 \text{ mV s}^{-1}$  for 1st cycle, 2nd cycle and 3rd cycle.

After the structural reorganization during the first cycle, another reduction peak appears at  $\sim 3.64 \text{ V}$  with its corresponding anodic peak pair at  $\sim 3.66 \text{ V}$  can be observed in second cycle (Figure 4-32). Another weak anodic peak can be observed at  $\sim 3.25 \text{ V}$  which is corresponding to the cathodic peak pair at  $\sim 3.14 \text{ V}$ . Similar phenomenon is observed in galvanostatic cycling curve (Figure 4-33) in which there are addition of short plateaus between  $3.0 - 4.0 \text{ V}$  after several cycles. The structural reorganization allows more active sites to be available for lithium intercalation, so there is a slight increment of capacity at second cycle onwards (Figure 4-33(b)). Besides, consecutive oxidation peaks in first anodic sweep which splits into two at  $\sim 2.66$  and  $\sim 2.74 \text{ V}$  has smeared into a single peak at  $\sim 2.66 \text{ V}$  in subsequent cycles. This indicates NVO is able to provide better lithium transportation pathway with its exposed (020) facets and single crystal structure, whereas LVO frequently encountered lithium ion trapping, resulting in capacity fading upon prolonged cycling.[148, 174]

From Figure 4-32(b), it is obvious that NVO-HNB reacts with lithium in a similar behavior as NVO-SNB. However, the area underneath the curve is relatively larger for the NVO-SNB, indicating higher amount of lithium intercalation. This observation supports the phenomena of higher specific capacities were achieved by NVO-SNB (Figure 4-34) because it has more unblocked interstitial sites which enable facile transportation of lithium ions. Other peaks position remained almost the same as that in first cycle, showing the good reversibility of electrochemical reaction.

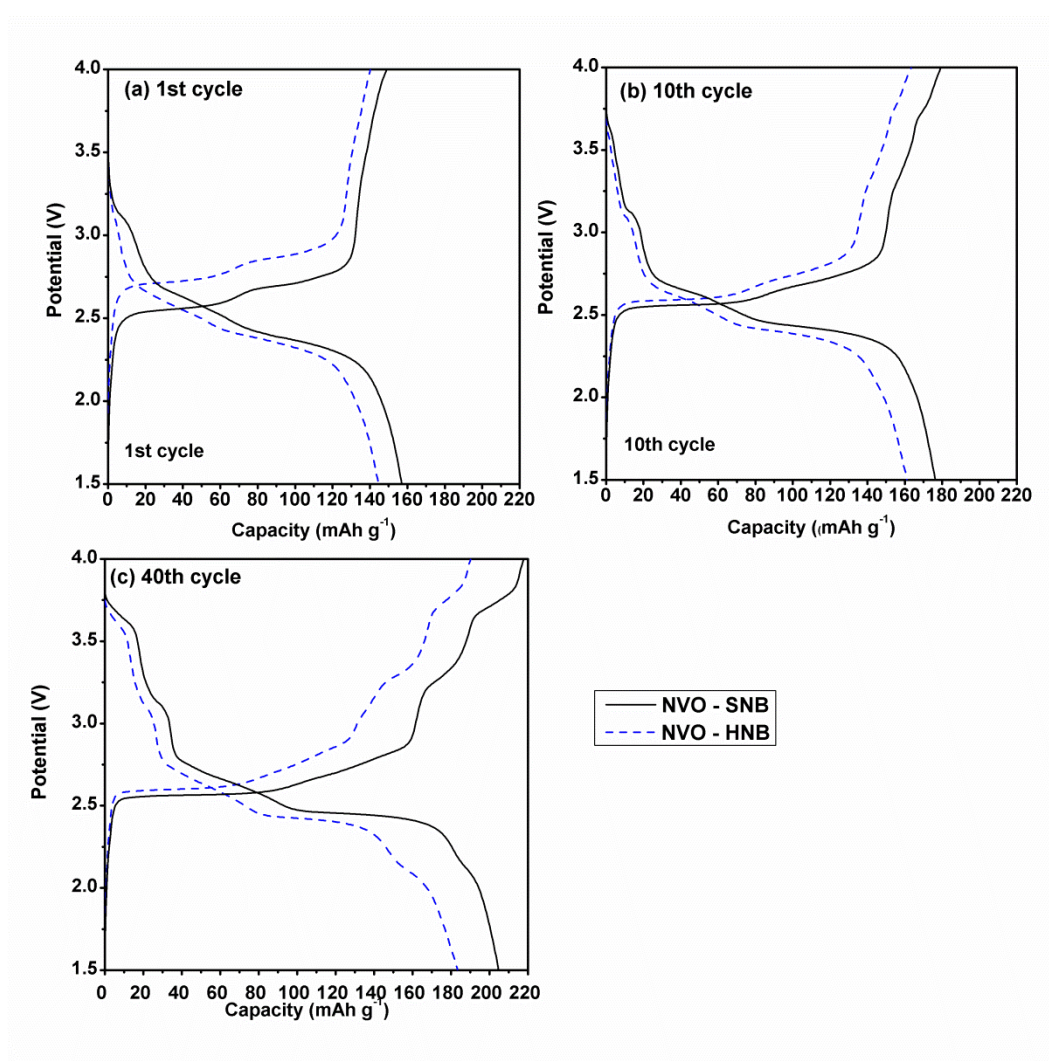


**Figure 4-33** Galvanostatic cycling of NVO-SNB and NVO-HNB for (a) 1st cycle, (b) 10th cycle and (c) 40th cycle.

The long term electrochemical performances of NVO were also investigated by galvanostatic discharging/charging at a current density of 200 mA g<sup>-1</sup> with a voltage cut-off of 1.5-4.0 V *versus* Li<sup>+</sup>/Li (Figure 4-34). Initial discharge capacities for NVO-SNB and NVO-HNB are ~156 mAh g<sup>-1</sup> and ~162 mAh g<sup>-1</sup> respectively. Upon a prolonged cycling, NVO-SNB can achieve maximum discharge capacity of ~218 mAh g<sup>-1</sup> (~2.6 moles of lithium ions) whereas for maximum discharge capacity by NVO-HNB was ~197 mAh g<sup>-1</sup> (~2.3 moles of lithium ions). During initial stage of cycling, the capacities can be observed to be increasing, which is due to reorganization of structure which involves relaxation of interlayer upon repeated lithium insertion, resulting in better lithium diffusion pathway, as similarly reported in other works[91, 162]. However, the capacity NVO-HNB starts to decline after 30 cycles and able to attain retention of ~173 mAh g<sup>-1</sup> (~2.0 moles of lithium ions) at 100 cycles. On the other hand, NVO-SNB attains



stabilization and its retention at 100 cycle is  $\sim 207 \text{ mAh g}^{-1}$  ( $\sim 2.4$  moles of lithium ions) which is  $\sim 95\%$  of the maximum achievable discharge capacity.

The rate capability of NVO-SNB and NVO-HNB were also examined by galvanostatic cycling at different current densities. The NVO-SNB is able to deliver a maximum discharge capacity of  $\sim 223 \text{ mAh g}^{-1}$  ( $\sim 2.6$  moles of lithium ions) at the current density of  $50 \text{ mA g}^{-1}$ . A high discharge capacities of  $\sim 195 \text{ mAh g}^{-1}$  ( $\sim 2.2$  moles of lithium ions) and  $\sim 168 \text{ mAh g}^{-1}$  ( $\sim 1.9$  moles of lithium ions) can be obtained at current densities of  $300 \text{ mA g}^{-1}$  and  $1200 \text{ mA g}^{-1}$  correspondingly. The overall specific capacities achieved in this study were comparably higher than the reported  $\text{NaV}_3\text{O}_8$  nanoflakes (with  $\text{Na}_{0.33}\text{V}_2\text{O}_5$  as impurity) prepared by wet chemical synthesis[91] and  $\text{Na}_{1.1}\text{V}_3\text{O}_{7.9}$  nanobelt (with  $\text{NaV}_6\text{O}_{15}$  as impurity) prepared by hydrothermal synthesis[90].

Overall, the NVO-SNB has demonstrated better battery performances than NVO-HNB in terms of capacity, cyclability and rate capability. As discussed earlier, NVO-SNB with preferentially exposed (100) facet offers directly accessible lithium transportation channels during charging and discharging. This structural feature promotes fast lithium diffusion kinetics, leading to high rate capability. The crystal plane orientation of NVO-SNB is more efficient in providing a smooth diffusion pathway and shorter diffusion length over NVO-HNB in which lithium diffusion channels are more hindered. It will be more difficult for lithium ions to access through the diffusion channels to reach the active sites for lithium insertion. Besides, the active sites available for lithium insertion and extraction in standalone NVO-SNB are not overlapped or interrupted, so it renders efficient lithium ions and electronic transportation pathway which benefits in capacity and cyclability. .

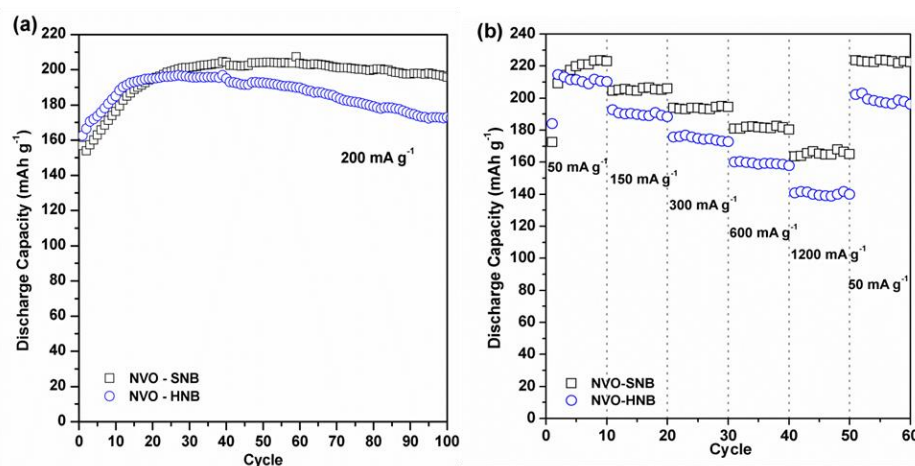


**Figure 4-34** (a) Cycling performance of NVO-SNB and NVO-HNB at current density of  $200 \text{ mA g}^{-1}$  (b) Rate capability at various current densities.

## 4.2 $\text{Li}_2\text{NiTiO}_4$

To break through the boundary of LIB cathodes which was generally restricted by materials with periodical arrangement of cations, the investigation on the applicability of disordered rocksalt-based material was conducted. In this section,  $\text{Li}_2\text{NiTiO}_4$  with partially ordered and disordered structure was synthesized by sol gel method. Partially ordered rocksalt-based  $\text{Li}_2\text{NiTiO}_4$  had shown better electrochemical performance due to existence of lithium-rich domains within the lattice providing feasible lithium diffusion route. Hence, the lithium content in  $\text{Li}_2\text{NiTiO}_4$  was varied to produce  $\text{Li}_{2.4}\text{Ni}_{0.9}\text{Ti}_{0.95}\text{O}_4$  and  $\text{Li}_{3.2}\text{Ni}_{0.8}\text{Ti}_{0.8}\text{O}_4$  to explore the possibility on enhancement of battery performance by creating more lithium-rich cluster within the lattice.

Besides, carbon coating on partially ordered  $\text{Li}_2\text{NiTiO}_4$  was carried out to enhance its electrochemical performance by bringing the particles into close proximity for faster electron transfer.

### 4.2.1 Sol gel synthesized $\text{Li}_2\text{NiTiO}_4$ nanoparticles: Materials characterization

The XRD patterns of the two  $\text{Li}_2\text{NiTiO}_4$  samples are shown in Figure 4-35(a). The XRD pattern of the ordered sample could be indexed on a monoclinic cell and fits well to the space group  $C12/c1$  as proposed by Sebastian *et al.*[120] The partially ordered phase of  $\text{Li}_2\text{NiTiO}_4$  (LNT-PO) was isostructural with  $\text{Li}_2\text{TiO}_3$ . The peaks at  $2\theta = 18.42^\circ, 35.95^\circ, 37.17^\circ, 43.71^\circ$  and  $62.51^\circ$  correspond to  $(hkl) = (002), (\bar{1}31), (113), (\bar{1}33)$  and  $(312)$  Miller indices respectively. The lattice parameters refined using Rietveld method are  $a = 5.092(5) \text{ \AA}, b = 8.800(9) \text{ \AA}, c = 9.728(7) \text{ \AA}, \beta = 99.51(7)^\circ$  ( $R_{\text{wp}} = 1.42; R_p = 1.10$ ).

The disordered sample (LNT-DO) could be indexed on a cubic rocksalt structure (space group  $Fm\bar{3}m$ ) with lattice parameter of  $a = 4.150(4) \text{ \AA}$  ( $R_{\text{wp}} = 2.18; R_p = 1.70$ ) (Figure 4.35(b)). The Li and transition metals (Ni and Ti) are evenly occupy the octahedral sites in cubic closely packed oxygen lattice.

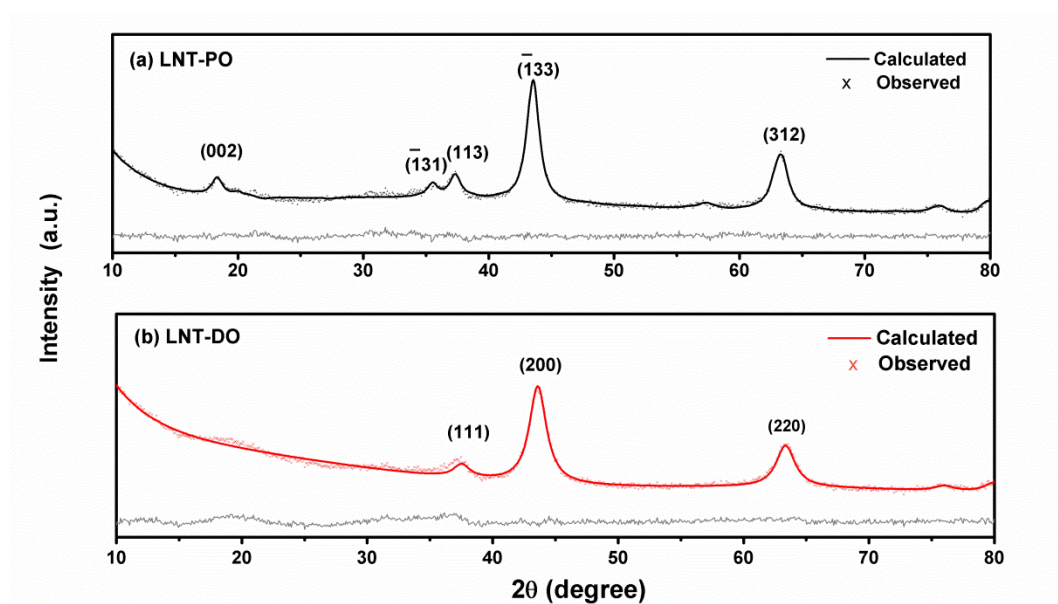
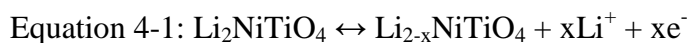


**Figure 4-35** Powder XRD results of (a) LNT-PO and (b) LNT-DO.

#### 4.2.2 Sol gel synthesized $\text{Li}_2\text{NiTiO}_4$ nanoparticles: Electrochemical performance

The electrochemical redox process of  $\text{Li}_2\text{NiTiO}_4$  can be represented as below:



in which the maximum exchange of 2 mol of lithium ion per formula unit attributes to a maximum theoretical specific capacity of  $290 \text{ mAh g}^{-1}$ .

The first charge and discharge profiles of the LNT-PO and LNT-DO at a current density of  $10 \text{ mA g}^{-1}$  are shown in Figure 4-36. Both samples were first charged to 5 V from the open circuit potential state at a current density of  $10 \text{ mA g}^{-1}$  for lithium ions extraction before discharging.

In the beginning of first charge, a steep plateau was shown at 3.9 V extending up to 4.5 V for disordered sample and 4.7 V for LNT-PO, indicating the first oxidation of  $\text{Ni}^{2+}$  to  $\text{Ni}^{3+}$ . The second voltage step began to appear at 4.8 V, representing the onset of second lithium extraction, associated with the subsequent oxidation process to  $\text{Ni}^{4+}$  [17, 19].

The LNT-DO exhibited shorter plateau regions than that of LNT-PO, resulting in lower capacity obtained. This is because the disordered rocksalt structure of LNT-DO with random cation distribution of lithium and transition metals in octahedral sites creates

obstruction on lithium ion diffusion pathway. Therefore, less lithium ions are able to be extracted compared with the LNT-PO with more well-ordered lithium layers.

For LNT-PO, it was possible to extract  $\sim 1.8$  lithium ion per formula unit after first charge corresponding to capacity of  $\sim 262 \text{ mAh g}^{-1}$  whereas for disordered sample is  $\sim 1.4$  lithium ion corresponding to  $\sim 205 \text{ mAh g}^{-1}$ .

However, the irreversible discharge capacity for LNT-PO is  $\sim 240 \text{ mAh g}^{-1}$  ( $\sim 1.7$  lithium ion per formula unit) whereas for LNT-DO is  $\sim 168 \text{ mAh g}^{-1}$  ( $\sim 1.2$  lithium ion per formula unit). The first cycle capacity loss and polarization may be due to formation of new phase during the first charging process and irreversibility of structural change.

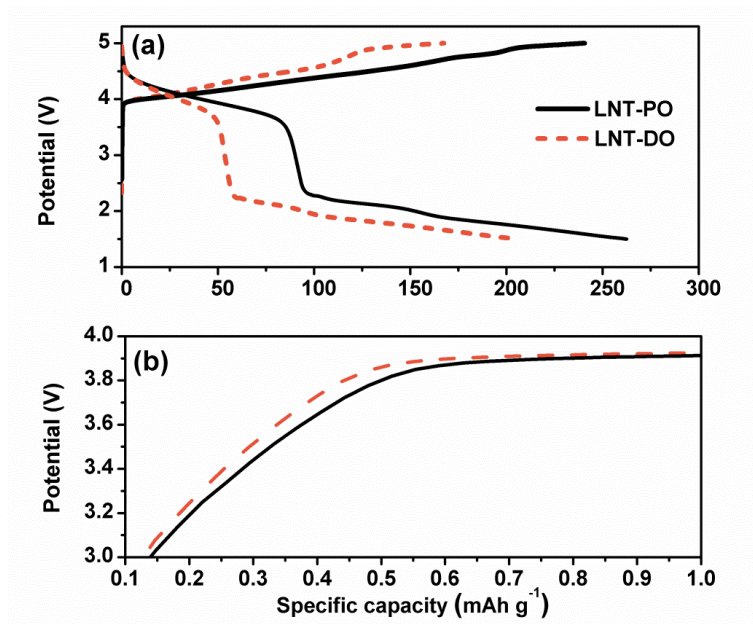


**Figure 4-36** (a) Galvanostatic profiles of partially ordered structured (LNT-PO) disordered structured (LNT-DO)  $\text{Li}_2\text{NiTiO}_4$  for first cycle at current density of  $10 \text{ mA g}^{-1}$ . (b) Magnified first charge profile between 3.0 – 4.0 V.

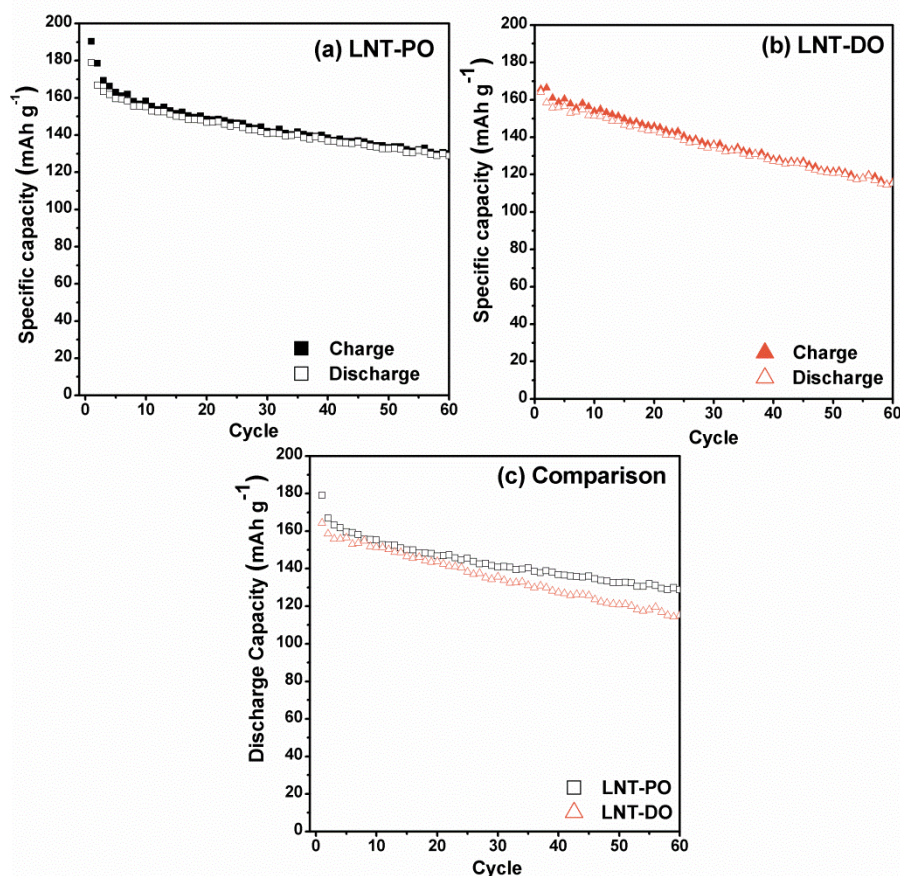
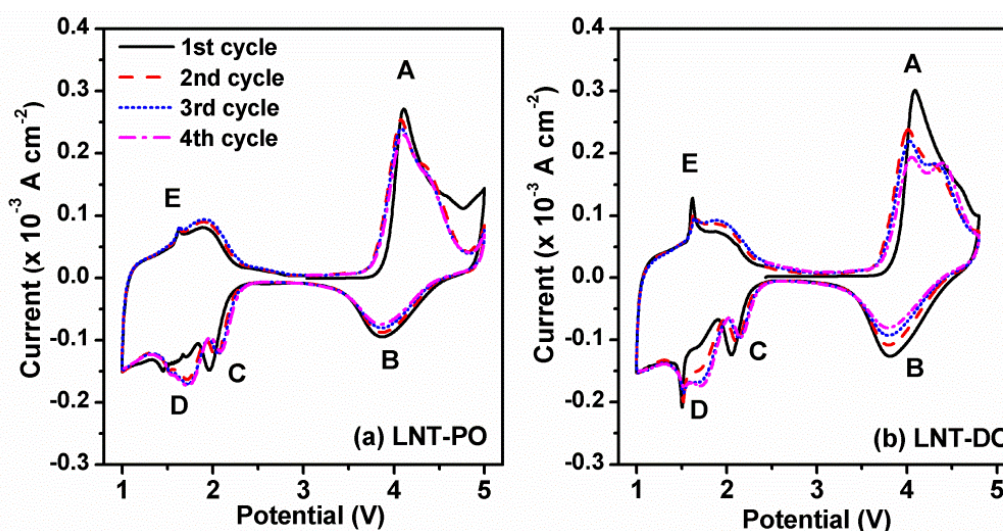


**Figure 4-37** Cycling performance of (a) LNT-PO, (b) LNT-DO at current density of 29 mA g<sup>-1</sup>, (c) comparison of discharge capacities between LNT-PO and LNT-DO.

Figures 4-36 shows the cycling performance of LNT-PO and LNT-DO under 29 mA g<sup>-1</sup> respectively. From Figure 4-37(c), LNT-PO exhibited slightly better cycling retention than LNT-DO. The capacity retention after 60 cycles for LNT-PO was ~72% which was slightly higher than LNT-DO of 69%.

The main reason causing capacity fading for LNT-DO was demonstrated to be structural changes in the long-range order within the cubic rocksalt structure due to irreversible local octahedral deformation around the transition metal ion as reported for Li<sub>2</sub>FeTiO<sub>4</sub> and Li<sub>2</sub>CoTiO<sub>4</sub> [18, 111]. For LNT-PO, the first capacity loss was less significant. This may be attributed to cation migration which reduces the cation ordering upon lithium extraction during first charge. From the perspective of prolonged cycling (e.g. more than 20 cycles), LNT-PO showed better capacity retention. This was possibly due to some phase changes or existence of certain extent of cation ordering within the structure, creating less obstruction for lithium ion diffusion pathway.





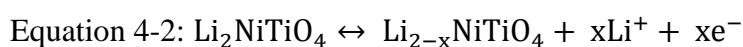
**Figure 4-38** CV profiles of (a) LNT-PO and (b) LNT-DO for first four cycles at scan rate of  $0.1 \text{ mV s}^{-1}$ .

Figure 4-38 presents the CV curves of the LNT-PO and LNT-DO respectively with at a scan rate of  $0.1 \text{ mV s}^{-1}$  versus  $\text{Li}^+/\text{Li}$  between 5.0 V (charge cutoff) and 1.0 V (discharge cutoff). In overall, the CV profiles of both LNT-PO and LNT-DO were coherent with each other, indicating identical electrochemical reactions. In the region between the anodic switching potential (5.0 V vs.  $\text{Li}^+/\text{Li}$ ), one obvious oxidation peak (A) appeared at 4.2 V, indicating the oxidation of  $\text{Ni}^{2+}$  to  $\text{Ni}^{4+}$  [17]. This was correlated to the first pseudo charge plateau observed in galvanostatic profiles for both pristine LNT-PO and LNT-DO, starting from  $\sim 3.9 \text{ V}$  extending up to 5.0 V. This indicates the onset of lithium extraction by oxidation of  $\text{Ni}^{2+}/\text{Ni}^{4+}$ , which is consistent with other reported works [16, 17, 19].

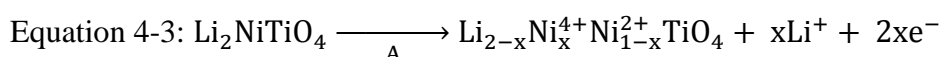
During the initial cathodic scan, reduction of  $\text{Ni}^{4+}$  to  $\text{Ni}^{3+}$  was observed as peak B at  $\sim 3.8 \text{ V}$ . Peak D was associated with reduction of  $\text{Ti}^{4+}$  to  $\text{Ti}^{3+}$  while peak E was corresponding to the reversible oxidation peak of  $\text{Ti}^{3+}$ , which was also shown in reported  $\text{Li}_2\text{CoTiO}_4$  [111]. This was in good agreement with the galvanostatic profile as shown in Figure 4-35, the discharge plateau at  $\sim 3.8 \text{ V}$  indicates reduction of  $\text{Ni}^{4+}$ , whereas the plateau at  $\sim 1.8 \text{ V}$  indicates reduction of  $\text{Ti}^{4+}$ .

It is worth noting that another small reduction peak C at  $\sim 2.0 \text{ V}$  was appeared in the reduction process. It was presumed that some of the  $\text{Ni}^{3+}$  was not completely reduce to  $\text{Ni}^{2+}$  at potential above 3.0 V due to cation mixing effect between Ni and Li. Thus, it is proposed to be associated with reduction of residual  $\text{Ni}^{3+}$  to  $\text{Ni}^{2+}$  [19] by extending the lower voltage limit to 1.5 V. [175-178] This phenomena was also observed in ordered rocksalt Li-Ni-O based material system in which occupation of divalent  $\text{Ni}^{2+}$  onto the Li

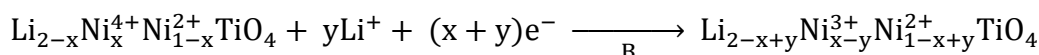
layer site usually occurs during synthesis. In this study, the ordered structure of  $\text{Li}_2\text{NiTiO}_4$  contains partially ordered structure, isostructural with  $\text{Li}_2\text{TiO}_3$  with certain degree of lithium and nickel cation mixing within the lithium-rich and lithium-poor layers respectively.[120] The as-proposed partially ordered structure is isostructural with  $\text{Li}_2\text{TiO}_3$  which has a  $\alpha\text{-NaFeO}_2$  related structure. Hence, the LNT-PO resembles the  $\text{LiNiO}_2$  which has the  $\alpha\text{-NaFeO}_2$  structure but with additional  $\text{Ti}^{4+}$  as “pillars” within the framework. Similar cation mixing between Ni and Li may be expected to occur during synthesis of  $\text{Li}_2\text{NiTiO}_4$ . After the first charging with lithium extraction, ideally the reaction should proceed reversibly as described below during subsequent discharge (Equation 4-2).



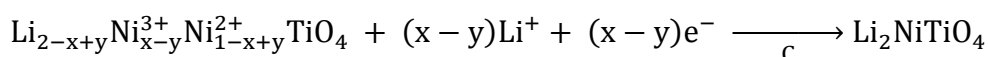
However, due to site mixing of Ni and Li, there may be slower electrochemical reaction kinetic causing difficulty in insertion of lithium during discharge. The reactions A, B and C may proceed as described below (Equation 4-3, 4-4 and 4-5):



Equation 4-4:



Equation 4-5:



The reduction peak at  $\sim 2.0$  V (C) was proposed to be associated with the complete formation of divalent  $\text{Ni}^{2+}$  in the Li sites of oxides.

Another hypothesis proposed for the appearance of this reduction peak C was associated with the additional insertion of lithium into  $\text{LiNiO}_2$  to form  $\text{Li}_2\text{NiO}_2$  by electrochemical means, which may be applied as similar as in  $\text{Li}_2\text{NiTiO}_4$ . The additional reduction peak does not appear in reported CV of  $\text{Li}_2\text{CoTiO}_4$ [111] in Yang and co-workers' work because  $\text{Li}_2\text{CoO}_2$  does not form electrochemically by extending the lower voltage limit[179]. Hence, the phase transformation for LNT upon electrochemical cycling is different from  $\text{Li}_2\text{CoTiO}_4$ . This involves formation of stacking faults and phase transformation.[177, 179]

Besides, a broad current peak at  $\sim 4.5$  V during the 1<sup>st</sup> cycle appeared to be narrower in 2<sup>nd</sup> and 3<sup>rd</sup> cycle, which suggests an irreversible electrochemical reaction has occurred.

This is consistent with the curve polarization between galvanostatic charge and discharge profile for 1<sup>st</sup> cycle and subsequent cycle which can be observed in Figure 4-35. The irreversibility may be due to (i) structural changes due to cation migration or formation of new phase; (ii) oxygen removal from crystal lattice upon lithium extraction during charge process[111, 180]. The latter reason may account for the capacity fading, as reported in literature, in which the oxygen release may react with electrolyte components, forming surface film, preventing redox reaction involving lithium extraction/insertion[18, 181, 182]. Phase transformation and local structural disorder of the electrode upon cycling also contribute to decrement in capacity. To date, the explicit mechanism of capacity fading of cathode materials is not fully understood.[183]

Based on our results for comparison of the electrochemical performances for LNT-DO and LNT-PO, LNT-PO with partially ordered structure had exhibited better battery performance in terms of capacity and cyclability. This shows that cation ordering affects the reversibility of electrochemical reactions. As reported in previous studies, materials with disordered cation arrangement are not suitable for reversible lithium intercalation due to lack of distinct diffusion channel for lithium ions.[110] By tailoring the material structural properties via creation of interconnected local lithium-rich domains, lithium ions will be able to diffuse through the lattice.[15] This was well aligned with our study in which the LNT-PO composing alternating layers of lithium rich  $[\text{Li}_{2/3}(\text{NiTi})_{1/3}]$  and lithium poor  $[\text{Li}_{1/3}(\text{NiTi})_{2/3}]$  cations had exhibited better electrochemical performance than the LNT-DO with random arrangement of cations octahedral within the lattice.

### 4.2.3 Sol gel synthesized lithium excess LNT nanoparticles: Materials characterization

Two lithium excess LNT compounds with chemical formula  $\text{Li}_{2.4}\text{Ni}_{0.9}\text{Ti}_{0.95}\text{O}_4$  (denoted by LNT2.4) and  $\text{Li}_{3.2}\text{Ni}_{0.8}\text{Ti}_{0.8}\text{O}_4$  (LNT3.6) had been prepared by sol gel method. The purpose to synthesize these lithium excess, off-stoichiometric LNTs was to create local lithium-rich clusters within the lattice to investigate the possibility of improvement in battery performance. With additional lithium ions replacing some of the metallic ions within the lattice had lead to formation of disordered structure as presented in XRD patterns obtained (Figure 4-39). Rietveld refinement had been conducted and confirmed the formation of LNT2.4 and LNT3.6 with disordered cubic rocksalt structure (space



group  $Fm\bar{3}m$ ). The corresponding lattice parameters were 4.165(4) Å for LNT2.4 and 4.158(3) Å for LNT3.6 respectively.

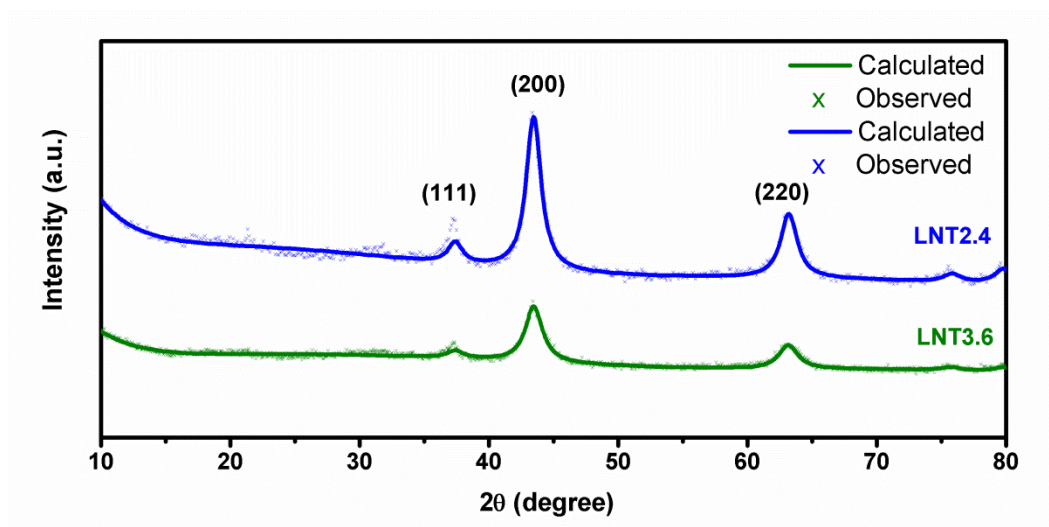


**Figure 4-39** XRD patterns of LNT2.4 and LNT3.6, the structural information was derived by Rietveld refinement method.

#### 4.2.4 Sol gel synthesized lithium excess LNT nanoparticles: Comparison of electrochemical performance

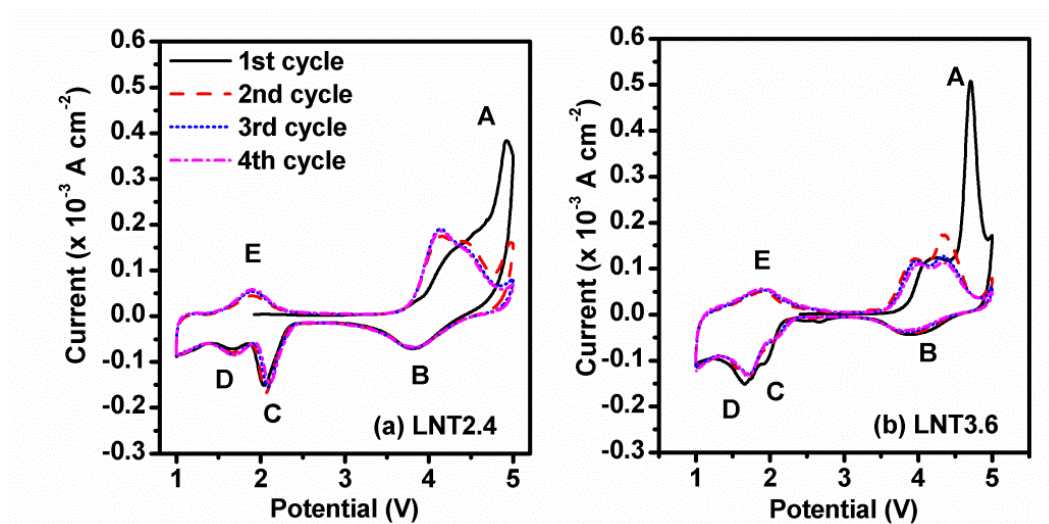


**Figure 4-40** CV scans of (a) LNT2.4 and (b) LNT3.6 for first three cycles at scan rate of 0.1 mV s<sup>-1</sup>.

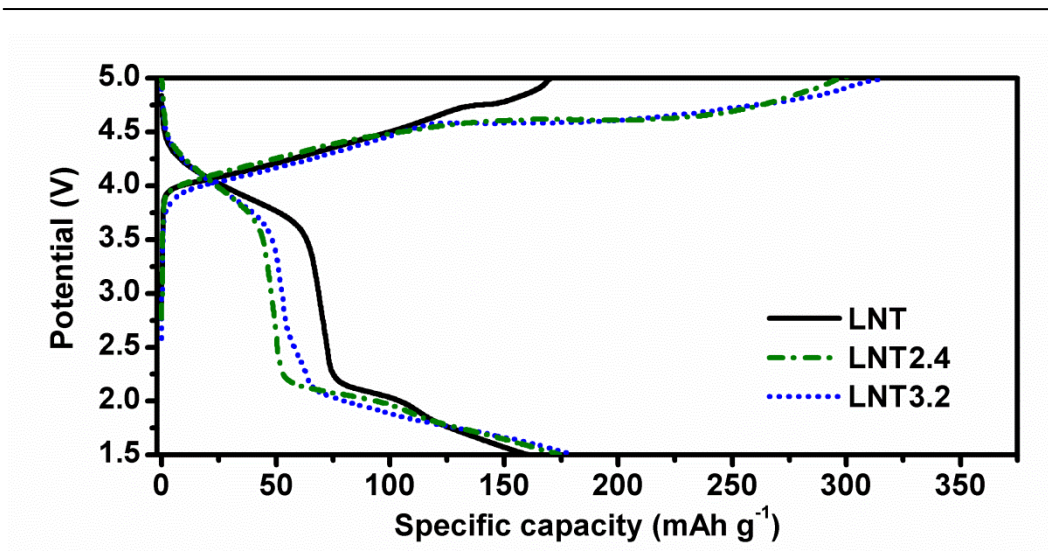


**Figure 4-41** First galvanostatic cycling of LNT, LNT2.4 and LNT3.6.

The CV profiles for LNT2.4 and LNT3.6 were almost consistent with the CV of LNT-PO and LNT-DO as discussed in Section 4.2.2. The main difference could be observed was the higher intensity for oxidation peak (A), spanning towards larger range until 5.0 V compared to the CV curve of LNT-PO (Figure 4-40). Due to excess lithium added into the original lattice, more lithium ions could be removed during the first charging.

The first galvanostatic charging profiles (Figure 4-41) for LNT2.4 and LNT3.6 exhibited longer plateau extending towards 5.0 V, compared to charging curve of LNT-PO, supported our observation in CV scans. However, this high intense redox peak was not appearing in subsequent cycles. During subsequent cycles, similar redox peaks to that of stoichiometric LNT-PO could be observed for LNT2.4 and LNT3.6. This showed that the first cycle reaction was not reversible. The extending plateau for lithium excess LNT2.4 and LNT3.6 was possibly related to simultaneous removal of oxygen with the lithium ions which had been reported in many studies of lithium excess compounds employed as LIB cathodes.[180, 184, 185] Figure 4-42 shows the cycling performance of LNT-PO, LNT2.4 and LNT3.6 at current density of 29 mA g<sup>-1</sup>. LNT3.6 achieved highest first charge capacity of ~316 mAh g<sup>-1</sup>, which was higher than the theoretical capacity of 290 mAh g<sup>-1</sup> for LNT, but with discharge capacity of ~181 mAh g<sup>-1</sup>. The presence of anomalous capacity supported the occurrence of oxygen loss which had been demonstrated in other studies.[180, 186] For LNT2.4, the first charge capacity exhibited was ~260 mAh g<sup>-1</sup> and discharge capacity was ~175 mAh g<sup>-1</sup>. Both LNT2.4 and LNT3.6 with lithium excess had exhibited higher initial capacities than that of LNT-PO (~170 mAh g<sup>-1</sup> (charge); ~161 mAh g<sup>-1</sup> (discharge)). By comparing the cycling stability, LNT-

PO achieved better capacity retention of ~81%, compared to LNT2.4 of ~68% and LNT3.6 of ~65% after 20 cycles. Hence, when the lithium amount was increased for LNT, it was not beneficial in terms of cyclability for battery performance. Capacity fading was more severe due to oxygen removal from the lattice during initial charging. Structural collapse possibly occur which contributes to deterioration of electrochemical performance.

Therefore, tailoring of degree of cation disorder is vital in preserving the structural stability upon prolonged cycling. Better battery performance could be achieved by LNT-PO whereas introduction of excessive cation disorder in LNT2.4 and LNT3.6 had caused it more vulnerable to structural destruction when the lithium ions are being extracted, as supported by the lower cycling retention of lithium excess LNT2.4 (~68%) and LNT3.6 (~65%) compared to stoichiometric LNT-PO (~81%).

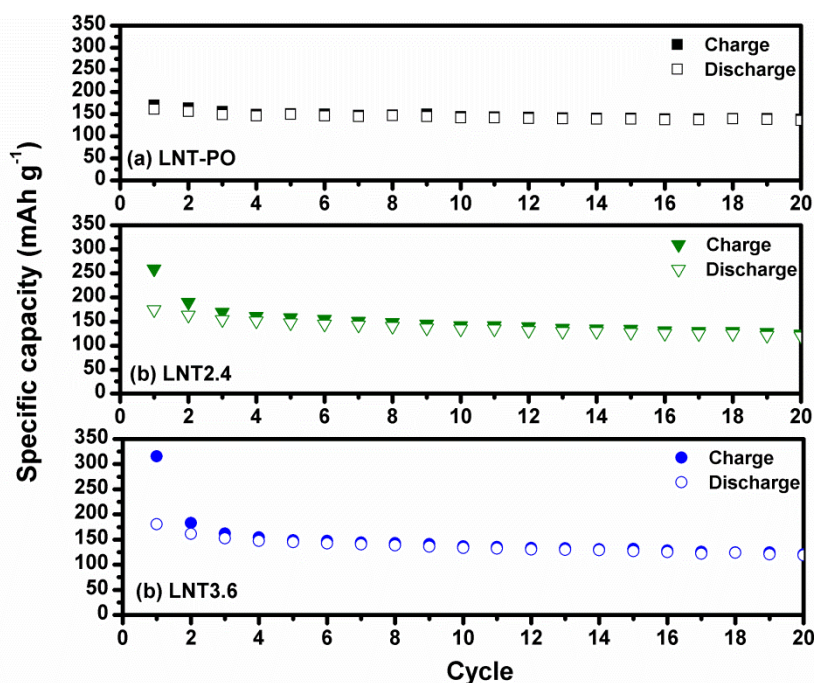
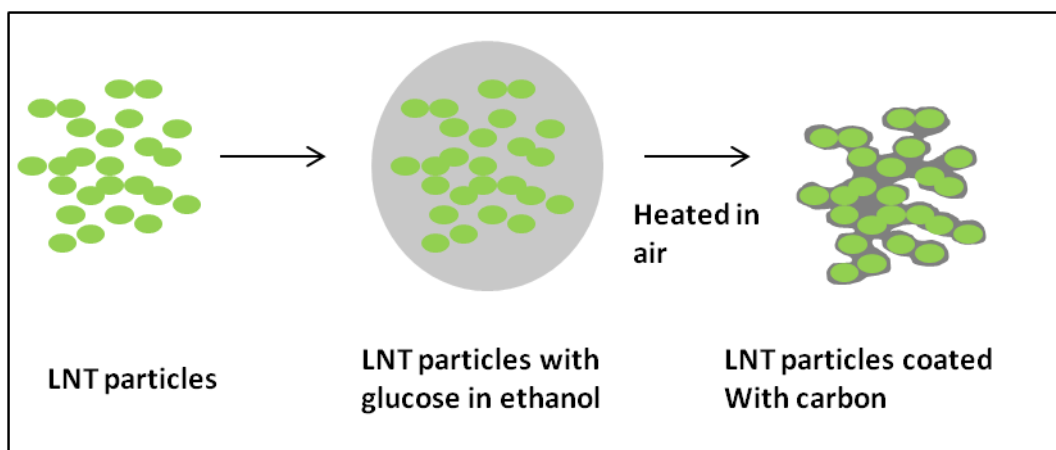


**Figure 4-42** Cycling performance of (a) LNT-PO, (b) LNT2.4 and (c) LNT3.6 at current density of 29 mA g<sup>-1</sup>.

#### 4.2.5 Effect of carbon coating on sol gel synthesized Li<sub>2</sub>NiTiO<sub>4</sub> nanoparticles: Materials characterization

Pristine LNT-PO delivered an initial discharge capacity of ~ 161 mAh g<sup>-1</sup>, but the retention depletes to ~ 81% of the initial value after 20 cycles, most likely due to poor conductivity or irreversible electrochemical reactions for this material as mentioned earlier. Carbon coating was attempted to improve the conductivity of LNT-PO (Scheme

4-3). Carbon coating procedure is usually performed by wet chemistry which requires pyrolysis of organic compounds in inert atmosphere at high temperature of about 700 – 900 °C[187, 188]. Since the preparation of  $\text{Li}_2\text{NiTiO}_4$  requires air atmosphere, it is difficult to employ the wet chemistry procedure to produce carbon coating in our study. Besides, carbon might reduce the transition metal ions in inert atmosphere during high temperature calcination, and introduces defects to the material structure. In this study, carbon coating was prepared by using glucose as carbon source at low pyrolysis temperature, which requires only short heating time in air. Similar carbon coating has been done and reported for other cathode materials[189, 190].



**Scheme 4-3** Schematic illustration of formation process for carbon-coated  $\text{Li}_2\text{NiTiO}_4$  with partially ordered structure (LNT-PO). Thin layer of carbon coating is formed on the surface of agglomerated particles and brings the particles into close proximity.

In order to estimate the amount of carbon presented in LNT/C-3 and LNT/C-8, TGA was conducted in ambient atmosphere and shown in Figure 4-43. The weight loss below 200 °C was related to the moisture adsorbed on the material. Observed weight loss in TGA above 200 °C was corresponded to the amount of carbon present in the material. The TGA results suggested that the amount of carbon present in LNT/C-3 was ~ 1.5 wt% and LNT/C-8 was ~ 4.5 wt% respectively, indicating the formation of carbon by decomposition of glucose after calcination process.



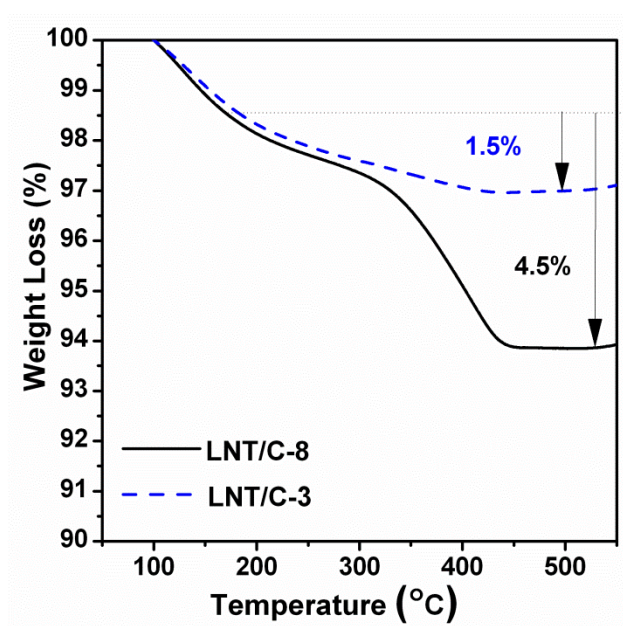


**Figure 4-43** TGA of LNT/C-3 and LNT/C-8.

There was no impurity phase observed in XRD patterns (Figure 4-44) for the carbon coated samples, which suggests that the crystal structure of LNT-PO was not affected by the carbon coating.

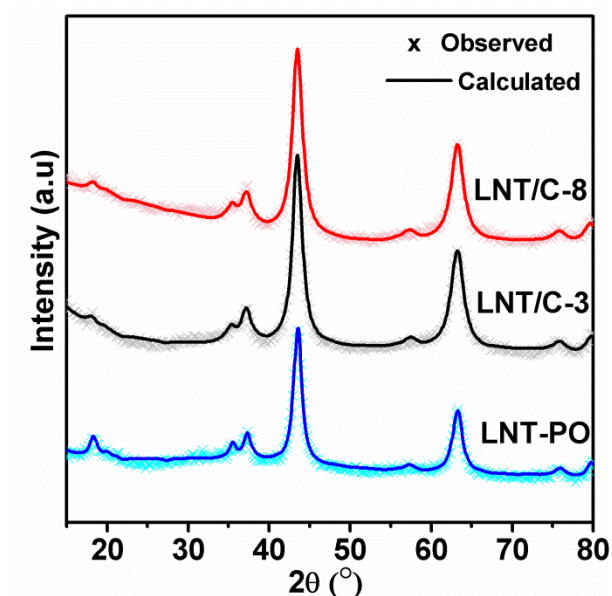


**Figure 4-44** Observed and calculated XRD patterns of pristine LNT-PO, LNT/C-3 and LNT/C-8.

Figure 4-45 shows the FESEM images of as-prepared LNT-PO, carbon coated LNT/C-3 and LNT/C-8. For pristine LNT-PO (Figure 4-45(a)), the nanoparticles were

agglomerated to form bigger, non-uniform particles in micron size, with smooth and clean surface. For carbon coated LNT/C-3 (Figure 4-45(b)), the surfaces were observed to be rougher, and agglomerated particles were partially covered with carbon. When the amount of glucose were increased to increase the amount of carbon coating for LNT/C-8, the agglomerated particles were encapsulated by thin carbon layer as shown in Figure 4-45(c). Similar SEM images were also observed for other carbon coated cathode materials.[123, 190] It can be seen from the HRTEM images that the agglomerated particles were coated by more homogeneous amorphous carbon particles for LNT/C-8 compared to that of LNT/C-3.

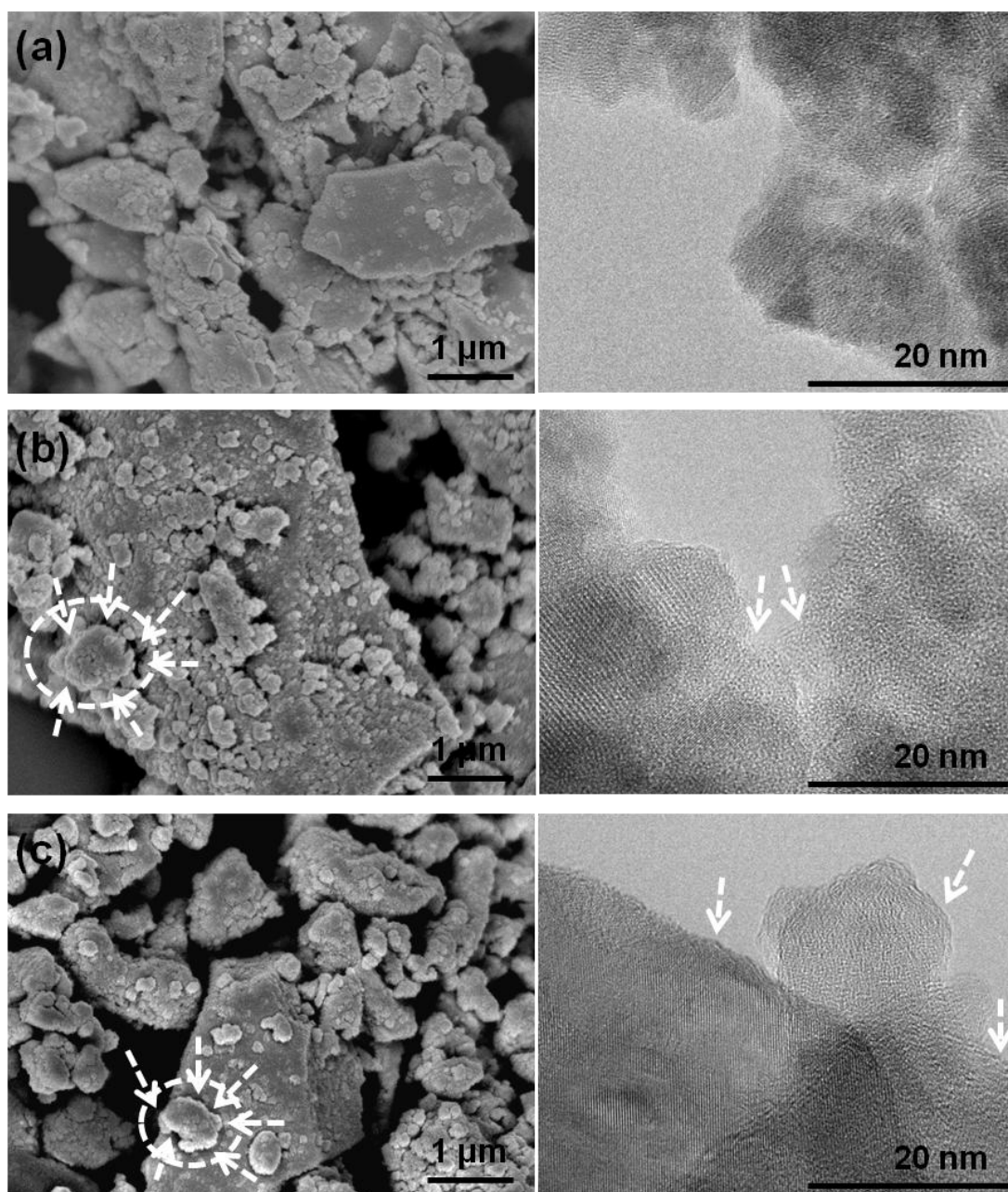


**Figure 4-45** FESEM (left) and HRTEM (right) images of (a) LNT-PO; (b) LNT/C-3; and (c) LNT/C-8

### 4.2.6 Effect of carbon coating on sol gel synthesized $\text{Li}_2\text{NiTiO}_4$ nanoparticles: Electrochemical performance

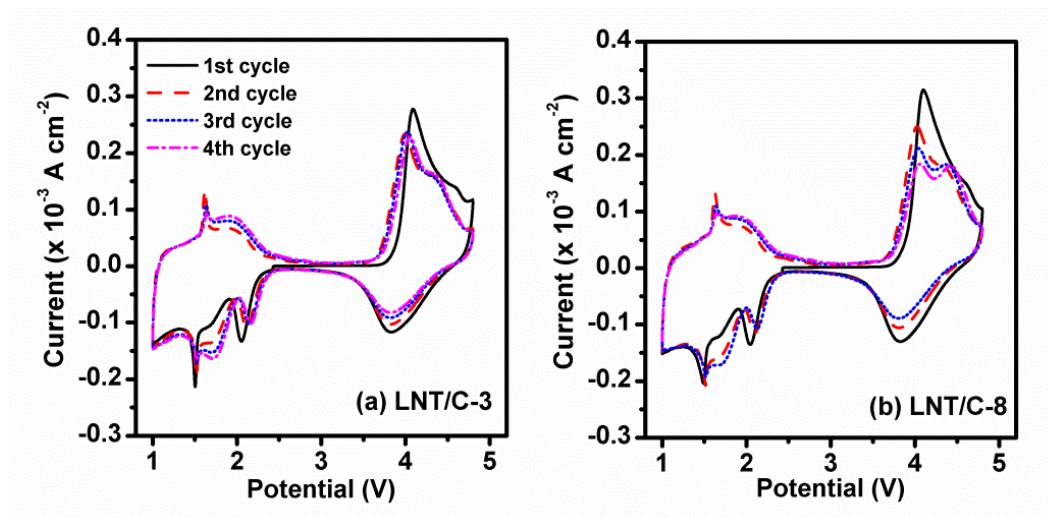


**Figure 4-46** CV scans of (a) LNT/C-3 and (b) LNT/C-8 at scan rate of  $0.1 \text{ mV s}^{-1}$  - between the potential range of 1.0 to 5.0 V

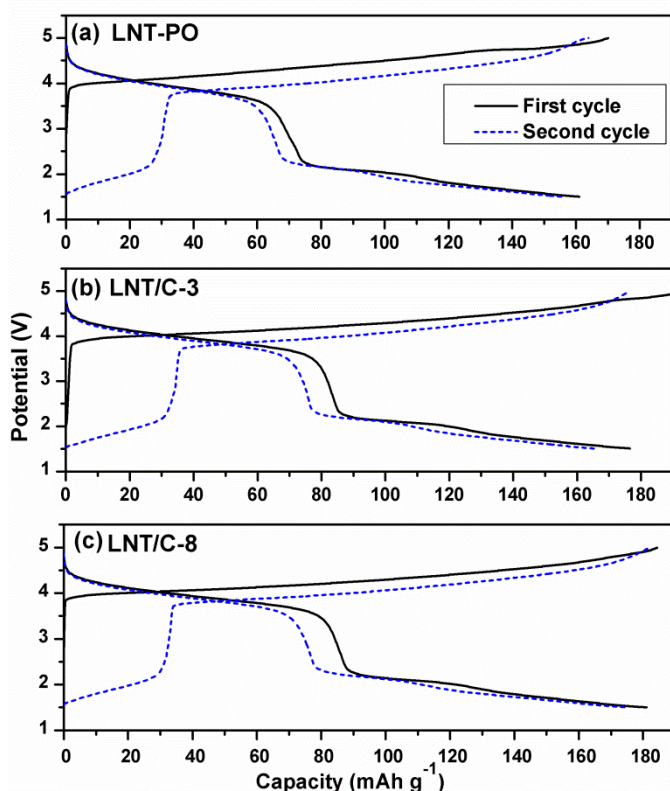


**Figure 4-47** First and second galvanostatic cycling of (a) LNT-PO, (b) LNT/C-3 and (c) LNT/C-8 at current density of  $29 \text{ mA g}^{-1}$ .

The CV profiles of carbon coated LNT/C-3 and LNT/C-8 were in coherent with pristine LNT-PO as discussed in Section 4.2.2. The redox peaks as observed in CV scans were well aligned with plateau as shown in galvanostatic charging/discharging profiles (Figure 4-47). The area underneath the CV curve of LNT/C-8 was slightly larger than that of LNT/C-3, indicating higher amount of lithium intercalation. This observation supported the phenomenon of higher specific capacities achieved by LNT/C-8 (Figure 4-48) due to improvement in electronic conductivity by carbon coating.

Figure 4-48(a) shows the comparison of cycling performance between the pristine LNT-PO and carbon coated LNT/C at current density of 29 mAh g<sup>-1</sup>. The first discharge capacity for carbon coated samples LNT/C-3 and LNT/C-8 were ~ 178 mAh g<sup>-1</sup> and ~ 181 mAh g<sup>-1</sup> respectively. Higher initial discharge capacity for carbon coated samples can be attributed to the improved electronic conductivity due to carbon coating. The cycled LNT/C-3 and LNT/C-8 retained ~ 84 % and ~ 87 % of their initial capacity after 20 cycles. The capacity retention rate for both LNT/C do not differ much from that of pristine LNT-PO. This indicates that electronic conductivity is not the main factor for capacity fading in long term cycling. The capacity fading may be due to irreversible structural changes, involving phase transition from ordered structure to disordered structure upon galvanostatic cycling which will be discussed in Section 5.3.2.

Rate capability studies were conducted to investigate the effect of carbon coating on electrochemical performance at different current densities as shown in Figure 4-48(b). The electrochemical performance as shown by LNT/C-8 is slightly better than that of LNT/C-3, hence LNT/C-8 was chosen for comparison with pristine LNT-PO in rate capability studies. Carbon coating is beneficial in improving the overall capacities at different current densities as summarized in Table 4-6. This suggests that the improvement in rate capability is due to the increased conductivity by carbon coating which connects the LNT-PO particles in close proximity, contributing to the good conducting channel for the electron mobility.



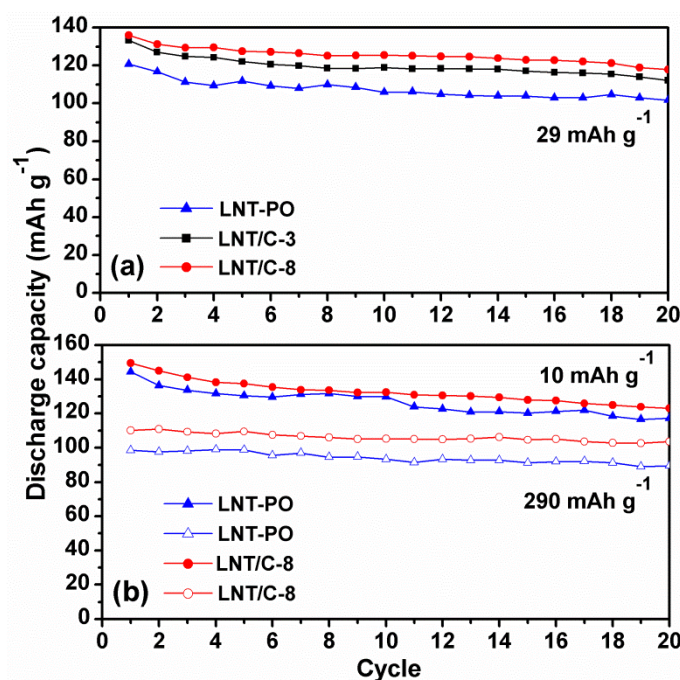


**Figure 4-48** Cycling performance of LNT-PO, LNT/C-3 and LNT/C-8 at current density of 29 mA g<sup>-1</sup>; (b) Cycling test at current density of 10 mA g<sup>-1</sup> and 290 mA g<sup>-1</sup> for LNT-PO and LNT/C-8.

**Table 4-6** Table of first discharge capacities for LNT-PO and LNT/C-8 at different current densities.

Current density (mA g <sup>-1</sup> )	LNT-PO	LNT/C-8	Increment (%)
	First discharge capacity (mAh g <sup>-1</sup> )	First discharge capacity (mAh g <sup>-1</sup> )	
10	192.5	199.3	3.5
29	160.9	181.2	12.6
290	131.5	147.9	11.7

To validate the effect of carbon coating on the electrochemical performance of Li<sub>2</sub>NiTiO<sub>4</sub>, electrochemical impedance spectroscopy (EIS) was carried out on LNT, LNT/C-3 and LNT/C-8 respectively, and the corresponding Nyquist plot is presented in Figure 4-49. EIS is a versatile electrochemical method to understand electrical properties of materials and its interface. From Figure 4-49, the measured EIS showed single semicircle within the high frequency range, followed by a straight line for all three samples. The diameter of the semicircle at high frequency is related to the interfacial charge-transfer (CT)

impedance and the diameter of the high frequency semicircle decreased with increasing carbon content, suggesting lower CT impedance for the carbon coated samples. This indicates the improvement in electronic conductivity for LNT/C-3 and LNT/C-8 as reflected in the electrochemical studies.

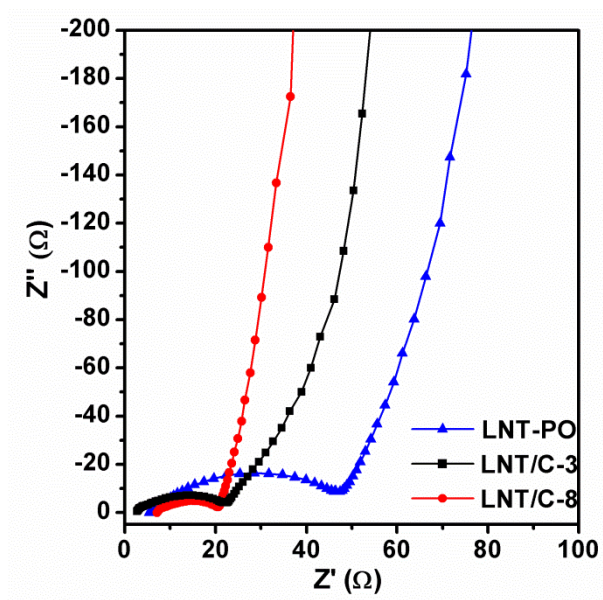


**Figure 4-49** Nyquist plot of pristine LNT-PO, LNT/C-3 and LNT/C-8.

# Chapter 5 Discussion

This chapter is categorized into three sections. The first section covers the effect of nanostructuring of LIB cathodes. The influence of particle size was elaborated by using  $\text{Li}_{1.2}\text{V}_3\text{O}_8$  as case study. The study was then extended to benefits of 1D nanobelts in improving lithium diffusion kinetics.

Since the electrochemical performance of ordered rocksalt structure was generally hampered by structural destruction upon cycling, cation substitution was conducted to improve the structural stability. The influence of cation substitution was discussed in details by linking electrochemical characteristics with structural properties.

The third section focuses on structural evolution in correlation with lithium intercalation and deintercalation processes. *Ex situ* characterization technique was utilized to understand the effect of lithium activities on changes in structural framework.

## 5.1 Effect of nanostructuring

### 5.1.1 Effect of particle size

During charging and discharging of LIBs, lithium ions will solvate through the electrolyte, move from the cathode to anode and vice versa. There are three main steps involved in this process, which are (i) lithium ion transportation within the solid state electrode materials, (ii) charge transfer at the interface between the electrode and electrolyte and (iii) lithium ion motion in the electrolyte. Hence, solid state diffusion is the main consideration for the rate determining of these steps. Numerous efforts have been devoted in materials nanosizing to enhance diffusion kinetics by downsizing the rate-limiting diffusion length of lithium ions to nanometer scale.[191] However, the enhancement of electrochemical performance by employing nanomaterials is far more complicated than reducing the diffusion distance itself. Based on many reported studies, downsizing particles into nano-level had imposed great influences on materials intrinsic characteristics[192, 193] which will be reflected in electrochemical properties when they are applied in LIBs. Common observations include unanticipated kinetics[194],

anomalous or larger capacities[195, 196], smearing out of the galvanostatic curve[197, 198], *etc.*, which leads to simultaneous advantages and challenges for LIB performance.

Effect of particle size on electrochemical performance was investigated by using LVO-NP prepared by different sintering temperature (refer to Section 4.1.1 and 4.1.2). By using lower sintering temperature to produce LVO-NP with smaller particle size, the capacity degradation became more severe. EIS were conducted to understand the kinetics of electrodes and the reasons accounted for capacity deterioration. The measurements were taken before cycling and after 20<sup>th</sup> cycle in which capacity stabilization were achieved by all LVO-NP300, LVO-NP400 and LVO-NP500 (refer to Figure 4-5). The Nyquist plots for all LVO-NPs consisted of a depressed semicircle with a high-frequency semicircle and a medium-frequency semicircle overlapped each other followed by a long low frequency dispersive line. The spectra were fitted to a modified two parallel RC circuit[143] represented in Figure 5-1 and the fitting results were listed in Table 5-1. The equivalent circuit model comprises of the electrolyte resistance ( $R_e$ );  $R_{sf}$  and  $CPE_{sf}$  refer to the resistance and associated constant phase element due to surface passivating layer respectively.  $R_{ct}$  and  $CPE_{ct}$  are related to the charge transfer resistance and associated constant phase element; and  $W_s$  is related to Warburg impedance.

The  $R_{sf}$  was greatly influenced by particle size. LVO-NP300 had the highest value due to larger surface area for formation of passivating film. This value had increased during 20<sup>th</sup> cycle, which was well aligned with the galvanostatic cycling, in which drastic capacity drop was observed during initial stage until stabilization after ~20 cycles. LVO-NP300 had achieved highest specific capacity for first cycle, possibly due to lowest charge transfer resistance between particles as reflected by low  $R_{ct}$  value as the passivating film was just initiated on the electrode surface but was not yet propagated throughout the particles. This supported our earlier observation in which there was no additional redox peaks during first cycle in CV profile of LVO-NP300.

The  $R_{sf}$  values for all LVO-NPs had increased in 20<sup>th</sup> cycle compared to that of before cycling, indicating higher extend of surface film formation upon cycling due to side reactions with electrolyte.[82] As the surface film formation had propagated into interparticle level, this affected the  $R_{ct}$  which was increased in 20<sup>th</sup> cycle compared to that of before cycling for all LVO-NPs. Besides, the  $R_{ct}$  will also be affected by agglomeration of particles upon repeated lithium insertion and extraction which causes gradual capacity fading, as similarly observed in LVO-NP500.

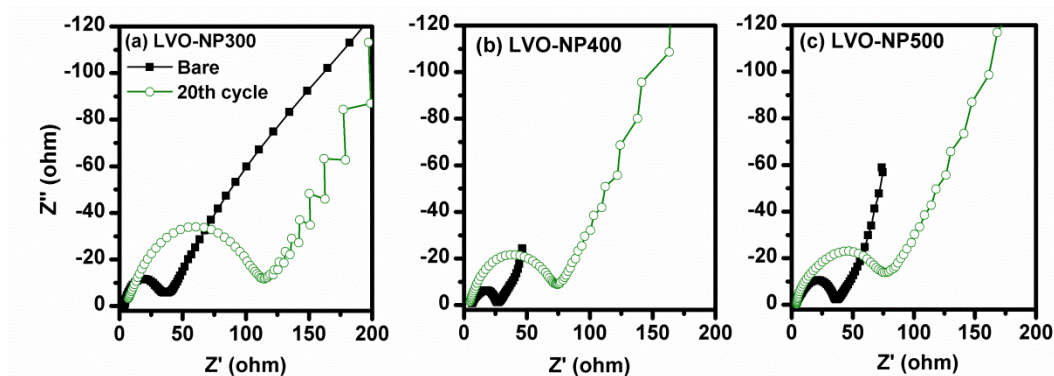


**Figure 5-1** Nyquist plots for (a) LVO-NP300, (b) LVO-NP400 and (c) LVO-NP500



**Figure 5-2** Equivalent circuit used to fit the Nyquist plot (Figure 5-1). The circuit elements are denoted as electrolyte resistance ( $R_e$ ), impedance of surface passivating film ( $R_{sf}$ ), associated constant phase element ( $CPE_{sf}$ ), charge transfer resistance ( $R_{ct}$ ) and the Warburg impedance ( $W$ ).

**Table 5-1** Impedance values of ball milled  $Li_{1.2}V_3O_8$  based on Nyquist plot in Figure 5-1 using the circuit in Figure 5-2

Sample	Cycle	$R_{sf}$ ( $\Omega$ )	$CPE_{sf}$ ( $\mu F$ )	$R_{ct}$ ( $\Omega$ )	$CPE_{ct}$ (mF)
<b>LVO-NP300</b>	0 (Bare)	22	0.9	17	0.50
	20 <sup>th</sup>	50	1.2	110	0.05
<b>LVO-NP400</b>	0 (Bare)	12	0.2	20	0.70
	20 <sup>th</sup>	30	1.0	73	0.01
<b>LVO-NP500</b>	0 (Bare)	5	0.005	30	0.78
	20 <sup>th</sup>	20	0.85	60	0.07

Based on our observations, downsizing the particles size of LVO-NP would induce higher reactivity towards electrolyte, leading to passive film formation.[82, 199] Alteration of electrolyte composition and passivation of particles' surface eventually leads to severe capacity fading upon prolonged cycling. Eventhough superior electrochemical performance can be achieved by effort of materials nanosizing.[200, 201] downsizing the

particle size into “excessive” nano-level may incur several issues including decrease in tap density[202] and increase in percolation threshold[203]. While higher specific capacity can be obtained by materials nanosizing with improved ionic and electronic conductivities,[20, 204-206] its higher surface area and lower packing density may also aggravate interfacial side reactions which are detrimental for battery performance. Hence, there is a limit on going “nano” in tailoring the particle size as to promote the interfacial reaction between the electrode materials and electrolyte to an optimum level in which undesired side reactions can be minimized.[199, 202] In the case study of LVO-NPs, particle size of ~150 nm is deemed to be optimum without causing undesired reactions. In other word, it is essential to achieve good compromise between high capacity and stable cyclability. To attain the optimum electrochemical performance for LIBs, the morphology of electrodes also play an important part in governing the diffusion kinetics, which will be further discussed in Section 5.1.2.

### 5.1.2 Effect of morphology

To enhance electrochemical performance of electrodes in LIBs, optimum nanosizing of particles is beneficial in reducing the diffusion pathway and fastening reaction kinetics. To date, there are vast quantities of reported work focus on zero-dimensional (0D) nanostructure which comprises nano-length in three dimensions.[193, 207] In this thesis, the findings on 0D systems, generally nanoparticles, for LIB applications had been extended to one-dimensional (1D) systems, mostly nanobelts.

1D nanostructures such as nanowires, nanobelts, nanofibers, *etc.* have been widely employed in energy storage applications. Better electrochemical performance can be anticipated due to more effective ion and electron transport along the longitudinal direction with the provided 1D electronic wiring.[121, 166, 168, 169] Thus, numerous efforts have been devoted to produce 1D nanomaterials with high aspect ratio to be employed in battery applications. Among the techniques to fabricate 1D nanostructures, electrospinning has been extensively employed for many years as a versatile and cost-effective method to obtain 1D nanomaterials with tunable morphology and size to be used for many applications.[121] Moreover, it is a template-free method which does not require complicated purification process which may hamper the quality of final yield. As discussed earlier, electrospun LVO and NVO nanobelts with standalone and hierarchical configurations had been synthesized respectively. Their battery performances upon

prolonged cycling are summarized in Table 5-2 in comparison with their counterparts of nanoparticles. LVO-NP300 and LVO-NP400 were omitted from the comparison as their long term cycling performance was influenced by electrolyte decomposition as discussed earlier.

**Table 5-2** Comparison of electrochemical performance between  $\text{Li}_{1.2}\text{V}_3\text{O}_8$  and  $\text{Na}_{1.2}\text{V}_3\text{O}_8$  with different morphologies synthesized by electrospinning and HEBM

Sample	Morphology	Specific capacity ( $\text{mAh g}^{-1}$ )		
		1 <sup>st</sup> cycle	30 <sup>th</sup> cycle	100 <sup>th</sup> cycle
<b>LVO-NP500</b>	nanoparticles	212	191	171
<b>LVO-HNB400</b>	hierarchical nanobelt	262	242	215
<b>LVO-SNB500</b>	single nanobelt	221	207	197
<b>NVO-NP400</b>	nanoparticles	179	86	39
<b>NVO-NP500</b>	nanoparticles	132	136	81
<b>NVO-HNB</b>	hierarchical nanobelt	162	196	173
<b>NVO-SNB</b>	single nanobelt	157	202	196

Overall, the specific capacities achieved by nanobelts were higher than the nanoparticles counterpart for both LVO and NVO respectively. Efficient electron transport along the longitudinal direction of nanobelt had enabled them to outperform the electrochemical performance exhibited by nanoparticles in which charge transport is dependent on interparticle connectivity.[208] Besides, tunable nanobelt with plate-like morphology is beneficial in facilitating faster lithium diffusion kinetics compared to nanoparticles.[148] In order to elucidate the differences in diffusion kinetics of nanoparticles and nanobelt, the average diffusion time for both morphologies can be estimated by applying solid state diffusion principle,[209] which can be described by the equation as shown below:

$$\text{Equation 5-1: } \tau = L^2/2D$$

where diffusion time,  $\tau$  is proportional to diffusion length,  $L$  and  $D$  represents diffusivity.

Assuming a nanoparticle with ideal spherical shape of radius  $R$ , the diffusion time required for a lithium ion at a distance  $r$  from the center of the nanoparticle to move into the interior of nanoparticle can be estimated as:

$$\text{Equation 5-2: } \tau = (R - r)^2/2D$$

Hence, average diffusion time for lithium ion movement can be described by integration over nanoparticles of radius less than  $R$ :

$$\text{Equation 5-3: } \tau_{avg}^{sphere} = \frac{1}{2VD} \left( \int_0^R 4\pi r^2 (R-r)^2 dr \right) = R^2/(20D)$$

where volume of nanoparticles is  $V = 4\pi R^3/3$

On the other hand, for a high aspect ratio nanobelt with thickness ( $c$ ) far smaller than length ( $a$ ) and width ( $b$ ), lithium ions diffusion occurs mainly through the open faces.[210] Hence, the average diffusion time is integration over half of the thickness as described below:

$$\text{Equation 5-4: } \tau_{avg}^{plate} = \frac{1}{VD} \left( \int_0^{\frac{c}{2}} ab l^2 dl \right) = c^2/(24D)$$

where the volume is  $V = abc$ .

By employing equation 5-3 and equation 5-4, the relationship between average diffusion time for nanoparticle and nanobelt with the same volume can be represented in Figure 5-3. By applying the diffusivity reported for  $\text{Li}_{1.2}\text{V}_3\text{O}_8$  ( $\sim 10^{-10} \text{ cm}^2 \text{ s}^{-1}$ ),[60] with the thickness of as-synthesized nanobelt varied from 20 to 30 nm, the average diffusion time increases gradually but drastic change is experienced by nanoparticle with the same volume. Hence, this mathematical tabulation explains the advantageous of nanobelt configuration in contributing faster diffusion kinetics than nanoparticle.

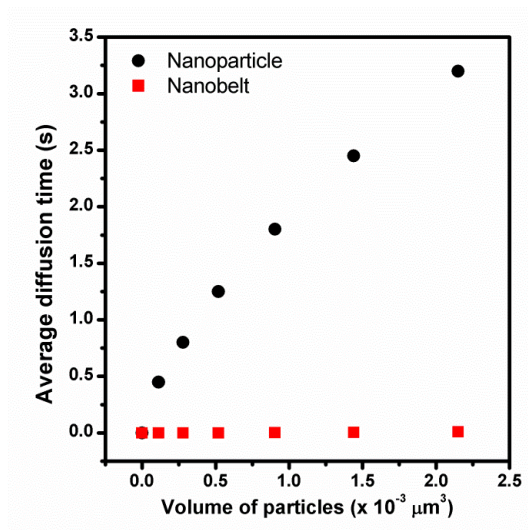


**Figure 5-3** Average diffusion time for nanoparticle and nanobelt with the same volume.



## 5.2 Effect of cation substitution

### 5.2.1 Substitution at vanadium sites of $\text{Li}_{1.2}\text{V}_3\text{O}_8$

As discussed earlier (Section 4.1.5), LVO-HNB400 had exhibited higher specific capacity than that of LVO-SNB500 during galvanostatic cycling. However, in terms of cycling stability, LVO-SNB500 achieved better capacity retention than that of LVO-HNB400. In order to preserve the high specific capacities while improving the cycling stability, minor substitution of vanadium with aluminum in LVO-HNB400 had been attempted. The electrochemical performance of LVA5O in terms of capacities and cyclability had outperformed the pristine LVO-HNB400 based on the experimental results presented in Section 4.1.7 and summarized in Table 5-3.

**Table 5-3** Comparison of battery performance between pristine LVO-HNB400, LVA3O and LVA5O.

Sample	Average working potential at current density of 200 and 600 mA g <sup>-1</sup>				Polarization (200/600 mA g <sup>-1</sup> )	Capacity (200/600 mA g <sup>-1</sup> )		Capacity retention (200/600 mA g <sup>-1</sup> ) (%)
	200 mA g <sup>-1</sup>		600 mA g <sup>-1</sup>			1 <sup>st</sup> cycle	100 <sup>th</sup> cycle	
	Charge	Discharge	Charge	Discharge				
LVO-HNB400	2.83	2.50	2.97	2.48	0.33/0.49	249/219	211/177	85/81
LVA3O	2.79	2.53	2.90	2.50	0.26/0.40	215/194	189/182	88/94
LVA5O	2.78	2.54	2.90	2.54	0.24/0.36	256/231	219/205	86/88

To investigate the beneficial effect of minor aluminium substitution on battery performance of LVO-HNB400, it is important to have detailed understanding on the lithium insertion and extraction into LVO. As discussed by using CV scans of LVO in Section 4.1.7, the lithium insertion was initiated at ~2.72 V via the single phase reaction with lithium ions occupying empty tetrahedral sites. As shown by the extending galvanostatic discharging curves of pristine and aluminum substituted LVO-HNB400, there was a pseudo plateau extending from ~2.75 to 2.5 V (Figure 5-4(a)), which was in agreement with observation from CV scans. At this stage, ~1.5 moles of lithium ions were inserted into tetrahedral sites.[140, 152] This was then followed by a two-phase

transformation from  $\text{Li}_3\text{V}_3\text{O}_8$  to  $\text{Li}_4\text{V}_3\text{O}_8$  with the two phase coexisted, as reflected by the flat plateau at  $\sim 2.50$  V (Figure 5-4(a)).[140] The last stage at  $\sim 2.26$  V was attributed to complete formation of  $\text{Li}_4\text{V}_3\text{O}_8$  with all the lithium ions octahedrally coordinated. This process was accompanied with shortening of V-O bonds forming rocksalt structure constituting  $\text{VO}_6$  and  $\text{LiO}_6$  octahedral within the lattice. It was a slower kinetic transition compared to other reactions as it involved lithium diffusion through the grains of newly formed  $\text{Li}_4\text{V}_3\text{O}_8$  phase. Commonly, this two-phase transition is deemed to be a critical step which contributes to deteriorated cycling as reported in many studies. As this process requires partial displacement of lithium ions and alteration of V-O bonds, it is usually accompanied with structural collapse which leads to irreversible electrochemical activity in long term cycling.[68, 81]

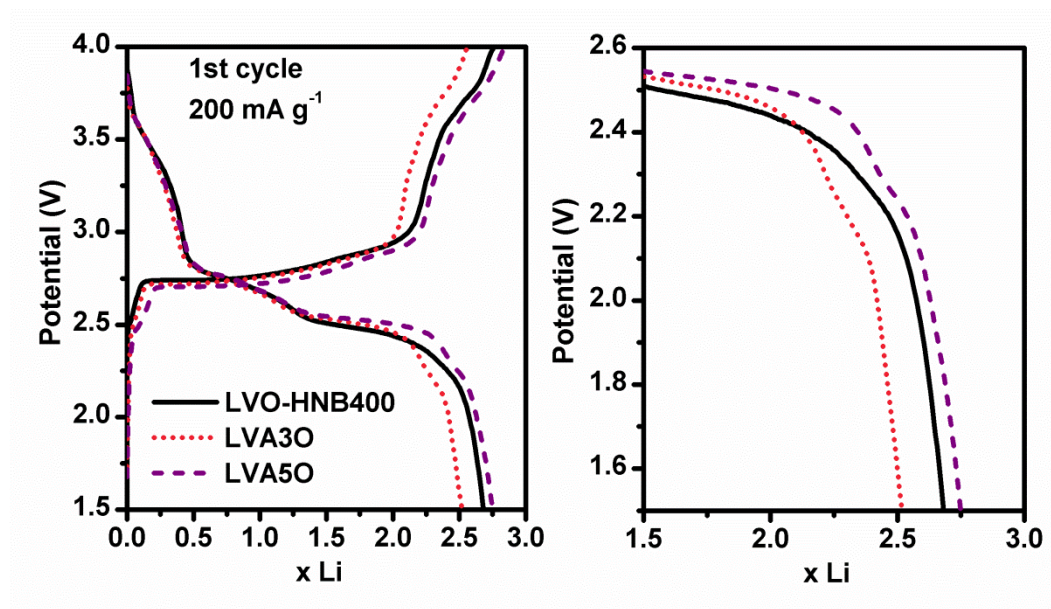


**Figure 5-4** (a) First galvanostatic profiles of pristine LVO, LVA3O and LVA5O at current density of  $200 \text{ mA g}^{-1}$ , (b) Magnified view within potential range of 1.5-1.6 V

As mentioned in Section 4.1.7, a distinct shoulder-like plateau could be observed between  $\sim 2.3$  V to  $2.1$  V in galvanostatic charging and discharging curves of LVA3O and LVA5O when they were cycled at  $200 \text{ mA g}^{-1}$  (Figure 5-4(b)). This behavior was well-aligned with the increment in intensity of the redox peak at  $\sim 2.26$  V (cathodic) and  $\sim 2.55$  V (anodic) in CV scans of LVA3O and LVA5O compared to that of pristine LVO-HNB400 (Section 4.1.7). This shoulder-like plateau was not distinctive in galvanostatic profile of pristine LVO-HNB400, instead a smearing-down curve could be observed. This was

possibly because the electrochemical behavior at  $\sim 2.26$  V was less reactive for pristine LVO-HNB400 compared to LVA3O and LVA5O.

In this study, by performing minor substitution of vanadium by aluminum atoms in LVO-HNB400, the distinguishable shoulder-like plateau indicates higher reactivity of this process in LVA3O and LVA5O compared to pristine LVO-HNB400. This indicates that the structural collapse was possibly circumvented by underpinning of the layered structure by foreign aluminum atoms which were not involved in electrochemical reactions. This was well-supported by the lower polarization observed for aluminum substituted LVO-HNB400, indicating better reversibility of electrochemical reactions (Table 5-3). Similar benefits of structural underpinning of lattice structure by minor substitution with alien atoms had been reported in many studies.[24, 211]

However, the overall capacities achieved by LVA3O were lower than the pristine LVO-HNB400 while higher capacities were exhibited by higher aluminum content in LVA5O. This was because the aluminum content in LVA3O was sufficient to pin the layered structure during the phase transition but yet to contribute additional advantage as observed in LVA5O with higher amount of aluminum. This additional advantage could be well illustrated by relating to the FTIR analysis (Figure 4-15) as shown in Section 4.1.6.

According to crystallography analysis by Wadsley[212], most the lithium ions shall reside at the octahedral sites, with the neighboring oxygen ions of  $\text{VO}_6$  units, in the lattice of  $\text{Li}_{1+x}\text{V}_3\text{O}_8$ . If this is the case, three types of  $\text{V}=\text{O}$  bonds with respective bond lengths can be differentiated within the lattice, with the intensity ratios of 1: 1: 1 as evaluated theoretically.[213] As shown in Table 5-4 of the list of intensity ratios for all the LVO samples presented in this thesis, all the ratios were deviated from the theoretical ratios of 1: 1: 1. These deviations could be observed in many reported studies[72, 130] for LVO compounds. Wadsley[212] had specified in his work that the lithium ions are capable to reside in octahedral and tetrahedral sites within the  $\text{Li}_{1+x}\text{V}_3\text{O}_8$  ( $x < 1.0$ ) crystal lattice due to its small size. The deviations of the intensity ratios from the theoretical value are caused by the inconsistent occupation of lithium ions between octahedral and tetrahedral sites.[133] This in turns affects the uniformity of  $\text{V}=\text{O}$  bonds which has strong interaction with the lithium layers. If the lithium ions which should be residing at the octahedral sites occupy the neighboring tetrahedral sites, this is undetectable by x-ray diffraction,[212] but this can be indirectly postulated from IR spectroscopy.

Ideally, it is more favorable for the lithium ions to be resided in octahedral sites in the as-synthesized compound. According to Hong *et al.*[214], positioning of lithium ions into octahedral sites for original lattice reduces the number of  $sp^3$  oxygen orbital available for bonding with incoming lithium ions. Hence, the interaction between incoming lithium and oxygen will be sufficiently weak to be displaced during the phase transition from  $Li_{1+x}V_3O_8$  to  $Li_4V_3O_8$ . This is a primary consideration as the lithium ions inserted should occupy at the correct sites for them to be displaced and facilitate the phase transformation so that more lithium ions can be intercalated, leads to complete formation of  $Li_4V_3O_8$ . [119]

As aluminum was being introduced into the lattice, V-O-V bonds would be interrupted as shown by the small band shift mentioned earlier and V=O groups may be affected as well. Possibly, this may strengthen the affinity of the lithium ions going into octahedral sites due to their interactions with the three V=O groups. Therefore, the intensity ratios of the peaks attributed to V=O bonds were becoming closer to the theoretical ratios of 1: 1: 1 as the amount of aluminum increased from  $x = 0.03$  to  $x = 0.05$  replacing vanadium in LVO-HNB400, which is from 1.5: 1.2: 1.0 to 1.3: 1.2: 1.0.

**Table 5-4** The V=O stretching frequencies for all LVO samples and their relative intensities

Samples	Wavenumber, $\nu$ ( $cm^{-1}$ )	Relative intensity
LVO-NP300	1000	2.0
	972	1.3
	956	1.0
LVO-NP400	1000	1.9
	972	1.3
	956	1.0
LVO-NP500	999	1.5
	972	1.1
	956	1.0
LVO-HNB400	1000	2.1
	971	1.3
	957	1.0
LVO-SNB500	999	1.6

	971	1.3
	957	1.0
LVA3O	1000	1.5
	970	1.2
	957	1.0
LVA5O	1000	1.3
	971	1.2
	956	1.0

By looking into the galvanostatic discharging/charging profiles of LVA3O and LVA5O at current density of  $200 \text{ mA g}^{-1}$ , the flat plateau at  $\sim 2.5 \text{ V}$ , just before the shoulder-like plateau was shorter for LVA3O (Figure 5-4(b)). It was extended until  $\sim 2.5 \text{ Li}$  for LVA5O compared to  $\sim 2.25 \text{ Li}$  for LVA3O. This indicates that less lithium ions were being inserted into LVA3O, which supports that some of the lithium ions may occupy sites with higher energy barrier which are more difficult to be displaced to induce the two-phase structural transition.

It is harder to justify how much lithium ions have been inserted into pristine LVO-HNB400 during this two-phase transition as this reaction was overlapped with the formation of  $\text{Li}_4\text{V}_3\text{O}_8$  as represented by a pseudo plateau which was rapidly smearing downwards. However, the lower capacity exhibited by LVA3O than pristine LVO-HNB400 was possibly due to higher degree of long-range ordering as the  $\text{VO}_n$  polyhedral layer was stabilized by aluminum atoms.[134]

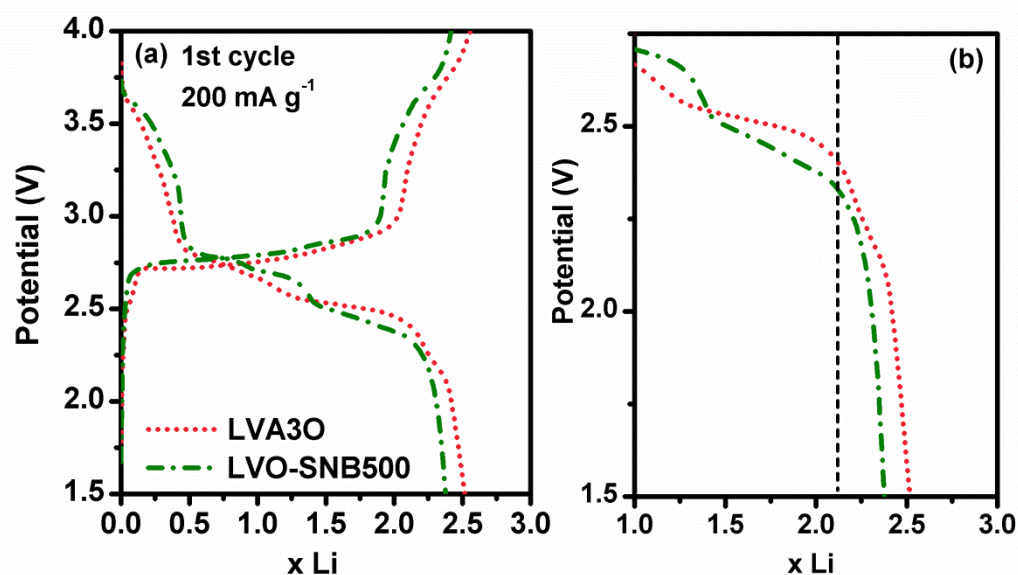


**Figure 5-5** (a) First galvanostatic curve of LVA3O and LVO-SNB500 at current density of 200 mA g<sup>-1</sup>, (b) magnified view within potential range of 1.5- 2.75 V.

Similarly, by comparing the galvanostatic curve of LVA3O and LVO-SNB500, the lengths of the flat plateau at ~2.5 V were almost identical. This was well-aligned with the explanation based on FTIR analysis provided earlier. LVA3O (1.5: 1.2: 1.0) and LVO-SNB500 (1.6: 1.3: 1.0) exhibited almost identical intensity ratio for V=O bonds, indicating similar irregularity of lithium sites occupation within the lattice. This supports the observation of similar lithium content being inserted during the two-phase transformation at ~2.5 V. This further verifies the additional advantage possessed by LVA5O in inducing the proper positioning of lithium ions into octahedral sites within the original lattice.

The cycling stability of LVA3O was better than that of pristine LVO-HNB400 and LVA5O even at high current density of 600 mA g<sup>-1</sup>. As the amount of lithium ion inserted for LVA3O was only ~2.0 Li when tested at high current density (Figure 5-6(a)), this only leads to formation of Li<sub>3</sub>V<sub>3</sub>O<sub>8</sub>. Hence, the electrochemical reaction only involved single-phase transformation constituting the lithium ion insertion into available tetrahedral sites without the occurrence of two-phase transition. This was well supported by the absence of another pseudo plateau after ~2.3 V for LVA3O (Figure 5-6(b)). The superior cycling stability of ~94% was possibly due to excellent reversibility of single-phase transition behavior at high current density. Eventhough the cycling stability of LVA5O was almost similar to that of pristine LVO-HNB400 when they are cycled at 200 mA g<sup>-1</sup>, larger improvement had been exhibited at higher current density of 600 mA g<sup>-1</sup> (Table 5-3). As



two-phase transition was involved for both pristine LVO-HNB400 and LVA50, the beneficial effect of structural underpinning by aluminum was more evident as structural destruction of LVO-HNB400 were more severe when cycled at high current density. Hence, the capacity deterioration of pristine LVO-HNB400 could be observed to be the worse among all of them (Table 5-3).

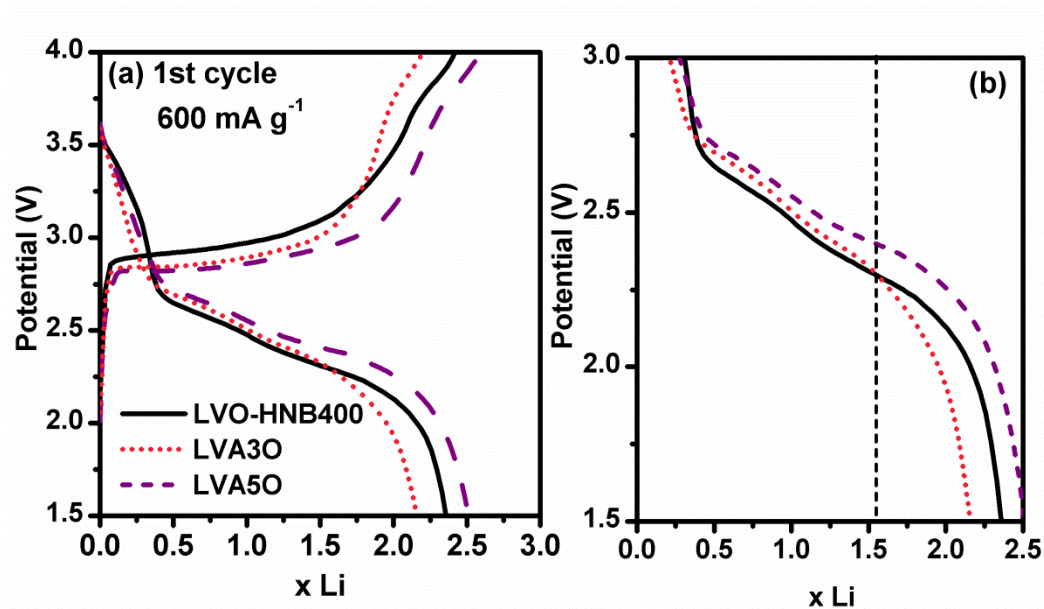


**Figure 5-6** (a) First galvanostatic profiles of LVO-HNB400, LVA3O and LVA5O at current density of 500 mA g<sup>-1</sup>, (b) Magnified view within potential range of 1.5-3.0 V.

In summary, minor aluminum substitution into vanadium sites of LVO-HNB400 was able to contribute better capacity retention by imposing interlayer “pinning” effect during two-phase transformation which was often associated by structural destruction during lithium insertion and extraction. Better electrochemical reversibility had been exhibited as supported by lower polarization between charging and discharging. If the amount of aluminum was optimized sufficiently, this would facilitate the proper occupation of lithium into octahedral sites within original lattice. This would further improve the overall capacities due to less hindrance to incoming lithium ions during two-phase transition.

### 5.2.2 Substitution at lithium sites of Li<sub>1.2</sub>V<sub>3</sub>O<sub>8</sub>

As mentioned in Section 4.1.10, full substitution of lithium ions (0.76 Å) in LVO with larger sodium ions (1.02 Å)[157] had been conducted to investigate its impact on battery performance. The effect of morphology on electrochemical properties of both LVO and

NVO had been conducted respectively. Discussions about better electrochemical performance contributed by 1D nanobelt over 0D nanoparticles had been provided in Section 5.1.2.

Upon investigation on influence of full substitution of sodium in LVO, another interesting finding were obtained. Other than the nanostructuring effect, the crystallinity of LVO and NVO constituting the regularity of atomic arrangement also plays a vital role in influencing the battery performance. This section will first cover the general comparison of electrochemical behavior between LVO and NVO followed by discussion on the effect of crystallinity on their battery performance.

### 5.2.2.1 General comparison between $\text{Li}_{1.2}\text{V}_3\text{O}_8$ and $\text{Na}_{1.2}\text{V}_3\text{O}_8$

Figure 5-7 shows the comparison of electrochemical behaviour of LVO-HNB and NVO-SNB. LVO-HNB400 had exhibited higher specific capacities than that of LVO-SNB500 due to structural characteristic (Section 5.2.2.2), hence LVO-HNB400 was chosen for comparison purpose. In the case of NVO, due to existence of exposed facet which provides facile channels for lithium diffusion, hierarchical configurations of nanobelts (NVO-HNB) was not beneficial due to overlapped active sites for lithium insertion and extraction, which leads to capacity deterioration.

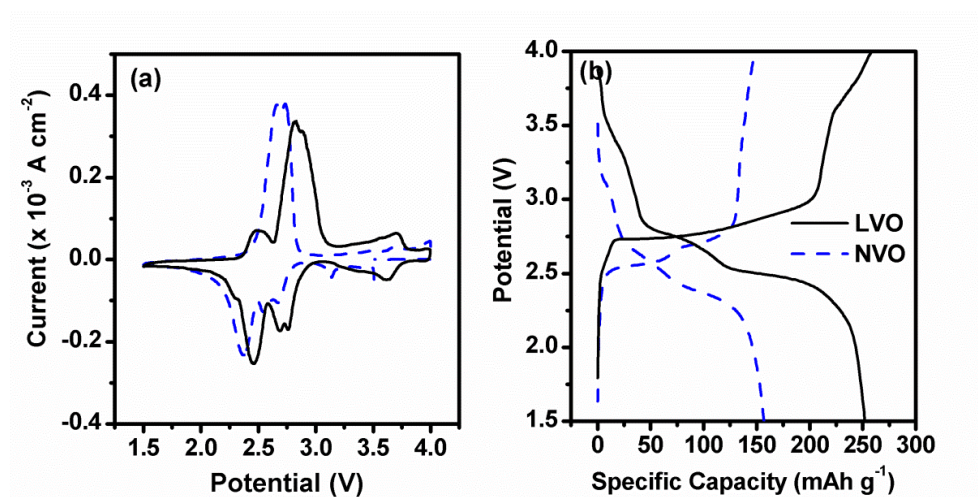


**Figure 5-7** Comparison between electrochemical behaviour of LVO-HNB400 and NVO-SNB by (a) CV scans at  $0.1 \text{ mV s}^{-1}$  and (b) galvanostatic cycling at current density of  $200 \text{ mA g}^{-1}$ .



**Table 5-5** Comparison between battery performance of LVO-HNB and NVO-SNB

Sample	Working potential (V)	Current density (mA g <sup>-1</sup> )	Capacity (no. of lithium ions)		
			1st cycle	40th cycle	100th cycle
<b>LVO-HNB400</b>	~3.0	200	262 (2.8)	239 (2.5)	215 (2.3)
<b>NVO-SNB</b>	~2.8	200	157 (1.8)	204 (2.3)	196 (2.3)

Generally, the electrochemical activities of both LVO and NVO involved multi-step lithium insertion and extraction as presented by several redox peaks in CV scans and multiple plateaus in galvanostatic profiles (Figure 5-4). The main difference between the CV scan of LVO-HNB400 and NVO-SNB was the appearance of shallow cathodic peak at ~2.26 V and its coupled peak pair at ~2.50 V in anodic sweep. This coupled peak pair is associated with the phase transition leading to formation of  $\text{Li}_4\text{V}_3\text{O}_8$  (Section 5.2.1). For NVO-SNB, there is no appearance of these peaks, indicating the absence of this two-phase transformation though both of the compounds are isostructural.[160]

Table 5-5 summaries the general comparisons between the electrochemical performances of LVO-HNB and NVO-SNB. In overall, the specific capacities of LVO-HNB were higher than that of NVO-SNB. The larger interlayer spacing contributed by substitution of sodium at lithium sites of LVO did not enhance overall capacities. This is because the diffusivity of lithium within NVO is still similar to that in LVO though with larger interlayer distance.[161] According to the galvanostatic results, the practical energy density achievable by LVO was ~786 Wh kg<sup>-1</sup> whereas for NVO was ~571 Wh kg<sup>-1</sup>. However, it would be interesting to study the lithium intercalation mechanism of NVO since its electrochemical reactions are distinguishable from LVO which involves the additional step of phase transition. Further discussions including structural evolution of NVO upon lithium insertion and extraction will be presented in Section 5.3.1.

### 5.2.2.2 Effect of crystallinity on electrochemical behavior of $\text{Li}_{1.2}\text{V}_3\text{O}_8$ and $\text{Na}_{1.2}\text{V}_3\text{O}_8$

Lithium insertion and extraction into ordered rocksalt-based LVO and NVO relies on the facile lithium diffusion path within the lattice. The atomic regularity and structural flexibility are to be at optimum condition to minimize the hindrance to incoming lithium ions due to electrostatic repulsion with pre-existing lithium in the lattice. The effect of crystallinity on electrochemical performance of LVO and NVO will be discussed in depth on the basis of FTIR analysis and battery performance in this section.

Table 5-6 lists the stretching frequencies of V-O-V bonds for all LVO and NVO synthesized in this thesis. By comparing the asymmetric frequencies of V-O-V bonds of all the LVO samples, they did not differ much with each other. However, the symmetric stretching frequencies between them showed more distinct band shift from each other,  $\sim 20\text{-}30\text{ cm}^{-1}$  according to sintering conditions as mentioned earlier. Both of these V-O-V vibration modes are related to stretching of V-O-V chains which lengthen along c-axis, majorly constituting  $\text{VO}_n$  polyhedra (Figure 5-8).[173] As the sintering temperature increases, higher energy is supplied for formation of more rigid arrangement of the structural framework. As the V-O-V symmetric vibration mode is shifted to lower wavenumber, this indicates higher degree of long-range ordering within the structure.[131]

The degree of long-range ordering affects the structural rearrangement during lithium insertion process. Less degree of long-range ordering may be beneficial in enabling high lithium mobility through the lithium layers due to flexibility of adjacent V-O units. If the long-range ordering is restricted to some extent, the adjacent units are able to expand the layers accordingly to balance off the contraction caused by electrostatic repulsion between incoming lithium and pre-existing lithium or sodium ions.

**Table 5-6** The V-O-V asymmetric and symmetric stretching frequencies for all LVO and NVO samples and their electrochemical performance.

Sample	Wavenumber, $\nu\text{ (cm}^{-1}\text{)}$		Specific capacity		Capacity retention (%)
	V-O-V asymmetric	V-O-V symmetric	1 <sup>st</sup> cycle	100 <sup>th</sup> cycle	
<b>LVO-NP300</b>	746	542-605	320	50	15
<b>LVO-NP400</b>	755	604	256	125	49
<b>LVO-NP500</b>	750	585	216	171	79

<b>LVO-HNB400</b>	753	603	249	211	82
<b>LVO-SNB500</b>	755	577	221	197	84
<b>NVO-NP400</b>	764	583	179	39	22
<b>NVO-NP500</b>	764	550	132	81	61
<b>NVO-HNB</b>	769	571	162	173	~100
<b>NVO-SNB</b>	762	553	157	196	~100

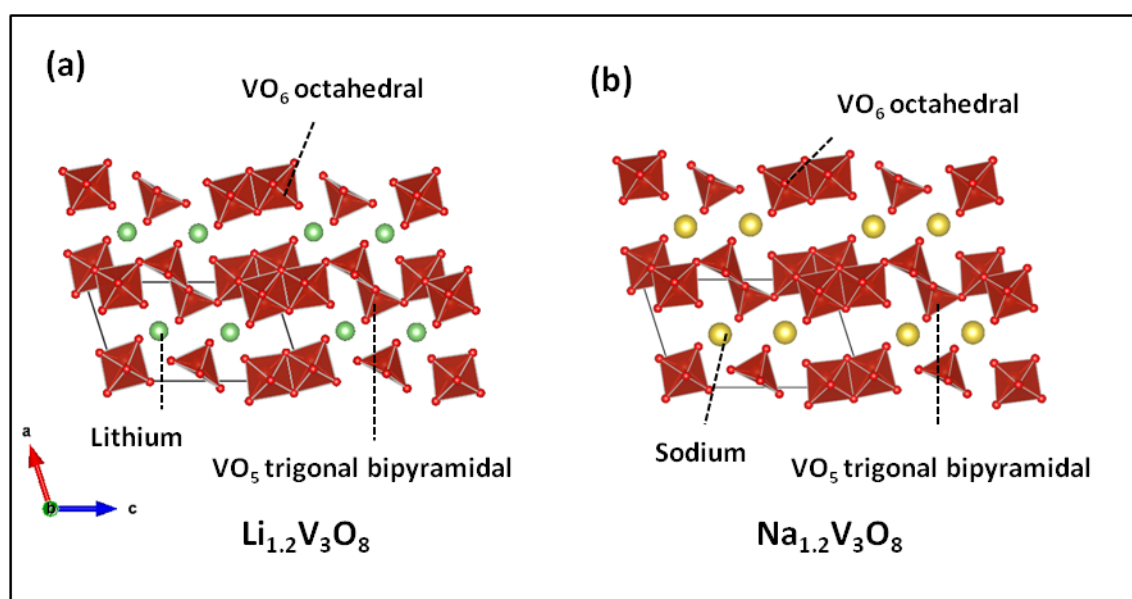


**Figure 5-8** Crystal structure of (a)  $\text{Li}_{1.2}\text{V}_3\text{O}_8$  and (b)  $\text{Na}_{1.2}\text{V}_3\text{O}_8$

By comparing LVO-NP400 ( $604\text{ cm}^{-1}$ ) and LVO-HNB400 ( $603\text{ cm}^{-1}$ ), their V-O-V symmetric stretching frequencies were almost identical. Similarly, the stretching frequencies for LVO-NP500 ( $585\text{ cm}^{-1}$ ) and LVO-SNB500 ( $575\text{ cm}^{-1}$ ) were closed to each other due to same sintering temperature. Hence, it could be deduced that the degree of long-range ordering for LVO-NP400 is similar to that of LVO-HNB400, and sufficiently flexible to enable facile lithium mobility as reflected by similar initial capacity achieved by both of them. However, the cycling stability of LVO-NP400 was hampered by side reactions with electrolyte (Section 5.1.1). This issue associated with particle size had been resolved by producing 1D nanobelts, as supported by the better capacity retention achieved by LVO-HNB400. On the contrary, LVO-NP500 and LVO-SNB500 constitutes more long-range ordering contains more rigid structure. The framework is less flexible to enable more lithium intercalation due to low diffusivity but

robust enough to reduce structural destruction induced by two-phase transition as discussed earlier. Hence, lower overall capacities but slightly better capacity retention was achieved by LVO-NP500 and LVO-SNB500 compared to LVO-NP400 and LVO-HNB400 respectively. In order to retain the optimum degree of long-range ordering for LVO-HNB400, better cycling stability with higher capacities were achieved by minor aluminium substitution as discussed in Section 5.2.1.

On contrary, for NVO to achieve better battery performance in terms of capacity and cyclability, more degree of long-range ordering is advantageous. This was reflected in better cycling stability achieved by NVO-NP500 ( $550\text{ cm}^{-1}$ ) and NVO-SNB ( $553\text{ cm}^{-1}$ ) with lower V-O-V symmetric stretching frequencies than NVO-NP400 ( $583\text{ cm}^{-1}$ ) and NVO-HNB ( $571\text{ cm}^{-1}$ ). The long-range ordering in NVO-NP500 and NVO-SNB is sufficiently high for the sodium ions to act as a pillar in the interlayer, but not a hindrance to lithium mobility. Less degree of ordering in NVO-NP400 and NVO-HNB leads to deteriorated battery performance due to obstruction of smooth lithium diffusion by sodium ions in the lattice.[163] For NVO-NP500, lower capacities achieved were due to larger particles resulted in longer distance for lithium movement into the lattice (Figure 4-20). Improvement in electrochemical performance of NVO was achieved by nanostructuring strategy. NVO-HNB and NVO-SNB with exposed (020) facet which enabled facile lithium diffusion had been prepared (Section 4.1.11). Enhancement of electrochemical performance was achieved by NVO-SNB due to preferred crystal orientation providing smooth and fast lithium transportation pathway (Section 4.1.12).

## 5.3 Lithium intercalation/deintercalation mechanism into rocksalt structure

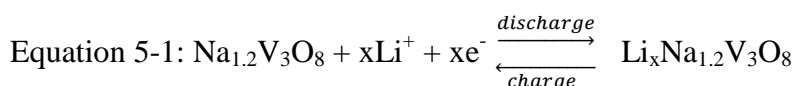
This section covers the discussion on structural changes during lithium intercalation and extraction process, by using *ex situ* XRD characterization technique.

### 5.3.1 Structural evolution study of $\text{Na}_{1.2}\text{V}_3\text{O}_8$ nanobelts

To further investigate the lithium ions insertion and extraction mechanism, *ex situ* XRD was performed on the cycled NVO-SNB electrode (Figure 5-9). When the NVO-SNB was discharged to different states of charge, the lattice parameter was expected to expand upon lithium insertion due to electrostatic repulsion of the incoming lithium ions and

sodium ions within the lattice; this shall be accompanied with shifting of the diffraction peaks to lower  $2\theta$  direction. When NVO-SNB was discharged, the diffraction peak of (100) was observed to be first shifted to higher value then to lower value followed by returning closed to initial state (Figure 5-9(a)). The effect of strong interaction due to formation of bonding between inserted lithium ions and oxygen ions from  $\text{VO}_n$  polyhedral forming the layers has overcome the electrostatic repulsion between the lithium and sodium ions. This leads to shrinkage of the interlayer as observed in the shift of diffraction peak (100) (Figure 5-9(a)) and (200) (Figure 5-9(c)) during discharging. On the other hand, a reverse trend of peak shifting was observed at the peak of  $(10\bar{4})$  (Figure 5-9(c)). The shrinkage of the interlayer spacing along  $a$ -axis has leads to slight expansion along the  $c$ -axis due to distortion of the lattice. This is similar to the structural changes as observed in previous studies[145, 152, 161, 215] on  $\text{Li}_{1+x}\text{V}_3\text{O}_8$ .

As in the case of  $\text{Li}_{1+x}\text{V}_3\text{O}_8$ , the capacity deterioration is associated with structural instability due to irreversible phase transition during lithium insertion and extraction.[148, 149, 174] In the *ex situ* XRD pattern (Figure 5-9), no new phase formation was observed for NVO-SNB other than broadening and shifting of diffraction peaks. This indicates balanced expansion and shrinkage was occurred within the unit cell to accommodate the lithium insertion into NVO lattice upon discharging and charging. The sodium ions within the lattice act as pillars to accommodate the lithium insertion and extraction according to the equation as shown:



By comparing the CV curves (Figure 4-32) of first and subsequent cycles, additional peaks were observed at  $\sim 3.25$  V during anodic sweep in subsequent cycles and the intensity of most of the redox peaks had increased. Similar incident of capacity increment during initial stage had been reported for layered structured materials.[91, 162, 215] During the first cycle, the shrinkage of interlayer due to sudden influx of lithium ions possibly reduces the amount of lithium ions can be intercalated into NVO. After structural reorganization in a few subsequent cycles, migration of sodium ions within the framework may be generated within a small extent, sufficient enough to relax the interlayer as to facilitate the formation of more facile lithium diffusion route so that more incoming lithium can be inserted.

NVO-SNB is capable to maintain the structural integrity with the sodium ions as the pillars connecting the interlayer, preventing collapse of the framework. This aligns with

the previous study by Pasquali *et al.*[158] In their work, they had ruled out the possibility of lattice damage due to sodium deposition upon lithium intercalation as the amount of sodium ions could be removed was only  $0.02 \text{ mol}^{-1}$  within the potential range of 3.8 to 4.5 V by over-charging NVO electrodes. Ion exchange between incoming lithium and sodium ions in the parent lattice is unlikely to occur.

Hence, this explains the better cycling retention achieved by NVO-SNB as compared to other vanadium based oxides as cathode materials for LIBs. For example,  $\text{V}_2\text{O}_5$  suffers from amorphization upon prolonged cycling due to destruction of the primary structural framework which leads to poor cycling stability.[216] Although  $\text{Li}_{1+x}\text{V}_3\text{O}_8$  possesses better cycling stability than  $\text{V}_2\text{O}_5$ , its electrochemical performance is usually hampered by lithium ion trapping[148, 174] and detrimental side reactions with electrolyte[82]. This issue had been resolved in this thesis by tailoring the nanostructure and optimum ion substitution at the vanadium sites as discussed in Section 4.1.7. Furthermore, the observations in this section had supported that the presence of sodium ions in NVO is beneficial as a buffer to ease drastic changes in lattice structure while undergoing structural reorganization at the same time upon lithium insertion and extraction.

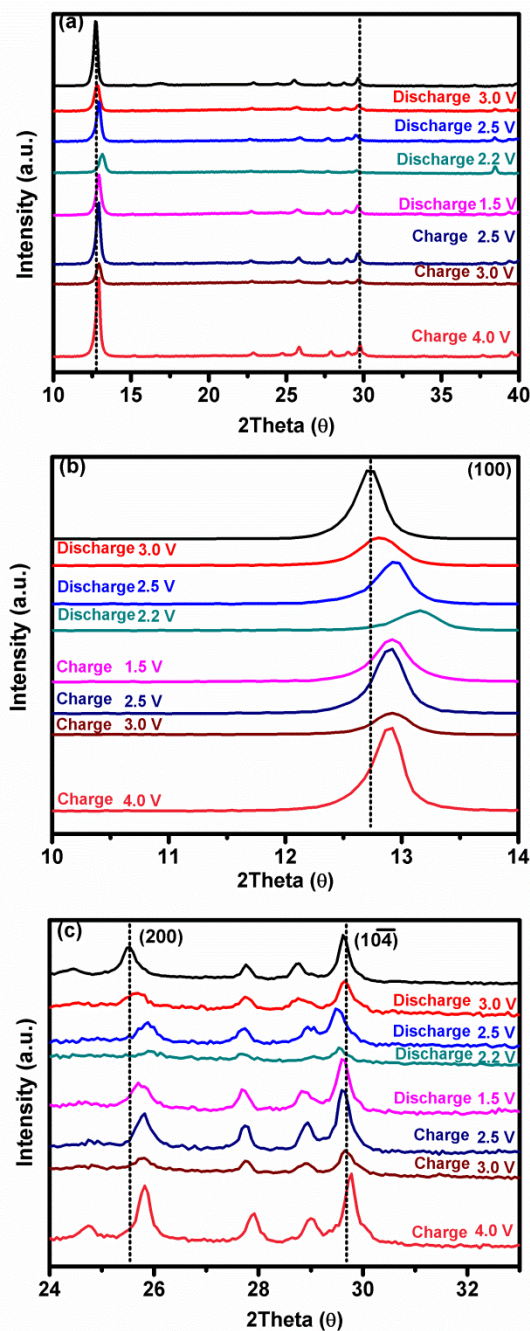


**Figure 5-9** The XRD pattern of NVO-SNB at different states of discharge and charge, (b) and (c) showing enlarged portion of partial XRD patterns.

### 5.3.2 Structural evolution study of $\text{Li}_2\text{NiTiO}_4$

Figure 5-10 shows the selected regions of *ex situ* XRD patterns of the cycled LNT-PO during charging and discharging. *Ex situ* XRD patterns were collected before and after each of the four plateaus (upper  $\sim 5.0$  V, lower 3.6 V, 2.0 V, and  $\sim 1.5$  V). From Figures 5-10(a) and (b), peak shifting due to changing lattice parameter as lithium ions are

extracted and reinserted can be observed. Significant peak broadening can be noted especially after charging to 5.0 V, indicating larger degree of disorder or electrode inhomogeneity, decrease in particle size, or increased strain.

From Figure 5-10(c), the 002 peak disappeared after charging and does not appear after discharge. This indicates that certain degree of cationic disorder had been introduced into the structure after lithium ion extraction, leading to gradual capacity fading, as mentioned in Section 4.2.4.

Table 5-7 presents the results of Rietveld refinement of the fresh and cycled electrodes. We shall expect shrinkage of all lattice parameter when lithium ions are extracted during charging. However, after charging to 5.0 V, there was volume expansion with  $a$  and  $c$ -parameter increased while  $b$ -parameter decreased upon lithium extraction, suggesting a structural change which is not simply due to lithium content. It was possibly due to initiation of cation mixing within the lattice, propagates gradually upon long term cycling.

The lattice parameter change was irreversible after discharge to 1.5 V. The volume change was ~2.4 %, considered to be much smaller compared to other ordered rocksalt-based cathodes which usually show larger volume change of ~9%.[217, 218] Excessive strain induced by large volume change is detrimental to battery performance as this will lead to microcracks between and within particles, prevents interparticles' charge transfer and eventually results in capacity fading. Furthermore, the operating voltage window of  $\text{Li}_2\text{NiTiO}_4$  (~4.3 V) was higher than  $\text{LiCoO}_2$  (~3.9 V). Hence,  $\text{Li}_2\text{NiTiO}_4$  had shown potential applicability as high energy density cathode in LIB.

**Table 5-7** Results of Rietveld refinement of the fresh and cycled electrodes.

States of charge	$a$ (Å)	$b$ (Å)	$c$ (Å)	$V$ (Å <sup>3</sup> )	Crystallite size (nm)
<b>Fresh</b>	5.076(1)	8.790(1)	9.731(1)	428.3(1)	5.7(3)
<b>Charge to 5.0 V</b>	5.263(1)	8.568(2)	9.804(2)	434.2(2)	4.0(2)
<b>Discharge to 3.6 V</b>	5.258(7)	8.721(9)	9.726(8)	439.0(8)	5.6(2)
<b>Discharge to 2.0 V</b>	5.260(2)	8.825(1)	9.535(2)	434.3(2)	5.4(5)
<b>Discharge to 1.5 V</b>	5.248(1)	8.828(9)	9.571(3)	435.6(2)	5.7(3)



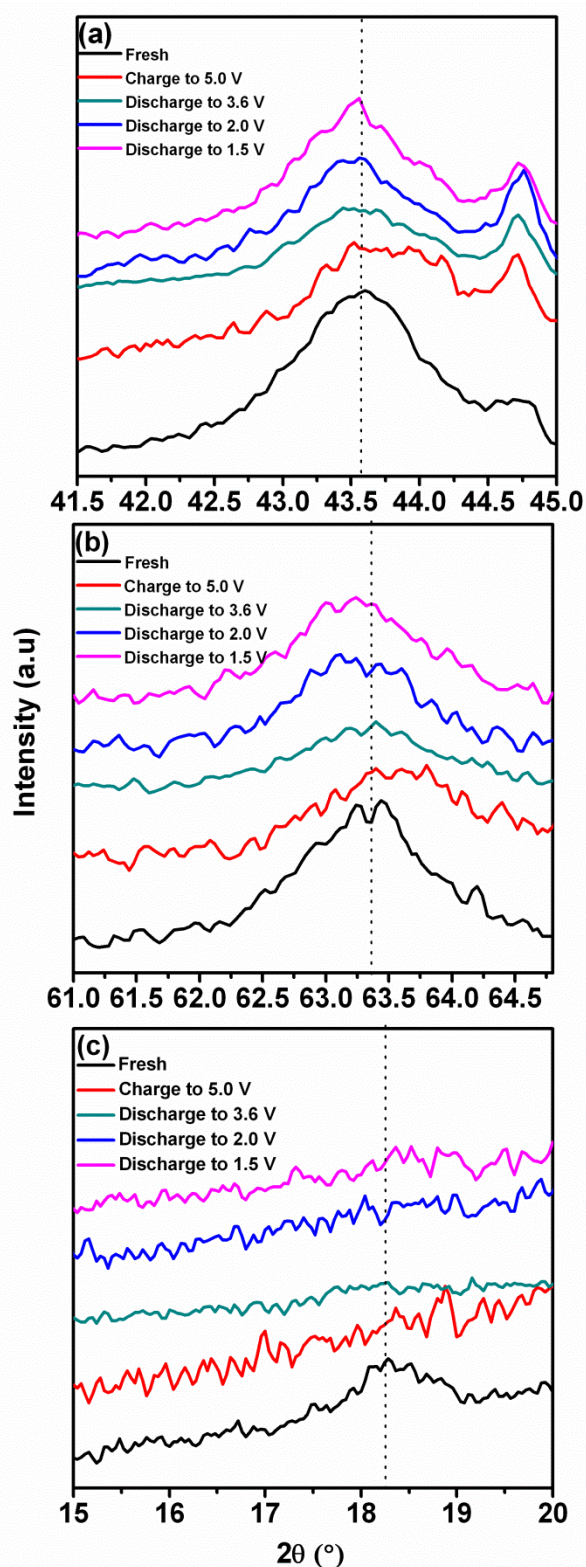


**Figure 5-10** Selected regions of ex situ XRD patterns for pristine  $\text{Li}_2\text{NiTiO}_4$  electrode materials during charging and discharging – (a)  $\bar{1}33$  peak; (b)  $312$  peak; (c)  $002$  peak. The  $002$  peak disappeared after charging and does not appear after discharge. This indicates that certain degree of cationic disorder had been introduced into the structure after lithium ion extraction.

## Chapter 6 Conclusion

This thesis presents detailed investigation on lithium intercalation into rocksalt structure with different degree of cation ordering. Besides, the applicability of nanostructured cathode materials is studied.

Synthesis methods such as electrospinning, HEBM and sol gel were employed to prepare lithium transition metal oxides with different morphologies and size distribution. Particle size distribution has to be optimized accordingly as to minimize undesired electrolytic reaction. By using  $\text{Li}_{1.2}\text{V}_3\text{O}_8$  nanoparticles as a subject of study, an optimum particle range of  $\sim 150$  nm were identified to be suitable in maximizing the applicability of nanomaterials as high performance cathodes. By extending the investigation on effect of nanostructuring from 0D nanoparticles to 1D nanobelt, the lithium diffusion kinetics of nanobelts is a few orders faster than nanoparticles which contribute to better battery performance by nanobelts. In this context, simple and versatile electrospinning method was employed to tailor the configuration of nanobelts (hierarchical or standalone) by altering the sintering condition. Primarily,  $\text{Li}_{1.2}\text{V}_3\text{O}_8$  hierarchical nanobelt and single nanobelt achieved high capacities of  $\sim 215$  mAh  $\text{g}^{-1}$  and  $\sim 195$  mAh  $\text{g}^{-1}$  respectively after 100 cycles, which were higher than their corresponding nanoparticles with capacities of 171 mAh  $\text{g}^{-1}$ . Similarly,  $\text{Na}_{1.2}\text{V}_3\text{O}_8$  hierarchical and single nanobelt exhibited capacity of  $\sim 173$  mAh  $\text{g}^{-1}$  and  $\sim 196$  mAh  $\text{g}^{-1}$  after 100 cycles respectively, which were also much higher than the corresponding nanoparticles with  $\sim 39$  mAh  $\text{g}^{-1}$ . Therefore, 1D nanobelts with high aspect ratio had outperformed 0D nanoparticles due to improved ionic and electronic conductivity. By downsizing only the thickness into lower range ( $\sim 20$ - $30$  nm) is advantageous in enhancing lithium diffusion kinetics, meanwhile the width ( $\sim 150$  nm) and length ( $\sim 1$   $\mu\text{m}$ ) are sustained within optimum size range to reduce electrolytic side reaction. The 1D configuration also enhances fast electron transfer in longitudinal direction compared to 0D nanoparticles in which charge transport is highly dependent on interparticle connectivity. In order to enhance the charge transfer between 0D nanoparticles, carbon coating had been employed on  $\text{Li}_2\text{NiTiO}_4$  with partially ordered structure. Carbon coated  $\text{Li}_2\text{NiTiO}_4$  achieved capacity of  $\sim 181$  mAh  $\text{g}^{-1}$ , which was higher

than the pristine  $\text{Li}_2\text{NiTiO}_4$  ( $\sim 161 \text{ mAh g}^{-1}$ ). The carbon coating enhances electronic conductivity by bringing the particles into close proximity as demonstrated by EIS study.

Generally, cathodes with ordered rocksalt structure are usually associated with structural collapse which leads to capacity fading. Therefore, the effectiveness of cation substitution on  $\text{Li}_{1.2}\text{V}_3\text{O}_8$  was testified in this thesis and its contributions to structural stability were proposed based on electrochemical and structural characterization. Although substitution of lithium ( $0.76 \text{ \AA}$ ) with larger sodium ion ( $1.02 \text{ \AA}$ ) [157] leads to larger interlayer spacing, this did not increase the specific capacities obtained. For  $\text{Na}_{1.2}\text{V}_3\text{O}_8$ , the capacities showed increasing trend followed by stabilization upon long term cycling. This is slightly different from the gradual decreasing trend observed for  $\text{Li}_{1.2}\text{V}_3\text{O}_8$ . *Ex situ* XRD characterization of cycled  $\text{Na}_{1.2}\text{V}_3\text{O}_8$  was carried out to understand the correlation between the increasing trend of capacities and structural evolution during lithium insertion and extraction. The lithium insertion mechanism was proposed to be associated with gradual relaxation of the lattice structure to accommodate incoming lithium insertion. The sodium ions act as pillars which support the framework, so that the structural integrity is preserved upon prolonged cycling. This was supported by the observations of balanced expansion and shrinkage of the lattice parameters at different states of charge/discharge. Besides, two-phase transition which is usually observed in  $\text{Li}_{1.2}\text{V}_3\text{O}_8$  does not applied to  $\text{Na}_{1.2}\text{V}_3\text{O}_8$ . This was further verified by no impurities formation observed in *ex situ* XRD study for  $\text{Na}_{1.2}\text{V}_3\text{O}_8$ .

Minor substitution of aluminum on vanadium sites of  $\text{Li}_{1.2}\text{V}_3\text{O}_8$  was proposed to tackle the core issue of structural collapse due to phase transformation during lithium insertion. Most reported works on cation substitution into  $\text{Li}_{1.2}\text{V}_3\text{O}_8$  involved replacement with cations of larger ionic radius to increase the interlayer spacing as to improve lithium diffusivity. This is the first report on enhancement of battery performance by substitution of vanadium ( $0.540 \text{ \AA}$ ) with aluminum ( $0.535 \text{ \AA}$ )[157] of similar ionic radius. The improvement in electrochemical performance with aluminum substitution was reflected by better cycling retention. By analyzing the electrochemical behavior of aluminum substituted sample and pristine sample, the effective role of aluminum in structural stabilization during two-phase transition was proposed. The major role of aluminum was served to ‘pin’ the interlayer during two-phase transition from  $\text{Li}_3\text{V}_3\text{O}_8$  to  $\text{Li}_4\text{V}_3\text{O}_8$ . As the amount of aluminum was further increased sufficiently, the regularity positioning of lithium ions into octahedral sites was facilitated. Due to elimination of hindrance to incoming lithium ions, higher capacities was achieved.

To investigate the lithium intercalation into disordered rocksalt structure,  $\text{Li}_2\text{NiTiO}_4$  with partially ordered and disordered structure were synthesized by a versatile and cost effective sol gel method. Better capacity retention was achieved by partially ordered structure with alternating lithium-rich and lithium-poor layers. This structural arrangement enable formation of lithium percolation network throughout the lattice, thus lithium diffusion is more feasible compared to disordered structure with random arrangement of lithium and transition metal octahedral. *Ex situ* XRD characterization was conducted on cycled  $\text{Li}_2\text{NiTiO}_4$  with partially ordered structure. A possible reason contributing to gradual capacity loss was due to transition from the partially ordered phase to disordered phase arose from introduction of higher degree of cation mixing after lithium extraction. Alteration from stoichiometric  $\text{Li}_2\text{NiTiO}_4$  to lithium excess compounds was attempted to investigate the possibility on improvement of battery performance. However, the lithium composition in as-synthesized  $\text{Li}_{2.4}\text{Ni}_{0.9}\text{Ti}_{0.95}\text{O}_4$  and  $\text{Li}_{3.2}\text{Ni}_{0.8}\text{Ti}_{0.8}\text{O}_4$  was possibly too “excess” which resulted in structural collapse after first discharge when most of the lithium was removed. The structural destruction was further aggravated by simultaneous oxygen release upon lithium extraction. Hence, the degree of cation disorder has to be optimized to enhance battery performance. Optimized extent of cation disorder is beneficial in imposing less mechanical strain upon lithium insertion and extraction. This was reflected by smaller volume change of ~2% in partially ordered  $\text{Li}_2\text{-NiTiO}_4$  compared to other ordered-rocksalt based materials as reported in literature.

## 6.1 Novel Contributions

Based on the studies conducted in this thesis, several scientific and technological contributions have been made and are summarized in the following sections.

### 6.1.1 Scientific contributions

- Synthesis of  $\text{AV}_3\text{O}_8$  (A = Li, Na) by using electrospinning method to fabricate nano-architected nanobelts (hierarchical and standalone) by altering the sintering conditions. High aspect ratio nanobelt with tunable dimensions enhanced electrochemical performance due to improved electronic and ionic conductivities.
- Investigation on the effect of particle size distribution and morphology on electrochemical behaviour upon lithium insertion and extraction.

- 
- Fundamental studies on cation substitution in  $\text{Li}_{1.2}\text{V}_3\text{O}_8$  and the impact on electrochemical characteristics.
  - Investigation on correlation between lithium storage behaviour and structural transformation of lithium transition metal oxide as cathode for LIBs
  - Exploration of lithium intercalation into disordered rocksalt structure and related study on influence of cation ordering on electrochemical properties

### 6.1.2 Technological significances

- Developed scalable sol gel technique to produce high voltage cathodes ( $\text{Li}_2\text{NiTiO}_4$ )
- Investigated methods to improve long term cycling performance of  $\text{Li}_2\text{NiTiO}_4$  and  $\text{AV}_3\text{O}_8$  ( $\text{A} = \text{Li}, \text{Na}$ ).

# Chapter 7 Recommendations for Future Works

Based on the work done in this thesis, the following future works are suggested to further develop a better commercial cathode to replace currently available  $\text{LiCoO}_2$  for LIB application.

## 7.1 Fundamental studies on structural evolution by *in situ* characterizations

In this thesis, the structural evolution of  $\text{Na}_{1.2}\text{V}_3\text{O}_8$  and  $\text{Li}_2\text{NiTiO}_4$  was studied using *ex situ* XRD characterization. The electrodes were cycled at different states of charge and collected for *ex situ* characterization. There may be uncertainties arose due to delay in retrieving the structural information from the cycled electrodes. Hence, the further understanding of real time reaction between lithium ions and lithium transition metal oxides are restricted. It will be beneficial to investigate the correlation between reaction mechanism and structural changes by using *in situ* XRD characterization.

The investigation on the effect of aluminium substitution in  $\text{Li}_{1.2}\text{V}_3\text{O}_8$  was conducted on the basis of their electrochemical characteristics supported with FTIR characterization. Eventhough the influence of aluminium substitution on electrochemical properties can be indirectly postulated from the experimental observations; it will be interesting to utilize real time measurements of its structural properties to obtain more insights about the reaction mechanism. By combining *in situ* FTIR characterization with x-ray absorption near edge structure spectroscopy (XANES), it will be possible to obtain more information regarding the local structural modification. As the lithium sites of tetrahedral or octahedral positions are well characterized in different energy content, the positioning of lithium may change the bond length and geometrical arrangement of vanadium atoms which will be reflected in XANES spectra.

## 7.2 Exploration on mixed-metal solid solution derivative of $\text{Li}_2\text{Ni}_{1-x}\text{MTiO}_4$ ( $\text{M} = \text{Fe}, \text{Co}$ )

In present work, gradual capacity loss due to transition from partially ordered structure to disordered structure of  $\text{Li}_2\text{NiTiO}_4$  could be deduced from the observations of ex situ characterization studies.

Previous studies have shown that the electrochemical properties and safety of most nickel-based electrode materials are greatly influenced by the cation mixing of  $\text{Ni}^{2+}$  ions in the  $\text{Li}^+$  sites. This can occur due to experimental conditions during synthesis or cation migration during lithium extraction, forming disordered structure which affects the lithium ion transport pathway. In order to retain the partially ordered state, we propose exploration on substitution with other transition metal ions such as Fe or/and Co. This additional another transition metal ion within the lattice may be able to inhibit migration of nickel ions into lithium ions upon lithium removal. Therefore, the feasible percolation network for lithium transportation within the original lattice, imparts structural stabilization.

By substitution of Ni with Fe or/and Co, alteration of operating voltage windows is possible with changing voltage plateau. It is possible to increase the lower voltage limit which is around 1.5 V to higher value. Higher capacity is possible to be obtained within smaller voltage window. Moreover, the performance of mixed metal compounds with combination of two or three transition metal may demonstrate superiority compared to pure composition as proven in ordered rocksalt  $\text{LiMO}_2$  cathodes (e.g.  $\text{Li}(\text{Co}_{1/3}\text{Mn}_{1/3}\text{Ni}_{1/3})\text{O}_2$ ). [219]

## 7.3 Application in Full LIB

To validate the applicability of rocksalt-based  $\text{Li}_{1.2}\text{V}_3\text{O}_8$  and  $\text{Li}_2\text{NiTiO}_4$  in LIB, the as-synthesized materials can be assembled *versus* anode as LIB full cell. The research on full cell can include testing with various anode materials, including graphite,  $\text{Li}_4\text{Ti}_5\text{O}_{12}$ , *etc.* by taking into consideration of voltage range, electrochemical reversibility and optimization of mass ratio between cathode and anode. Besides, experiments on long term cycling and thermal stability of full cell applications accompanied with further improvement effort are required to ensure the materials' suitability in large scale applications.

# References

- [1] O. Ellabban, H. Abu-Rub, and F. Blaabjerg, "Renewable energy resources: Current status, future prospects and their enabling technology," *Renewable and Sustainable Energy Reviews*, vol. 39, pp. 748-764, 2014.
- [2] M. K. Nazeeruddin, E. Baranoff, and M. Grätzel, "Dye-sensitized solar cells: A brief overview," *Solar Energy*, vol. 85, pp. 1172-1178, 2011.
- [3] L. Lu, H. Yang, and J. Burnett, "Investigation on wind power potential on Hong Kong islands—an analysis of wind power and wind turbine characteristics," *Renewable Energy*, vol. 27, pp. 1-12, 2002.
- [4] Z. Gong and Y. Yang, "Recent advances in the research of polyanion-type cathode materials for Li-ion batteries," *Energy and Environmental Science*, vol. 4, pp. 3223-3242, 2011.
- [5] C. Rosenkranz, "Deep Cycle Batteries for Plug-in Hybrid Workshop," presented at the EVS-20 Plug-in Hybrid Workshop, Monaco, 2003.
- [6] M. M. Thackeray, C. Wolverton, and E. D. Isaacs, "Electrical energy storage for transportation—approaching the limits of, and going beyond, lithium-ion batteries," *Energy & Environmental Science*, vol. 5, pp. 7854-7863, 2012.
- [7] T. Nagaura and K. Tozawa, *Prog. Batteries Sol. Cells*, vol. 9, pp. 209-217, 1990.
- [8] V. Etacheri, R. Marom, R. Elazari, G. Salitra, and D. Aurbach, "Challenges in the development of advanced Li-ion batteries: A review," *Energy and Environmental Science*, vol. 4, pp. 3243-3262, 2011.
- [9] K. Mizushima, P. C. Jones, P. J. Wiseman, and J. B. Goodenough, " $\text{Li}_x\text{CoO}_2$  ( $0 < x < 1$ ): A new cathode material for batteries of high energy density," *Materials Research Bulletin*, vol. 15, pp. 783-789, 1980.
- [10] J. Choi and A. Manthiram, "Role of chemical and structural stabilities on the electrochemical properties of layered  $\text{LiNi}_{1/3}\text{Mn}_{1/3}\text{Co}_{1/3}\text{O}_2$  cathodes," *Journal of the Electrochemical Society*, vol. 152, pp. A1714-A1718, 2005.
- [11] F. Cheng and J. Chen, "Transition metal vanadium oxides and vanadate materials for lithium batteries," *Journal of Materials Chemistry*, vol. 21, pp. 9841-9848, 2011.
- [12] P. Kalyani and N. Kalaiselvi, "Various aspects of  $\text{LiNiO}_2$  chemistry: A review," *Science and Technology of Advanced Materials*, vol. 6, pp. 689-703, 2005.
- [13] E. S. Lee, K. W. Nam, E. Hu, and A. Manthiram, "Influence of cation ordering and lattice distortion on the charge-discharge behavior of  $\text{LiMn}_{1.5}\text{Ni}_{0.5}\text{O}_4$  Spinel between 5.0 and 2.0 V," *Chemistry of Materials*, vol. 24, pp. 3610-3620, 2012.
- [14] J. Lee, A. Urban, X. Li, D. Su, G. Hautier, and G. Ceder, "Unlocking the Potential of Cation-Disordered Oxides for Rechargeable Lithium Batteries," *Science*, vol. 343, pp. 519-522, 2014.
- [15] A. Urban, J. Lee, and G. Ceder, "The Configurational Space of Rocksalt-Type Oxides for High-Capacity Lithium Battery Electrodes," *Advanced Energy Materials*, pp. n/a-n/a, 2014.
- [16] M. Kůzma, R. Dominko, A. Meden, D. Makovec, M. Bele, J. Jamnik, and M. Gaberšček, "Electrochemical activity of  $\text{Li}_2\text{FeTiO}_4$  and  $\text{Li}_2\text{MnTiO}_4$  as potential active materials for Li ion batteries: A comparison with  $\text{Li}_2\text{NiTiO}_4$ ," *Journal of Power Sources*, vol. 189, pp. 81-88, 2009.
- [17] S. R. S. Prabakaran, M. S. Michael, H. Ikuta, Y. Uchimoto, and M. Wakihara, " $\text{Li}_2\text{NiTiO}_4$  - A new positive electrode for lithium batteries: Soft-chemistry synthesis and electrochemical characterization," *Solid State Ionics*, vol. 172, pp. 39-45, 2004.



- [18] M. Kuezma, R. Dominko, D. Hanžel, A. Kodre, I. Arčon, A. Meden, and M. Gaberšček, "Detailed in situ investigation of the electrochemical processes in  $\text{Li}_2\text{FeTiO}_4$  cathodes," *Journal of the Electrochemical Society*, vol. 156, pp. A809-A816, 2009.
- [19] L. Zhang, H. Noguchi, D. Li, T. Muta, X. Wang, M. Yoshio, and I. Taniguchi, "Synthesis and electrochemistry of cubic rocksalt Li-Ni-Ti-O compounds in the phase diagram of  $\text{LiNiO}_2$ - $\text{LiTiO}_2$ - $\text{Li}[\text{Li}_{1/3}\text{Ti}_{2/3}]\text{O}_2$ ," *Journal of Power Sources*, vol. 185, pp. 534-541, 2008.
- [20] K. T. Lee and J. Cho, "Roles of nanosize in lithium reactive nanomaterials for lithium ion batteries," *Nano Today*, vol. 6, pp. 28-41, 2011.
- [21] Z. Chen, Y. Qin, K. Amine, and Y. K. Sun, "Role of surface coating on cathode materials for lithium-ion batteries," *Journal of Materials Chemistry*, vol. 20, pp. 7606-7612, 2010.
- [22] A. Mauger and C. Julien, "Surface modifications of electrode materials for lithium-ion batteries: Status and trends," *Ionics*, vol. 20, pp. 751-787, 2014.
- [23] G. T. K. Fey, C. Z. Lu, J. D. Huang, T. P. Kumar, and Y. C. Chang, "Nanoparticulate coatings for enhanced cyclability of  $\text{LiCoO}_2$  cathodes," *Journal of Power Sources*, vol. 146, pp. 65-70, 2005.
- [24] T. E. Conry, A. Mehta, J. Cabana, and M. M. Doeff, "Structural Underpinnings of the Enhanced Cycling Stability upon Al-Substitution in  $\text{LiNi}_{0.45}\text{Mn}_{0.45}\text{Co}_{0.1-y}\text{Al}_y\text{O}_2$  Positive Electrode Materials for Li-ion Batteries," *Chemistry of Materials*, vol. 24, pp. 3307-3317, 2012/09/11 2012.
- [25] E.-S. Lee and A. Manthiram, "Influence of doping on the cation ordering and charge-discharge behavior of  $\text{LiMn}_{1.5}\text{Ni}_{0.5-x}\text{M}_x\text{O}_4$  ( $\text{M} = \text{Cr, Fe, Co, and Ga}$ ) spinels between 5.0 and 2.0 V," *Journal of Materials Chemistry A*, vol. 1, pp. 3118-3126, 2013.
- [26] C. R. Fell, "Structural Factors Affecting Lithium Transport in Lithium-excess Layered Cathode Materials," Doctor of Philosophy, University of Florida, Gainesville, 2012.
- [27] K. Ozawa, "Lithium-ion rechargeable batteries with  $\text{LiCoO}_2$  and carbon electrodes: the  $\text{LiCoO}_2/\text{C}$  system," *Solid State Ionics*, vol. 69, pp. 212-221, 1994.
- [28] M. B. Armand, "Intercalation electrode," *Materials for Advanced Batteries*, 1980.
- [29] P. Hagenmuller, "Intercalation chemistry and chemical bonding," *Journal of Power Sources*, vol. 90, pp. 9-12, 2000.
- [30] M. Broussely, P. Biensan, and B. Simon, "Lithium insertion into host materials: the key to success for Li ion batteries," *Electrochimica Acta*, vol. 45, pp. 3-22, 1999.
- [31] M. M. Thackeray, W. I. F. David, P. G. Bruce, and J. B. Goodenough, "Lithium insertion into manganese spinels," *Materials Research Bulletin*, vol. 18, pp. 461-472, 1983.
- [32] D. Aurbach, M. D. Levi, K. Gamulski, B. Markovsky, G. Salitra, E. Levi, U. Heider, L. Heider, and R. Oesten, "Capacity fading of  $\text{Li}_x\text{Mn}_2\text{O}_4$  spinel electrodes studied by XRD and electroanalytical techniques," *Journal of Power Sources*, vol. 81-82, pp. 472-479, 1999.
- [33] Y. Shin and A. Manthiram, "Factors Influencing the Capacity Fade of Spinel Lithium Manganese Oxides," *Journal of the Electrochemical Society*, vol. 151, pp. A204-A208, 2004.
- [34] Y. J. Lee, S. H. Park, C. Eng, J. B. Parise, and C. P. Grey, "Cation ordering and electrochemical properties of the cathode materials  $\text{LiZn}_x\text{Mn}_{2-x}\text{O}_4$ ,  $0 < x \leq 0.5$ : A 6Li magic-angle spinning NMR spectroscopy and diffraction study," *Chemistry of Materials*, vol. 14, pp. 194-205, 2002.
- [35] T. Ohzuku, S. Takeda, and M. Iwanaga, "Solid-state redox potentials for  $\text{Li}[\text{Me}_{1/2}\text{Mn}_{3/2}]\text{O}_4$  ( $\text{Me}$ : 3d-transition metal) having spinel-framework structures: A series of 5 volt materials for advanced lithium-ion batteries," *Journal of Power Sources*, vol. 81-82, pp. 90-94, 1999.
- [36] L. Hernán, J. Morales, L. Sánchez, and J. Santos, "Use of Li-M-Mn-O [ $\text{M} = \text{Co, Cr, Ti}$ ] spinels prepared by a sol-gel method as cathodes in high-voltage lithium batteries," *Solid State Ionics*, vol. 118, pp. 179-185, 1999.
- [37] J. H. Kim, S. T. Myung, C. S. Yoon, S. G. Kang, and Y. K. Sun, "Comparative Study of  $\text{LiNi}_{0.5}\text{Mn}_{1.5}\text{O}_{4-\delta}$  and  $\text{LiNi}_{0.5}\text{Mn}_{1.5}\text{O}_4$  Cathodes Having Two Crystallographic Structures:  $\text{Fd}3\text{m}$  and  $\text{P4 } 332$ ," *Chemistry of Materials*, vol. 16, pp. 906-914, 2004.

- 
- [38] K. Mizushima, P. C. Jones, P. J. Wiseman, and J. B. Goodenough, " $\text{Li}_x\text{CoO}_2$  ( $0 < x \leq 1$ ): A new cathode material for batteries of high energy density," *Materials Research Bulletin*, vol. 15, pp. 783-789, 1980.
  - [39] G. G. Amatucci, J. M. Tarascon, and L. C. Klein, " $\text{CoO}_2$ , the end member of the  $\text{Li}_x\text{CoO}_2$  solid solution," *Journal of the Electrochemical Society*, vol. 143, pp. 1114-1123, 1996.
  - [40] M. S. Whittingham, "The Role of Ternary Phases in Cathode Reactions," *Journal of the Electrochemical Society*, vol. 123, pp. 315-320, 1976.
  - [41] P. Y. Zavalij and M. S. Whittingham, "Structural chemistry of vanadium oxides with open frameworks," *Acta Crystallographica Section B*, vol. 55, pp. 627-663, 1999.
  - [42] D. W. Murphy, P. A. Christian, F. J. DiSalvo, and J. V. Waszczak, "Lithium incorporation by vanadium pentoxide," *Inorganic Chemistry*, vol. 18, pp. 2800-2803, 1979/10/01 1979.
  - [43] C. Delmas and H. Cognac-Auradou, "Formation of the  $\omega$ -type phase by lithium intercalation in (Mo, V) oxides deriving from  $\text{V}_2\text{O}_5$ ," *Journal of Power Sources*, vol. 54, pp. 406-410, 1995.
  - [44] C. K. Chan, H. Peng, R. D. Twisten, K. Jarausch, X. F. Zhang, and Y. Cui, "Fast, completely reversible Li insertion in vanadium pentoxide nanoribbons," *Nano Letters*, vol. 7, pp. 490-495, 2007.
  - [45] S. Jouanneau, A. Verbaere, and D. Guyomard, "A combined X-ray and neutron Rietveld study of the chemically lithiated electrode materials  $\text{Li}_{2.7}\text{V}_3\text{O}_8$  and  $\text{Li}_{4.8}\text{V}_3\text{O}_8$ ," *Journal of Solid State Chemistry*, vol. 178, pp. 22-27, 2005.
  - [46] J. Muster, G. T. Kim, V. Krstić, J. G. Park, Y. W. Park, S. Roth, and M. Burghard, "Electrical Transport Through Individual Vanadium Pentoxide Nanowires," *Advanced Materials*, vol. 12, pp. 420-424, 2000.
  - [47] R. Baddour-Hadjean, J. P. Pereira-Ramos, C. Navone, and M. Smirnov, "Raman Microspectrometry Study of Electrochemical Lithium Intercalation into Sputtered Crystalline  $\text{V}_2\text{O}_5$  Thin Films," *Chemistry of Materials*, vol. 20, pp. 1916-1923, 2008/03/01 2008.
  - [48] Y. Wang, K. Takahashi, K. H. Lee, and G. Z. Cao, "Nanostructured Vanadium Oxide Electrodes for Enhanced Lithium-Ion Intercalation," *Advanced Functional Materials*, vol. 16, pp. 1133-1144, 2006.
  - [49] Y. Wang and G. Cao, "Developments in Nanostructured Cathode Materials for High-Performance Lithium-Ion Batteries," *Advanced Materials*, vol. 20, pp. 2251-2269, 2008.
  - [50] A. Pan, J.-G. Zhang, Z. Nie, G. Cao, B. W. Arey, G. Li, S.-q. Liang, and J. Liu, "Facile synthesized nanorod structured vanadium pentoxide for high-rate lithium batteries," *Journal of Materials Chemistry*, vol. 20, pp. 9193-9199, 2010.
  - [51] K.-H. Kim, D.-K. Roh, I. Song, B.-C. Lee, and S.-H. Baeck, "Enhanced performance as a lithium-ion battery cathode of electrodeposited  $\text{V}_2\text{O}_5$  thin films by e-beam irradiation," *Journal of Solid State Electrochemistry*, vol. 14, pp. 1801-1805, 2010/10/01 2010.
  - [52] C. V. S. Reddy, S. A. Wicker, E. H. Walker, Q. L. Williams, and R. R. Kalluru, "Vanadium Oxide Nanorods for Li-Ion Battery Applications," *Journal of the Electrochemical Society*, vol. 155, pp. A599-A602, 2008.
  - [53] Y. Li, J. Yao, E. Uchaker, J. Yang, Y. Huang, M. Zhang, and G. Cao, "Leaf-Like  $\text{V}_2\text{O}_5$  Nanosheets Fabricated by a Facile Green Approach as High Energy Cathode Material for Lithium-Ion Batteries," *Advanced Energy Materials*, vol. 3, pp. 1171-1175, 2013.
  - [54] L. Mai, L. Xu, C. Han, X. Xu, Y. Luo, S. Zhao, and Y. Zhao, "Electrospun Ultralong Hierarchical Vanadium Oxide Nanowires with High Performance for Lithium Ion Batteries," *Nano Letters*, vol. 10, pp. 4750-4755, 2010/11/10 2010.
  - [55] Y. Wang, H. J. Zhang, K. W. Siah, C. C. Wong, J. Lin, and A. Borgna, "One pot synthesis of self-assembled  $\text{V}_2\text{O}_5$  nanobelt membrane/capsule-like hydrated precursor as improved cathode for Li-ion battery," *Journal of Materials Chemistry*, vol. 21, pp. 10336-10341, 2011.

- 
- [56] Y. L. Cheah, N. Gupta, S. S. Pramana, V. Aravindan, G. Wee, and M. Srinivasan, "Morphology, structure and electrochemical properties of single phase electrospun vanadium pentoxide nanofibers for lithium ion batteries," *Journal of Power Sources*, vol. 196, pp. 6465-6472, 2011.
- [57] S. Wang, Z. Lu, D. Wang, C. Li, C. Chen, and Y. Yin, "Porous monodisperse  $V_2O_5$  microspheres as cathode materials for lithium-ion batteries," *Journal of Materials Chemistry*, vol. 21, pp. 6365-6369, 2011.
- [58] Y. Tang, X. Rui, Y. Zhang, T. M. Lim, Z. Dong, H. H. Hng, X. Chen, Q. Yan, and Z. Chen, "Vanadium pentoxide cathode materials for high-performance lithium-ion batteries enabled by a hierarchical nanoflower structure via an electrochemical process," *Journal of Materials Chemistry A*, vol. 1, pp. 82-88, 2013.
- [59] A. Q. Pan, H. B. Wu, L. Zhang, and X. W. Lou, "Uniform  $V_2O_5$  nanosheet-assembled hollow microflowers with excellent lithium storage properties," *Energy & Environmental Science*, vol. 6, pp. 1476-1479, 2013.
- [60] A. Pan, J. Liu, J.-G. Zhang, G. Cao, W. Xu, Z. Nie, X. Jie, D. Choi, B. W. Arey, C. Wang, and S. Liang, "Template free synthesis of  $LiV_3O_8$  nanorods as a cathode material for high-rate secondary lithium batteries," *Journal of Materials Chemistry*, vol. 21, pp. 1153-1161, 2011.
- [61] T. J. Patey, S. H. Ng, R. Büchel, N. Tran, F. Krumeich, J. Wang, H. K. Liu, and P. Novák, "Electrochemistry of  $LiV_3O_8$  Nanoparticles Made by Flame Spray Pyrolysis," *Electrochemical and Solid-State Letters*, vol. 11, pp. A46-A50, 2008.
- [62] N. Tran, K. G. Bramnik, H. Hibst, J. Prölß, N. Mrona, M. Holzapfel, W. Scheifele, and P. Novák, "Spray-Drying Synthesis and Electrochemical Performance of Lithium Vanadates as Positive Electrode Materials for Lithium Batteries," *Journal of the Electrochemical Society*, vol. 155, pp. A384-A389, 2008.
- [63] M. Dubarry, J. Gaubicher, P. Moreau, and D. Guyomard, "Formation of  $Li_{1+x}V_3O_8$  /  $\beta$ - $Li_{1/3}V_2O_5$  / C Nanocomposites by Carboreduction and the Resulting Improvement in Li Capacity Retention," *Journal of the Electrochemical Society*, vol. 153, pp. A295-A300, 2006.
- [64] Y. Q. Qiao, J. P. Tu, X. L. Wang, J. Zhang, Y. X. Yu, and C. D. Gu, "Self-assembled synthesis of hierarchical waferlike porous Li-V-O composites as cathode materials for lithium ion batteries," *Journal of Physical Chemistry C*, vol. 115, pp. 25508-25518, 2011.
- [65] D. Sun, G. Jin, H. Wang, X. Huang, Y. Ren, J. Jiang, H. He, and Y. Tang, " $Li_xV_2O_5/LiV_3O_8$  nanoflakes with significantly improved electrochemical performance for Li-ion batteries," *Journal of Materials Chemistry A*, vol. 2, pp. 8009-8016, 2014.
- [66] Y. Zhou, H.-F. Yue, X.-Y. Zhang, and X.-Y. Deng, "Preparation and characterization of  $LiV_3O_8$  cathode material for lithium secondary batteries through an EDTA-sol-gel method," *Solid State Ionics*, vol. 179, pp. 1763-1767, 2008.
- [67] F. Wu, L. Wang, C. Wu, Y. Bai, and F. Wang, "Study on  $Li_{1+x}V_3O_8$  synthesized by microwave sol-gel route," *Materials Chemistry and Physics*, vol. 115, pp. 707-711, 2009.
- [68] K. Kim, S. H. Park, T. H. Kwon, J. E. Park, H. Ahn, and M. J. Lee, "Characterization of Li-V-O nanorod phases and their effect on electrochemical properties of  $Li_{1+x}V_3O_8$  cathode materials synthesized by hydrothermal reaction and subsequent heat treatment," *Electrochimica Acta*, vol. 89, pp. 708-716, 2013.
- [69] H. Liu, Y. Wang, K. Wang, and H. Zhou, "Synthesis and electrochemical properties of single-crystalline  $LiV_3O_8$  nanorods as cathode materials for rechargeable lithium batteries," *Journal of Power Sources*, vol. 192, pp. 668-673, 2009.
- [70] L. Liu, L. Jiao, J. Sun, Y. Zhang, M. Zhao, H. Yuan, and Y. Wang, "Electrochemical properties of submicron-sized  $LiV_3O_8$  synthesized by a low-temperature reaction route," *Journal of Alloys and Compounds*, vol. 471, pp. 352-356, 2009.
- [71] X. Xu, Y. Z. Luo, L. Q. Mai, Y. L. Zhao, Q. Y. An, L. Xu, F. Hu, L. Zhang, and Q. J. Zhang, "Topotactically synthesized ultralong  $LiV_3O_8$  nanowire cathode materials for high-rate and long-life rechargeable lithium batteries," *NPG Asia Materials*, vol. 4, 2012.

- 
- [72] H. Liu, Y. Wang, W. Yang, and H. Zhou, "A large capacity of  $\text{LiV}_3\text{O}_8$  cathode material for rechargeable lithium-based batteries," *Electrochimica Acta*, vol. 56, pp. 1392-1398, 2011.
  - [73] W. Wu, J. Ding, H. Peng, and G. Li, "Synthesis and electrochemical properties of single-crystalline  $\text{LiV}_3\text{O}_8$  nanobelts for rechargeable lithium batteries," *Materials Letters*, vol. 65, pp. 2155-2157, 2011.
  - [74] Y. Gu and F. Jian, "Facile preparation and electrochemical properties of large-scale  $\text{Li}_{1+x}\text{V}_3\text{O}_8$  nanobelts," *Journal of Sol-Gel Science and Technology*, vol. 46, pp. 161-165, 2008/05/01 2008.
  - [75] H. Ma, Z. Yuan, F. Cheng, J. Liang, Z. Tao, and J. Chen, "Synthesis and electrochemical properties of porous  $\text{LiV}_3\text{O}_8$  as cathode materials for lithium-ion batteries," *Journal of Alloys and Compounds*, vol. 509, pp. 6030-6035, 2011.
  - [76] Y. Gu, D. Chen, X. Jiao, and F. Liu, "Linear attachment of  $\text{Li}_{1+a}\text{V}_3\text{O}_8$  nanosheets to 1-dimensional (1D) arrays: fabrication, characterization, and electrochemical properties," *Journal of Materials Chemistry*, vol. 16, pp. 4361-4366, 2006.
  - [77] S. Huang, Y. Lu, T. Q. Wang, C. D. Gu, X. L. Wang, and J. P. Tu, "Polyacrylamide-assisted freeze drying synthesis of hierarchical plate-arrayed  $\text{LiV}_3\text{O}_8$  for high-rate lithium-ion batteries," *Journal of Power Sources*, vol. 235, pp. 256-264, 2013.
  - [78] A. Pan, J.-G. Zhang, G. Cao, S. Liang, C. Wang, Z. Nie, B. W. Arey, W. Xu, D. Liu, J. Xiao, G. Li, and J. Liu, "Nanosheet-structured  $\text{LiV}_3\text{O}_8$  with high capacity and excellent stability for high energy lithium batteries," *Journal of Materials Chemistry*, vol. 21, pp. 10077-10084, 2011.
  - [79] S. Jouanneau, A. Le Gai La Salle, A. Verbaere, and D. Guyomard, "The origin of capacity fading upon lithium cycling in  $\text{Li}_{1.1}\text{V}_3\text{O}_8$ ," *Journal of the Electrochemical Society*, vol. 152, pp. A1660-A1667, 2005.
  - [80] J. H. Lee, J. K. Lee, and W. Y. Yoon, "Electrochemical Analysis of the Effect of Cr Coating the  $\text{LiV}_3\text{O}_8$  Cathode in a Lithium Ion Battery with a Lithium Powder Anode," *ACS Applied Materials & Interfaces*, vol. 5, pp. 7058-7064, 2013/08/14 2013.
  - [81] J. Shu, M. Shui, D. Xu, Y. Ren, D. Wang, Q. Wang, R. Ma, W. Zheng, S. Gao, L. Hou, J. Xu, J. Cui, Z. Zhu, and M. Li, "Large-scale synthesis of  $\text{Li}_{1.15}\text{V}_3\text{O}_8$  nanobelts and their lithium storage behavior studied by in situ X-ray diffraction," *Journal of Materials Chemistry*, vol. 22, pp. 3035-3043, 2012.
  - [82] F. Tanguy, J. Gaubicher, and D. Guyomard, "Capacity fading on cycling nano size grains of  $\text{Li}_{1.1}\text{V}_3\text{O}_8$ , electrochemical investigation," *Electrochimica Acta*, vol. 55, pp. 3979-3986, 2010.
  - [83] Q. Shi, R. Hu, M. Zeng, M. Dai, and M. Zhu, "The cycle performance and capacity fading mechanism of a  $\text{LiV}_3\text{O}_8$  thin-film electrode with a mixed amorphous-nanocrystalline microstructure," *Electrochimica Acta*, vol. 56, pp. 9329-9336, 2011.
  - [84] X. Ren, S. Hu, C. Shi, P. Zhang, Q. Yuan, and J. Liu, "Preparation of Ga-doped lithium trivanadates as cathode materials for lithium-ion batteries," *Electrochimica Acta*, vol. 63, pp. 232-237, 2012.
  - [85] X. Ren, S. Hu, C. Shi, P. Zhang, Q. Yuan, and J. Liu, "Preparation and electrochemical properties of Zr-doped  $\text{LiV}_3\text{O}_8$  cathode materials for lithium-ion batteries," *Journal of Solid State Electrochemistry*, vol. 16, pp. 2135-2141, 2012/06/01 2012.
  - [86] J. Sun, L. Jiao, L. Liu, X. Wei, L. Yang, S. Liu, H. Yuan, and Y. Wang, "Synthesis and Electrochemical Performance of  $\text{Ti}^{4+}$  Doped  $\text{LiV}_3\text{O}_8$ ," *Chinese Journal of Chemistry*, vol. 27, pp. 863-867, 2009.
  - [87] S. V. Pouchko, A. K. Ivanov-Schitz, F. G. B. Ooms, and J. Schoonman, "Lithium insertion into  $\gamma$ -type vanadium oxide bronzes doped with molybdenum(VI) and tungsten(VI) ions," *Solid State Ionics*, vol. 144, pp. 151-161, 2001.
  - [88] P. Rozier, M. Morcrette, P. Martin, L. Laffont, and J. M. Tarascon, "Solid solution ( $\text{Li}_{1.3-y}\text{Cu}_y$ ) $\text{V}_3\text{O}_8$ : Structure and electrochemistry," *Chemistry of Materials*, vol. 17, pp. 984-991, 2005.

- 
- [89] J. Sun, L. Jiao, H. Yuan, L. Liu, X. Wei, Y. Miao, L. Yang, and Y. Wang, "Preparation and electrochemical performance of  $\text{Ag}_x\text{Li}_{1-x}\text{V}_3\text{O}_8$ ," *Journal of Alloys and Compounds*, vol. 472, pp. 363-366, 2009.
- [90] S. Liang, J. Zhou, G. Fang, J. Liu, Y. Tang, X. Li, and A. Pan, "Ultrathin  $\text{Na}_{1.1}\text{V}_3\text{O}_{7.9}$  Nanobelts with Superior Performance as Cathode Materials for Lithium-Ion Batteries," *ACS Applied Materials & Interfaces*, vol. 5, pp. 8704-8709, 2013/09/11 2013.
- [91] Y. Tang, D. Sun, H. Wang, X. Huang, H. Zhang, S. Liu, and Y. Liu, "Synthesis and electrochemical properties of  $\text{NaV}_3\text{O}_8$  nanoflakes as high-performance cathode for Li-ion battery," *RSC Advances*, vol. 4, pp. 8328-8334, 2014.
- [92] H. Wang, S. Liu, Y. Ren, W. Wang, and A. Tang, "Ultrathin  $\text{Na}_{1.08}\text{V}_3\text{O}_8$  nanosheets-a novel cathode material with superior rate capability and cycling stability for Li-ion batteries," *Energy & Environmental Science*, vol. 5, pp. 6173-6179, 2012.
- [93] H. Wang, W. Wang, Y. Ren, K. Huang, and S. Liu, "A new cathode material  $\text{Na}_2\text{V}_6\text{O}_{16} \cdot x\text{H}_2\text{O}$  nanowire for lithium ion battery," *Journal of Power Sources*, vol. 199, pp. 263-269, 2012.
- [94] S. Liang, T. Chen, A. Pan, D. Liu, Q. Zhu, and G. Cao, "Synthesis of  $\text{Na}_{1.25}\text{V}_3\text{O}_8$  Nanobelts with Excellent Long-Term Stability for Rechargeable Lithium-Ion Batteries," *ACS Applied Materials & Interfaces*, vol. 5, pp. 11913-11917, 2013/11/27 2013.
- [95] R. Baddour-Hadjean, A. Boudaoud, S. Bach, N. Emery, and J.-P. Pereira-Ramos, "A Comparative Insight of Potassium Vanadates as Positive Electrode Materials for Li Batteries: Influence of the Long-Range and Local Structure," *Inorganic Chemistry*, vol. 53, pp. 1764-1772, 2014/02/03 2014.
- [96] V. Manev, A. Momchilov, A. Nassalevska, G. Pistoia, and M. Pasquali, "Potassium vanadates — promising materials for secondary lithium batteries," *Journal of Power Sources*, vol. 44, pp. 561-568, 1993.
- [97] K. West, B. Zachau-Christiansen, T. Jacobsen, and S. Skaarup, "Layered potassium vanadium oxides as host materials for lithium and sodium insertion," *Solid State Ionics*, vol. 40-41, Part 2, pp. 585-588, 1990.
- [98] S. Liang, T. Chen, A. Pan, J. Zhou, Y. Tang, and R. Wu, "Facile synthesis of belt-like  $\text{Ag}_{1.2}\text{V}_3\text{O}_8$  with excellent stability for rechargeable lithium batteries," *Journal of Power Sources*, vol. 233, pp. 304-308, 2013.
- [99] L. Liu, L. Jiao, J. Sun, Y. Zhang, M. Zhao, H. Yuan, and Y. Wang, "Electrochemical performance of  $\text{LiV}_{3-x}\text{Ni}_x\text{O}_8$  cathode materials synthesized by a novel low-temperature solid-state method," *Electrochimica Acta*, vol. 53, pp. 7321-7325, 2008.
- [100] L. Jiao, H. Li, H. Yuan, and Y. Wang, "Preparation of copper-doped  $\text{LiV}_3\text{O}_8$  composite by a simple addition of the doping metal as cathode materials for lithium-ion batteries," *Materials Letters*, vol. 62, pp. 3937-3939, 2008.
- [101] Y. Feng, Y. Li, and F. Hou, "Preparation and electrochemical properties of Cr doped  $\text{LiV}_3\text{O}_8$  cathode for lithium ion batteries," *Materials Letters*, vol. 63, pp. 1338-1340, 2009.
- [102] C. Q. Feng, L. F. Huang, Z. P. Guo, J. Z. Wang, and H. K. Liu, "Synthesis and electrochemical properties of  $\text{LiY}_{0.1}\text{V}_3\text{O}_8$ ," *Journal of Power Sources*, vol. 174, pp. 548-551, 2007.
- [103] Z.-j. Wu and Y. Zhou, "Effect of Ce-doping on the structure and electrochemical performance of lithium trivanadate prepared by a citrate sol-gel method," *Journal of Power Sources*, vol. 199, pp. 300-307, 2012.
- [104] L. Liu, H. Zhang, Y. Zhai, and Y. Tian, "Influences of  $\text{Nd}^{3+}$  doping on structure and electrochemical performance of layered  $\text{Li}_{1.05}\text{V}_3\text{O}_8$ ," *Journal of Rare Earths*, vol. 29, pp. 150-154, 2011.
- [105] M. Zhao, L. Jiao, H. Yuan, Y. Feng, and M. Zhang, "Study on the silicon doped lithium trivanadate as cathode material for rechargeable lithium batteries," *Solid State Ionics*, vol. 178, pp. 387-391, 2007.
- [106] T. A. Hewston and B. L. Chamberland, "A Survey of first-row ternary oxides  $\text{LiMO}_2$  ( $\text{M} = \text{Sc-Cu}$ )," *Journal of Physics and Chemistry of Solids*, vol. 48, pp. 97-108, 1987.

- 
- [107] E. J. Wu, P. D. Tepesch, and G. Ceder, "Size and charge effects on the structural stability of  $\text{LiMO}_2$  (M = transition metal) compounds," *Philosophical Magazine Part B*, vol. 77, pp. 1039-1047, 1998/04/01 1998.
- [108] M. Tabuchi, S. Tsutsui, C. Masquelier, R. Kanno, K. Ado, I. Matsubara, S. Nasu, and H. Kageyama, "Effect of Cation Arrangement on the Magnetic Properties of Lithium Ferrites ( $\text{LiFeO}_2$ ) Prepared by Hydrothermal Reaction and Post-annealing Method," *Journal of Solid State Chemistry*, vol. 140, pp. 159-167, 1998.
- [109] M. Tabuchi, K. Ado, H. Sakaebe, C. Masquelier, H. Kageyama, and O. Nakamura, "Preparation of  $\text{AFeO}_2$  (A = Li, Na) by hydrothermal method," *Solid State Ionics*, vol. 79, pp. 220-226, 1995.
- [110] E.-S. Lee, K.-W. Nam, E. Hu, and A. Manthiram, "Influence of Cation Ordering and Lattice Distortion on the Charge–Discharge Behavior of  $\text{LiMn}_{1.5}\text{Ni}_{0.5}\text{O}_4$  Spinel between 5.0 and 2.0 V," *Chemistry of Materials*, vol. 24, pp. 3610-3620, 2012/09/25 2012.
- [111] M. Yang, X. Zhao, Y. Bian, L. Ma, Y. Ding, and X. Shen, "Cation disordered rock salt phase  $\text{Li}_2\text{CoTiO}_4$  as a potential cathode material for Li-ion batteries," *Journal of Materials Chemistry*, vol. 22, pp. 6200-6205, 2012.
- [112] M. S. Islam and C. A. J. Fisher, "Lithium and sodium battery cathode materials: computational insights into voltage, diffusion and nanostructural properties," *Chemical Society Reviews*, vol. 43, pp. 185-204, 2014.
- [113] A. Van der Ven and G. Ceder, "Lithium Diffusion in Layered  $\text{Li}_x\text{CoO}_2$ ," *Electrochemical and Solid-State Letters*, vol. 3, pp. 301-304, 2000.
- [114] A. Van der Ven and G. Ceder, "Lithium diffusion mechanisms in layered intercalation compounds," *Journal of Power Sources*, vol. 97–98, pp. 529-531, 2001.
- [115] A. Van der Ven, J. Bhattacharya, and A. A. Belak, "Understanding Li Diffusion in Li-Intercalation Compounds," *Accounts of Chemical Research*, vol. 46, pp. 1216-1225, 2013/05/21 2012.
- [116] M. Jiang, B. Key, Y. S. Meng, and C. P. Grey, "Electrochemical and Structural Study of the Layered, "Li-Excess" Lithium-Ion Battery Electrode Material  $\text{Li}[\text{Li}_{1/9}\text{Ni}_{1/3}\text{Mn}_{5/9}]\text{O}_2$ ," *Chemistry of Materials*, vol. 21, pp. 2733-2745, 2009/07/14 2009.
- [117] M. M. Thackeray, S.-H. Kang, C. S. Johnson, J. T. Vaughey, R. Benedek, and S. A. Hackney, " $\text{Li}_2\text{MnO}_3$ -stabilized  $\text{LiMO}_2$  (M = Mn, Ni, Co) electrodes for lithium-ion batteries," *Journal of Materials Chemistry*, vol. 17, pp. 3112-3125, 2007.
- [118] V. Pralong, V. Gopal, V. Caignaert, V. Duffort, and B. Raveau, "Lithium-Rich Rock-Salt-Type Vanadate as Energy Storage Cathode:  $\text{Li}_{2-x}\text{VO}_3$ ," *Chemistry of Materials*, vol. 24, pp. 12-14, 2012/01/10 2011.
- [119] G. Pistoia, S. Panero, M. Tocci, R. V. Moshtev, and V. Manev, "Solid solutions  $\text{Li}_{1+x}\text{V}_3\text{O}_8$  as cathodes for high rate secondary Li batteries," *Solid State Ionics*, vol. 13, pp. 311-318, 1984.
- [120] L. Sebastian and J. Gopalakrishnan, " $\text{Li}_2\text{MTiO}_4$  (M = Mn, Fe, Co, Ni): New cation-disordered rocksalt oxides exhibiting oxidative deintercalation of lithium. Synthesis of an ordered  $\text{Li}_2\text{NiTiO}_4$ ," *Journal of Solid State Chemistry*, vol. 172, pp. 171-177, 2003.
- [121] S. Kalluri, K. H. Seng, Z. Guo, H. K. Liu, and S. X. Dou, "Electrospun lithium metal oxide cathode materials for lithium-ion batteries," *RSC Advances*, vol. 3, pp. 25576-25601, 2013.
- [122] X. Zhang, L. Ji, O. Toprakci, Y. Liang, and M. Alcoutlabi, "Electrospun nanofiber-based anodes, cathodes, and separators for advanced lithium-ion batteries," *Polymer Reviews*, vol. 51, pp. 239-264, 2011.
- [123] M. S. H. K.C.Patil, Tanu Rattan, S.T.Aruna, *Chemistry of Nanocrystalline Oxide Materials: Combustion Synthesis, Properties and Applications*: World Scientific Publishing Co. Pte. Ltd, 2008.
- [124] R. W. Cheary and A. Coelho, "A fundamental parameters approach to x-ray line-profile fitting," *J. Appl. Crystallogr.*, vol. 25, p. 109, 1992.
- [125] B. AXS, "TOPAS, Total Pattern Analysis Rietveld software," 4.2 ed, 1999.

- 
- [126] G. Socrates, *Infrared and Raman Characteristic Group Frequencies: Tables and Charts*: John Wiley & Sons, 2004.
  - [127] S. Brodowski, W. Amelung, L. Haumaier, C. Abetz, and W. Zech, "Morphological and chemical properties of black carbon in physical soil fractions as revealed by scanning electron microscopy and energy-dispersive X-ray spectroscopy," *Geoderma*, vol. 128, pp. 116-129, 2005.
  - [128] Y. L. Cheah, V. Aravindan, and S. Madhavi, "Improved Elevated Temperature Performance of Al-Intercalated  $V_2O_5$  Electrospun Nanofibers for Lithium-Ion Batteries," *ACS Applied Materials & Interfaces*, vol. 4, pp. 3270-3277, 2012/06/27 2012.
  - [129] R. Tossici, R. Marassi, M. Berrettoni, S. Stizza, and G. Pistoia, "Study of amorphous and crystalline  $Li_{1+x}V_3O_8$  by FTIR, XAS and electrochemical techniques," *Solid State Ionics*, vol. 57, pp. 227-234, 1992.
  - [130] G. Yang, G. Wang, and W. Hou, "Microwave Solid-State Synthesis of  $LiV_3O_8$  as Cathode Material for Lithium Batteries," *The Journal of Physical Chemistry B*, vol. 109, pp. 11186-11196, 2005/06/01 2005.
  - [131] X. Zhang and R. Frech, "Spectroscopic investigation of  $Li_{1+x}V_3O_8$ ," *Electrochimica Acta*, vol. 43, pp. 861-868, 1998.
  - [132] W. Gordy, "A Relation between Bond Force Constants, Bond Orders, Bond Lengths, and the Electronegativities of the Bonded Atoms," *The Journal of Chemical Physics*, vol. 14, pp. 305-320, 1946.
  - [133] Y. Kera, "Infrared study of alkali tri- and hexavanadates as formed from their melts," *Journal of Solid State Chemistry*, vol. 51, pp. 205-211, 1984.
  - [134] J. Kawakita, T. Kato, Y. Katayama, T. Miura, and T. Kishi, "Lithium insertion behaviour of  $Li_{1+x}V_3O_8$  with different degrees of crystallinity," *Journal of Power Sources*, vol. 81-82, pp. 448-453, 1999.
  - [135] H. He, G. Jin, H. Wang, X. Huang, Z. Chen, D. Sun, and Y. Tang, "Annealed  $NaV_3O_8$  nanowires with good cycling stability as a novel cathode for Na-ion batteries," *Journal of Materials Chemistry A*, vol. 2, pp. 3563-3570, 2014.
  - [136] C. O'Dwyer, D. Navas, V. Lavayen, E. Benavente, M. A. Santa Ana, G. González, S. B. Newcomb, and C. M. Sotomayor Torres, "Nano-Urchin: The Formation and Structure of High-Density Spherical Clusters of Vanadium Oxide Nanotubes," *Chemistry of Materials*, vol. 18, pp. 3016-3022, 2006/06/01 2006.
  - [137] N. Pinna, M. Willinger, K. Weiss, J. Urban, and R. Schlögl, "Local Structure of Nanoscopic Materials:  $V_2O_5$  Nanorods and Nanowires," *Nano Letters*, vol. 3, pp. 1131-1134, 2003/08/01 2003.
  - [138] M. Malta and R. M. Torresi, "Electrochemical and kinetic studies of lithium intercalation in composite nanofibers of vanadium oxide/polyaniline," *Electrochimica Acta*, vol. 50, pp. 5009-5014, 2005.
  - [139] P. S. a. D. Joniaková, "Vibrational spectra of vanadium(V) compounds. II. Vibrational spectra of divanadates with nonlinear bridge VOV," *Chemical Papers*, vol. 29, pp. 381-386, 1975.
  - [140] L. A. de Picciotto, K. T. Adendorff, D. C. Liles, and M. M. Thackeray, "Structural characterization of  $Li_{1+x}V_3O_8$  insertion electrodes by single-crystal X-ray diffraction," *Solid State Ionics*, vol. 62, pp. 297-307, 1993.
  - [141] G. Pistoia, M. Pasquali, G. Wang, and L. Li, "Li /  $Li_{1+x}V_3O_8$  Secondary Batteries: Synthesis and Characterization of an Amorphous Form of the Cathode," *Journal of the Electrochemical Society*, vol. 137, pp. 2365-2370, 1990.
  - [142] T. Jiang and M. L. Falk, "Calculations of the thermodynamic and kinetic properties of  $Li_{1+x}V_3O_8$ ," *Physical Review B*, vol. 85, p. 245111, 2012.
  - [143] S. Sarkar, H. Banda, and S. Mitra, "High capacity lithium-ion battery cathode using  $LiV_3O_8$  nanorods," *Electrochimica Acta*, vol. 99, pp. 242-252, 2013.
  - [144] Y. Liu, X. Zhou, and Y. Guo, "Structure and electrochemical performance of  $LiV_3O_8$  synthesized by solid-state routine with quenching in freezing atmosphere," *Materials Chemistry and Physics*, vol. 114, pp. 915-919, 2009.

- 
- [145] J. Kawakita, Y. Katayama, T. Miura, and T. Kishi, "Structural properties of  $\text{Li}_{1+x}\text{V}_3\text{O}_8$  upon lithium insertion at ambient and high temperature," *Solid State Ionics*, vol. 107, pp. 145-152, 1998.
  - [146] S. Jouanneau, A. Le Gal La Salle, A. Verbaere, M. Deschamps, S. Lascaud, and D. Guyomard, "Influence of the morphology on the Li insertion properties of  $\text{Li}_{1.1}\text{V}_3\text{O}_8$ ," *Journal of Materials Chemistry*, vol. 13, pp. 921-927, 2003.
  - [147] S. Jouanneau, A. Verbaere, S. Lascaud, and D. Guyomard, "Improvement of the lithium insertion properties of  $\text{Li}_{1.1}\text{V}_3\text{O}_8$ ," *Solid State Ionics*, vol. 177, pp. 311-315, 2006.
  - [148] S. Sarkar, A. Bhowmik, M. D. Bharadwaj, and S. Mitra, "Phase transition, electrochemistry, and structural studies of high rate  $\text{Li}_x\text{V}_3\text{O}_8$  cathode with nanoplate morphology," *Journal of the Electrochemical Society*, vol. 161, pp. A14-A22, 2014.
  - [149] J. Kawakita, T. Miura, and T. Kishi, "Lithium insertion and extraction kinetics of  $\text{Li}_{1+x}\text{V}_3\text{O}_8$ ," *Journal of Power Sources*, vol. 83, pp. 79-83, 1999.
  - [150] A. Manthiram, "Materials Challenges and Opportunities of Lithium Ion Batteries," *The Journal of Physical Chemistry Letters*, vol. 2, pp. 176-184, 2011/02/03 2011.
  - [151] H.-g. Wang, D.-l. Ma, Y. Huang, and X.-b. Zhang, "Electrospun  $\text{V}_2\text{O}_5$  Nanostructures with Controllable Morphology as High-Performance Cathode Materials for Lithium-Ion Batteries," *Chemistry – A European Journal*, vol. 18, pp. 8987-8993, 2012.
  - [152] J. Kawakita, T. Miura, and T. Kishi, "Charging characteristics of  $\text{Li}_{1+x}\text{V}_3\text{O}_8$ ," *Solid State Ionics*, vol. 118, pp. 141-147, 1999.
  - [153] J. Xu, H. Zhang, T. Zhang, Q. Pan, and Y. Gui, "Influence of heat-treatment temperature on crystal structure, morphology and electrochemical properties of  $\text{LiV}_3\text{O}_8$  prepared by hydrothermal reaction," *Journal of Alloys and Compounds*, vol. 467, pp. 327-331, 2009.
  - [154] G. Pistoia, M. Pasquali, Y. Geronov, V. Manev, and R. V. Moshtev, "Small particle-size lithium-vanadium oxide: An improved cathode material for high rate rechargeable lithium batteries," *Journal of Power Sources*, vol. 27, pp. 35-43, 1989.
  - [155] J. Dai, S. F. Y. Li, Z. Gao, and K. S. Siow, "Low - Temperature Synthesized  $\text{LiV}_3\text{O}_8$  as a Cathode Material for Rechargeable Lithium Batteries," *Journal of the Electrochemical Society*, vol. 145, pp. 3057-3062, 1998.
  - [156] J. Feng, X. Liu, X. Zhang, J. Jiang, J. Zhao, and M. Wang, "Effects of synthesis methods on  $\text{Li}_{1+x}\text{V}_3\text{O}_8$  as cathodes in lithium-ion batteries," *Journal of the Electrochemical Society*, vol. 156, pp. A768-A771, 2009.
  - [157] R. Shannon, "Revised effective ionic radii and systematic studies of interatomic distances in halides and chalcogenides," *Acta Crystallographica Section A*, vol. 32, pp. 751-767, 1976.
  - [158] M. Pasquali and G. Pistoia, "Lithium intercalation in  $\text{Na}_{1+x}\text{V}_3\text{O}_8$  synthesized by a solution technique," *Electrochimica Acta*, vol. 36, pp. 1549-1553, 1991.
  - [159] M. E. Spahr, P. Novák, W. Scheifele, O. Haas, and R. Nesper, "Electrochemistry of chemically lithiated  $\text{NaV}_3\text{O}_8$ : A positive electrode material for use in rechargeable lithium-ion batteries," *Journal of the Electrochemical Society*, vol. 145, pp. 421-427, 1998.
  - [160] J. Kawakita, K. Makino, Y. Katayama, T. Miura, and T. Kishi, "Preparation and lithium insertion behaviour of  $\text{Li}_y\text{Na}_{1.2-y}\text{V}_3\text{O}_8$ ," *Solid State Ionics*, vol. 99, pp. 165-171, 1997.
  - [161] J. Kawakita, T. Miura, and T. Kishi, "Comparison of  $\text{Na}_{1+x}\text{V}_3\text{O}_8$  with  $\text{Li}_{1+x}\text{V}_3\text{O}_8$  as lithium insertion host," *Solid State Ionics*, vol. 124, pp. 21-28, 1999.
  - [162] H. Liu, Y. Wang, L. Li, K. Wang, E. Hosono, and H. Zhou, "Facile synthesis of  $\text{NaV}_6\text{O}_{15}$  nanorods and its electrochemical behavior as cathode material in rechargeable lithium batteries," *Journal of Materials Chemistry*, vol. 19, pp. 7885-7891, 2009.
  - [163] J. Kawakita, T. Miura, and T. Kishi, "Effect of crystallinity on lithium insertion behaviour of  $\text{Na}_{1+x}\text{V}_3\text{O}_8$ ," *Solid State Ionics*, vol. 124, pp. 29-35, 1999.
  - [164] L. Liang, M. Zhou, and Y. Xie, "Electrospun Hierarchical  $\text{LiV}_3\text{O}_8$  Nanofibers Assembled from Nanosheets with Exposed {100} Facets and their Enhanced Performance in Aqueous Lithium-Ion Batteries," *Chemistry – An Asian Journal*, vol. 7, pp. 565-571, 2012.



- [165] L. Li, S. Peng, Y. Cheah, Y. Ko, P. Teh, G. Wee, C. Wong, and M. Srinivasan, "Electrospun Hierarchical  $\text{CaCo}_2\text{O}_4$  Nanofibers with Excellent Lithium Storage Properties," *Chemistry – A European Journal*, vol. 19, pp. 14823-14830, 2013.
- [166] G. Wee, H. Z. Soh, Y. L. Cheah, S. G. Mhaisalkar, and M. Srinivasan, "Synthesis and electrochemical properties of electrospun  $\text{V}_2\text{O}_5$  nanofibers as supercapacitor electrodes," *Journal of Materials Chemistry*, vol. 20, pp. 6720-6725, 2010.
- [167] O. Toprakci, L. Ji, Z. Lin, H. A. K. Toprakci, and X. Zhang, "Fabrication and electrochemical characteristics of electrospun  $\text{LiFePO}_4$ /carbon composite fibers for lithium-ion batteries," *Journal of Power Sources*, vol. 196, pp. 7692-7699, 2011.
- [168] P. F. Teh, Y. Sharma, S. S. Pramana, and M. Srinivasan, "Nanoweb anodes composed of one-dimensional, high aspect ratio, size tunable electrospun  $\text{ZnFe}_2\text{O}_4$  nanofibers for lithium ion batteries," *Journal of Materials Chemistry*, vol. 21, pp. 14999-15008, 2011.
- [169] P. F. Teh, Y. Sharma, Y. W. Ko, S. S. Pramana, and M. Srinivasan, "Tuning the morphology of  $\text{ZnMn}_2\text{O}_4$  lithium ion battery anodes by electrospinning and its effect on electrochemical performance," *RSC Advances*, vol. 3, pp. 2812-2821, 2013.
- [170] Y. Wu, P. Zhu, X. Zhao, M. V. Reddy, S. Peng, B. V. R. Chowdari, and S. Ramakrishna, "Highly improved rechargeable stability for lithium/silver vanadium oxide battery induced via electrospinning technique," *Journal of Materials Chemistry A*, vol. 1, pp. 852-859, 2013.
- [171] Y. Feng, Y. Li, and F. Hou, "Boron doped lithium trivanadate as a cathode material for an enhanced rechargeable lithium ion batteries," *Journal of Power Sources*, vol. 187, pp. 224-228, 2009.
- [172] Y. Kera and K. Hirota, "Infrared spectroscopic study of oxygen species in vanadium pentoxide with reference to its activity in catalytic oxidation," *Journal of Physical Chemistry*, vol. 73, pp. 3973-3981, 1969.
- [173] Y. Kera, "IR Spectra of Cs-Vanadates and its Catalytic Properties," in *Studies in Surface Science and Catalysis* vol. 7, ed, 1981, pp. 1400-1401.
- [174] K. Kim, S. H. Park, T. H. Kwon, J. E. Park, H. Ahn, and M.-J. Lee, "Characterization of Li-V-O nanorod phases and their effect on electrochemical properties of  $\text{Li}_{1+x}\text{V}_3\text{O}_8$  cathode materials synthesized by hydrothermal reaction and subsequent heat treatment," *Electrochimica Acta*, vol. 89, pp. 708-716, 2013.
- [175] E. Zhecheva, R. Stoyanova, R. Alcántara, P. Lavela, and J. L. Tirado, "Comparative analysis of the changes in local Ni/Mn environment in lithium–nickel–manganese oxides with layered and spinel structure during electrochemical extraction and reinsertion of lithium," *Journal of Power Sources*, vol. 174, pp. 519-523, 2007.
- [176] C. S. Johnson, J. S. Kim, A. J. Kropf, A. J. Kahaian, J. T. Vaughey, L. M. L. Fransson, K. Edström, and M. M. Thackeray, "Structural characterization of layered  $\text{Li}_x\text{Ni}_{0.5}\text{Mn}_{0.5}\text{O}_2$  ( $0 < x \leq 2$ ) oxide electrodes for Li batteries," *Chemistry of Materials*, vol. 15, pp. 2313-2322, 2003.
- [177] C. S. Johnson, J.-S. Kim, A. Jeremy Kropf, A. J. Kahaian, J. T. Vaughey, and M. M. Thackeray, "The role of  $\text{Li}_2\text{MO}_2$  structures (M=metal ion) in the electrochemistry of  $(x)\text{LiMn}_{0.5}\text{Ni}_{0.5}\text{O}_2 \cdot (1-x)\text{Li}_2\text{TiO}_3$  electrodes for lithium-ion batteries," *Electrochemistry Communications*, vol. 4, pp. 492-498, 2002.
- [178] J. S. Kim, C. S. Johnson, J. T. Vaughey, M. M. Thackeray, S. A. Hackney, W. Yoon, and C. P. Grey, "Electrochemical and structural properties of  $x\text{Li}_2\text{M}'\text{O}_3 \cdot (1-x)\text{LiMn}_{0.5}\text{Ni}_{0.5}\text{O}_2$  electrodes for lithium batteries ( $\text{M}' = \text{Ti, Mn, Zr}$ ;  $0 \leq x \leq 0.3$ )," *Chemistry of Materials*, vol. 16, pp. 1996-2006, 2004.
- [179] J. R. Dahn, U. von Sacken, and C. A. Michal, "Structure and electrochemistry of  $\text{Li}_{1+y}\text{NiO}_2$  and a new  $\text{Li}_2\text{NiO}_2$  phase with the  $\text{Ni}(\text{OH})_2$  structure," *Solid State Ionics*, vol. 44, pp. 87-97, 1990.
- [180] Z. Lu and J. R. Dahn, "Understanding the anomalous capacity of  $\text{Li}/\text{Li}[\text{Ni}_x\text{Li}_{(1/3-2x/3)}\text{Mn}_{(2/3-x/3)}]\text{O}_2$  cells using in situ X-ray diffraction and electrochemical studies," *Journal of the Electrochemical Society*, vol. 149, pp. A815-A822, 2002.

- 
- [181] N. Yabuuchi, K. Yoshii, S. T. Myung, I. Nakai, and S. Komaba, "Detailed studies of a high-capacity electrode material for rechargeable batteries,  $\text{Li}_2\text{MnO}_3\text{-LiCo}_{1/3}\text{Ni}_{1/3}\text{Mn}_{1/3}\text{O}_2$ ," *Journal of the American Chemical Society*, vol. 133, pp. 4404-4419, 2011.
  - [182] J. Hong, H. D. Lim, M. Lee, S. W. Kim, H. Kim, S. T. Oh, G. C. Chung, and K. Kang, "Critical role of oxygen evolved from layered Li-Excess metal oxides in lithium rechargeable batteries," *Chemistry of Materials*, vol. 24, pp. 2692-2697, 2012.
  - [183] J. Vetter, P. Novák, M. R. Wagner, C. Veit, K. C. Möller, J. O. Besenhard, M. Winter, M. Wohlfahrt-Mehrens, C. Vogler, and A. Hammouche, "Ageing mechanisms in lithium-ion batteries," *Journal of Power Sources*, vol. 147, pp. 269-281, 2005.
  - [184] A. van Bommel, L. J. Krause, and J. R. Dahn, "Investigation of the Irreversible Capacity Loss in the Lithium-Rich Oxide  $\text{Li}[\text{Li}_{1/5}\text{Ni}_{1/5}\text{Mn}_{3/5}]\text{O}_2$ ," *Journal of the Electrochemical Society*, vol. 158, pp. A731-A735, 2011.
  - [185] J. Kikkawa, T. Akita, M. Tabuchi, K. Tatsumi, and M. Kohyama, "Participation of Oxygen in Charge/Discharge Reactions in  $\text{Li}_{1.2}\text{Mn}_{0.4}\text{Fe}_{0.4}\text{O}_2$ : Evidence of Removal/Reinsertion of Oxide Ions," *Journal of the Electrochemical Society*, vol. 158, pp. A760-A768, 2011.
  - [186] A. R. Armstrong, M. Holzapfel, P. Novák, C. S. Johnson, S. H. Kang, M. M. Thackeray, and P. G. Bruce, "Demonstrating oxygen loss and associated structural reorganization in the lithium battery cathode  $\text{Li}[\text{Ni}_{0.2}\text{Li}_{0.2}\text{Mn}_{0.6}]\text{O}_2$ ," *Journal of the American Chemical Society*, vol. 128, pp. 8694-8698, 2006.
  - [187] T. Horikawa, K. Ogawa, K. Mizuno, J. Hayashi, and K. Muroyama, "Preparation and characterization of the carbonized material of phenol-formaldehyde resin with addition of various organic substances," *Carbon*, vol. 41, pp. 465-472, 2003.
  - [188] Y. S. Lee, J. H. Lee, Y. W. Kim, Y. K. Sun, and S. M. Lee, "Rapidly solidified Ti-Si alloys/carbon composites as anode for Li-ion batteries," *Electrochimica Acta*, vol. 52, pp. 1523-1526, 2006.
  - [189] A. Hashem, A. Abdel Ghany, K. Nikolowski, and H. Ehrenberg, "Effect of carbon coating process on the structure and electrochemical performance of  $\text{LiNi}_{0.5}\text{Mn}_{0.5}\text{O}_2$  used as cathode in Li-ion batteries," *Ionics*, vol. 16, pp. 305-310, 2010/05/01 2010.
  - [190] B. Lin, Z. Wen, X. Wang, and Y. Liu, "Preparation and characterization of carbon-coated  $\text{Li}[\text{Ni}_{1/3}\text{Co}_{1/3}\text{Mn}_{1/3}]\text{O}_2$  cathode material for lithium-ion batteries," *Journal of Solid State Electrochemistry*, vol. 14, pp. 1807-1811, 2010/10/01 2010.
  - [191] P. G. Bruce, B. Scrosati, and J. M. Tarascon, "Nanomaterials for rechargeable lithium batteries," *Angewandte Chemie - International Edition*, vol. 47, pp. 2930-2946, 2008.
  - [192] J. Maier, "Nanoionics: Ion transport and electrochemical storage in confined systems," *Nature Materials*, vol. 4, pp. 805-815, 2005.
  - [193] A. S. Aricò, P. Bruce, B. Scrosati, J. M. Tarascon, and W. Van Schalkwijk, "Nanostructured materials for advanced energy conversion and storage devices," *Nature Materials*, vol. 4, pp. 366-377, 2005.
  - [194] B. Kang and G. Ceder, "Battery materials for ultrafast charging and discharging," *Nature*, vol. 458, pp. 190-193, 2009.
  - [195] Y. S. Hu, L. Kienle, Y. G. Guo, and J. Maier, "High lithium electroactivity of nanometer-sized rutile  $\text{TiO}_2$ ," *Advanced Materials*, vol. 18, pp. 1421-1426, 2006.
  - [196] P. Balaya, H. Li, L. Kienle, and J. Maier, "Fully reversible homogeneous and heterogeneous Li storage in  $\text{RuO}_2$  with high capacity," *Advanced Functional Materials*, vol. 13, pp. 621-625, 2003.
  - [197] N. Meethong, H. Y. S. Huang, W. C. Carter, and Y. M. Chiang, "Size-dependent lithium miscibility gap in nanoscale  $\text{Li}_{1-x}\text{FePO}_4$ ," *Electrochemical and Solid-State Letters*, vol. 10, pp. 134-138, 2007.
  - [198] G. Sudant, E. Baudrin, D. Larcher, and J. M. Tarascon, "Electrochemical lithium reactivity with nanotextured anatase-type  $\text{TiO}_2$ ," *Journal of Materials Chemistry*, vol. 15, pp. 1263-1269, 2005.
  - [199] M. Wagemaker and F. M. Mulder, "Properties and Promises of Nanosized Insertion Materials for Li-Ion Batteries," *Accounts of Chemical Research*, vol. 46, pp. 1206-1215, 2013/05/21 2012.

- 
- [200] Y. Wang, H. Li, P. He, E. Hosono, and H. Zhou, "Nano active materials for lithium-ion batteries," *Nanoscale*, vol. 2, pp. 1294-1305, 2010.
  - [201] C. Wu and Y. Xie, "Promising vanadium oxide and hydroxide nanostructures: from energy storage to energy saving," *Energy & Environmental Science*, vol. 3, pp. 1191-1206, 2010.
  - [202] M. S. Whittingham, "Inorganic nanomaterials for batteries," *Dalton Transactions*, pp. 5424-5431, 2008.
  - [203] D. He and N. N. Ekere, "Effect of particle size ratio on the conducting percolation threshold of granular conductive-insulating composites," *Journal of Physics D: Applied Physics*, vol. 37, pp. 1848-1852, 2004.
  - [204] R. Mukherjee, R. Krishnan, T.-M. Lu, and N. Koratkar, "Nanostructured electrodes for high-power lithium ion batteries," *Nano Energy*, vol. 1, pp. 518-533, 2012.
  - [205] R. Pitchai, V. Thavasi, S. G. Mhaisalkar, and S. Ramakrishna, "Nanostructured cathode materials: a key for better performance in Li-ion batteries," *Journal of Materials Chemistry*, vol. 21, pp. 11040-11051, 2011.
  - [206] M.-K. Song, S. Park, F. M. Alamgir, J. Cho, and M. Liu, "Nanostructured electrodes for lithium-ion and lithium-air batteries: the latest developments, challenges, and perspectives," *Materials Science and Engineering: R: Reports*, vol. 72, pp. 203-252, 2011.
  - [207] A. Manthiram, A. Vadivel Murugan, A. Sarkar, and T. Muraliganth, "Nanostructured electrode materials for electrochemical energy storage and conversion," *Energy & Environmental Science*, vol. 1, pp. 621-638, 2008.
  - [208] D. T. Schoen, S. Meister, H. Peng, C. Chan, Y. Yang, and Y. Cui, "Phase transformations in one-dimensional materials: Applications in electronics and energy sciences," *Journal of Materials Chemistry*, vol. 19, pp. 5879-5890, 2009.
  - [209] X. Chen, E. Pomerantseva, K. Gregorczyk, R. Ghodssi, and G. Rubloff, "Cathodic ALD  $V_2O_5$  thin films for high-rate electrochemical energy storage," *RSC Advances*, vol. 3, pp. 4294-4302, 2013.
  - [210] D. Liu and G. Cao, "Engineering nanostructured electrodes and fabrication of film electrodes for efficient lithium ion intercalation," *Energy and Environmental Science*, vol. 3, pp. 1218-1237, 2010.
  - [211] Y. Lu, L. Wang, J. Song, D. Zhang, M. Xu, and J. B. Goodenough, "Aluminum-stabilized NASICON-structured  $Li_3V_2(PO_4)_3$ ," *Journal of Materials Chemistry A*, vol. 1, pp. 68-72, 2013.
  - [212] A. Wadsley, "Crystal chemistry of non-stoichiometric pentavalent vanadium oxides: crystal structure of  $Li_{1+x}V_3O_8$ ," *Acta Crystallographica*, vol. 10, pp. 261-267, 1957.
  - [213] I. D. Brown and R. D. Shannon, "Empirical bond-strength-bond-length curves for oxides," *Acta Crystallographica Section A*, vol. 29, pp. 266-282, 1973.
  - [214] H. Y. P. Hong, "Solid electrolytes containing both mobile and immobile alkali ions," *Journal of Power Sources*, vol. 5, pp. 137-142, 1980.
  - [215] M. Shui, W. Zheng, J. Shu, Q. Wang, S. Gao, D. Xu, L. Chen, L. Feng, and Y. Ren, "Synthesis, spectral character, electrochemical performance and in situ structure studies of  $Li_{1+x}V_3O_8$  cathode material prepared by tartaric acid assisted sol-gel process," *Materials Research Bulletin*, vol. 47, pp. 2455-2459, 2012.
  - [216] C. Delmas, H. Cognac-Auradou, J. M. Cocciantelli, M. Ménétrier, and J. P. Doumerc, "The  $Li_xV_2O_5$  system: An overview of the structure modifications induced by the lithium intercalation," *Solid State Ionics*, vol. 69, pp. 257-264, 1994.
  - [217] J. N. Reimers and J. R. Dahn, "Electrochemical and in situ x-ray diffraction studies of lithium intercalation in  $Li_xCoO_2$ ," *Journal of the Electrochemical Society*, vol. 139, pp. 2091-2097, 1992.
  - [218] K. Dokko, M. Nishizawa, S. Horikoshi, T. Itoh, M. Mohamedi, and I. Uchida, "In Situ Observation of  $LiNiO_2$  Single-Particle Fracture during Li-Ion Extraction and Insertion," *Electrochemical and Solid-State Letters*, vol. 3, pp. 125-127, 2000.

- 
- [219] Y. Koyama, N. Yabuuchi, I. Tanaka, H. Adachi, and T. Ohzuku, "Solid-State Chemistry and Electrochemistry of  $\text{LiCo}_{1/3}\text{Ni}_{1/3}\text{Mn}_{1/3}\text{O}_2$  for Advanced Lithium-Ion Batteries: I. First-Principles Calculation on the Crystal and Electronic Structures," *Journal of the Electrochemical Society*, vol. 151, pp. A1545-A1551, 2004.

# Publications

**Y.W. Ko**, P.F. The, S.S. Pramana, C. Wong, Y.L Cheah, L. Li, S. Madhavi, Electrospun single phase  $\text{Na}_{1.2}\text{V}_3\text{O}_8$  with tunable morphology as high performance cathode material for lithium-ion batteries, *ChemElectroChem*, In Press.

P.F. Teh, Y. Sharma, **Y.W. Ko**, S.S. Pramana, S. Madhavi, Tuning the morphology of  $\text{ZnMn}_2\text{O}_4$  lithium ion battery anodes by electrospinning and its effect on electrochemical performance, *RSC Advances*, 2013, 3, (8), 2812-2821.

P.F. Teh, S.S. Pramana, Y. Sharma, **Y.W. Ko**, S. Madhavi, Electrospun  $\text{Zn}_{1-x}\text{Mn}_x\text{Fe}_2\text{O}_4$  nanofibers as anodes for lithium-ion batteries and the impact of mixed transition metallic oxides on battery performance, *ACS Applied Materials & Interfaces*, 2013, 5, (12), 5461-5467.

L. Li, S. Peng, Y. L. Cheah, **Y.W. Ko**, P. F. Teh, G. Wee, C. Wong, S. Madhavi, Electrospun hierarchical  $\text{CaCo}_2\text{O}_4$  nanofibers with excellent lithium storage properties, *Chemistry – A European Journal*, 2013, 19, (44), 14823-14830

L. Li, Y.L. Cheah, **Y.W. Ko**, P.F. Teh, G. Wee, C. Wong, S. Peng, S. Madhavi, The facile synthesis of hierarchical porous flower-like  $\text{NiCo}_2\text{O}_4$  with superior lithium storage properties, *Journal of Materials Chemistry A*, 2013, 1, (36), 10935-10941.

L. Li, S. Peng, Y. L. Cheah, J. Wang, P. F. Teh, **Y.W. Ko**, C. Wong, S. Madhavi, Electrospun eggroll-like  $\text{CaSnO}_3$  nanotubes with high lithium storage performance, *Nanoscale*, 2013, 5, (1), 134-138.

L. Li, S. Peng, Y. L. Cheah, P. F. Teh, J. Wang, G. Wee, **Y.W. Ko**, C. Wong, S. Madhavi, Electrospun porous  $\text{NiCo}_2\text{O}_4$  nanotubes as advanced electrodes for electrochemical capacitors, *Chemistry - A European Journal*, 2013, 19, (19), 5892-5898.

L. Li, S. Peng, J. Wang, Y.L. Cheah, P. F. Teh, **Y.W. Ko**, C. Wong, S. Madhavi, Facile approach to prepare porous  $\text{CaSnO}_3$  nanotubes via a single spinneret electrospinning technique as anodes for lithium ion batteries, *ACS Applied Materials and Interfaces*, 2012, 4, (11), 6005-6012.